Sindre Engzelius Gylver

Feeding of Alumina in Molten Cryolite Bath

Doctoral thesis

NTNU
Norwegian University of
Science and Technology

Sindre Engzelius Gylver

Feeding of Alumina in Molten Cryolite Bath

Thesis for the Degree of Philosophiae Doctor

Trondheim, January 2023

Norwegian University of Science and Technology
Faculty of Natural Sciences
Department of Materials Science and Engineering

NTNU
Norwegian University of
Science and Technology

Preface

This thesis has been submitted to Norwegian University of Science and Technology, NTNU, in partial fulfillment of the requirements for the Degree of Philosophiae Doctor.

The work was performed at the Department of Materials Science and Engineering at NTNU in Trondheim from 2018 to 2022. The work was supervised by Kristian Etienne Einarsrud (Main supervisor, Professor, NTNU) and Espen Sandnes (Co-supervisor, Associate Professor, NTNU).

Trondheim, 2022-09-28

Sindre Engzelius Gylver

Summary

Alumina is the principal raw-material used for the production of aluminum in the Hall-Héroult process and is fed to the electrolytic bath in batches regularly. Maintaining a stable concentration in the bath is important in order to achieve an efficient process, hence requiring alumina to disperse, dissolve and distribute fast. However, bath might freeze around the particles, creating rafts that will prevent alumina from dissolve. A better understanding in how rafts form and disintegrate is necessary in order to improve the feeding process. Studies have been conducted in both lab and industrial scale, and with numerical modeling.

In an industrial cell, the concentration of Hydrogen Fluorides (HF) was measured continuously over 43 consecutive days, in order to establish dependencies between HF-emission and alumina feeding, as well as operational conditions. The measurement revealed that HF-concentration is higher when the feeding frequency is high, and it increases rapidly after each feeding, followed by its slower decline. The longer decline might be caused by the formation of rafts, where HF can get trapped inside the structure.

Feeding of alumina was simulated in a model at room temperature, where bath and alumina were respectively replaced by water and organic particles. The effect of particle size distribution, temperature difference between particles and liquid, and gas induced convection were investigated. All of the mention parameters had a significant effect on the raft floating time, where particle size had the highest impact. Halving the average particle size resulted in an almost five-fold increase on floating time.

A method for creating and extraction of rafts in a lab cell has been developed, and further adapted for recordings from above. The effect of alumina temperature, chemical changes due to gas treatment, water content, Lithium Fluoride in the bath and fines have on raft formation was studied.

When 4 g secondary alumina is added to the melt, a raft is formed, with mass loss rates between 0.8 and 1.6 $\mathrm{g\,min^{-1}}$. They were found to have a porous structure in the middle and flakes of frozen bath around them, with an average porosity of 8.2%. Rafts formed from primary alumina had a lower porosity, 0.8 % on average, hence indicating that the pores in rafts are formed due to release of components added to powder during the dry scrubbing process.

Increased alumina temperature will decrease the amount of bath freezing around the dose, and rafts were seen to be formed up to 500-600 °C.

Rafts created from fines were smaller in size, but their mass loss was lower compared

with bulk, between 0.1 and 1 $\mathrm{g\,min^{-1}}$. Video recordings confirmed that the lower mass is due to a poorer spreading of powder, hence resulting in lesser bath freezing.

In parallel, Computational Fluid Dynamics (CFD) in OpenFOAM was used to develop a continuous multiphase framework based on the Volume of Fluid (VOF) method for simulating the alumina feeding process. An immiscible incompressible multiphase model accounting for transfer of mass, momentum and energy was developed, and two models were implemented and verified.

A framework for modeling solidification was developed, modeling the solidified phase as a fluid with (artificially) high viscosity. The model was found to exhibit desired effects when the raft was considered to be a rigid object, with stronger damping effect for thicker layer of freeze. When alumina is assumed to be a Newtonian phase, the effect is not visible, as the spreading of the dose will inhibit a sufficient large layer of freeze to be formed.

Modeling of the alumina particles was realized by the µ(I)-rheology, which was implemented as a viscosity model. A parametric study was conducted, where an alumina dose collapsed on a flat surface. The study identified the rheology parameters μ_2 and I_0 to be of high importance. They are currently not been measured for alumina, and further experiments should quantify their values.

Applying µ(I)-rheology in a case where alumina is added into bath of cryolite showed that the dose spreads out and creates a flat structure with nonuniform thickness. The model also allows for pieces to disperse into the melt of detach from the main dose, which is in accordance with what has been observed in lab experiments.

The models were also successfully coupled together, where the raft shape as described above was formed and frozen bath aided in holding the structure together.

iv

Sammendrag

Alumina er et råstoff som brukes til produksjon av aluminium i Hall-Héroult-prosessen, og mates til elektrolysebadet regelmessig i batcher. Å opprettholde en stabil konsentrasjon i badet er viktig for å oppnå en effektiv prosess, og krever derfor at alumina dispergeres, løses opp og fordeles raskt. Bad kan imidlertid fryse rundt partiklene, og skape flåter som vil hindre alumina i å løse seg opp. En bedre forståelse av hvordan flåter dannes og løses opp er nødvendig for å forbedre mateprosessen. Studier har blitt utført i både laboratorie- og industriskala, og med numerisk modellering.

I en industricelle ble konsentrasjonen av hydrogenfluorider (HF) målt kontinuerlig over 43 påfølgende dager, for å etablere avhengigheter mellom HF-utslipp og tilførsel av alumina, samt driftsforhold. Målingen viste at HF-konsentrasjonen er høyere når matefrekvensen er høy, og den øker raskt etter hver mating, etterfulgt av langsommere nedgang. Den lengre nedgangen kan være forårsaket av dannelsen av flåter, hvor HF kan bli fanget inne i strukturen.

Mating av alumina ble simulert i en modell ved romtemperatur, hvor bad og alumina ble erstattet med henholdsvis vann og organiske partikler. Effekten av partikkelstørrelsesfordeling, temperaturforskjell mellom partikler og væske og gassindusert konveksjon ble undersøkt. Alle de nevnte parameterne hadde en signifikant effekt på flåtens flytetid, hvor partikkelstørrelsen hadde størst innvirkning. Halvering av den gjennomsnittlige partikkelstørrelsen resulterte i en fire ganger økning i flytetid.

En metode for dannelse og uttak av flåter i en labcelle er utviklet, og videre tilpasset for videoopptak ovenfra. Effekten av aluminatemperatur, kjemiske endringer på grunn av gassrens, vanninnhold, litiumfluorid i bad, og finstoff har på flåtedannelsen ble studert.

Når 4 g sekundær alumina tilsettes badet, dannes en flåte, med massetapsrater mellom 0,8 og 1,6 $g\,min^{-1}$. De ble funnet å ha en porøs struktur i midten og flak av frosset bad rundt seg, med en gjennomsnittlig porøsitet på 8,2

Økt aluminatemperatur vil redusere mengden bad som fryser rundt dosen, og det ble sett at flåter ble dannet opp til 500-600 °C.

Flåter laget av finstoff var mindre i størrelse, men massetapet var lavere sammenlignet med bulk, mellom 0,1 og 1 $g\,min^{-1}$. Videoopptak bekreftet at den lavere massen skyldes dårligere spredning av pulver, noe som resulterer i mindre frysing av bad.

Samtidig har numeriske simuleringer blitt brukt i OpenFOAM for å utvikle et kontinuerlig flerfaserammeverk basert på Volume of Fluid (VOF)-metoden for å simulere mateprosessen. En ikke-blandbar, inkompressibel, flerfasemodell som løser masse, moment- og energibalansen ble utviklet, og to modeller ble implementert og verifisert.

Et rammeverk for modellering av påfrysning ble utviklet, som modellerer den frysende fasen som en væske med (kunstig) høy viskositet. Modellen viste ønskede effekter når flåten ble ansett å være et rigid objekt, med sterkere dempende effekt for tykkere fryselag. Når alumina betraktes som en Newtonsk fase, er effekten ikke synlig, da spredning av dose vil hindre at et tilstrekkelig stort lag med frysing dannes. Modellering av aluminapartiklene ble realisert ved µ(I)-reologien, som ble implementert som en viskositetsmodell. En parametrisk studie ble utført, hvor en aluminadose kollapset på en flat overflate. Studien identifiserte at reologiparametrene μ_2 og I_0 var av høy betydning. De er foreløpig ikke målt for alumina, og ytterligere eksperimenter bør kvantifisere deres verdier.

Bruk av µ(I)-reologi i et case hvor alumina ble tilsatt i et kryolittbad viste at dosen sprer seg ut og skaper en flat struktur med ujevn tykkelse. Modellen gjør det også mulig for biter å spre seg i smelten eller løsne fra hoveddosen, noe som er i samsvar med det som er observert i laboratorieeksperimenter.

Modellene ble også vellykket koblet sammen, hvor flåteformen som beskrevet ovenfor ble dannet og frosset bad hjalp til med å holde strukturen sammen.

Acknowledgment

First of all, I must thank my supervisor Professor Kristian Etienne Einarsrud for his excellent advice and great discussion, often including more or less successful jokes. This thesis would not have been realized without you.

I also wish to express my gratitude towards my co-supervisor Associate Professor Espen Sandnes for good discussions as well. Being a part of the SFI have given me the benefit of close collaboration with industry partner. I wish to express my gratitude towards all the participants of the alumina group, who have showed interest in my work and provided me with industrial perspectives.

I will also acknowledge SINTEF for the use of their laboratory facilities and research engineer Henrik Gudbrandsen for his advice and help during my experiments. Hydro has been very helpful with providing materials for my experiments and analyses, which I greatly appreciate. Alcoa Mosjøen have also been a contributor of great importance, giving me the opportunity to work at their plant in 2017, thus motivating me to continuing with a PhD. I am also grateful for the multiple visits with good discussions and the opportunity to do measurements at their site.

I have been lucky to have collaborated with numerous students, and I must therefore give an extra shout-out to Åste Follo, Simen Aase, Sigmund Forberg and Simen Bekkevoll, the latter one twice, for all the good work you have done. I would also like to thank Dr. Luis Bracamonte, who was working on the same topic as me, for a good collaboration.

I would also like to thank both the administrative and technical staff at the Department for helping me out with smaller and larger problems. The same goes for the staff at the Resource, Energy and Environment, who have been my regularly discussion lunch partners. I will also show my gratitude to the INPUT-group for including me during my duty work at Kalvskinnet, and for all the wine I won in their lottery.

The sport union NTNUI, in particular the orienteering group and Studenterhytta, has provided me with lifelong friends and activities outside my studies, which I am very grateful of.

Finally, I wish to thank my friends and family for supporting and motivating me throughout all these years.

S.E.G.

Contents

List of Figures

List of Tables

Nomenclature

Abbreviations

ACD   Anodic Cathodic Distance

BET   Braunauer, Emmet and Teller

CCD   Critical Current Density

CFD   Computational Fluid Dynamics

CT   Computed Tomography

FVM   Finite Volume Method

GTC   Gas Treatment Center

KTGF   Kinetic Theory of Granular Flow

LOI   Loss on Ignition

MOI   Moisture on Ignition

PIV   Particle image velocimetry

PSD   Particle size distribution

SEM   Scanning Electron Microscopy

SGA   Smelter Grade Alumina

SPH   Smoothed particle Hydrodynamics

VOF   Volume of Fluid

XRD   X-ray Diffraction

Chemical Symbols

$Al(OH)_3$ Gibbsite

Al_2O_3 Alumina

AlF_3 Aluminum Fluoride

$AlO(OH)$ Bohemite

Al Aluminum

CaF_2 Calcium Fluoride

CaO   Calcium oxide

CO_2 Carbondioxide

C   Carbon

Fe_2O_3 Iron(III)oxide

H_2O Water

HF   Hydrogen fluoride

KF   Potassium Fluoride

LiF   Lithium Fluoride

MgF_2 Magnesium Fluoride

Na_2O Sodium oxide

Na_3AlF_6 Cryolite

P_2O_5 Phosphorus pentoxide

SiO_2 Silica

Mathematical Symbols

α Volumetric phase fraction

$\bar{C}$ Average concentration

$\bar{T}_L$ Temperature constant

$\bar{T}_{ref}$ Reference temperature

$\boldsymbol{\sigma}$ Cauchy stress sensor

$\boldsymbol{\tau}$ Shear stress sensor

$\boldsymbol{D}$ Strain rate tensor

$\boldsymbol{F}$ Body force

$\boldsymbol{g}$ Gravity, body force

$\boldsymbol{q}$ Heat flux

$\boldsymbol{u}$ Velocity

χ Arbitrary property

$\dot{R}$	Mass source term
κ	Thermal conductivity
μ', A	μ(I)-properties
μ_1, μ_2, I_0	μ(I)-properties
μ_∞, a, I_1	μ(I)-properties
ν	Kinematic viscosity
ν_t	Turbulent viscosity
ν_{sol}	Artificial solidification viscosity
ρ	Density
τ	Viscosus shear rate tensor
$\tilde{A}$	Exponential solidification constant
$\tilde{m}, \tilde{n}$	Power law constants
A'	Surface area
a_0, L_0, H_0	Granular column parameters
C	Concentration
C_v	Damping strength constant
C_{sat}	Alumina saturation concentration
D	Strain rate
E	Energy
g_s	Volumetric solid fraction
H	Entalphy
I	Inertial number
K	Dissolution rate constant
L	Latent heat of fusion
m	Mass
p	Pressure
Q	Heat

S	Source term
T	Temperature
T_M	Melting temperature
U	Internal energy
V	Control volume
W	Work

Subscripts

a	Alumina
b	Bath
ca	Average feeding cycle value
ca	Feeding cycle
fa	Average feeding value
fa	Feeding
g	Gas phase
g	Gas
i, k, j	Arbitrary phases
ks	Interphase interactions
m	Mixture
ST	Surface tension
x, y, z	Cartesian coordinates

Part I

Introduction and Background

Chapter 1: Introduction

1.1 Production of aluminum

Aluminum is a lightweight metal, used in multiple applications, spanning from food packaging to cars and building material and is relatively easy to recycle. The metal is not found in pure form and is primarily produced through the Hall-Héroult process, discovered in 1886 by Charles Hall and Paul Héroult independently of each other [1]. In this process, alumina (Al_2O_3) is dissolved into a bath of molten salts consisting mainly of cryolite (Na_3AlF_6) and aluminum fluoride (AlF_3) at approximately 960°C. Dissolved alumina reacts with carbon by electrolysis, creating aluminum according to the following simplified reaction:

$$\frac{1}{2}Al_2O_3 + \frac{3}{2}C \longrightarrow Al + \frac{3}{2}CO_2. \tag{1.1}$$
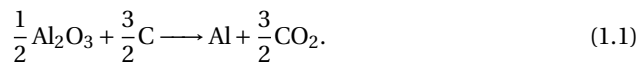
Figure 1.1 shows the cross section of the cell. The metal will form at the bottom of the cell and must be tapped out regularly.
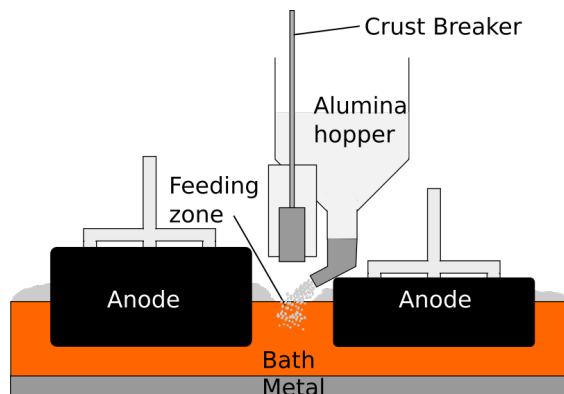
Figure 1.1: Cross section of a Hall-Héroult cell, where a feeder is placed in the center channel of the cell

About 13 kWh is required to produce one kilogram of aluminum [2], which is above the theoretical consumption derived from thermodynamics. Norway alone produces about 1.3 million tons of aluminum each year [3], [4], requiring about 17 TWh, which is around 10 % of Norway's total electricity production [5]. Even a small reduction in energy consumption will hence have a large impact of the total energy usage.

Alumina is added to the melt regularly by point feeders, and about 1 kg of powder is added each 1-3 minute. First, a crust breaker ensures that there is an opening in the cover material for alumina to be fed in, before the powder is added in the melt from a hopper, also illustrated in figure 1.1. Ultimately, the powder should disperse and dissolve fast, shown as the green path in figure 1.2. However, a slower path also exists, where alumina agglomerate together with bath and form what is known as an agglomerate, or a raft, which will hinder the powder from dissolving. This raft can float on the bath surface or on the bath-metal interface (orange path) or sink to the bottom and form sludge (red path).
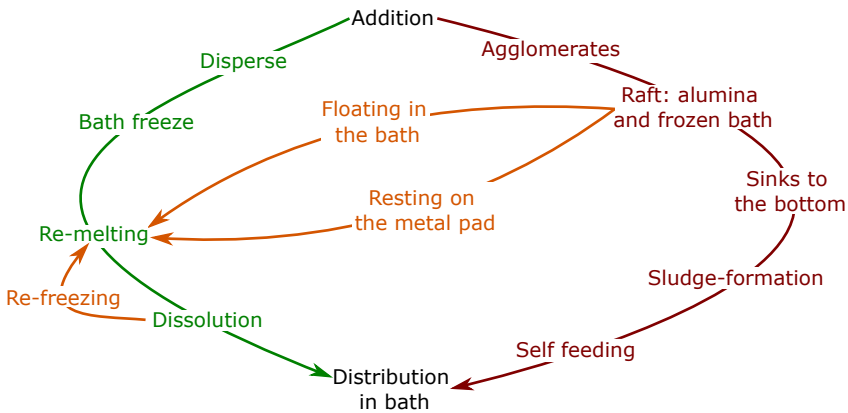
Figure 1.2: Possible paths for dissolution of alumina, redrawn from Solheim and Skybakmoen [6].

Failing to maintain a high enough alumina concentration in the bath (about 2 wt%) will result in anode effects, causing an increase in energy consumption, emissions of hazardous perfluorcarbon gases and instabilities in the cell [7]. On the other hand, adding too large amounts of alumina will favor the formation of sludge, which also leads to disturbances an poorer electric conductivity [8].

In recent years, reliable delivery, feeding and distribution have become a more critical factor for the aluminum smelters. Production cells are becoming larger while the number of feeders is not increased proportionally. In addition, the interpolar distance, i.e the distance between anode and metal pad, is also decreased to achieve higher energy efficiency [9]. These new adaptions have consequences for alumina feeding, as the powder must be distributed properly over a larger bath area and there is lesser available volume to dissolve in.

Another challenge for smelters is that they will normally receive alumina from different suppliers with various behavior and dissolution time [10], and they must hence adapt

their operations continuously. Detailed observations in industrial cells are very challenging and experiments in smaller scale as well as physical and numerical modeling are necessary in order to increase our understanding of the dissolution process. Increased knowledge on how the alumina behaves when added to the bath will aid the development of new feeder technology, ultimately contributing to further reductions in energy consumption.

1.2 Scope of work and outline

The aim of this thesis is to increase current knowledge related to alumina feeding through three different approaches: campaigns at industrial cells, laboratory experiments and numerical modeling. The goals are:

1. Investigate how feeding influences hydrogen fluoride emissions compared to other operations.

2. Model the alumina feeding process in a physical model at room temperature.

3. Develop a reproducible method for extraction of rafts at lab scale.

4. Use the developed method to investigate how different alumina properties and operational conditions affect the mass and structure of rafts.

5. Develop a numerical model for solidification and melting in a multiphase formulation.

6. Develop and apply a numerical model for how alumina (which is a powder) can be modeled with a continuous (Eulerian) framework.

7. Identify or develop a numerical model accounting for transfer of mass, momentum and energy, where the effects of the two models listed in 5 and 6 can be studied.

Part I includes this chapter and provides an introduction to alumina production, handling and properties. It also contains an introduction to the modeling framework, which are required to put the following chapters into context. In addition, a short introduction into modeling fluid flows is given. Part II gives a detailed description of the alumina feeding and reviews work that different research groups have conducted divided in industrial measurements, lab-scale work and numerical modeling. The same division is done in the following parts, where part III gives detailed descriptions of the methods used and IV summarizes and discusses the results. Part V provides conclusions, and suggests further work. Following the conclusions, the complete manuscripts produced in the current work are attached for reference. A short summary of the manuscript and the contributions from the author are given in the following section.

1.3 Contributions

This thesis is written as an article collection, and this section summarizes the work presented in the primary publications, and also states the different authors' contributions. In all of the publications, Kristian Etienne Einarsrud has contributed with supervision, discussion and reviewing of the results and revision of the manuscripts.

Primary Contributions

Paper I: S. E. Gylver, A. Solheim, H. Gudbrandsen, Å. H. Follo, and K. E. Einarsrud, "Lab Scale Experiments on Alumina Raft Formation," in *Light Metals 2020*, Springer Cham, 2020, pp. 659–663.

The first author (Sindre Engzelius Gylver) extracted the samples as a function of holding time, characterized them in light microscopy, prepared the manuscript and presented the findings at TMS 2020. Åste Hegglid Follo conducted Computed tomography (CT) scanning, while Henrik Gudbrandsen extracted samples for the preheating measurements. Asbjørn Solheim contributed with calculations, suggestions and revisions of the manuscript.

Paper II: S. E. Gylver, Å. H. Follo, V. Aulie, H. M. Granlund, A. Sørhuus, E. Sandnes, K. E. Einarsrud, "On Gaseous Emissions During Alumina Feeding," in Light Metals 2021, Springer Cham, 2021, pp. 504–510.

The first author (Sindre Engzelius Gylver) analyzed the measurements, supervised Åste Hegglid Follo on the experimental setup, prepared the manuscript and presented it at TMS 2021. Industrial measurements were conducted by Vegard Aulie and Helene Marie Granlund, while Anders Sørhuus prepared the setup. Åste H. Follo executed the experiments at lab scale, including the Loss on Ignition (LOI) measurements, extraction of samples and CT scanning.

Paper III: S. E. Gylver, S. Aase, S. Bekkevoll, S. A. K. Forberg, and K. E. Einarsrud, "A Water Model Study of Alumina Feeding and Dispersion," in Light Metals 2022, Springer Cham, 2022, pp. 357–362.

This paper is based on the work of the Bachelor thesis [11] by Simen Aase, Simen Bekkevoll and Sigmund Andres Kvammen Forberg, which conducted the experiments. The current author (Sindre Engzelius Gylver) prepared the setup, did statistical analysis of results and supervised the students together with Kristian Etienne Einarsrud. The current author prepared the manuscript and presented it at TMS 2022. The water model was designed and built by SINTEF Industry (Stein Tore Johansen and Fredrik Brun Larsen) as a separate deliverable in SFI Metal Production

Paper IV: L. Bracamonte , S. E. Gylver, K. E. Einarsrud, E. Sandnes: "Influence of Secondary Alumina Properties on Alumina Dissolution in Cryolite Melt"

The current author performed MOI/LOI-analysis together with Luis Bracamonte and extracted samples of alumina rafts from bath with different LiF-content. The paper still remains to be published, and this thesis contains a memo with the current authors contribution. The full manuscript can be found in the PhD thesis of Luis Bracamonte [82].

Paper V: S.E. Gylver, S. Bekkevoll, S. Rørvik and K. E Einarsrud: "The Formation and Disintegration of Rafts from Different Aluminas and Fines" *Metals*, 12, 1876.

The paper is based on the Master thesis [12] of Simen Bekkevoll, who extracted the samples and recorded alumina addition, where the first author (Sindre Engzelius Gylver) co-supervised the student. He also assisted Simen in improving the current setup, and conducted some of the experiments. Stein Rørvik performed the characterization and analysis of samples using CT.

Paper VI: S. E. Gylver and K. E. Einarsrud "CFD Modelling of Solidification and Melting of Bath during Raft Formation". Will be published in *Light Metals 2023*.

The current author developed the model, prepared and ran simulations, and wrote the manuscript.

Paper VII: S.E. Gylver and K.E Einarsrud: "Modeling alumina feeding with the μ(I)-rheology". Submitted to *Metallurgical and Materials Transactions B*, currently under review.

The current author developed the model prepared and ran simulations, and wrote the manuscript.

Secondary contributions

S. E. Gylver, N. H. Omdahl, A. K. Prytz, A. J. Meyer, L. P. Lossius, and K. E. Einarsrud, "Alumina Feeding and Raft Formation: Raft Collection and Process Parameters," in Light Metals 2019, Springer Cham, 2019, pp. 659–666.

The main author (Sindre Engzelius Gylver) contributed with preparation of the manuscript and presented it at TMS 2019. Since the measurements were conducted prior to this PhD, the findings from this paper is included as a part of the literature review in chapter 5.

S. E. Gylver, N. H. Omdahl, S. Rørvik, I. Hansen, A. Nautnes, S. N. Neverdal and K.E Einarsrud: "The Micro- and Macrostructure of Alumina Rafts," in Light Metals 2019, Springer Cham, 2019, pp. 689–696.

The main author (Sindre Engzelius Gylver) contributed with preparation of the manuscript. Since the measurements were conducted prior to this PhD, the findings from this paper is included as a part of the literature review in chapter 5.

S. E. Gylver and K. E. Einarsrud: "Formation of Alumina Rafts in a Lab Scale Furnace". Poster presented at TMS 2019.

Poster based on preliminary results later described in Paper I.

Chapter 2: Alumina

2.1 Production of alumina

Bauxite is an ore rich on elemental Aluminum in the form of hydrates such as gibbsite $(Al(OH)_3)$, bohemite and diaspore (AlOOH). It contains several other elements as well, in particular iron compounds, and refining is therefore required to obtain smelter grade alumina (SGA). This is mostly achieved through the Bayer process [13], described by the process chart in figure 2.1.
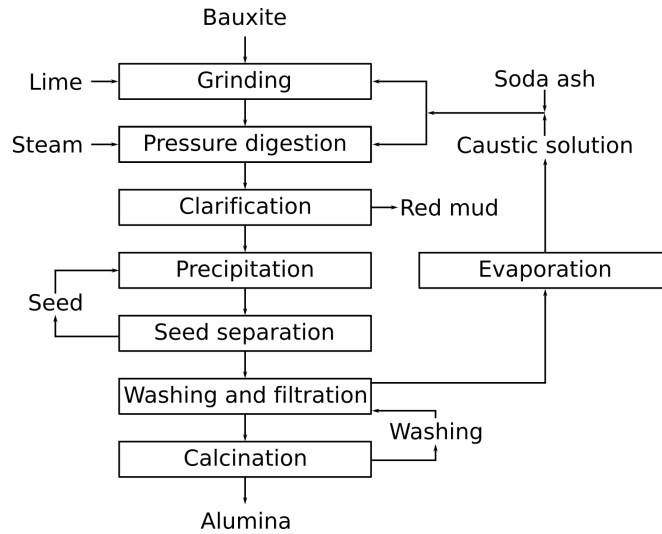
Figure 2.1: Flowchart of the Bayer process from bauxite to primary alumina, redrawn from Grjotheim and Kvande [15].

In the first step, known as digestion, Bauxite is crushed down and leached into a strong caustic solution at high pressure and temperature, thus starting an extracting mechanism given by the following reactions:

$$Al(OH)_3 + Na^+ + OH^- \Longleftrightarrow Al(OH)_4{}^- + Na^+, \qquad (2.1)$$

$$AlOOH + Na^+ + OH^- + H_2O \Longleftrightarrow Al(OH)_4{}^- + Na^+. \qquad (2.2)$$
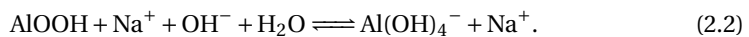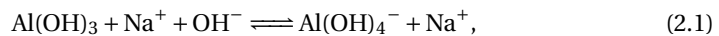
Most of the alumina is now dissolved in the solution, while other compounds, such as Fe_2O_3 are not, and can now be removed by filtration as red mud. After clarification, the dissolved aluminum compounds are formed back to hydrates through seeding, having a higher purity than prior to the process. The alumina is still hydrated, in a form known as gibbsite ($Al(OH)_3$), and calcination is required to remove the hydroxides and obtain alumina suitable for the Hall-Héroult process. In general, gibbsite is being exposed to heating, forming other forms of hydrates depending on pathway, shown in figure 2.2. α-alumina is without any hydrates but achieving pure α requires high amounts of energy and is not desired by the smelters either.
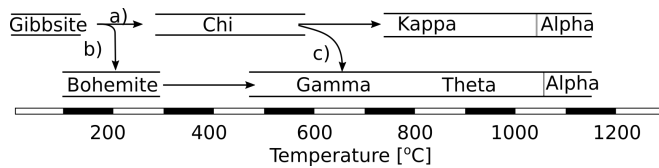
Figure 2.2: Possible reactions pathways for dehydration of alumina, redrawn from Whittington and Ilievski [16]. In case of the Bayer process, b) is found to be the dominant path.

2.2 Alumina handling and feeding

The refineries and smelters are in many cases not collocated and alumina must therefore be transported over a long distance by trains and/or ships. After unloading alumina is transported through several silos and treatments centers, illustrated in figure 2.3 [17]. Since alumina is received in large batches that may last for several months, large silos called port silos are placed in proximity of the port, with capacities up to 85 000 tons [18].
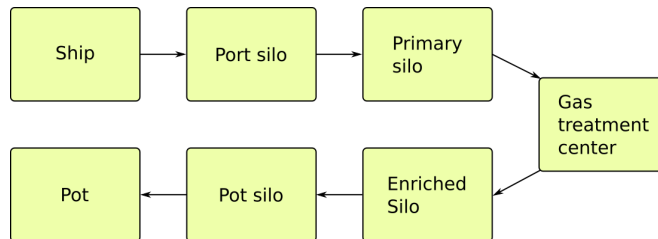
Figure 2.3: Flowsheet of alumina handling, from being delivered to the port until entering the pot.

Alumina is further transported to what is called a primary silo by air slides, belt conveyors or trucks [17]. From the primary silo, alumina is transported to a gas treatment

center (GTC), where it is used as a cleansing agent for the pot fumes in a dry scrubber. Gaseous impurities, in particular fluorides, are adsorbed on the alumina surface and hence being recirculated back to the pots, having environmental and economic benefits. Bag filters placed at the same location will hinder particulates, such as solid bath and carbon dust, from being emitted. The alumina can now be called secondary, and is transported into a new silo, called the enriched silo [15]. It is now ready to be fed to cells and is transported from the silo to pots by air slides, cranes or trucks. Each feeder has its own alumina hopper, where alumina is stored prior to addition. There are two main types of point feeders, one containing a crust breaker where feeding is done from the side, and one where the point feeder and crust breaker is integrated in one part. Feeders are mainly placed in the center channel of the cell or at other location suited for the best distribution of alumina [19].

2.3 Alumina properties

Refineries will perform analysis and create a certificate of analysis before shipping their material, and some smelters will also do analysis on received material as well. This section will present the most frequently used properties.

Impurities

Several impurities are found in alumina, often as different oxides. The most common are Na_2O and CaO that will create disturbances to the bath chemistry [14], while SiO_2 and Fe_2O_3 are undesired as they will contaminate the metal. P_2O_5 is found in lesser degree, but even small amounts will have a negative impact on the current efficiency [19].

α-alumina

As stated in section 2.1, α-alumina is formed through heat-treatment, and the content of it can hence be interpreted as degree of calcination. In the certificate of analysis, the percentage of α-alumina must be interpreted as the mass percentage of a typical grain in the batch that will have this structure [19].

Particle size distribution (PSD)

Alumina received by a smelter will have a typical distribution ranging from 20 to 150 µm. The particle size distribution can be decided by sieving [20] or laser diffraction. The content of fines is also important for smelters, where fines are particles with diameter below 40 µm, while a superfine fraction is defined to be below 20 µm [21].

Angle of repose

This property is defined as the angle a batch of alumina will have when being poured from a fixed distance onto a horizontal surface, described in the standard [22]. It will provide an overview on the resistance for the grains to slide above on each other, i.e. the flowability of the powder.

Attrition index

Attrition index is a measure on how good the alumina grains can withstand handling without breaking apart. It is important as alumina should not break up into fines during the transportation to and at the smelter. The principle is to impact grains onto a metal plate with a jet of pressurized air and compare amount of fines before and after impact [19].

BET Surface area

A technique named after Braunauer, Emmet and Teller, where the surface area of particles is calculated through physisorption of nitrogen, details are given in the ISO-standard 8008 [23]. It is affected by the thermal treatment in the Bayer process, and hence also linked to the amount of α-alumina. A high surface area is desired as it will increase the powder's efficiency in the dry scrubbing process.

Density

Density can be measured in two ways, the true and bulk. The bulk density is most commonly used and also have two ways of being measured, as Loose Bulk Density and True Bulk Density [24], having typical values between 0.9 and 1.15 $kg\,dm^{-3}$. Controlling of this parameter during operations is important, as modern point feeders add a fixed volume, not mass, into the cells.

MOI and LOI

The Loss on Ignition (LOI) describes the mass loss alumina will have when being heated up, and is measured over two different intervals, 25-300 and 300-1000 °C according to the international standard [25]. The lower interval is also known as Moisture on Ignition, MOI, as the mass loss is in this case mostly related to release of adsorbed water on the particle surface. Temperature intervals deviating from the standard exists, and it is suggested to divide the interval between 25-300°C in two at 110 °C [26] as most of the adsorbed water is found at the lowest interval. It is also discussed that this method does not capture gibbsite content properly [27], which will be released both above and below

300 °C. LOI is also correlated to the α-content, BET surface area, as a low LOI indicates a high degree of calcination.

Flow funnel time

Flow funnel time is defined as the time required for alumina to flow through a funnel and can be measured quite easily. A high funnel time means that alumina is hard to flow through their system and is often associated with a higher amount of fines. No standardized method exists, but Alcoa and many refineries use a setup as described by Lindsay and Lavoie [19]. Descriptions are also available at produces of such equipment [28], [29]

Desired properties

Table 2.1 summarizes desired specifications for SGA. These values are however not only proposed for ensuring good dissolution behavior as other properties are also desired. Alumina should, among other things, move efficiently through the handling system, clean the off-gas for HF and other impurities, create cover materials with sufficient quality, have low enough impurity levels and have an acceptable price [19]. Desired values might also vary depending on smelter technology.

Table 2.1: Overview of desired specifications for Smelter Grade Alumina.

Property	Desired value
Na_2O	Below 0.30 % [19]
Fe_2O_3	Below 0.015 % [19]
SiO_2	Below 0.015 % [19]
P_2O_5	Below 0.01 % [19]
α-content	Below 10 % [19]
Fines (>45 µm)	Below 8 % [14]
Superfines (>20 µm)	Below 0.5 % [14]
Angle of repose	30-35° [14]
Attrition index	Below 20 [19]
MOI	Below 0.5% [14]
LOI	0.6-0.9 [14]%
BET Surface area	70-80 $m^2 g^{-1} m^{-1}$ [19]
Flowability	Below 85 s with the Flow funnel Alcoa standard [19]

Chapter 3: Fundamentals of flowing systems

When modeling flows of fluids or particles, mathematical equations are formulated based on the conservation laws of physics, namely that mass cannot be created or destroyed, Newtons second law of motion (momentum) and first law of thermodynamics (energy) [30]. To formulate a set of mathematical equations based on these laws, a framework must be chosen. The Eulerian and the Lagrangian frameworks are most common and will be presented further.

Using a fluid as an example, one can assume that it can divided up into very small elements, in a size that cannot be seen by the eye, but still consisting of multiple molecules. Each of these elements will share the same physical quantities (velocity, density, temperature etc.). In a Lagrangian framework, one will follow the same fluid element as time passes and updated quantities will be identified in its new position [31]. In an Eulerian framework, the quantities are measured at a fixed position, and the location of the different fluid elements are not known. How the two framework will describe a fluid flow is shown schematically in figure 3.1.
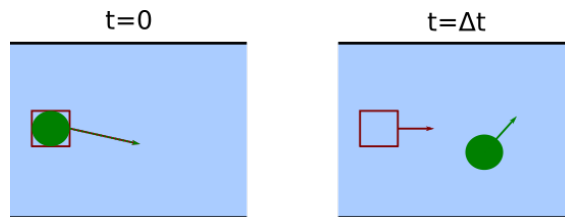
Figure 3.1: Illustration of the Eulerian (red) and Lagrangian (green) framework for a flow at two different times.

There will in some cases also be several components present in the system and they can have different frameworks as well. In figure 3.2, a blue fluid is expressed with a Eulerian framework at all time, while the framework for the red phase varies [32]. When several components are present, it is necessary to account for that there might be interactions between them, such as surface tension. These interactions can be complicated to model and in some cases, such when few particles are present in a fluid, it is reasonable that the fluid will affect the particles' movement, but not the other way around. This is known as a one way coupling and is the top row in figure 3.2. [32]. If this cannot be assumed, a two way coupling must be used, as shown in the lower row. An exam-

ple of a two way coupling is when a component reacts into another one. This will then affect both the mass- momentum and energy balance for both components.

After choosing a framework and formulating the governing equations, they must be solved. They are rarely solvable analytically and require numerical solutions such as those provided by Computational Fluid Mechanics (CFD) [30], [33], discussed further in chapter 10.
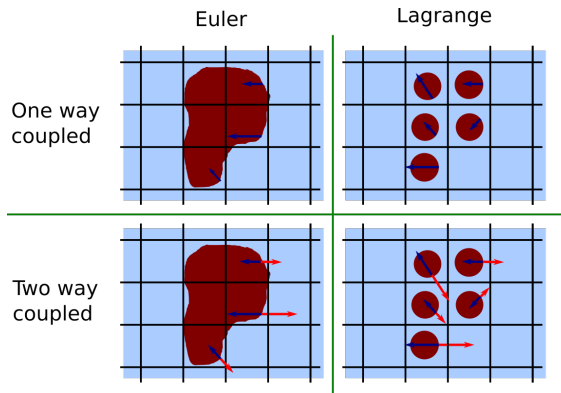
Figure 3.2: Different possible configurations for a multiphase system with one phase in a Eulerian frame (blue) and another phase (red), which have an Eulerian frame on reference on left and Lagrangian on right. Blue arrows indicates whether the blue phase interacts with the red phase, while red arrows indicates if the red phase interacts with the blue one.

Part II

Literature review

Chapter 4: Context

As mentioned in chapter 1, alumina is added in batches by point feeders placed at one or several locations in the cell. It is added in an electrolyte of molten salts, consisting of cryolite Na_3AlF_6, with addition of mainly AlF_3 and CaF_2. Convection in the bath, mainly due to the magnetic field at the metal pad and anodic bubbles [15], will aid alumina in dispersing and distributing throughout the cell.

Other salts, such as LiF, KF and MgF_2 may be added to the bath to increase electrical conductivity and reduce liquidus temperature, thus achieving a lower operating temperature. The desired operation temperature for a cell is between 5 to 10 °C above the liquidus, where the excess temperature is named superheat. Empirical formulas exist [34] to calculate the saturation solubility of the alumina based on the concentration of additives in the melt and operating temperature. In real operations, smelters try to maintain a stable concentration between 2 to 4 wt%, to avoid anode effects and sludge formation. The alumina feeding frequency is varied between overfeeding, i.e shorter time between each feeding, and underfeeding, more thoroughly explained in the book by Grjotheim and Welch [15].

The feeding and dissolution process can be divided up in a four step process [9], [35], as illustrated in figure 4.1.

1. A batch of alumina hits the bath surface, where a part of the batch will be sufficiently dispersed and dissolve almost immediately in the melt.

2. For the particles left, a layer of frozen bath will form around them, creating a solid structure consisting of frozen bath and alumina, called a raft. Frozen bath hinders contact between liquid and powder, and phase-transition of alumina from γ to α will create platelets [36], enhancing its mechanical strength.

3. Heat is required to melt the frozen bath and will hence be rate determining in this step [6], [37].

4. Finally, when the molten bath and particles are in contact again, dissolution can occur further. Since the dissolution reaction itself is endothermic, bath might freeze on the particles again, hence repeating step two to four. When sufficient amount of heat is available the dissolution process is limited by mass transfer [6], [35], [38].
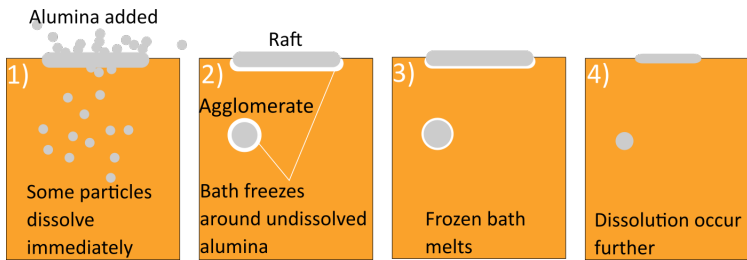
Figure 4.1: Four step illustration of alumina addition and dissolution [9], [37].

Both the cell conditions and alumina properties will impact the dissolution behavior. Kuschel and Welch [39] suggest that changes in the cell conditions, in particular velocity of the electrolyte and superheat have a larger impact on the dissolution than the alumina properties. However, having high agitation and superheat, which promote fast dissolution is hard to control and is typically disturbing for a cell. Alumina properties might not have the largest impact, but they can still change between shipments, and thus affecting operations.

It is evident that a smelter desires an alumina type that immediately dissolves and distributes evenly in the cell. Much work has therefore been done over the last decades to gain better understanding, in order to optimize the feeding. Besides alumina properties, operating conditions and chemistry of the electrolyte have been studied. The next chapters will review the work that has been conducted in industrial and laboratory scale, respectively in chapter 5 and 6. A review of relevant modeling work is described in chapter 7.

Chapter 5: Industrial studies

Studies at industrial sites are somewhat scarce, probably due to the high complexity and that some research remains internal within the industry. This chapter reviews the available studies on alumina dissolution with focus on those that discuss the formation of rafts and agglomerates, as well as the relation alumina dissolution have to emission of hydrogen fluoride (HF).

It is no doubt that alumina properties will affect the efficiency of the cells. According to Lindsay [40], high amounts of fines, in particular the superfines below 20 μm, have a very negative impact, even if the PSD in general is coarse. Flowability is pointed out to be an important parameter for the general performance, as it is closely related to the PSD and is easier to measure on a regular basis. The challenge of obtaining reliable results in industrial scale is also discussed, and the author proposes that the sampling period should be at least 15 months without notable process disturbances, and that there must be one or more major shifts in the fine fraction or flow funnel time in order to observe any effect.

Continuous alumina sampling and measurements over a period of 3.5 years in an Alcoa smelter [41] revealed a variation of flowability of alumina received to different pots in the line, due to segregation in the delivery system. A significant change in the flow funnel time was seen when the alumina supplier was changed, and also during a week, due to segregation of alumina in the silos. Studies at a smelter in Germany [42], where multiple alumina parameters were measured, points out the α-content in the fines to be the most influential parameter on the current efficiency.

Studies of alumina raft formation have mostly been restricted to individual pots. Rafts have been known to exists for several decades, but few researchers have tried to sample and characterize them. Rolseth and Thonstad [43] collected rafts formed from a point feeder, which was possible to due to removal of an anode. Both primary and secondary aluminas were added, and the secondary alumina had a grayer an more porous structure than the one formed from primary. The reasons for the different appearance were however not discussed.

Walker *et al.* [44] monitored the cell temperature and studied the formation of alumina agglomerates in a cell. Measurements of the temperature inside a feeding hole revealed a fast recovery after addition, and it was thus believed that alumina is transported away or sinking down in the cell. Further, they put a meshed stainless steel metal basket in

the feeding zone and retrieved the content at four different holding times. Agglomerates were found to have an ellipsoidal form, 1-2 cm high and 1-5 cm in diameter and increasing density by time that surpasses the density of bath, indicating sludge formation. They also immersed 15 grams alumina powder in a thin aluminum basket to study the freezing and infiltration of bath around a formed agglomerate. Depending on the α-content, agglomerates were dimensionally stable up to 300-500 seconds, highest for pure α-alumina, and AlF$_3$-rich bath was found infiltrate the inner structure before the frozen shell of bath forming around the raft was able to melt away.

Kobbeltvedt *et al.* [45], [46] monitored the temperature in the side channel of a cell, approximately 1.5 anode length away from the feeder. They saw a larger drop in temperature when the feeding hole was open between the feedings, indicating that during a closed hole, alumina might be preheated before entering the cell. However, the variation of temperature drop is higher, indicating that the amount of alumina dissolving will vary from feeding to feeding. In addition, the dissolution rate was slower for a closed feeding hole, explained by sintering and interlocking of grains might occur while the alumina rests on the top of the closed feeding hole, ultimately resulting in agglomerates that are hard to dissolve.

Scanning electron microscopy (SEM) analysis on three different positions in rafts skimmed off from a cell was performed by Dando *et al.* [47]. On the top part, frozen bath is the only material that glue the raft together, while in the middle part, near the bath surface, alumina was seen to have undergone a phase transformation and created platelets of α-alumina, together with frozen bath. At the bottom of the raft, some alumina can still be observed, but most of the area consisted of alumina-rich eutectic phases trapped inside a matrix of bath.

Prior to this doctoral thesis, extended work was done to study the raft formation and collect samples in pots at Alcoa Mosjøen [48], [49]. In these pots, the alumina feeder is placed in between the anodes close to the tapping hole, making observations possible without needing to remove anodes. Observations and recordings were conducted in two parts, where the second part also involved extracting samples from the pot. Rafts were found to form, and spread out on the available open surface area present, shown in figure 5.1, with floating time varying from 5 to 140 seconds. Available surface area and bath motion were found to affect the floating time, together with temperature, composition of bath, as well as moisture and fluoride content in the alumina [48].

Sampled rafts, with an example shown in figure 5.2, were further characterized [49] by Computed Tomography (CT), SEM and X-ray diffraction (XRD). CT revealed that the interior of the raft consisted of several smaller and larger cavities, with an average porosity
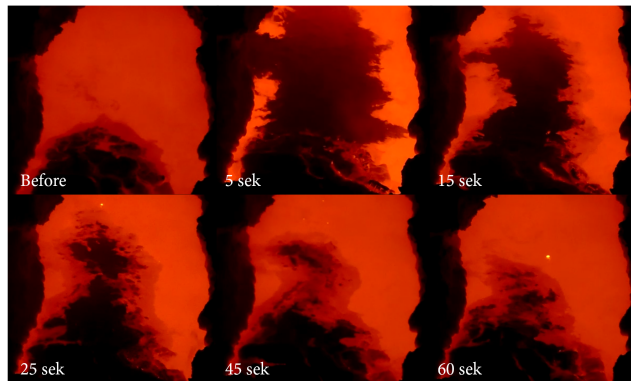
Figure 5.1: Recordings of alumina feeding at a cell from Alcoa Mosjøen [48]. The time is set relative to the time of feeding. Used with permission of The Minerals, Metals & Materials Society.

values of 12.72 %. The bottom layer is very dense because of the sampling method. The high porosity found in the rafts will aid the buoyancy and hence the ability for a raft to float. Carbon dust was observed to follow the solidification direction, and the pores seems to contain more carbon than the rest of the structure. The SEM-analysis indicate that the alumina content increase while the bath content decline as one goes from the bottom to the top of the raft. The AlF_3 concentration is increased in the same direction, which indicates an infiltration of bath going upwards. Pores are also seen in bath that is freezing under a cold anode [50], without being able to conclude on the origin.
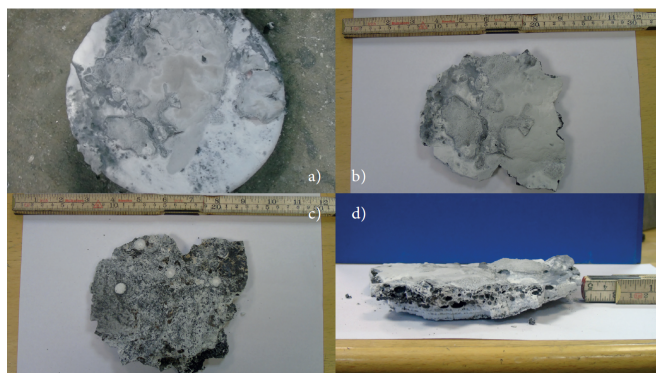
Figure 5.2: Images of an industrial raft from an electrolysis cell, collected from Alcoa Mosjøen [48]. a) On the sampler right after collection, b) from the top, c) from the bottom, d) from the side. Used with permission of The Minerals, Metals & Materials Society.

The reason for the pores and cavities in rafts is discussed to be due to HF-gas, which is formed when water reacts with either entrained bath [51]

$$\frac{2}{3}\,AlF_3\,(l) + H_2O\,(g) \longrightarrow 2\,HF\,(g) + \frac{1}{3}\,Al_2O_3\,(diss), \tag{5.1}$$

or by hydrolysis of pot fume

$$NaAlF_4\,(g) + H_2O\,(g) \longrightarrow \frac{1}{3}\,Al_2O_3\,(s) + \frac{1}{3}\,Na_3AlF_6\,(s) + 2\,HF\,(g). \tag{5.2}$$
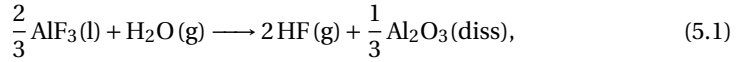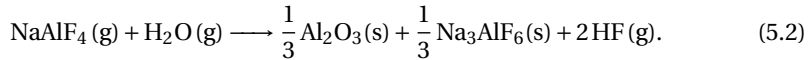
Alumina is the main contributor of water and hence the HF content [52]. The hydroxides might also contribute in the same manner as water, but it has also been suggested that HF can be formed through an electrochemical reaction [52].

Measurements of HF content in the duct at several different smelters reveal a peak short time after an alumina addition and also correlations between HF concentration and feeding cycle [53]–[56]. The decrease in HF content after an addition is however decreasing slowly and HF being trapped inside rafts and then being slowly released has been discussed as a possibility by Slaugenhaupt *et al.* [53]. The same authors also observed a decrease in HF being emitted when closing the feeding hole, hence pointing out the importance of reducing the available open surface of bath. Sommerseth *et al.* [54] measured the water content simultaneously and observe a correlation between water and HF-content, supporting that alumina is the main source for the water that produces HF. Regular operations might also affect the HF-content, in particular anode change and metal tapping [55], which will result in a change in the structure of the crust. Another factor that might affect the HF-generation is moisture in air [19], where more HF might be generated during summer, when the air is hotter and moister.

Summary

The current literature suggests that particle size and thus flowability of alumina have a significant effect on the current efficiency and performance of the cells. It is also clear that formation of alumina rafts occurs in modern cells, and it can rest on the bath surface for several minutes after feeding. From samples, it is found that a raft is a porous structure consisting of mainly a mixture of bath and alumina, but carbon dust is also present. The origin of the pores is not thoroughly investigated yet, but since fewer pores are found in agglomerates created from primary alumina, it is a strong indication that they are formed due to products from the dry scrubbing process. The pores might be linked to the formation of HF, which is found to be closely linked to the feeding of alumina.

Chapter 6: Laboratory studies

6.1 Introduction

As stated in the previous chapter, achieving repeatable conditions and good parameter control is challenging in an industrial cell. Therefore, the use of lab scale experiments is quite widespread, with several different techniques. This chapter will focus on methods that are used to measure the alumina dissolution and the techniques can be roughly divided into the following categories: electrochemical techniques, see-through cells, measurements of samples including gravimetric analysis, and observations/recordings. With these methods the effect of properties for both bath and alumina, as well as other operating conditions can be measured and quantified.

Electrochemical measurements to monitor the alumina concentration of the bath in situ has been widely used, where voltammetry and Critical Current Density (CCD) are the most common methods. The principle is to induce an anode effect on a carbon electrode through a voltametric sweep, where a limiting current density that is proportional to the concentration of oxy-anions in the melt will be reached [57]. A drawback is that some of the anode will be consumed over time and that evolution of CO_2 might disturb the measurements. Right calibration and good design of experiments are needed for methods to be robust and reproducible [57].

The oldest techniques used is simply to add alumina into bath and observe the behavior [37], [58]. In more modern work, the addition of alumina can be recorded, and images post processed, providing good opportunities to measure surface areas and wetting of powder by image analysis [59]. Recordings have also been pointed out as an important tool when evaluating the performance of an alumina delivered from a supplier [10] and also as a supporting technique to confirm the dissolution by other methods [39], [60].

See-through cells have existed for a long time and discussed in *Light Metals* as early as 1974 [61], but extensive usage of them has been limited to the last few years. In this setup, bath is melted in a crucible made of quartz, which will become transparent when reaching a sufficient temperature, and dissolution can hence be observed from the side or bottom [36]. It is possible to combine see-through cells with gravimetric methods [62], hence being able to also measure weight of created agglomerates as they are dissolved.

Retrieving samples are also necessary to understand alumina dissolution. It can be used

to observe bath infiltration and interactions with alumina [63]–[65], decide upon the mechanical strength [66] or the dissolution rates [6]. It is also possible to apply gravimetric methods [67], [68], where the dissolution rate can be measured in situ.

6.2 Studies of different parameters

Table 6.1 and 6.2 summarize which parameters different studies have investigated, divided between operating conditions and alumina properties.

Table 6.1: Summary of studies that have investigated the effect operational conditions have on alumina dissolution, including measurement methods.

Author	Method	Superheat	LiF-content	Al_2O_3-content	Other additives	Convection	Addition method	Sample size	preheating
Alarie *et al.* [68]	Gravimetry	X		X	X	X			
Bracamonte *et al.* [69]	See-through			X					
Bagshaw *et al.* [70]	Voltammetry		X			X		X	
Gerlach *et al.* [71]	Bath samples		X						
Hovland *et al.* [72]	Voltammetry					X		X	
Jain *et al.* [8], [73]	Voltammetry		X	X					
Kaszás *et al.* [64], [65]	Compressed discs			X					
Kaszás *et al.* [59]	Recording	X						X	
Kuschel and Welch[74][39]	Voltammetry and recordings	X		X	X	X	X		
Kobbeltvedt *et al.* [45], [75]	Voltammetry	X				X			X
Rolseth *et al.* [76]	Voltammetry							X	
Rye *et al.* [77]	CCD	X	X						X
Thonstad *et al.* [37]	Observations				X			X	X
Vasyunina *et al.* [78]	Voltammetry and observations				X				
Walker *et al.* [63]	Samples	X		X	X	X			
Yang *et al.* [62], [79]	See-through	X		X					

Some trends between different parameters and dissolution rate can be seen. Increased convection and movement in the bath will increase the dissolution rate, unless the added batch is very small [35], as it will aid the dispersion of alumina grains, hence increasing the fraction of the batch that is dissolved in the fast first step. Feeding conditions that aid dispersion will also have the same effect, which can be achieved by increasing the fall height, resulting in a higher velocity of the fed batch when entering the bath [70].

Table 6.2: Summary of studies that have investigated the effect alumina properties have on its dissolution, including measurement methods.

Author	Method	Dry scrubbing	MOI/LOI	α/γ-content	Fines	Carbon content	BET
Bagshaw *et al.* [70], [80]	Voltammetry	X	X	X	X		X
Bracamonte *et al.* [81], [82]	See-through	X			X		
Dando *et al.* [47]	Voltammetry		X				
Gerlach *et al.* [71]	Other			X			
Haverkamp *et al.* [83]	Voltammetry	X	X				
Hyland *et al.* [52]	Voltammtery		X				
Isaeva *et al.* [84]	Observations		X	X	X		
Kaszás [85]	Recordings and samples		X	X		X	
Kheiri *et al.* [87][86]	Samples	X		X	X	X	
Kobbeltvedt *et al.* [45]	Voltammtery	X					
Kuschel and Welch [74][39]	Voltammetry and recordings		X	X	X		X
Liu *et al.* [88]	See-through			X			
Rolseth *et al.* [43]	Samples and CCD	X		X			
Rye *et al.* [77]	CCD	X		X		X	
Sommerseth *et al.* [89]	HF-measurements	X	X				
Thonstad *et al.* [37]	Observations			X	X		
Townsend *et al.* [58]	Observations and samples	X			X		
Yang *et al.* [79], [90]–[92]	See-through	X	X	X		X	X
Østbø [36]	Heat treatment	X	X	X		X	X

Increased superheat will reduce the freezing of bath around the alumina batch, thus preventing agglomeration. Kuschel and Welch [39] found superheat to be more important when there is little convection in the bath. Kaszás *et al.* [59] added alumina into a bath in a 7.6×7.6 cm^2 squared crucible with different superheats, and saw that higher superheat did not affect the wetting of the powder, but a faster disintegration and a larger spreading of rafts was seen when the superheat was increased by 10 °C. A challenge with their setup was to maintain thermal balance in the bath, as the heat continuously leaked out of the furnace.

When increasing the superheat, one might need to be careful, as it can either be acquired by increasing the bath temperature or by maintaining a constant temperature and introduce additives such as AlF$_3$, CaF$_2$ or LiF, which will decrease the liquidus temperature of the melt. These additives will reduce the solubility of alumina [34] and are found to have a larger or similar effect on the dissolution rate in the comprehensive study by Alarie *et al.* [68]. In that study, the effect of LiF was however not investigated, but other studies [77] indicated that the dissolution time do not change in a bath containing 5 wt% LiF, if a superheat of 20 °C is maintained. Bagshaw *et al.* [70] did not observe any change in dissolution rate up to 1.6 wt% LiF and 10 °C superheat, but at 5 wt%, and same superheat, sludging was seen.

Alarie *et al.* [93] reviewed several of the presented studies [68], [71], [73], [80], [84] and developed an empirical model that could predict the dissolution rate only considering the content of Al$_2$O$_3$ and AlF$_3$, and bath temperature. Other parameters were discarded mainly due to correlation with existing parameters, lack of sufficient and coherent descriptions of them between the different papers or too small variation for any effect to occur. However, the model cannot explain the papers where alumina properties have been investigated and resulted in a significant variation of dissolution time [71], [73], [80].

Preheating the alumina might aid the initial dispersion and decrease the formation of frozen bath around the added batch. Kobbeltvedt *et al.* [45] compared the dissolution rates between non-preheated and preheated alumina at 600 °C. A batch of approximately 140 g alumina was added to 6500 g of bath, and dissolution rate was determined by continuously withdrawing bath samples and analyzing them with a LECO oxygen determinator. They saw a significantly faster dissolution of the preheated batch, as lesser bath froze around the particles, hence avoiding agglomeration. Thonstad *et al.* [37], on the other hand, could not see any effect in their experiments, but that might be due to very small batch sizes, while Rye *et al.* [77] saw a faster dissolution for alumina preheated to 700 °C.

Fine alumina particles are found to have a negative effect on the dissolution, in particular the size fraction below 21 μm. Kuschel and Welch [39] investigated discrete size fractions, and an increase in dissolution time for lower particle size was observed, but their investigations were mainly done between 50 and 80 μm. Their main challenge when studying finer fractions was that the powder tended to blow back when being fed to cell, thus never reaching the bath. Kheiri *et al.* [87] sampled artificial crust samples from 5 grams of alumina that was held in a melt for 20 seconds, and saw that types with higher fraction of grains below 40 μm forms lighter crusts in term of density, and is weaker. This has also been observed by Townsend and Boxall [58].

High α-content is in general found to increase dissolution time [37], [71]. α-content will be dependent on the heat treatment method during the Bayer-process, and it is pointed out that the range of α-content in SGA becomes narrower [79], making it a less significant parameter. It is almost impossible to distinguish effect of α-alumina from MOI/LOI-content, illustrated in the work by Kuschel and Welch [39], where several types of alumina from different refineries were studied and all of them that were low on α also had high LOI.

Increasing LOI content is in general found to increase the dissolution rate, due to release of gases when a batch enters the bath, which will aid agitation and break the formed raft apart. Dando *et al.* [47] eliminated the different hydroxyles (Gibbsite, Boehmite, Gamma) and saw a decrease in dissolution rate as a fewer hydroxyles were present. Similar trends are seen by using a see-through cell [92], while Kuschel and Welch could see a change in dissolution time up to 20 % within a common range of LOI, and it is in particular when below 1 wt% that the dissolution time increases.

Dissolution time is in general found to decrease when primary alumina goes through the dry scrubber and becomes secondary. Bracamonte *et al.* [81] observed that the primary alumina tended to form a crust on the bath surface, while secondary dispersed into the melt and created a cloud of smaller pieces. Yang *et al.* [90] observed the same trend, and formation of bubbles was also observed for the secondary alumina. They compared several parameters that are changing during the dry scrubbing process and identified carbon content as the major effect on why the dissolution rate was increased. Water content, fluorides present as both adsorbed on the alumina and as particles were studied but was not found to have a high impact of the dissolution. This is partly in accordance with dissolution experiments done with CCD [83], where little effect on dissolution rate was seen when fluorinating alumina, while alumina exposed to humidity reduced the dissolution rate.

In later work, Yang *et al.* [91] concluded that carbon in the alumina can burn off when

added to the melt, creating agitation and hence aiding the dispersion and dissolution of alumina. A similar trend was observed by Østbø [36], who monitored the temperature response of alumina samples that are exposed to a hot environment and saw that carbon content will decrease the response time, due to combustion. Kaszás [85] disagrees, however, since in her experiments, alumina containing carbon kept its gray color after addition. Also, most of the atmosphere above a raft consists of CO_2 and not oxygen, which is needed for combustion to take place. Kaszás proposes that carbon particles will block alumina from sintering together, hence the formed raft structure will be weaker and disintegrate more easily.

The structure of crusts formed between primary and its corresponding secondary alumina was studied by Rolseth and Thonstad [43], and they observed that the crust from secondary alumina had a more grayish and porous structure. Townsend and Boxall [58] did similar experiments, where 4 or 8 grams of alumina were added to a bath, and withdrawn 10 and 180 seconds after addition, respectively, in order to observe the bath penetration and crust formation. They observed that the primary alumina either fell fast down to the crucible bottom, and in general, the crusts formed from primary alumina were stronger than the ones created from secondary alumina. Kheiri *et al.* [86] also saw the same tendency towards crust strength, and crust from secondary alumina also tended to have lower density. By adding carbon in primary alumina and retrieving samples, they saw a reduction in density and lifetime of the crust, while primary alumina exposed to moisture or hydrogen fluoride did not have the same effect. Kaszás [65] created rafts by adding 14 grams of primary alumina into a melt and removing samples after 45 seconds, where the effect of drying the powder prior to addition was studied. Alumina dried on beforehand at 550 °C did not spread out as much on the surface, contained loose powder after addition, and had a denser structure. She suggests that the evaporating moisture in combination with freezing and agitation of bath simultaneously results in enclosed bubbles in the structure.

Summary

Considerable efforts have been put into investigating and identifying how different parameters affect the dissolution time. Correlations between dissolution time and bath chemistry, temperature and some of the alumina properties have been well established. However, for formation and disintegration of rafts, there are still aspects that are not fully understood. It is quite clear that higher superheat and preheating will hinder freezing and hence raft formation. From studies mainly of crusts, it is clear that rafts from secondary alumina are more porous and have lesser strength than the one formed from primary. The origins of the pores are still not fully known, but the current literature sug-

gest that carbon is the source rather than fluorides.

6.3 Physical modeling

Studying the interactions between bath and alumina in detail, in particular for a real scale cell is challenging due to the high temperature and hazardous gases that limit the availability to do detailed recordings and measurements. Physical modeling at room temperature is a possible approach to create models in real scale and still maintain safe and controlled conditions. Chesonis and LaCamera [94] created a full-scale model containing 8 anodes, in order to observe how interface motion and gas-driven flow affected the alumina distribution, while a smaller model consisting of two anodes was used to study the effect of local phenomena. When a three-phase model is considered, water represents the metal pad, and bath is replaced by a light mineral oil. In an air-bath system, the bath was replaced with water. By using resistance probes and sodium chloride as a tracer, they could simulate the distribution of alumina for different configurations and saw that the time to obtain steady state concentration was almost the half for pure gas driven flow relative to pure electromagnetic flow (35 vs 60 min). Due to the size of the model, they were also able to study how different feeder locations affected the distribution, and found that if only having one feeder, it should be placed in the center channel at the gap between two anodes, but two feeders will be even more convenient.

Particle image velocimetry (PIV) is a useful tool for quantifying velocity and turbulence in a physical model. A full-scale model consisting of three anodes was developed by Cooksey and Yang [95], where water was used to model the bath. They studied the effect of slotted anode and the ACD, and slotted anodes were found to increase the horizontal movement in the center channel and an increase of turbulence underneath the anode. This model has later been used to validate numerical models from CFD [96].

Water modeling has also been applied to study the movement on the bath metal interphase, and to simulate a raft floating on it [97], in order to verify derived models. The movement of fluid can be determined by PIV, and a high-speed camera combined with image processing can be used to track the position of the raft.

Kaszás [85] also attempted to simulate rafts on the bath-metal interface, using water as bath phase and ethyl trichlororate-acetate as metal, and monosodium-glutamate was used as a replacement for alumina. A fast dissolution was seen when injecting the powder into the bath at room temperature, while a frozen layer of ice would hinder contact between liquid and salt when the powder is cooled with frozen nitrogen. Crushing the powder enhanced its ability to clump together, since the higher surface area will increase the cohesive forces. When a big raft was formed on the surface, small chunks might release and sink down into water. When attempting to add higher quantities into

water, the salt might stick in the feeder, which is a drawback with this method.

Roger *et al.* [98], [99] added 10 g organic particles, which were cooled with liquid nitrogen down to -180 °C, into water, in order to validate their developed mathematical model. They observed a "finger"-formation, where frozen particles penetrate down the bath before freezing, which is also observed in see-through-cells [81]. Schlieren imaging was used to obtain information of thermal gradients occurring when the cold powder gets in contact with water, while PIV were used to obtain information of the natural convection occurring.

Schlieren imaging has also been applied in the recent work by Bouvais *et al.* [100] to understand the heat transfer and dissolution when a cold object is in contact with liquid. They were able to visualize convection both due to heat transfer and dissolving salt that change the density of water. This work also illustrated how a layer of frozen liquid will form around the structure, and that dissolution will be limited until the layer has melted away. The same paper also discusses some of the differences for water modeling, where the most obvious one is that water has the opposite density change when freezing and aid the buoyancy in opposition to bath.

Chapter 7: Modeling Studies

Mathematical modeling of the dissolution process has two main goals: firstly, to understand the local phenomena that cannot properly be studied experimentally, and secondly to predict how alumina will dissolve when being fed into a cell.

One can roughly divide modeling work in two branches, one related to the fundamentals on studying the mass transport and dissolution of the single grains and agglomerates, while the other models also consider movement of bath and can hence be used to estimate the distribution of alumina in a cell.

7.1 Dissolution of single grains and agglomerates

Haverkamp and Welch [38] derive two models that predict dissolution. The first is a shrinking sphere model for dispersed grains where dissolution is only dependent on surface area of the grains, while the other model is assuming that the dissolution is limited by mass transfer. In the last approximation, the mass rate of particle dissolving can be expressed as:

$$\frac{dm}{dt} = -KA'(C_{sat} - C),\tag{7.1}$$

where C and C_{sat} are respectively the alumina concentration in the bath and the saturation concentration. A' is the surface area of the particles while K is the dissolution rate constant. From their experiments, they estimated that K will be $10^{-6}\,\mathrm{m\,s^{-1}}$ for particles with an average size of 76.5 µm that are well dispersed in the melt.

Other authors have modeled several phenomena occurring when alumina enters the melt. Kovács *et al.* [101], [102] investigate the freezing, melting and dissolution of a cold alumina particle that is placed in the melt. They consider a particle in stagnant cryolite with a diameter of 50 µm and estimate the time of freezing, melting and dissolution to be respectively in the range of 500 µs, 100 ms and 17 s, indicating that mass transfer is the rate limiting step. The dissolution time is of the same order of magnitude as that found by Thonstad *et al.* [35] (4.1 s).

Dassylva-Raymond *et al.* [103] created an agglomeration model with five steps, considering the vaporization of moisture in alumina, freezing and melting of bath, infiltration, sintering and finally the dissolution. They studied spherical agglomerates with a diameter of 30 mm in a bath at 975 °C, where the superheat was 15 °C. The frozen layer was at its maximum 2 mm thick after 40 s and completely melted after 200 s. For a cylindrical

agglomerate with d=65 mm the maximum thickness layer is reached after 10 seconds, also 2 mm, and completely melted away after 140 s.

Kaszás *et al.* [104] describe the challenges related in developing a floating model for the rafts. They point out the lack of data for the contact angle between alumina and bath and irregular shape of particles as problematic. In later work [65], they measured the contact angle to be in the range between 29 and 34° and by assuming agglomerates to be spheres or cylindrical discs, they calculated that the density of small rafts spreading out on the entire surface can float even when exceeding the density of the molten bath.

7.2 Alumina distribution and dissolution

Theoretical studies on alumina feeding and distribution are given in table 7.1. Full scale studies consider the dissolution and distribution with real cell geometries, while in small scale, alumina is added in smaller amounts of liquid.

Table 7.1: Summary on how different works have modeled alumina feeding.

Author	Type	Fluid flow	Fluid-particle interactions	Dissolution based on	Consider rafts
Bardet *et al.* [105]	Full scale	CFD	One way Euler-Euler	Mass and Heat transfer	No
Bojarevics [106]–[108]	Full scale	Shallow water	One way Euler-Lagrange	Mass transfer rate law	Yes
Dion *et al.* [109]	Full scale	Prescribed	One way Euler-Euler	Mass transfer rate law	No
Einarsrud *et al.* [110]	Small Scale	CFD	Two way Euler Lagrange	-	No
Johansen *et al.* [111]	Full scale	Prescribed	One way Euler-Euler	Mass transfer rate law	No
Liu *et al.* [112]	Full scale	CFD	One way Euler-Lagrange	-	No
Rakotondramanana *et al.* [97], [113], [114]	Small scale	Constant wave	One way Euler-Lagrange	-	Yes
Roger *et al.* [98], [99], [115], [116]	Small scale	SPH	Two way Lagrange-Lagrange	Mass and heat transfer	Yes
Zhan *et al.* [117], [118]	Full scale	CFD	One way Euler-Euler	Mass and heat transfer	Yes
Zhang *et al.* [119]	Full scale	CFD	N/A	Time delay	No

The flow field will affect dispersion and movement of the alumina particles and rafts, and most works apply CFD to solve the velocity field. This is very time consuming and the reason why a prescribed velocity field, based on either earlier experiments or measurements from industrial cells, are also used. The shallow water approach, which is a quasi 2D-model [120], has been applied to model the magneto-hydrodynamics wave, and hence calculating the velocity field at the bath-metal interface. Roger *et al.* [98] use Smoothed Particle Hydrodynamics (SPH), hence modeling the fluid as Lagrangian particles. Each particle will then have its own force balance that must be calculated in order to obtain its velocity, but these types of calculations are more advantageous to run parallel on several cores than CFD-simulations.

Many of the studies do consider the particles added as Eulerian specie, either as co-herent lumps [109] or as an evenly spread out particles [105], [111], [118]. In case of treating the alumina in an Eulerian framework, the bath will affect the powder, but not the other way around. It is only the work by Einarsrud *et al.* [110] that there is two way coupling in an Euler-Lagrange framework, but the whole dose is simplified as a single rigid body. Modeling several particles is very computational time consuming, as seen in the work by Liu *et al.* [112], where only 10 grams alumina is added from a feeder, and the diameter is also set to be 5 mm, far higher than the real particle size. Roger *et al.* [98] have successfully implemented a two way-coupled particle fluid model, which is advantageous to run on several cores, as mentioned earlier.

In those models that include the dissolution of alumina, a mass transfer limited rate is mostly being assumed, as derived by Haverkamp and Welch [38], equation (7.1), where the value of K has been varied. The value can be derived as a mean of different exper-iments [109] or by derivation from the Ranz-Marshall-type Sherwood number correla-tion [111].

For the studies considering a combined mass- and heat-transfer model, the term $C_{sat} - C$ is often considered as the driving force for the mass transfer. To account for the pos-sibility that formation of frozen bath will hinder alumina from dissolving, Zhang *et al.* [119] apply a Heaviside step function for time to simulate the delay, which meant that no alumina could dissolve and distribute throughout the cell immediately after feed-ing. Bardet *et al.* [105] compared applying the step function on temperature and time and found that the results in the latter case had a higher variation and deviating more from industrial measurements, indicating that the heat transfer must be accounted for and that a time delay might be an oversimplification, as delayed time for a raft to dis-solve will strongly vary depending on the local available superheat. Another approach by Zhan *et al.* [117] uses a two-population balance model, where the small particles are assumed to dissolve by equation (7.1), while the heat transfer limits the dissolution of the larger ones. Roger *et al.* [98] simulate individual particles and two conditions must be fulfilled for dissolution to occur: the temperature must be above liquidus and the particle must be in contact with liquid that is not saturated with alumina. In their work, the dissolution rate is then not diffusion dependent, but will rather dissolve at a con-stant rate until the liquid is saturated.

Some of the presented models also account for the presence of rafts. The easiest approach is to still assume a mass transfer limited equation, but with a decreased mass transfer coefficient. The proportion of alumina being dispersed and forming raft, as well as an estimated mass transfer coefficient, must be given as an input [108] or estimated from experimental data [109], [118].

Smaller scale studies are focused on the formation and dynamics of an individual raft. At a smaller scale, events during alumina feeding can be studied in detailed, such as the dynamics of a batch hitting the bath [110] or a raft floating on a bath- metal interface [114]. Roger *et al.* [116] simulate the formation of rafts in detail by injecting cold powder into the bath, where an enthalpy method was applied to model freezing. In practice, the liquid particles will obtain solid behavior when the temperature is below the set melting point. Their method also allowed for alumina to be glued together in areas where bath was present, by applying a cohesive force between alumina particles that were in contact with liquid at a low enough temperature.

Summary

Models have been developed in several research groups, where the aim is to predict the dissolution and distribution of alumina, and hence being applied in order to optimize the process. Many of the models assume a constant dissolution rate, but experimental work and observations have found that this might not be the case, due to formations of rafts and agglomerates. In those models where raft formation is considered, the number of particles actually forming the rafts are uncertain, and do not consider that the ratio dispersed-agglomerated alumina may vary from feeding to feeding. Smaller scale work and experiments are thus necessary in order to create simplified sub-models that can be applied in the full-scale ones.

Another challenge with the current model that applies CFD is to formulate alumina in a cost-effective and a realistic way. A 1 kg batch will consist of millions of particles with multiple sizes and being able to track each particle individually is impractical. Being able to describe this phase through a continuous formulation is very beneficial, due to the availability of additional physical models and compatibility with already established frameworks.

Part III

Methodology

Chapter 8: Industrial Methodology

An industrial campaign where raft formation was recorded and rafts sampled was already conducted and sent for publishing prior to the start of this thesis [48], [49]. The literature study shows that it is very challenging to correlate operational parameters with raft formation. A further study must be conducted over several years and demand a lot of resources. It was therefore decided to limit industrial campaigns. Since the formation of HF is related to feeding of alumina, it was decided to perform an industrial campaign related to the formation of HF.

The industrial campaign was published in paper II. To measure the HF-content Laser-Gas™ II SP [121] from NEO monitors was used, which can measure the concentration of several gases by applying Tuneable Diode Laser Absorption Spectroscopy. This device was installed in the off-gas channel about 15 meters away of one cell at the Alcoa Mosjøen plant, and measured the HF-content regularly from July 4 to August 15 2019. The temperature and bath properties were measured every other day with STARprobe™ [122], as a part of the routine operations. Temperature was also increased for manually in a short period, by increasing the cell's voltage manually, and the temperature was then measured about every other hour, in total six times during that period.

The concentration was expressed as a function $C(t)$, and time-averaged values could be calculated between each feeding, $\bar{C}_{fa}$, and each feeding cycle, $\bar{C}_{ca}$:

$$\bar{C}_{fa} = \frac{1}{t_f} \int_{t_f} C(t) dt, \tag{8.1}$$

$$\bar{C}_{ca} = \frac{1}{t_c} \int_{t_c} C(t) dt, \tag{8.2}$$

where t_f represents the time between two subsequent feedings, while t_c represents the time for a feeding cycle, beginning when overfeeding starts.

These values were further used to study the effect of different parameters, as stated in table 8. The humidity data was received from a weather station a couple of kilometers away from the smelter [123].

Table 8.1: The properties investigated during the industrial measurement campaign.

Property	Response	How
Feeding cycle	$\bar{C}_{fa}$	Linear regression of the values from the point where overfeeding begins until the next one.
Anode change	$\bar{C}_{fa}$	Comparing the average of the 10 closest values before and after anode change.
Tapping	$\bar{C}_{fa}$	Comparing the average of the 10 closest values before and after tapping.
Temperature	$\bar{C}_{fa}$	Concentration at a temperature given as an average based on the five closest feeding before and after the measurements.
Humidity	$\bar{C}_{ca}$	Compare the values at a given time with the reported moisture content.

Chapter 9: Laboratory Methodology

9.1 Water modeling

Simulating alumina feeding using a water model is presented in paper III. The water model represents the cross section of a center channel in an industrial cell, illustrated in figure 9.1. Bubbles were created by running compressed air through perforated tubes with a diameter of 2 cm with 1 mm diameter placed every second cm on the tube. The bubbles on the long side will simulate the release of CO_2 from the anodes, while the bubbles formed at the short sides will simulate convection in the center channel. Ice chambers are placed on the short sides in order to maintain a low temperature of the water.
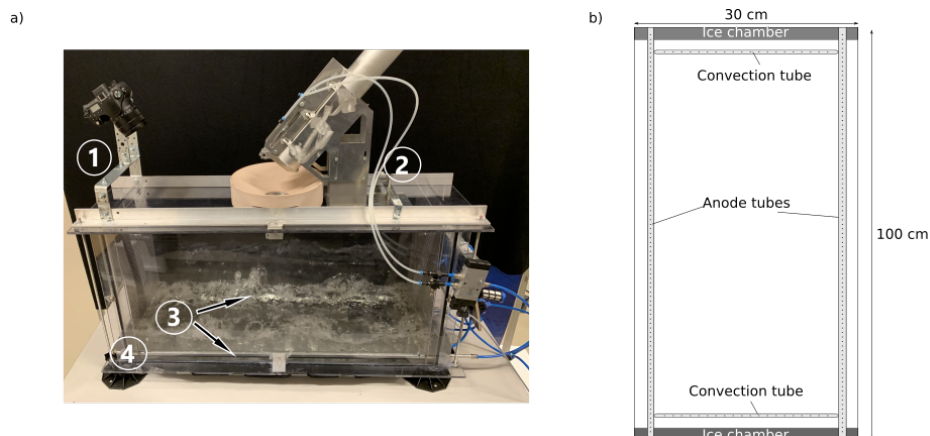
Figure 9.1: a) Image of the water model with 1: camera, 2: feeder, 3: pipes for simulating anodic bubbles, and 4: chambers for storing ice. b) Sketch of the water model seen from above. Figure republished from Gylver *et al.* [124]. Used with permission of The Minerals, Metals & Materials Society.

The feeder resembles a Pechiney feeder that can hold up to 1 L of powder and release the powder approximately 15 cm above the liquid. The powder replacing alumina should be safe to use, flow easily through the feeder and dissolve easily in water without discoloring it or creating foam. Initial trials with these criteria identified a commercial artificial sweetener, consisting mainly of maltodextrin and aspartame, as a good replacement. The powder was stored in a freezer holding -80 °C for at least 48 h prior to

41

the experiments, and had a temperature of approximately -50 °C upon feeding.

The effect of bubble frequency from anodes, temperature of the water and particle size of the powder was investigated in a 2 factor experiments with three replicates. The latter parameter was achieved by crushing the powder in a blender, and the PSD was measured in SEM. Overview of the experiments conducted are shown in table 9.1

Table 9.1: Experimental matrix with description of the different configurations considered.

Experiment	Particle size	Bubble frequency	Water temperature
1-3	Fine	Low	Low
4-6	Fine	Low	High
7-9	Fine	High	High
10-12	Fine	High	Low
13-15	Coarse	Low	High
16-18	Coarse	Low	Low
19-21	Coarse	High	Low
22-24	Coarse	High	High

9.2 Lab induced rafts

A method for extracting rafts at laboratory scale has been developed and investigated several parameters over multiple papers. The furnace is open on the top, and is heated up by elements going around the steel pipe with a diameter of 15 cm. It can be operated at temperatures up to 1200 °C, and the top is thermally insulated as much as possible to preserve heat.

A carbon crucible was filled with industrial bath and the temperature was monitored with a S-type thermocouple placed in a steel cap, immersed about 4 cm into the bath. Nitrogen was purged into the furnace continuously in order to decrease airburn on the carbon crucible. Alumina is fed into the melt through a 50 cm pipe, where a lid controlled by a spring feather is mounted on the bottom of it.
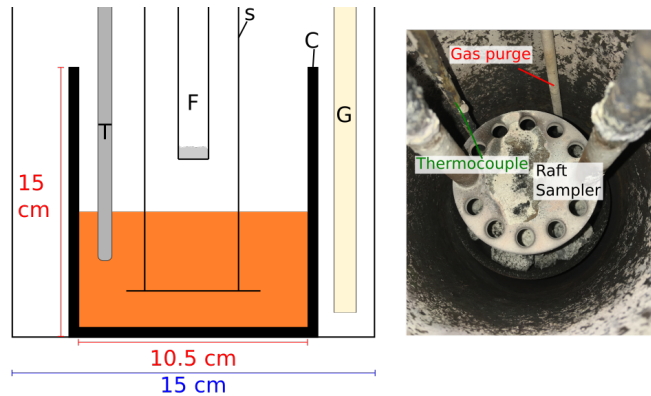
Figure 9.2: Left: Vertical cross section of the furnace, equipped with thermocouple (T), feeding pipe (F), raft sampler (S), carbon crucible (C) and gas purge (G). Right: Image of the furnace seen from above. Figure republished from Gylver *et al.* [125]. Used with permission of The Minerals, Metals & Materials Society.

Summary of the different experiments conducted are presented in table 9.2. For the experiments with varying LiF-content the superheat was set constant at 12 °C, which then will result in varying temperature as LiF has an impact on the liquidus of the melt [126]. It should be noted that different aluminas were used for the different experiments, please refer to the papers in question for an overview of alumina properties

Table 9.2: Overview of the different properties investigated in the open furnace. The crucible position states the height between the bottom of the crucible to the top of the furnace.

Parameter investigated	Presented in paper	Bath acidity	Initial Al_2O_3 content	Temperature	Crucible position	Drop height
Holding time	I	10.8 wt%	2.3 wt%	970 °C	41 cm	5 cm
Preheating	I	10.9 wt%	2.1 wt%	965 °C	41 cm	5 cm
Dry scrubbing	II	10.8 wt%	2.3 wt%	965 °C	41 cm	2 cm
MOI/LOI	II	10.8 wt%	2.3 wt%	965 °C	41 cm	2 cm
LiF-content	IV	9.0 wt%	2.0 wt%	Varying	41 cm	5 cm
Fines	V	10.6 wt%	3.8 wt%	970 °C	35 cm	5 cm
Alumina types	V	10.6 wt%	3.8 wt%	970 °C	35 cm	5 cm

The structure of selected rafts in paper I and II were further studied using μCT. The data was acquired using a Nikon XT H225 ST instrument (cone beam volume CT), using a tungsten reflection target and an aluminum filter of 1 mm.

CT were also applied in paper V, by a Nikon C1 compact large-envelope 5-axis X-ray μCT

instrument (cone beam volume CT). A tungsten 225 kV UltraFocus reflection target was used, with an acceleration voltage of 125 kV and a current of 175 µA. The X-rays were not filtered. The imaging was done with an integration time of 250 ms, amplification of 18 dB, with 6283 projections per 360°. The detector panel in the instrument is a Varex 1621 EHS with 2000x2000 pixels of size 200x200 µm, total panel size 40x40 cm^2. The distance from source to sample was 174.06 mm, distance from source to detector was 772.78 mm, resulting in a voxel size of 90.1 µm.

9.3 Recording alumina feeding

For the study in Paper V, the insulating materials covering the top of the furnace was opened, such that a GoPro Hero8 Black camera could record the bath surface as viewed in figure 9.3. 4 grams of alumina was added to the melt and the process was recorded until no more powder was visible on the bath surface.

Figure 9.3: Setup when recording the open furnace.

Chapter 10: Modeling Methodology

Several approaches for modeling alumina are described in chapter 7. This thesis investigates if a two-way coupled Euler-Euler formulation is a possible approach for modeling the formation of rafts by applying CFD. Section 10.1 provides an overview of governing equations for a single phase, while 10.2 extends it in order to be applied on a multiphase system. A possible approach for modeling solidification of bath and the alumina phase are presented respectively in 10.3 and 10.4. Section 10.5 will state the approximations and present modified equations, before a description of the used CFD-software, OpenFOAM, as well as the implementation of models is described in section 10.6. The last part of this chapter describes the different cases that are studied in this thesis.

10.1 Balance equations

The current section will present the equations and explain their physical purposes, and detailed derivations can be found elsewhere [127], [128].

The local accumulation of mass can be expressed as

$$\frac{\partial \rho}{\partial t} = -\nabla \cdot (\rho \boldsymbol{u}), \tag{10.1}$$

where a velocity vector $\boldsymbol{u} = \left[u_x, u_y, u_z\right]$ is introduced and ∇ is the differential operator.

The momentum, $\rho \boldsymbol{u}$, in a volume can change due to convection or forces acting on the fluid inside the control volume, both on the surface and on the body itself:

$$\frac{\partial}{\partial t} \left(\rho \boldsymbol{u}\right) = -\nabla \cdot \left(\rho \boldsymbol{u} \boldsymbol{u}\right) + \nabla \cdot \boldsymbol{\sigma} + \rho \boldsymbol{g}. \tag{10.2}$$

The gradient of the Cauchy stress tensor, $\nabla \cdot \boldsymbol{\sigma}$ and $\rho \boldsymbol{g}$ accounts for the surface and body forces, respectively. The Cauchy stress tensor can be separated into a pressure and a viscous force, resulting in:

$$\frac{\partial}{\partial t} \rho \boldsymbol{u} = -\nabla \cdot \left(\rho \boldsymbol{u} \boldsymbol{u}\right) - \nabla \cdot \boldsymbol{\tau} - \nabla p + \rho \boldsymbol{g}, \tag{10.3}$$

where $\boldsymbol{\tau}$ is the shear stress, and p is the pressure.

The shear stress is present due to viscosity and possible turbulence in the fluid, and can

be expressed as

$$\nabla \cdot \boldsymbol{\tau} = \nabla \cdot \left(2\rho\left[v + v_t\right]\boldsymbol{D}\right). \tag{10.4}$$

where v_t accounts for turbulent effects and v expresses the kinematic viscosity of the fluid. $\boldsymbol{D}$ is the strain rate tensor, defined as

$$\boldsymbol{D} = \tfrac{1}{2}\left(\nabla\boldsymbol{u} + (\nabla\boldsymbol{u})^T\right). \tag{10.5}$$

v is assumed to be constant for a Newtonian fluid [128]. For those fluids not obeying that law, a generalized Newtonian model is frequently applied, where the v can be expressed to be dependent on other factors of the system. A commonly applied model is the power law:

$$v = \frac{\tilde{m}}{\rho}D^{\tilde{n}-1}, \tag{10.6}$$

where $\tilde{m}$ and $\tilde{n}$ are material dependent constants. D is the strain rate, defined as

$$D = \sqrt{\tfrac{1}{2}\boldsymbol{D} : \boldsymbol{D}}. \tag{10.7}$$

The total energy E is expressed as a sum of both the internal and kinetic energy:

$$\frac{\partial}{\partial t}\left(\rho E\right) = -\nabla \cdot \left(\rho E\boldsymbol{u}\right) - \nabla \cdot \boldsymbol{q} + \rho(\boldsymbol{u}\cdot\boldsymbol{g}) - \nabla\cdot(p\boldsymbol{u}) - \nabla\cdot[\boldsymbol{\tau}\cdot\boldsymbol{u}] + S. \tag{10.8}$$

Energy change due to conduction is expressed by $\nabla \cdot \boldsymbol{q}$ and the term S accounts for heat sources, for example induction. Energy changes due to work originates from pressure forces, $\nabla \cdot (p\boldsymbol{u})$, viscous forces $\nabla \cdot [\boldsymbol{\tau}\cdot\boldsymbol{u}]$ and gravity, $\rho(\boldsymbol{u}\cdot\boldsymbol{g})$.

Several versions of the energy equation exist [128] and further derivations and simplifications will be based on the enthalpy equation:

$$\frac{\partial}{\partial t}\rho H - \frac{\partial}{\partial t}p = -\nabla \cdot \left(\rho\boldsymbol{u}H\right) - \nabla\cdot\boldsymbol{q} - (\boldsymbol{\tau}:\nabla\boldsymbol{u}) + \left(\nabla p\right)\cdot\boldsymbol{u} + S \tag{10.9}$$

The pressure contributions, $\frac{\partial}{\partial t}p$, $(\nabla p)\cdot\boldsymbol{u}$ is a result of the derivation. The term $\boldsymbol{\tau}:(\nabla\boldsymbol{u})$ will in this case account for rate of energy increase due to viscous dissipation.

10.2 Multiphase flow

When several phases co-exist, some adaptions are needed, since different phases might have different properties (for example density and viscosity) and they may interact with each other. By considering a control volume V, shown in figure 10.1, where three phases, noted i, j and k are present, the volumetric phase fraction, α_k, inside the con-

trol volume [129] is defined as

$$\alpha_k \equiv \frac{V_k}{V_i + V_j + V_k} = \frac{V_k}{V}, \tag{10.10}$$

where V_k is the volumetric amount of the component k that occupies the volume.
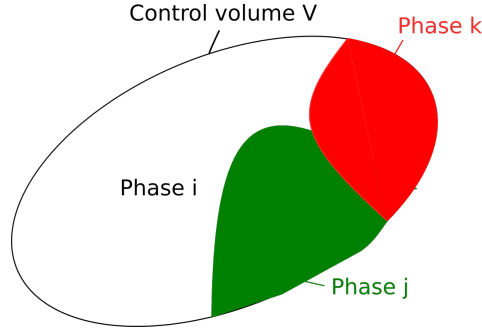
Figure 10.1: Control volume for a system consisting of three phases, i, j and k.

The conservation equations written in the previous section must be reformulated to account for that the phases can have different physical properties, as well considering the exchange of mass, momentum and energy between them. The presented equations are based on derivations by Drew and Passman [129]. The first approach is an N-fluid model, where the balance equations are formulated for each single component k. The balance of mass is

$$\frac{\partial \alpha_k \rho_k}{\partial t} + \nabla \cdot (\alpha_k \rho_k \boldsymbol{u}_k) = \dot{R}_k, \tag{10.11}$$

where ρ_k and $\boldsymbol{u}_k$ are respectively the density and velocity of component k, while $\dot{R}_k$ denotes the accumulations or decumulation of the phase due to interactions with other phases, for example chemical reactions.

The momentum equation can be written in the same manner:

$$\frac{\partial}{\partial t} \left(\alpha_k \rho_k \boldsymbol{u}_k \right) + \nabla \cdot \left(\alpha_k \rho_k \boldsymbol{u}_k \boldsymbol{u}_k \right) = -\nabla \left(\alpha_k p_k \right) + \nabla \cdot (\alpha_k \boldsymbol{\tau}_k) + \alpha_k \rho_k \boldsymbol{g} + \alpha_k \boldsymbol{F}_{ks}, \tag{10.12}$$

where $\boldsymbol{F}_{ks}$ denotes change in momentum due to interactions between k and other phases.

Finally, the energy equation is written as

$$\frac{\partial}{\partial t} \alpha_k \rho_k H_k - \frac{\partial}{\partial t} \alpha_k p_k$$
$$= -\nabla \cdot \left(\alpha_k \rho_k \boldsymbol{u}_k H_k \right) - \nabla \cdot \boldsymbol{q}_k - \boldsymbol{\tau}_k : (\nabla \boldsymbol{u}_k) + \left(\alpha_k \nabla p_k \right) \cdot \boldsymbol{u}_k + \alpha_k \rho_k S_k + \alpha_k S_{ks}, \tag{10.13}$$

where the last term, S_{ks}, accounts for the exchange of energy between phase k and other phases.

With this model, the balance equations must be solved for each phase, resulting in a total of $5N - 1$ equations for a system with N phases. In addition, the interaction terms between the different phases need additional modeling, increasing the complexity even more.

A simplified approach, known as the mixture model, is to assume that interactions between different phases cancel out. A property χ of the mixture will be calculated by weighing each individual property with the volumetric phase fraction:

$$\chi_m = \sum_{k=1}^{N} \alpha_k \chi_k, \tag{10.14}$$

for a system consisting of N phases. Definitions that express quantities in term of bulk values are needed. Velocity will be defined by the center of mass

$$\rho_m \boldsymbol{u} = \sum_{k=1}^{N} \alpha_k \rho_k \boldsymbol{u}_k, \tag{10.15}$$

and other systems variables, such as enthalpy and gravity, will be defined in the same manner [129].

Since the sums of interactions between phases become zero, the balance equations are

$$\frac{\partial \rho_m}{\partial t} + \nabla \cdot (\rho_m \boldsymbol{u}) = 0, \tag{10.16}$$

$$\frac{\partial}{\partial t} (\rho_m \boldsymbol{u}) = -\nabla \cdot (\rho_m \boldsymbol{u} \boldsymbol{u}) + \nabla \cdot \boldsymbol{\tau} - \nabla p + \rho_m \boldsymbol{g}, \tag{10.17}$$

$$\frac{\partial}{\partial t} \rho_m H - \frac{\partial}{\partial t} p = -\nabla \cdot (\rho_m \boldsymbol{u} H) - \nabla \cdot \boldsymbol{q} - \boldsymbol{\tau} : (\nabla \boldsymbol{u}) + (\nabla p) \cdot \boldsymbol{u} + S_m, \tag{10.18}$$

which are analogous to the single-phase equations, but with material properties corresponding to that of the mixture.

Volume of Fluid method

The volume of fluid method (VOF) is developed by Hirt and Nichols [130], in order to use the mixture equation (eq. (10.16)-(10.18)), but still being able to locate and track the interface between phases and account for interphasial interactions.

In this formulation, all properties and fields are volume averaged and by assuming that all the phases are incompressible, the phase fraction is solved by the conservation equa-

tion

$$\frac{\partial}{\partial t}(\alpha_k) + \nabla \cdot (\alpha_k \boldsymbol{u}) = 0, \tag{10.19}$$

and by the constraint for the last fluid

$$\sum_i^N \alpha_i = 1. \tag{10.20}$$

The interface is identified as areas where $0 < \alpha_k < 1$, while regions with $\alpha_k = 1$ contain only the k-th phase. Methods for calculating the interface vary, and details regarding different methods can in for instance be found in the article by Deshpande *et al.* [131].

The momentum equation considers interactions between the different phases and is written as

$$\frac{\partial}{\partial t}(\rho_m \boldsymbol{u}) = -\nabla \cdot (\rho_m \boldsymbol{u}\boldsymbol{u}) + \nabla \cdot \boldsymbol{\tau} - \nabla p + \rho_m \boldsymbol{g} + \boldsymbol{F}_{ST}. \tag{10.21}$$

$\boldsymbol{F}_{ST}$ accounts for the surface tensions between the different phases, which can be modeled with a continuum surface approach [132]. A similar approach is written for the energy equation:

$$\frac{\partial}{\partial t}\rho_m H - \frac{\partial}{\partial t}p = -\nabla \cdot (\rho_m \boldsymbol{u}H) - \nabla \cdot \boldsymbol{q} - \boldsymbol{\tau} : (\nabla \boldsymbol{u}) + (\nabla p) \cdot \boldsymbol{u} + \rho_m S_m + S_{km}, \tag{10.22}$$

where S_{km} describes energy transition between phases.

10.3 Modeling solidification and melting

A common strategy to model solidification is to apply source terms to the momentum and energy equation through what is known as the porosity-enthalpy method [133], [134]. In this method, a new parameter g_s expresses the fraction of liquid that is solidified within a control volume, which is temperature dependent. The easiest expression will be to assume an isothermal phase change to occur.

$$g_s = \begin{cases} 1 & \text{for } T < T_M, \\ 0 & \text{for } T > T_M, \end{cases} \tag{10.23}$$

At the melting point, a discontinuity in g_s occurs. More complicated forms also exist and can be found in the paper by Swaminathan and Voller [135].

The momentum and enthalpy balance for an incompressible fluid that can solidify, where buoyancy is written with the Boussinesq approximation, can hence be written as

$$\rho \frac{\partial}{\partial t}\boldsymbol{u} = -\rho \nabla \cdot (\boldsymbol{u}\boldsymbol{u}) + \nabla \boldsymbol{\tau} - \nabla p + \rho \boldsymbol{g}\beta(T - T_{ref}) + \boldsymbol{F}_d, \tag{10.24}$$

$$\rho c_p \frac{\partial}{\partial t}(T) = -c_p \rho \nabla \cdot (\boldsymbol{u} T) + \nabla \cdot (\kappa \nabla T) + \rho S_h, \tag{10.25}$$

where β is the coefficient of expansion and T_{ref} is a reference temperature. The term $\boldsymbol{F}_d$ dampens the velocity to zero when the liquid solidifies and is modeled as a porous media flow [134]

$$\boldsymbol{F}_d = -C \frac{(g_s)^2}{(1-g_s)^3 + q} \boldsymbol{u}, \tag{10.26}$$

where C is a constant that expresses the strength of the source term, normally in the order of 10^5. A small constant, q, is needed to avoid singularity, and $\boldsymbol{F_d}$ will dominate the momentum equation as g_s approaches one. S_h can be derived by comparing the energy equation for the solid and liquid [136]

$$S_h = \rho L \left[\frac{\partial g_s}{\partial t} + \nabla \cdot (\boldsymbol{u} g_s) \right]. \tag{10.27}$$

10.4 The μ(I)-rheology

Being able to describe granular flow as a continuum is highly beneficial for several applications, for example in predicting avalanches or to model sedimentation. A problem with these flows is the high variation in behavior, from solid-like when put at rest, to liquid-like when poured or flowing through a pipe [137]. Granular flows can roughly be separated into dense- and dilute (or fluidized) regimes, depending upon the relative distance between particles and the strength of their interactions. The fluidized regime has successfully been described by the kinetic theory for granular flow (KTGF) [138]. It is in particular in the dense regime, where the particles behave as a liquid where a there has been a lack of good descriptions.

The μ(I)-rheology is a possible approach to explain dense granular flows, which can be derived from relatively simple experiments [139], and further generalized into a three dimensional space [137]. The flow can be expressed as a generalized Newtonian fluid, where the viscosity is dependent on strain rate and pressure:

$$\nu = \frac{\mu(I)}{\sqrt{2}D} \frac{p}{\rho}. \tag{10.28}$$

$\mu(I)$ is a coefficient of friction

$$\mu(I) = \mu_1 + \frac{\mu_2 - \mu_1}{I_0/I + 1}, \tag{10.29}$$

where μ_1, μ_2 and I_0 are material properties, while I is the inertial number, defined as:

$$I = \frac{d\sqrt{2D}}{\sqrt{p/\rho}}.\qquad(10.30)$$

The presented model might for some cases be ill-posed for large and small I, and Barker *et al.*[140] have developed a regularized model, which will be applied in this work. In their proposal, some new parameters are needed, and a new expression is defined for a low inertial number

$$\mu = \begin{cases} \sqrt{\dfrac{a}{\log\left(\dfrac{A}{I}\right)}}, & \text{for } I \leq I_1 \\[3ex] \dfrac{\mu_1 I_0 + \mu_2 I + \mu_\infty I^2}{I_0 + I} & \text{for } I > I_1, \end{cases}\qquad(10.31)$$

where a and μ_∞ are new material dependent constants. I_1 is the lowest number possible where the equations are well posed, and is found by solving the equation

$$4\left(\frac{I\mu'}{\mu}\right)^2 - 4\left(\frac{I\mu'}{\mu}\right) + \mu^2\left(1 - \frac{I\mu'}{2\mu}\right) = 0,\qquad(10.32)$$

where

$$\mu' = \frac{\mathrm{d}\mu}{\mathrm{d}I},\qquad(10.33)$$

which can be determined by differentiating equation (10.29). A is a constant based on the other parameters:

$$A = I_1\left(\frac{a(I_0 + I_1)^2}{\left(\mu_1 I_0 + \mu_2 I_1 + \mu_\infty I_1^2\right)}\right).\qquad(10.34)$$

10.5 Formulations for alumina feeding

Some simplifications are done, as the current work was restricted to study the effect of the selected models, but should be revised if extending the model further.

Firstly, VOF is chosen as the framework for multiphase flow and all phases are assumed to be incompressible. In addition, no reactions occur and all interactions between the phases are modeled as surface tension. For the energy equation, viscous dissipation is neglected, conduction is assumed to be described with Fourier's law. In addition entalphy is assumed to be linear dependent with temperature, the heat capacity is constant. The balance equations are hence written as:

$$\frac{\partial \rho_m}{\partial t} + \nabla \cdot (\rho_m \boldsymbol{u}) = 0,\qquad(10.35)$$

$$\frac{\partial}{\partial t}\left(\rho_m \boldsymbol{u}\right) = -\nabla \cdot \left(\rho_m \boldsymbol{u}\boldsymbol{u}\right) + \nabla \cdot \boldsymbol{\tau} - \nabla p + \rho_m \boldsymbol{g} + \boldsymbol{F}_{ST} + \boldsymbol{F}_d. \tag{10.36}$$

$$c_{p,m}\frac{\partial}{\partial t}\left(\rho_m T\right) = -c_{p,m}\nabla \cdot \left(\rho_m \boldsymbol{u} T\right) + \nabla \cdot \left(\kappa_m \nabla T\right) + S_h. \tag{10.37}$$

For the solidification and melting case, some new adaptions are needed, since the solidification should only occur in the bath phase, the reformulated expression of g_s will be

$$g_s = \begin{cases} \alpha_b & \text{for } T < T_M, \\ 0 & \text{for } T > T_M, \end{cases} \tag{10.38}$$

For a time step $n+1$, the values of g_s are calculated by the algorithm

$$\begin{aligned} g_s^* &= g_s^n - \frac{\gamma c_p}{L}\left(T - T_M\right) \\ g_s^{n+1} &= \max\left[0, \min\left(\alpha_b, g_s^*\right)\right], \end{aligned} \tag{10.39}$$

where γ is an under-relaxation factor.

Equation (10.26) must also be reformulated, as this equation will set the velocity to zero, while in a multiphase system, it is the relative velocity that should have this behavior. A possible approach is to simulate the bath as a very viscous fluid when solid:

$$\boldsymbol{F}_d = \nu_{sol} \cdot \nabla^2 \boldsymbol{u}, \tag{10.40}$$

where ν_{sol} is dependent on temperature

$$\nu_{sol} = \begin{cases} \alpha_b C_v, & \text{for } T \leq T_s \\ \alpha_b C_v \exp\left[\tilde{A}\cdot(T_s - T))\right], & \text{for } T_s \leq T \leq T_L \\ 0 & \text{for } T > T_L \end{cases} \tag{10.41}$$

C_v accounts for the "strength" of source term, which will decay exponentially from the solidifying point T_s to T_L, while $\tilde{A}$ is a scaling factor. This parameter is set in order to avoid numerical issues that may occur when there is a strong difference in viscosity.

The μ(I)-rheology is implemented as stated in equation (10.28), where the viscosity value will be further averaged. The shear stress will hence be

$$\nabla \cdot \boldsymbol{\tau} = \nabla \cdot \left(2\rho_m \left[\nu_m + \nu_t\right] \boldsymbol{D}\right), \tag{10.42}$$

where ν_m must be calculated in each computational cell and then averaged.

10.6 Numerical realization

The equations presented in the previous section are nonlinear partial differential equation and analytical solutions of these equations are rare. Computational Fluid Dynamics provides a framework to solve these equations by numerical methods and is widely applied in problems spanning from simple laminar flows into complex multiphase cases involving reactions and heat transfer.

The equations derived in the previous sections are continuous, and in this work the Finite Volume Method (FVM) is applied. This corresponds to the Eulerian framework discussed in chapter 3, where the system investigated will be divided into control volumes, and the conservation equations will be solved in each of them. Hence, the partial differential equations for the continuous fields (such as temperature) will be converted into sets of linear equations with discrete field, corresponding to large matrices [33]. CFD can be divided into three main steps [30]:

1. Pre-processing, where all necessary initial information is given. It involves generating a computational domain, and divide them up into several smaller cell volumes, called a mesh. Schemes that discretize the equations must be defined together with suitable methods for solving them. Initial values and boundary conditions of the fields must also be defined, as well as other relevant properties (viscosity, heat capacity, etc.). In essence, the pre-processing steps will take all the information from the user and transform it into suitable equations that can be solved in the next step.

2. In the solver part, the equations that are provided from the pre-processing step are solved by numerical methods. The equations will be discretized into a linear equation for each cell, and ultimately creating a large matrix, that must be solved by iterative methods. If the problem is steady-state, the solver will run until desired criteria are met. If transient, data will be stored at the desired time steps. Detailed descriptions are for example found in the notes by Greenshields and Weller [33].

3. Post-processing, where results are extracted and visualized. The data given by the solvers consist of several files describing the values of different variables in each control volume. Visualization and extracting necessary data is therefore needed, which can be done with custom made code or existing software, for example Paraview [141].

A possible software that uses this framework is OpenFOAM [142], an open-source software based on C++, with a wide range of applications, including the availability to develop own solvers and models to add desired physics. The following section provide detailed descriptions on how the different models are implemented.

Implementing the energy equation

Since the incompressible solvers were isothermal, an additional energy equation was implemented. A temperature field is introduced, which are found by solving equation (10.37), implemented as stated in listing 10.1.

Listing 10.1: The implementation of the energy equation, eq (10.37) in OpenFOAM.

```
1   fvScalarMatrix TEqn
2   (
3     fvm::ddt(rho, T) +
4     fvm::div(rhoPhi,T)
5     - fvm::laplacian(mixture.kappaf()/mixture.cpf(), T)
6     ==
7     fvOptions(rho,T)
8   );
9
10  TEqn.relax();
11  fvOptions.constrain(TEqn);
12  TEqn.solve();
13  fvOptions.correct(T);
```

Equation 10.37 is written in line 2-6, where the phase-averaged values of thermal conductivity and heat capacity is returned by calling for the mixture equation. The temperature is then solved numerically at line 12.

Implementing solidification and melting

Solidification by adding extra source terms has already been successfully implemented in OpenFOAM [136] by the utility fvOptions. The current description is based on version 8, but in later versions fvOptions has been divided into two, fvConstraints and fvModels, where the developed model will be in the last category.

As seen in listing 10.1, a function fvOptions() is called. This provides an opportunity to add additional source terms to the balance equations, without needing to modify the solvers. Another benefit is that models created in the fvOptions utility can be used by multiple solvers.

fvOptions declares a function addSup, which is in the specific cases are defined. In the current work, the implementation of the viscous source term is stated in listing 10.2, where the function update() calculates the strength of the viscosity and the phase fraction solidified. Line 8 retrieves the velocity field and the term is added explicit to the momentum equation at line 9

Listing 10.2: Implementation of F_d from equation (10.40).

```
1    void Foam::fv::multiVOFSolidificationMelting::addSup
2    (
3    fvMatrix<vector>& eqn,
4    const label fieldi
5    )
6    {
7      update();
8      const volVectorField& UField = mesh_.lookupObject<volVectorField>("U");
9      eqn += nuSource_*fvm::laplacian(UField);
10   }
```

Listing 10.3: Implementation of the update function.

```
1    void Foam::fv::multiVOFSolidificationMelting::update()
2    {
3      alphaSolid_.oldTime();
4      nuSource_.oldTime();
5      const volScalarField& TVoF = mesh_.lookupObject<volScalarField>("T");
6      const volScalarField& alphaVoF = mesh_.lookupObject<volScalarField>(phaseName_);
7      forAll(cells_, i)
8      {
9        const label celli = cells_[i];
10       const scalar alphaSolidNew =
11       alphaSolid_[celli] -relax_*(TVoF[celli]-Tsol_)*CpL_/L_;
12       alphaSolid_[celli] = min (alphaVoF[celli],max(0,alphaSolidNew));
13       nuSource_[celli] = alphaVoF[celli]*pos(Tliq_ - TVoF[celli])*Cnu_*exp((Tsol_-TVoF[celli])*pos(TVoF[celli]-
                Tsol_)*A_);//(Tsol_-TVoF[celli])*), Cnu_)*pos(Tliq_-TVoF[celli]);
14     }
15
16     alphaSolid_.correctBoundaryConditions();
17   }
```

In listing 10.3, the fields g_s, v_{sol}, T and α_b from the previous time step is defined in line 3-6. A loop goes through all the computational cell and calculates new values of g_s by (10.39) in line 10-12, and line 13 corresponds to equation (10.41)

The term S_h is implemented in a similar manner in listing 10.4

Listing 10.4: The implementation of equation 10.27.

```
1    update();
2    dimensionedScalar L("L", dimEnergy/dimMass, L_); //Added in order to give L dimensions
3    dimensionedScalar CpVoF("CpVOF", dimEnergy/dimMass/dimTemperature ,CpL_);
4    eqn += L/CpVoF*(fvc::ddt(rho, alphaSolid_));
```

The observant reader might notice that the function update() is called both in the implementations of the momentum and energy equation, listing 10.2 and 10.4. The reason is that some OpenFOAM-solvers will solve the energy equation prior to the momentum equation. As the fvOptions utility should be as general as possible, the update() function must be called in both times in order to ensure that the field g_s is calculated. In practice, it will be identical for the same time step.

The μ(I)-viscosity model

The viscosity of the material is needed when solving the momentum equation (equation (10.36)). In our solver, where the PIMPLE-algorithm is used, viscosity is calculated during the prediction of the velocity field [131], described by the following equation:

$$\frac{\partial}{\partial t}\left(\rho_m \boldsymbol{u}\right) = -\nabla \cdot \left(\rho_m \boldsymbol{u}\boldsymbol{u}\right) + \nabla \cdot \boldsymbol{\tau}, \tag{10.43}$$

which is implemented in the file UEqn.H, shown in listing 10.5

Listing 10.5: U.Eqn for a two-phase and multiphase solver.

```
1    fvVectorMatrix UEqn
2    (
3    fvm::ddt(rho, U) + fvm::div(rhoPhi, U)
4    + MRF.DDt(rho, U)
5    + turbulence->divDevTau(rho, U)
6    ==
7    fvOptions(rho, U)
8    );
9
```

Line 4 is present in case of a moving mesh and line 7 provides an option for adding additional source terms, thoroughly explained in the previous section. Line 5 calls for the function divDevTau(rho,U), which will calculate the shear stress, expressed in equation (10.42), and in case of a laminar flow implemented as written in listing 10.6.

Listing 10.6: The function divDevTau in case of a laminar flow.

```
1    Foam::linearViscousStress<BasicMomentumTransportModel>::divDevTau
2    (
3    const volScalarField& rho,
4    volVectorField& U
5    ) const
6    {
7    return
8    (
9    - fvc::div((this->alpha_*rho*this->nuEff())*dev2(T(fvc::grad(U))))
10    - fvm::laplacian(this->alpha_*rho*this->nuEff(), U)
11    );
12    }
```

When applying in the case of VOF-case, the ρ and ν is already phase averaged, and hence the alpha value in line 8 and 9 will be uniform equal one. For incompressible cases, the viscosity for each separate phase will hence be calculated individually before being phase-averaged. OpenFOAM provides several different models for incompressible flows, which all inherits from the abstract base class viscosityModel. The benefit of programming this way is that a developed model can be implemented once and then applied by all solvers that use this base class.

The μ(I)-rheology is thus implemented as such a model. For simplicity, the code presented is for the original model, but the regularized model is available in appendix A. The current model is partly based on the one developed by Jarosch [143]. In the cur-

rent implementation, equations (10.7) and (10.28)-(10.30) is implemented as functions, showed in listings 10.7-10.10

Listing 10.7: Implementation of the granular viscosity function, equation (10.28).

```
1    Foam::tmp<Foam::volScalarField>
2    Foam::viscosityModels::muIMultiPhase::calcNu() const
3    {
4      Info<< "Calculating viscosity\n" << endl;
5      return max
6      (
7      nuMin_,
8      min
9      (
10     nuMax_,
11     (calcmuI())/(calcStrain()+dimensionedScalar("Vsmall", dimless/dimTime, 1e-09))*Pcalc()/rho_
12     )
13     );
14
15   }
16
```

Listing 10.8: Implementation of the μ(I)-function, equation (10.29).

```
1    Foam::tmp<Foam::volScalarField>
2    Foam::viscosityModels::muIMultiPhase::calcmuI() const
3    {
4      return mu1_ + (mu2_-mu1_)/(I0_/(max(calcI(),dimensionedScalar("Ismall", dimless, 1e-12)))+1);
5    }
6
```

Listing 10.9: Implementation of the inertial number, equation (10.30).

```
1    Foam::tmp<Foam::volScalarField>
2    Foam::viscosityModels::muIMultiPhase::calcI() const
3    {
4      return d_*calcStrain()/(sqrt(Pcalc()/rho_));
5    }
6
```

Listing 10.10: Implementation of the strain rate, equation (10.7).

```
1    Foam::tmp<Foam::volScalarField>
2    Foam::viscosityModels::muIMultiPhase::calcStrain() const
3    {
4      return sqrt(2.0)*mag(symm(fvc::grad(U_)));
5    }
6
```

A function PCalc() is also present, and defined in listing 10.11. This function reads the pressure field of the system and ensures that the pressure in all cells in the system is above a set minimum value.

Listing 10.11: The implementation of pressure field used to calculate the granular viscosity.

```
1    Foam::tmp<Foam::volScalarField>
2    Foam::viscosityModels::muIMultiPhase::Pcalc() const
3    {
4      const objectRegistry& db = U_.db();
5      if (db.foundObject<volScalarField>("p")) {
6        Info<< "Calculate I based on pressure" << endl;
7        const volScalarField& ptot = U_.mesh().lookupObject<volScalarField>("p");
8        return max(ptot, pMin_);
9
```

Solvers and algorithms

Mainly three solvers are used in this work, and they are chosen based on how many phases that are present in the different cases:

- PimpleFoam, a "transient solver for incompressible, turbulent flow of (generalized) Newtonian fluids". For single-phase flows

- interFoam, a solver for "two incompressible, isothermal immiscible fluids using a VOF phase-fraction method based on interface capturing approach". For two-phase flows

- multiphaseInterFoam, which use the same methods as interFoam, but is able to handle three or more phases.

In addition, the multiphase solvers have been modified to account for the temperature equation as written in listing 10.1.

Figure 10.2 shows the order on when the different equations are solved and where the code presented in 10.1-10.11 is implemented. Common for all solvers, is that the PIMPLE-algorithm resolves the pressure-velocity coupling. For the multiphase solvers, the transport equations for phase fraction, (10.19) and (10.20) are solved before the mixture properties are calculated from equation (10.14). These solvers will calculate the viscosity during the mixture calculations, while pimpleFoam will calculate when solving the momentum equation.
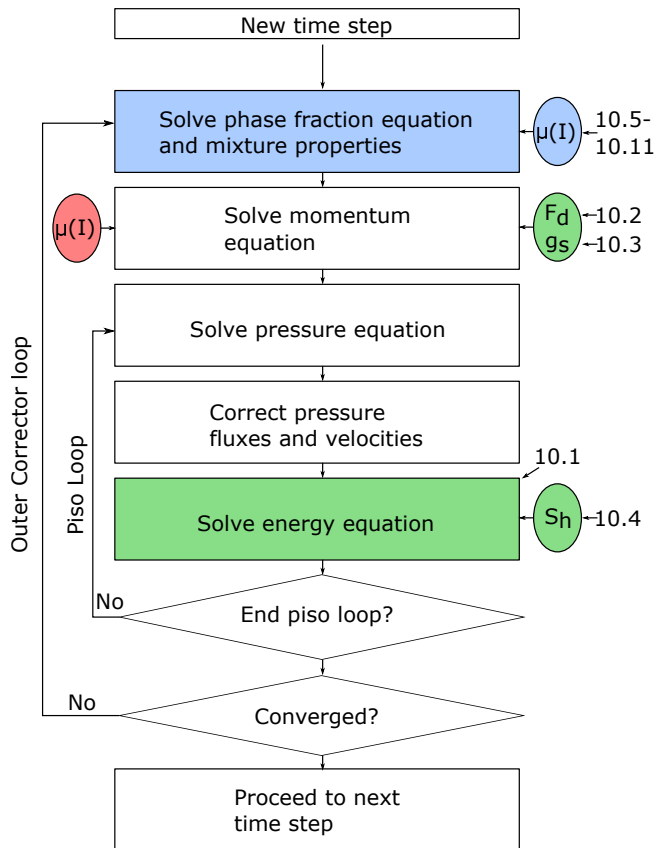
Figure 10.2: Algorithm for all the solvers used. Boxes in blue is applied for all multiphase solver and green boxes are only applied for the solvers considering the energy equation. The round circles denote where the different source terms and viscosity models are applied, where the red color is for pimpleFoam. The numbers on right hand side indicates where the code presented in listings 10.1-10.11 is implemented.

10.7 Overview of cases studied

Different cases were studied in Paper VI and VII, and a short description of all of them are given in table 10.1, including a benchmark case that has not been published.

Table 10.1: Summary of the different cases investigated in this thesis.

Case	Name	Solver	Purpose
		Paper VI	
1	Stefan case 2D	interTempFoam	Verify implementation of the energy equation and energy source term.
2	Rigid Floating body	interTempFoam	Investigate the momentum source term, effect of drop height, raft- and bath temperature and heat capacity of bath.
3	Feeding of a dose	multiphaseInter-TempFoam	Investigate the effect of the momentum source term when alumina is considered as its own phase.
		Paper VII	
4	Inclined Plane	pimpleFoam and interFoam	Verify the μ(I)-rheology for grains on an inclined plane as described by Lagrée *et al.* [144].
5	Column collapse	interFoam	Compare results with simulated data from Lagrée *et al.* [144].
6	Alumina collapse	interFoam	Sensitivity analysis of parameters for alumina.
7	Falling dose	interFoam	Sensitivity analysis for alumina falling on a flat surface.
8	Three-phase case	multiphaseInter-Foam	Simulate feeding of a dose in a pool of cryolite, where the μ(I)-rheology are applied.
9	Coupled case	multiphaseInter-TempFoam	Same as case 8, including the solidification model.
		This thesis only	
10	Benchmark cases	multiphaseInter-TempFoam	Cases for comparing how the different models affect the running time.

10.8 Heat transfer cases

The setups of the heat transfer cases are shown in figure 10.3. The following paragraphs provide a brief description of the cases, while additional details are found in the paper.

Stefan case

A slab of liquid with infinite length and temperature T_L with a freezing point at $T_m < T_L$ is considered. The left wall of the domain will have a temperature $T_s < T_m$ at $t = 0$, thus creating a moving phase front driven by diffusion, where the position of the solidifying
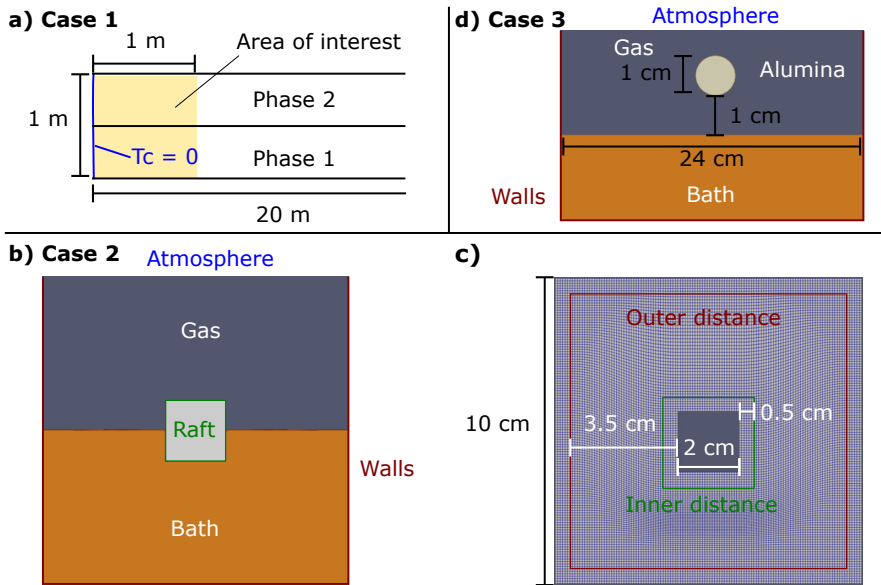
Figure 10.3: Overview of the cases investigated: **a) Case 1**: Stefan case. **Case 2**: Rigid body case, where **b)** shows boundaries and phases present, and **c)** the deformation of mesh with inner and outer distance. **d) Case 3**: Cold alumina dose falling into cryolitic bath.

front, $X(t)$, have an analytical solution [145]:

$$X(t) = 2\lambda\sqrt{g_s t}, \tag{10.44}$$

which then can be used for comparison. λ is found by solving the Stefan problem, described in paper VI and in the book by Alexiades and Solomon [145].

The case was set up as a 2D case consisting of four walls, where freezing occurs within a distance of 1 m from the left wall in the investigated time interval, marked as the area of interest. The right wall is 20 meters away, while the distance between upper and lower wall is 1 meter. The long geometry was used in order to obtain conditions similar to that of the analytical solution, i.e. an infinite domain. Properties of the phases are shown in table 10.2, and is set such as the Stefan number and thermal diffusivity of the phases are equal, thus resulting in the same value of λ and equal movement of the freezing fronts. The system has an initial temperature of 100 °C, while the left wall has a temperature of 0 °C. Since the case is without any convection and isothermal solidification occurs, only the first term in equation (10.27) was considered.

Table 10.2: Physical properties for case 1.

Property	Symbol	Phase 1	Phase 2	Unit
Density	ρ	1000	1	$kg\,m^{-3}$
Heat Capacity	c_p	1	1	$J\,kg^{-1}\,°C^{-1}$
Viscosity	ν	0.01	0.01	$m^2\,s^{-1}$
Thermal conductivity	κ	10	0.01	$W\,m^{-1}\,°C^{-1}$
Latent heat of fusions	L	10	10	$J\,kg^{-1}$
Melting point	T_M	10	10	°C

Rigid floating body

In this case, the raft is considered to be a cubic rigid object floating on a bath of cryolite with air above, as seen in figure 10.3**a)**. The cases are limited to 2D and the body is only allowed to move up and down. When movement of the rigid object occurs, the mesh is being deformed in the area that is set by an inner and outer distance away from the object, illustrated in figure 10.3**b)**.

A raft with density of 1200 $kg\,m^{-3}$, is partly immersed in the melt, with center of mass located 0.4 cm above the surface, and has a constant temperature below the melting point of the bath. A factorial design was performed, where the effects of bath- and raft-temperature, bath heat capacity and the raft's initial velocity, to illustrate the effect of different drop height, were varied. The values used are given in table 10.3 for the factors varied, and the other property values are given in table 10.7. The exception is the heat capacity of the air, which was set to be 10000 $J\,kg^{-1}\,°C^{-1}$ in order to avoid that bath freezes due to faster cooling of air. An additional case with reduced damping strength was also ran, where all factors besides the velocity were low.

Table 10.3: The low and high value of the parameters investigated for case 2.

Property	Low	High	Unit
Initial temperature	965	980	°C
Raft temperature	100	500	°C
Bath heat capacity	1600	2200	$J\,kg^{-1}\,°C^{-1}$
Initial velocity	0	0.03	$m\,s^{-1}$

Feeding of a dose

The third case simulates a dose of alumina falling into a liquid bath, where the effect of solidification and its interactions with several phases are investigated. For simplicity,

alumina is assumed to be a Newtonian fluid. The walls at the sides are placed a long distance away to avoid any unwanted boundary effects. A total of five cases were run, four where C_v was set to be respectively 0, 0.01, 0.1 and 1, while the last case was run without applying extra source terms.

10.9 Granular cases

Inclined plane and column collapse

When considering a single layer case along an inclined plane with an angle θ and boundary conditions as shown in figure 10.4a), an analytical solution for the velocity profile exists, as derived by Lagrée et al. [144]

$$u = \frac{2}{3} I_\theta \sqrt{g d \cos\theta \frac{H^3}{d^3}} \left[1 - \left(1 - \frac{y}{H} \right)^{3/2} \right]. \tag{10.45}$$

g is the magnitude of $\boldsymbol{g}$, d is the particle diameter and H is the height of the column. The inertial number in this case will then be constant:

$$I_\theta = I_0 \left[\frac{\tan(\theta) - \mu_1}{\mu_2 - \tan(\theta)} \right]. \tag{10.46}$$

The granular media is glass beads, with properties given in table 10.4. The angles θ is chosen such that I is well posed, and the viscosity model applied in this case therefore calculate $\mu(I)$ by equation (10.29). The cases are set up as 1D-cases with cyclic boundary conditions on the in- and outflow and the rest of the boundary condition on the top and bottom is as described in figure 10.4a). Four different cases for three different angles θ were studied. In case 4a, the viscosity model is applied with pimpleFoam to verify the model. Case 4b is a reproduction of case 4a in interFOAM, where both phases have identical properties, and should in principle yield the single-phase solution.

Table 10.4: Data used for case 4 and 5 based on experiments by Jop et al. [146].

Property	Symbol	Value
Particle diameter	d	0.5 mm
Bulk density	ρ_s	1500 kg m^{-3}
Rheology properties	μ_1	0.381
	μ_2	0.643
	I_0	0.279

Case 4c and 4d are also two-phase problems, where the effect of overlaying fluids is investigated. In case 4c, the velocity of the granular material should match the analytical solution since the fluid is light, while the denser one in 4d, is expected to affect the
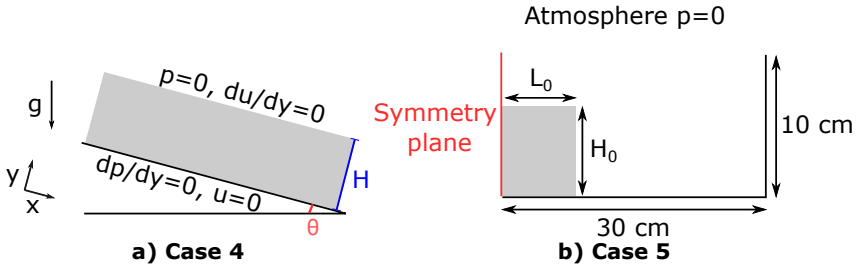
Figure 10.4: a) Sketch of a flow down an inclined plane, where H is the height of the column and θ is the incline. Boundary conditions for pressure and velocity are also described in the figure. b) Setup for the granular column collapse, where the left side is a symmetry plane. Right and lower boundary are described as a wall, and the top is an atmosphere.

velocity profile for the grains close to the interface [144].

A collapse of a granular column into a heap was reproduced from the work of Lagrée [144] in case 5. The system was set up as shown in figure 10.4b). Three cases were run as described in table 10.5, where the aspect ratio between height and length, a_0, is defined as

$$a_0 = \frac{L_0}{H_0}, \tag{10.47}$$

where H_0 and L_0 are the height and half of the length of the column. The two-phase solver interFoam was used, and the viscosity of the mixture was in this case calculated as a harmonic average:

$$\nu = \frac{1}{\alpha_1/\nu_1 + (1 - \alpha_1)/\nu_2}. \tag{10.48}$$

The density of the surrounding fluid was 1.5 kg m^{-3} and viscosity were constant for each case and stated in table 10.5.

Table 10.5: Overview of the three cases ran for the column collapse

Property	Symbol	Case 5a	Case 5b	Case 5c
Height-length ratio	a [-]	0.5	1.42	6.26
Initial length	L_0 [m]	0.0412	0.03261	0.0155
Initial height	H_0 [m]	0.0206	0.0463	0.0972
Fluid viscosity	ν_f [m^2 s^{-1}]	0.00120	0.00126	0.00060
Gravity	g [m s^{-2}]	2.06	4.63	9.72

Sensitivity cases

A parametric study was conducted in order to quantify the sensitivity of different parameters, and to get an overview on what values that might be suitable for alumina. To the authors' knowledge, no experiments for measuring μ(I)-parameters for alumina have been conducted. However, approximately values for bulk density ρ_a [14], particle diameter d, and angle of repose $\tan^{-1}\mu_1$ [19] are known.

The setup is an alumina-air system, shown in figure 10.5. In case 7, the geometry is different as the dose is dropped from a higher distance. However, the mesh has the same resolution as case 6.
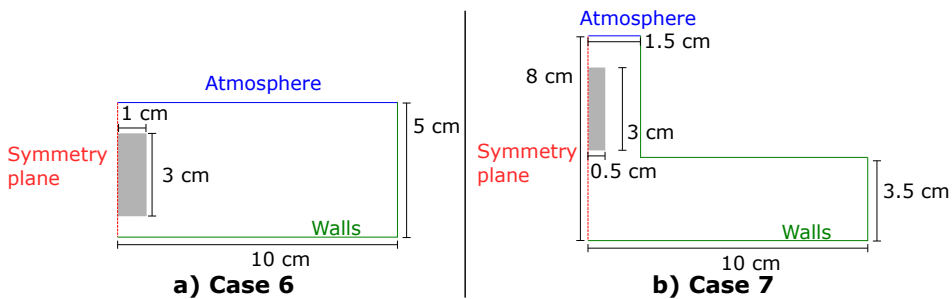
Figure 10.5: Setup for the parametric sensitivity cases, with dimensions and boundary conditions.

The studies were set as a 2^k study, where the cases had four factors each. The high and low values are given in table 10.6, while the rest of the parameters are given in table 10.7. The results from case 6 provided the basis for which parameters that were pursued in case 7, where the fall height and the regularized model also will be introduced.

Table 10.6: Overview of the three cases ran for the column collapse

Property	Low	High	Used in case
$\tan^{-1}\mu_2$	40°	60°	6 and 7
I_0	0.1	1	6 and 7
d	20 μm	100 μm	6
ρ	800 kg m^3	1 200 kg m^3	6
Fall height	2 cm	5 cm	7
Model	Original	Regularized	7

Statistical analyses were conducted in Minitab, where the responses was set to be the final height of the column and, an angle defined by the ratio height and length at y = 0.375 mm, sketched in figure 10.6.
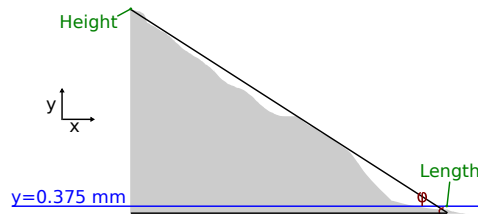
Figure 10.6: Sketch illustrating how the length, height and angle ϕ are defined in case 6 and 7.

Three-phase case

A case was simulating parts of the initial stage of alumina feeding, when the dose enters the molten bath, sketched in figure 10.7. One case was run with the µ(I)-rheology, while in the two reference cases, the granular media was assumed to be a Newtonian fluid with kinematic viscosity of 10^{-6} m^2 s^{-1} and 10^{-3} m^2 s^{-1}, respectively. The first case is to establish the differences between the developed model and liquid, while the other case with high viscosity is another possible approach to model the solid-state behavior occurring. The properties are otherwise given in table 10.7.
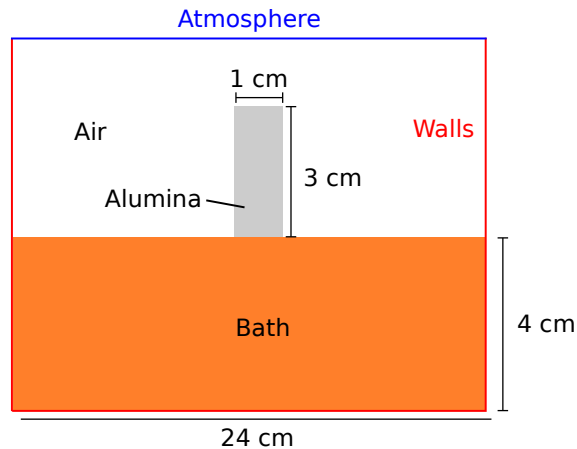
Figure 10.7: Setup of the initial conditions and boundary conditions for case 8, 9 and 10.

Coupled case

The former case was further extended to also account for the bath freeze model presented in case 2 and 3. The initial setup is therefore as shown in figure 10.7, but the energy equation and freezing model is included. The additional properties are given in table 10.7.

10.10 Benchmark cases

The presented cases have been utilized on different computers with various number of cores. Therefore, some benchmark cases in order to compare running time was conducted. The setup is the same as described in figure 10.7, where the base case is at isothermal conditions and the alumina dose is a Newtonian fluid with $v = 10^{-3} \text{m}^2\text{s}^{-1}$. The effect of adding a temperature field, applying the $\mu(I)$-rheology and allowing for solidification were investigated.

Table 10.7: Summary of the properties used. All properties are used in the benchmark case, case 10

Base case properties	Symbol	Value	Unit	Also used in case
Alumina density	ρ_a	1200	kg m^{-3}	3, 7, 8, 9,
Bath density	ρ_b	2000	kg m^{-3}	2, 3, 8
Gas density	ρ_g	1	kg m^{-3}	3, 7, 8, 9
Alumina viscosity	ν_a	10^{-3}	m^2s^{-1}	10^{-6} in 3
Bath viscosity	ν_b	10^{-6}	m^2s^{-1}	2, 3, 8
Gas viscosity	ν_g	$1.48{\cdot}10^{-5}$	m^2s^{-1}	3, 7, 8, 9
Gravity	g	9.81	m s^{-2}	2, 3, 4, 7, 8, 9
Themal properites				
Alumina heat capacity	$c_{p,a}$	1200	$\text{J kg}^{-1}\,{}^\circ\text{C}^{-1}$	3, 9
Bath heat capacity	$c_{p,b}$	2200	$\text{J kg}^{-1}\,{}^\circ\text{C}^{-1}$	2, 3, 9
Gas heat capacity	$c_{p,g}$	700	$\text{J kg}^{-1}\,{}^\circ\text{C}^{-1}$	3, 9
Alumina Thermal Conductivity	κ_a	8	$\text{W}\,{}^\circ\text{C}^{-1}\text{m}^{-1}$	3, 9
Bath Thermal Conductivity	κ_b	0.8	$\text{W}\,{}^\circ\text{C}^{-1}\text{m}^{-1}$	2, 3, 9
Gas Thermal Conductivity	κ_g	0.02	$\text{W}\,{}^\circ\text{C}^{-1}\text{m}^{-1}$	2, 3, 9
Initial temperature	T_i	960	$^\circ\text{C}$	3, 9
Initial temperature alumina	T_a	100	$^\circ\text{C}$	3, 9
Freezing and melting properties				
Latent Heat of Fusion	L	530 000	J kg^{-1}	2, 3, 9
Temperature constant	T_L	959	$^\circ\text{C}$	2, 3, 9
Melting point	T_M	950	$^\circ\text{C}$	2, 3, 9
Damping strength	C_v	10	m^2s^{-1}	9
Constant	$\tilde{A}$	1	-	2, 3, 9
μ(I)-properties				
Particle diameter	d	100	μm	7, 8, 9
Angle of repose	$\tan^{-1}\mu_1$	30	°	7, 8, 9
	$\tan^{-1}\mu_2$	60	°	8, 9
	I_0	1	-	8, 9
	μ_∞	0.05	-	7, 8, 9
	a	2.1	-	7, 8, 9

Part IV

Results and discussion

Chapter 11: Industrial Results

The current chapter contains a summary of the findings in paper II [147].

Figure 11.1 displays the measured HF-concentration as a function of time, where the red dots denote that a feeding occurs. A peak in HF-gas was observed about 30 seconds after feeding. In periods where the measurement frequency was high, the delay was calculated to be 31.73 ± 0.24 s.
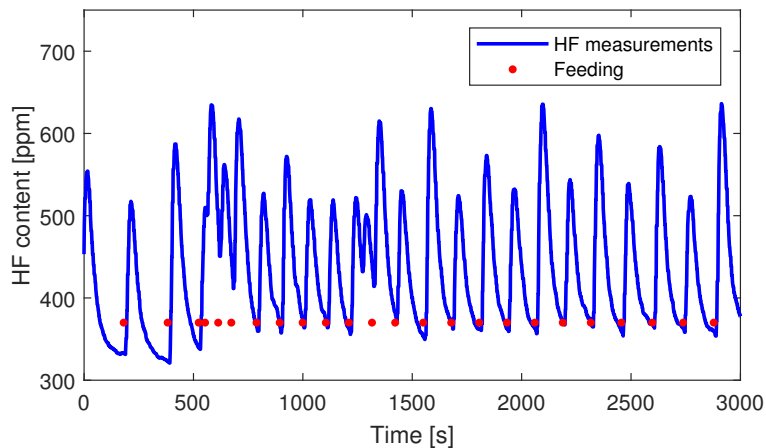
Figure 11.1: Typical concentration measurements of HF, where the red dots denotes the time when a feeding occurs.

Figure 11.2 displays two typical feeding cycles, together with the time averaged concentration for each feeding as defined in equation (8.1). A negative correlation is seen as the cycle goes towards underfeeding.
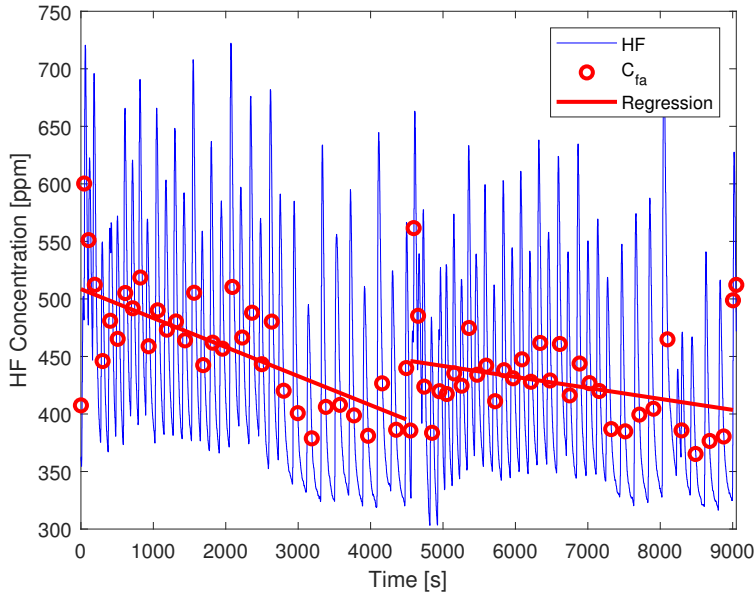
Figure 11.2: Two feeding cycles where $\bar{C}_{fa}$ represents the time averaged concentration for each feeding (defined in equation (8.1)), and its estimated regression lines are shown. Figure republished from paper II [147]. Copyright 2021 The Minerals, Metals & Materials Society. Used with permission

In figure 11.3, the effect average concentration of $\bar{C}_{fa}$ before and after anode change is shown. On average, the concentration after anode change is significant smaller than before.
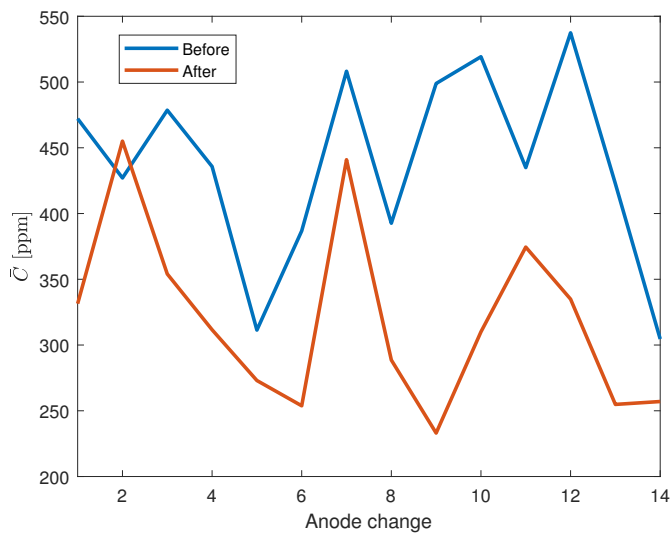
Figure 11.3: Calculated time averaged HF-concentration for 10 feedings right before/after anode change, where 14 different anode changes are considered. Figure republished from paper II [147]. Copyright 2021 The Minerals, Metals & Materials Society. Used with permission.

The temperature vs average HF-concentration is plotted in figure 11.4, where a positive correlation is shown.
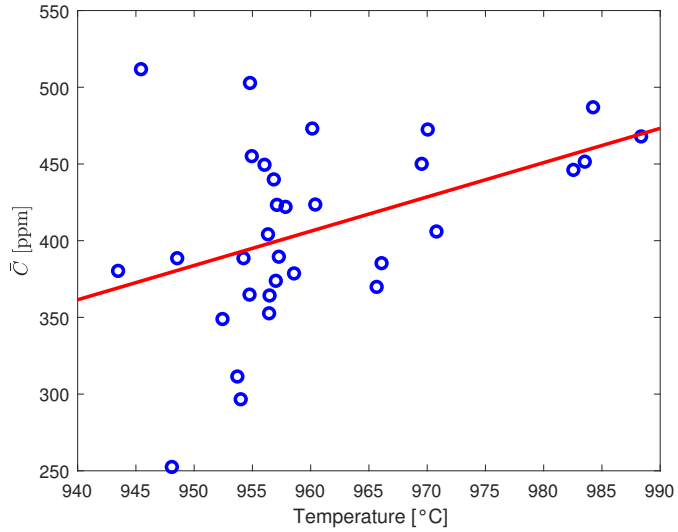
Figure 11.4: Temperatures and $\bar{C}$, where $\bar{C}$ is calculated as the mean of $\bar{C}_{fa}$ five feedings before and five feedings after the temperature was measured. Figure republished from paper II [147]. Copyright 2021 The Minerals, Metals & Materials Society. Used with permission.

A significant positive correlation is also found between $\bar{C}_{ca}$ and relative humidity, where figure 11.5 displays these values over three consecutive days.
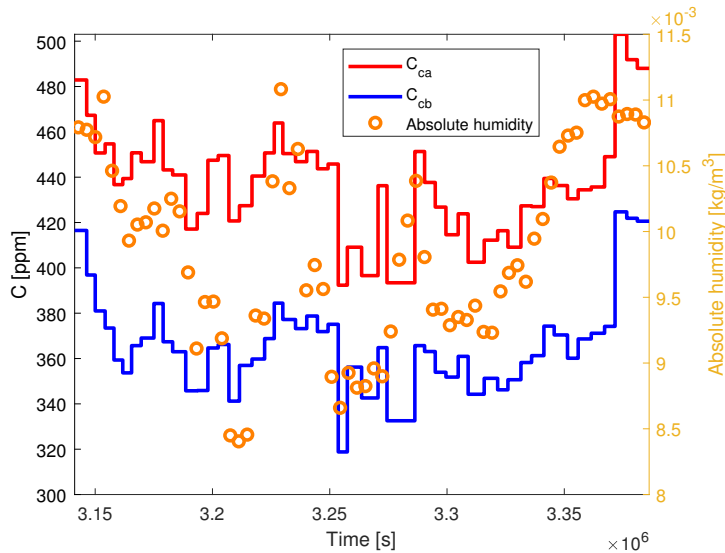
Figure 11.5: The calculated values of time averaged concentrations for each feeding interval, C_{ca} and baseline, C_{ba}, together with relative humidity plotted over 3 consecutive days. Figure republished from paper II [147]. Copyright 2021 The Minerals, Metals & Materials Society. Used with permission.

The results show a positive correlation between HF-content and the feeding frequency, where the HF concentration was higher when the cell was overfeeding, and each feeding event (red dots in figure 11.1) is typically followed by a peak in HF, which then drops off more slowly. Corresponding delays between feeding events and peak values have been observed in earlier measurements within the same cell technology [54]. Several factors are believed to contribute to this delay, relating to HF gas formation and subsequent transport from the bath and into the duct where concentrations are measured. Under normal conditions, this transport will take place through the feeding hole. If the feeding hole is closed, the time for the HF to arrive in the duct will increase, which can explain some of the variation seen in the measurements. As seen in Figure 11.1, the increase in HF content is rapid, and it declines more slowly. While this behavior is the expected response from a ideal reactor experiencing a pulse, e.g. feeding, the decline may also be related to delayed gas release arising when a formed raft disintegrates, as gas gets trapped inside its pores. Structural hydroxides are found to be released during dissolution [52], and might be a potential origin for the late arrival og HF.

Besides feeding cycle, anode change and bath temperature also seemed to affect the HF-generation seen in figures 11.3 and 11.4. However, after anode change, the feeding frequency is decreased, which will also reduce the formation of HF. A higher generation for HF was expected with increased temperature [51]. Higher levels of humidity also resulted in increased HF-concentration, due to more water that can react with fluorides, also expected [19]. Since the HF-content was only measured a few months during the summer, the variation in humidity might not be large enough to observe the full effect.

Chapter 12: Laboratory Results

12.1 Water model

This work is from paper III [124], where three replicates of each of the eight configuration were conducted, resulting in a total of 24 experiments. Images from selected experiments can be seen in figure 12.1, and table 12.1 shows average floating time, initial area, and rates. Analyzing the factorial design show that all the three parameters had a significant effect on the total floating time, with particle size as the largest one, followed by bubble frequency and temperature of the water.
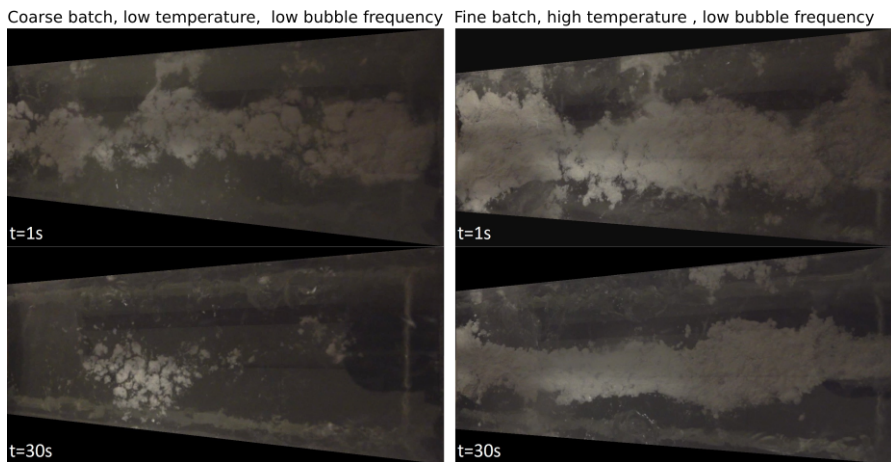
Figure 12.1: Images from two of the experiments from the water model, description given in the figure. Figure republished from Gylver *et al.* [124], and is used with permission of The Minerals, Metals & Materials Society.

Table 12.1: Results from the water model experiments. The rates are calculated as cm^2/s and normalized to the initial surface area. The configuration of the experiments are given in table 9.1.

Experiment number	Floating time [s]	Initial area [cm^2]	Total rate[%/s]	Initial rate[%/s]	Final rate [%/s]
1-3	530	1846	-0.13	-0.16	-0.11
4-6	303	1963	-0.24	-0.25	-0.23
7-9	192	1482	-0.27	-0.29	-0.24
10-12	258	1346	-0.18	-0.20	-0.15
13-15	65	1251	-1.21	-1.65	-0.81
16-18	123	1051	-0.62	-0.94	-0.31
19-21	50	657	-1.70	-3.27	-0.20

The current model was able to visualize the raft formation in an electrolysis cell. Comparison with recordings in an industrial cell showed closest similarity with the experiments carried out with the coarse batch and high bubble frequency. The review did not identify any other work modeling raft formation at this size scale, although several experiments on a smaller scale have been conducted [85], [98], [100].

The particle size had the largest impact on the floating time, with almost a five-fold increase in dissolution time when D_{50} was decreased with 50 %. For the coarser batch, a higher fraction of powder dissolved and dispersed within the first seconds after addition compared with the fine fraction, as seen in figure 12.1. Convection was also found to be significant, but is in this work only limited to the relative effect due to bubbles. Increased bubble frequency, and hence increased convection, led to shorter floating time and smaller initial size of the raft, due to better dispersion. It is also found to reduce the raft floating time in industrial cells [48] and decrease dissolution time in laboratory experiments [39]. The liquid temperature was also found to be significant, but the calculation from the paper revealed that the "high" water temperature in this work will correspond to a superheat of 24.6 °C, which is far higher than used in industrial operations.

12.2 Lab induced rafts

This section summarize up the results from the open-furnace experiments, described in paper I, II, IV and V.

Mass of rafts and reproducibility

The mass gain of the extracted samples in paper I [125] are shown in figure 12.2, and the mass of rafts were also measured in paper V [148], and the results are shown in figure 12.3, given as average mass with a 95 % confidence interval.
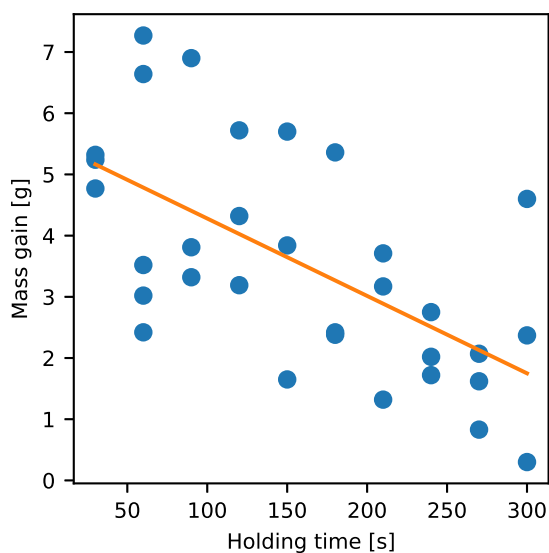
Figure 12.2: Mass gain of the collected rafts as a function of time in paper I [125], with linear regression line included.
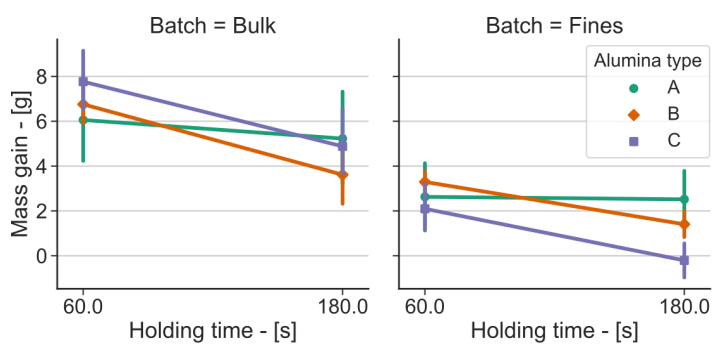
Figure 12.3: Average mass gain of the alumina type A, B and C in paper V, for bulk and fines at the extraction times 60 and 180 s. The error bars state a 95 % confidence interval.

The mass loss rates, calculated by linear regression, of the different types are shown in table 12.2, including its 95 % confidence interval.

Table 12.2: Mass loss rates and 95 % Confidence interval for the different alumina types.

Batch	Type	Mass loss Rate [g/min]	95 % Confidence Interval	Samples Collected
Paper I		-0.76 ± 0.36	[-1.12,-0.40]	32
Bulk	A	-0.42 ± 1.62	[-2.04, 1.21]	15
	B	-1.57 ± 1.07	[-2.64, -0.50]	10
	C	-1.44± 1.16	[-2.61, -0.28]	14
Fines	A	-0.06 ± 1.26	[-1.32, 1.21]	10
	B	-0.94 ± 0.47	[-1.41, -0.48]	10
	C	-0.89 ± 1.15	[-2.04, -0.27]	11

In the same paper, the dependence between trial number and the sample's deviation from its mean value were investigated, and is shown in figure 12.4

Since the lab conditions are within the validity range of the model by Alarie et al. [93], predicted dissolution rate can be calculated and compared with the observed one. Assuming $\dot{m}_{ref} = 2.4689$, the predicted dissolution rate will be 0.72 g min^{-1} for the conditions in Paper I, and 0.63 g min^{-1} for all the types in paper V, as the empirical equation only uses bath properties as variables. Five out of seven rates are found to be above predicted values (table 12.2), which should be expected, as the rate calculated in these sets of experiments are not the actual dissolution rate of alumina, but rather the mass loss rate of rafts, which will include melting of bath. As the mass of the collected rafts were found to more than double in size, one cannot directly translate these results to dissolution rate. In practice, the dissolution rate will probably be higher in the first minute, supported by the findings from video recordings (figures 12.18 and 12.16), where a higher amounts of powder seems to disappear during the first 25 seconds.
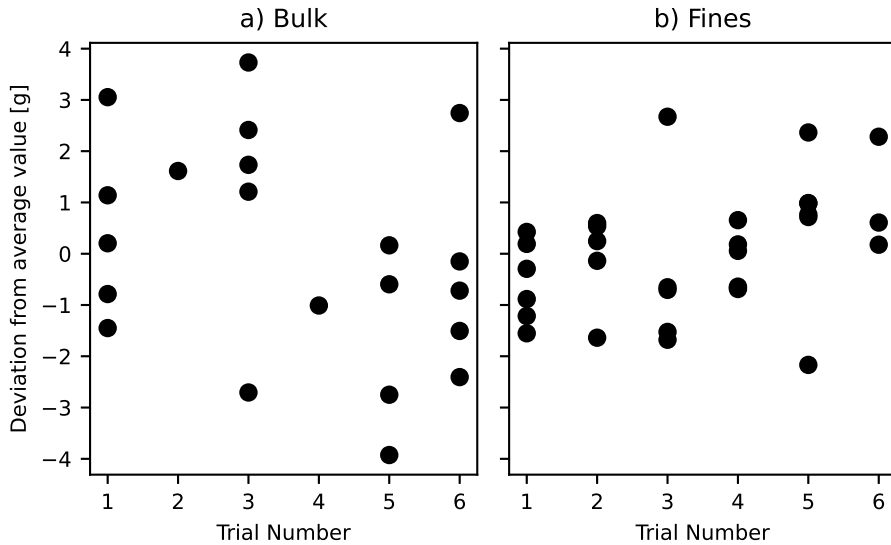
Figure 12.4: Trial number vs deviation from average value for the samples in paper V, divided between bulk (a)) and fines(b).

The confidence intervals reveal that there are still a considerable amounts of uncertainty in the data. On average, rafts collected from paper V by this method showed a variation of ±24% around the mean value. Stable thermal conditions are probably the biggest challenge. A higher temperature and hence superheat will reduce the mass of bath freezing around the powder, and hence mitigate the formation of rafts. Kuschel and Welch [39] emphasize that the superheat is in particular important when there is limited convection in the bath, which is the case in these experiments. Maintaining a stable superheat is challenging, since the furnace must be opened from the top to insert and remove raft samplers. Minor changes in superheat can affect the mass of the created rafts, hence explaining some of the variation seen in these experiments. In addition, the superheat might increase during the experiments, since the Al_2O_3-concentration will increase. For the bath in paper V, six additions where all alumina dissolves will lead to an increase of approximately 1.6 wt% Al_2O_3 and 9 °C increase of superheat [126], as the temperature is maintained constant. However, this is a worst-case scenario, as most of the alumina is expected to be removed out together with the raft. The investigations of deviation versus trial number, figure 12.4, did not observe that the mass of the rafts decreased with increasing trial number, which would have been the case, since lesser bath freeze at higher superheat. For fines, cf. figure 12.4b), the opposite trend is observed, with a slight increase in mass for the final trials. The data

is however scarce, only three points for trial 6, and a lack of exact temperature control might be the cause.

The current sampling technique is conducted with samplers of stainless steel, which are immersed into the melt before every sampling. This results in a decrease in temperature, and the duration for obtaining stable conditions varied between 30 min and up to more than an hour, and in some cases even longer. In addition, there will be pieces left on the raft sampler, as shown in figure 12.5. This might be the cause for lack of precision in some of the experiments, in particular seen after 60 and 90 seconds in figure 12.2.
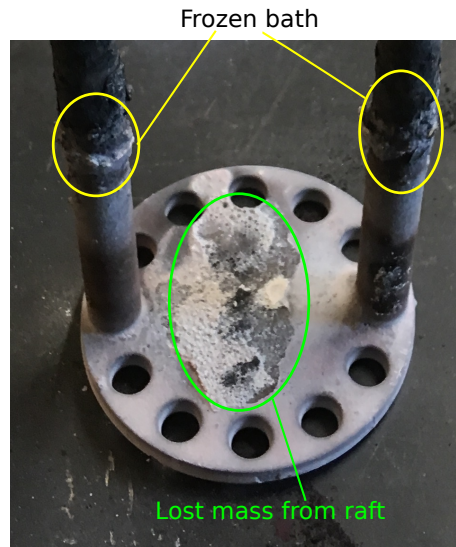
Figure 12.5: Image of a raft sampler after removal of a raft, where frozen bath left on the handles, and remains of rafts are highlighted.

A new design on a raft sampler could therefore be considered. An alternative might be to use platinum as applied in the see-through cell by Yang *et al.* [62]. Isaeva *et al.* [84] had a different design by creating a net of metal threads, which might also be suitable alternative for a plate.

Preheating

The mass gain for the preheated samples for the two different extraction time are shown in figure 12.6.

The experiments presented in figure 12.6 [125] show that preheating the alumina up to 500-600 °C will mitigate rafts from being formed, hence favoring the dispersion of the grains. Other researches [45], [77] have also found that rafts stop forming at this temperature interval. Preheating below this interval can be favorable, as the energy requirement to heating up alumina to the melting point is in the same magnitude as the energy required for the dissolution itself [149]. However, if a raft is formed from preheated alumina, removal of moisture and hydroxides from the powder may make it harder for the rafts to break apart [75].
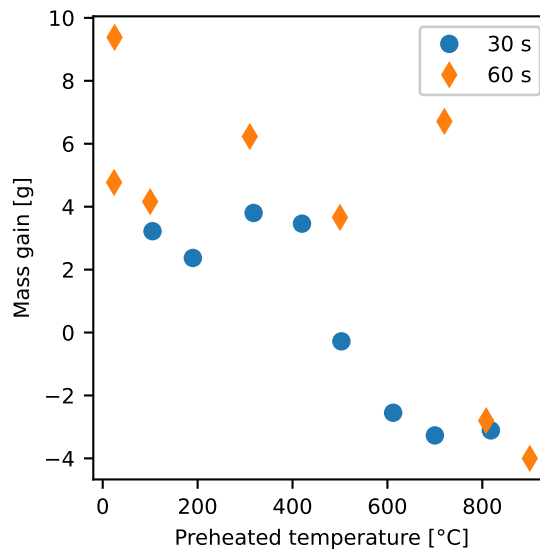
Figure 12.6: The mass gain of rafts for different preheated temperatures [125], where the extraction time were 30 (blue circles) and 60 (red diamonds) seconds.

LiF-content

For the experiments with varying LiF-content, rafts were extracted after 60 and 180 s, and their mass gain is shown in figure 12.7. The mass loss rate in these cases was calculated to be between 1.2 and 1.8 $g\,min^{-1}$.

These experiments were conducted in order to study the effect if LiF-content in bath would have an impact for the see-through cell experiments [81], where LiF is needed in order to acquire an acceptable operating temperature. The presented data suggests that after three minutes, rafts are somewhat bigger in the bath containing 5 wt% LiF, indicating somewhat slower dissolution. Poorer dissolution in LiF-modified baths is seen at 10 °C superheat [70], but not at 20 °C [77]. When relating this to the experiments in the see-through cell [82], where the superheat was 29 °C, the effect of LiF would probably be negligible.
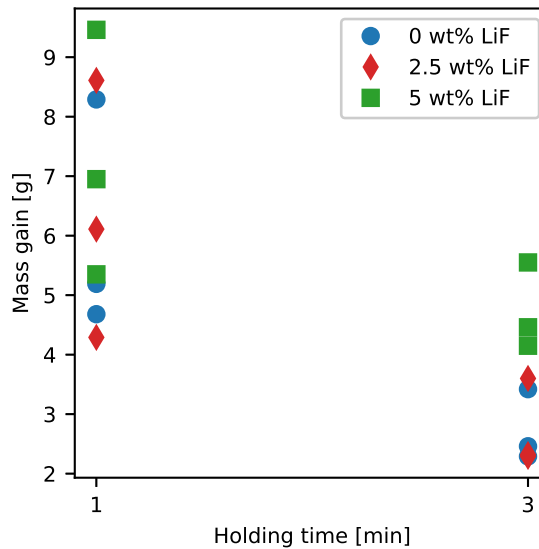
Figure 12.7: Mass gain of the collected rafts for three different compositions of LiF in the bath, from paper IV.

Raft appearance

Typical images of rafts are shown in figure 12.8. As could be seen, rafts created from secondary alumina consisted of thin long flakes, with a distinct bulge or a crater in the center of it. Rafts created from primary alumina were flatter, and without the bulge, but a crater in the center was also seen for these samples. The rafts created from fines had the shape of a compact pellets and were in general found to be smaller in size than the one collected from regular bulk alumina.

a) Secondary Alumina   b) Primary Alumina   c) Fines
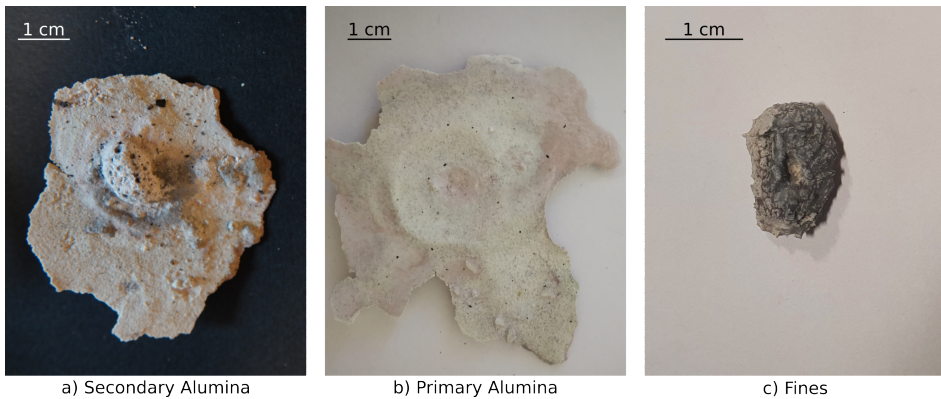
Figure 12.8: Typical appearance of rafts. a) Secondary alumina raft, collected in the experiments described in paper I. b) Primary alumina raft, collected in the experiments described in paper II. c) Raft from fines, collected in the experiments described in paper V.

CT images of the cross section of rafts are shown in figure 12.9 for samples of primary and secondary alumina, while a corresponding image for a raft created from fines is shown in figure 12.10. The grayscale is proportional to the X-ray linear attenuation at the given volume point. The linear attenuation coefficient depends on both the density and the atomic weight of the material; where the atomic weight has a higher influence than the density.
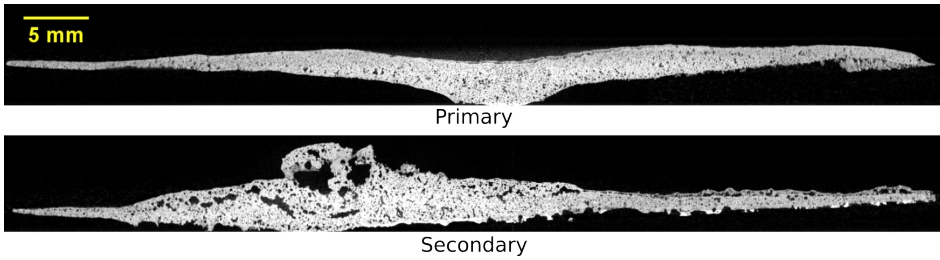
Figure 12.9: Cross sectional CT images of two rafts created from primary (upper) and secondary alumina (lower). The top of the raft is facing upwards. Figure republished from paper II [147]. Used with permission of The Minerals, Metals & Materials Society.
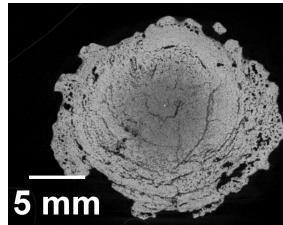
Figure 12.10: Cross sectional CT image of raft created from fines, where the top of the raft is facing upwards.

Cold experiments were also conducted, where the same mass of alumina was released from the same height onto a flat plane. Images from bulk and fines are shown in figure 12.11.

Bulk, type A	Bulk type A	Fines, type B
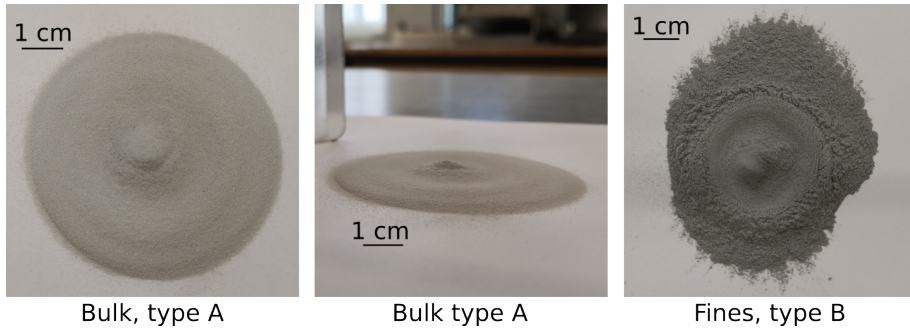
Figure 12.11: Results of cold experiments for bulk alumina, where 4 g alumina is released on to a flat pipe with a height of 5 cm.

In paper V, CT images provided the opportunity to generate 3D plots of the rafts, using the "Interactive 3D Surface Plot" plugin in ImageJ. The 3D plots are generated from projection images, representing the average attenuation values in the Z-direction, shown in figure 12.12d). By processing the images further, values corresponding to density and thickness of the rafts can be obtained, showed respectively for b) and c) in figure 12.12 and 12.13.
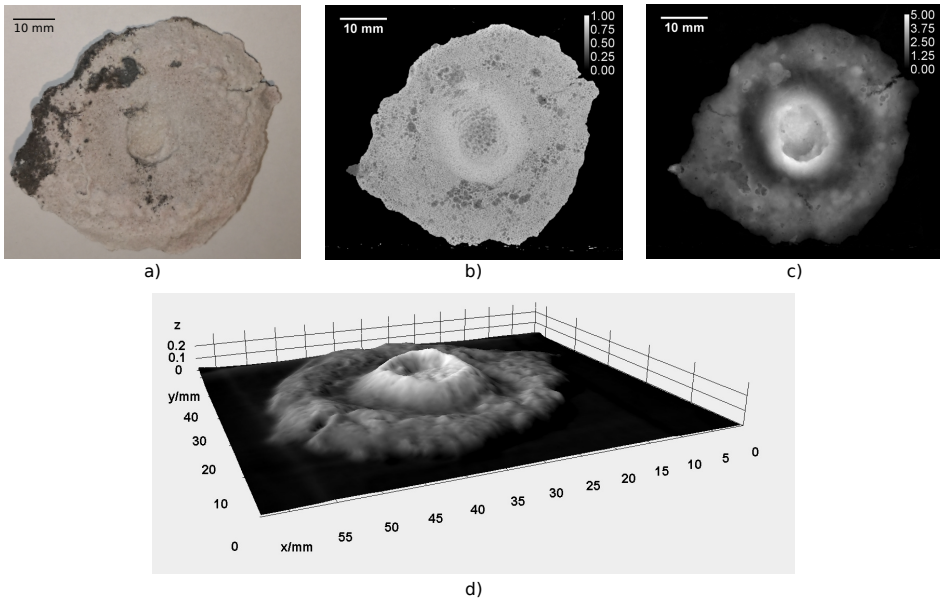
Figure 12.12: Images of a raft from alumina bulk type B. a) Image of raft from above. b) Projected CT image of the raft seen from above, displaying the average density. c) Projected CT image of the raft seen from above, displaying the thickness of the raft. The scale is given in mm. d) 3D-image plot seen from the side.
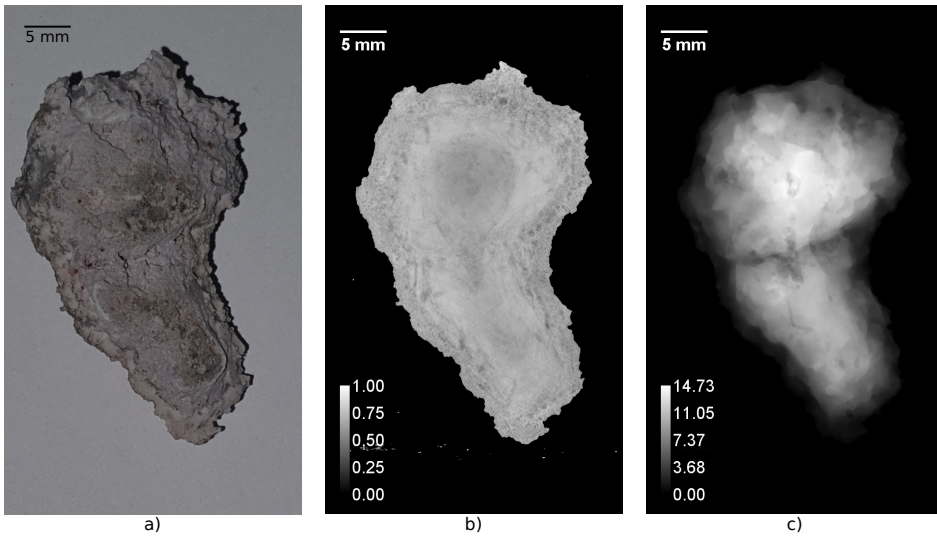
Figure 12.13: Images of a raft from alumina fines type A. a) Image of raft from above. b) Projected CT image of the raft seen from above, displaying the average density. c) Projected CT image of the raft seen from above, displaying the thickness of the raft. The scale is given in mm.

By comparing with cold experiments conducted on a flat plate figure 12.11, it is quite clear the structure of the raft is strongly influenced by the addition method. After the powder hits the surface, bath freeze around the cold particles that have not dissolved and strengthen the structure, which can be maintained for several minutes.

Porosity measurements

Porosity measurements were conducted in paper I, II and V, and is reported as the percentage of pores relative to the entire relative cross-sectional area for the samples measured. The values are summarized in table 12.3

Table 12.3: The average porosity values in the different campaigns.

Paper	Sample type	Samples analyzed	Average porosity
I	Secondary alumina	4	$7.1 \pm 1.9\,\%$
II	Primary alumina	9	$0.8 \pm 0.4\,\%$
II	Secondary alumina	9	$5.2 \pm 1.4\,\%$
V	Bulk alumina	9	$7.9 \pm 1.9\,\%$
V	Fines	9	$4.2 \pm 0.9\,\%$

For the MOI-LOI and primary vs secondary alumina experiments conducted in paper II [147], all samples were extracted after a holding time of 60 seconds. Figure 12.14 shows the porosity of the samples, respectively as a function of MOI (RT-160 °C) and LOI (350 - 1000 °C).
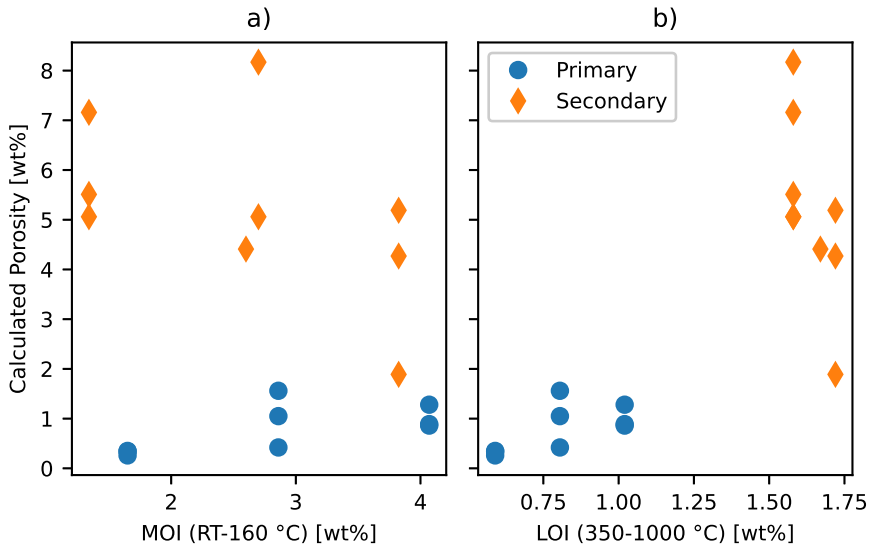
Figure 12.14: The calculated porosity for rafts created from primary (blue circles) and secondary (red diamonds) alumina, with different water contents-represented as LOI RT-1000 °C (a) and LOI 350–1000 °C (b).

The laboratory scale experiments in paper II were conducted in order to study if HF affects raft porosity, as discussed in chapter 11. By exposing alumina to humidity, more HF should be formed when the powder is added to the bath. However, as viewed in figure 12.14a), no significant trends can be found between the adsorbed water content and porosity, neither for primary nor secondary alumina. Although the data points are scarce, it supports the earlier hypothesis that adsorbed water will evaporate quite immediately after addition [26] and probably so fast that it escapes before the raft is created.

Kaszás [85] reported that evaporated moisture created enclosed bubbles, and hence higher porosity. The method is however different than in this work. Here, the alumina is hydrated, while Kászas heat-treated the alumina before addition, hence reducing the moisture content further and also removing structural hydroxides for the highest treatment temperature. It is also challenging to compare, as there is no reported porosity

values of the rafts itself.

Rafts extracted from secondary alumina are found to be more porous, also related to LOI (350-1000 °C), shown in figure 12.14b). The increased porosity is therefore a result of the dry scrubbing process, where fluorides and sulfur are adsorbed, and carbon dust and other particulates are mixed into the powder. That secondary alumina result in a more porous structure for rafts and crusts is already well established [43], [86], but this work cannot conclude which components are affecting it. A seen in figure 12.8, there is a difference in rafts created from primary and secondary alumina, where the latter is more porous and with a distinct bulge on the top, probably a result of gas formation.

Since CT-measurements have been conducted on industrial scale in earlier work [49], the values reported in this work (table 12.3) should be comparable. A coherent raft had a total porosity of 12.7 %, which is larger than the reported value from secondary bulk alumina in this work. In an industrial cell, anodic bubbles are present, that might get trapped inside the rafts. In addition, the doses in industrial cells are much larger than the one used in this work. With a larger dose, evaporating moisture or released HF might have more difficulties to escape, and hence contribute to increased porosity. If the formation is due to an electrochemical reaction [52] more HF would be formed in an industrial cell, as this setup was without any electrolysis.

Recordings of alumina addition

One video recording of each of the alumina types from the bulk and fines batch was performed during the experimental session. Figure 12.15 shows the feeding of alumina A, where sinking of small sub rafts denoted as a, b and c, are marked. Selected images of the feeding of alumina C is shown in figure 12.16 and the initial raft formation from fines are shown in figure 12.17.
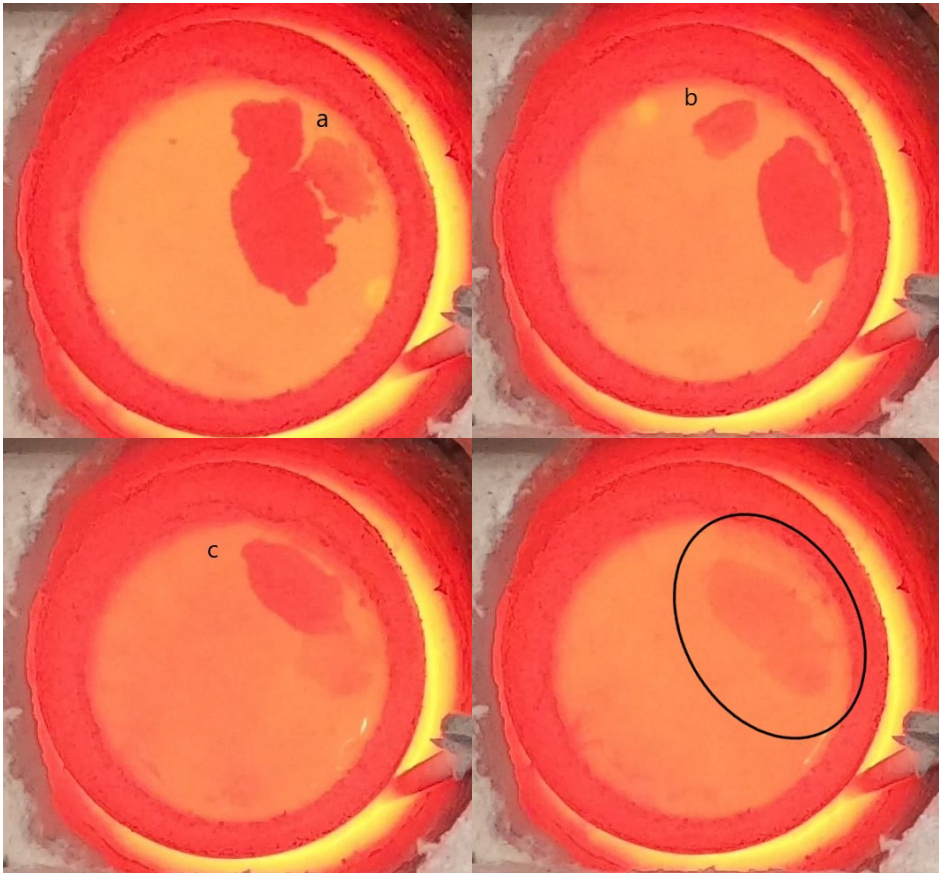
Figure 12.15: Images of descending subrafts a, b and c of bulk alumina type A, denoted in figure 12.18. In the last frame, it is possible to see the descended rafts on the bottom of the crucible.
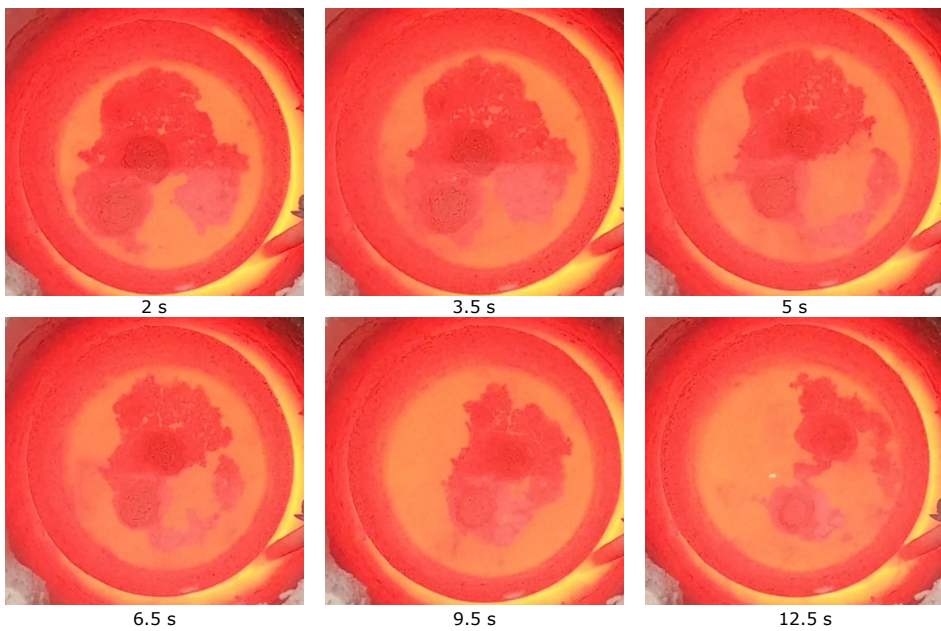
Figure 12.16: Selected images from the recording of alumina bulk type C showing the initial dissolution stage.
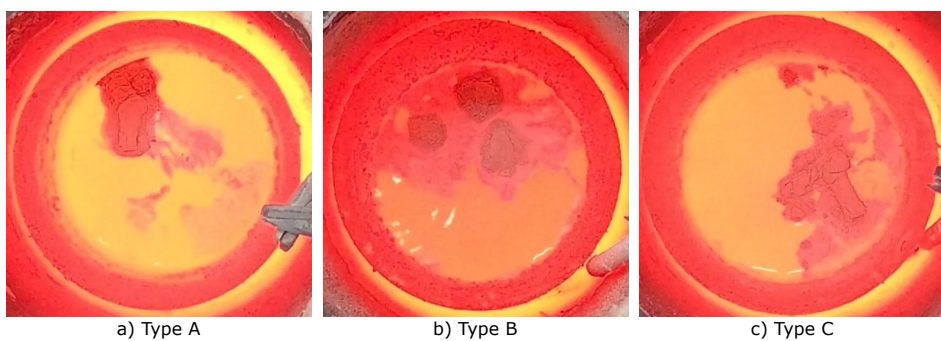
Figure 12.17: Selected images from the video recording of fines, selected from right after feeding to display the dispersion.

The videos were later treated in ImageJ [150] to measure raft area as a function of time.
As the quality of the recordings was not adequate for a fully automated image analysis,
raft area was measured by using a brushing tool in ImageJ on the images with sufficient
quality. The measurements performed in ImageJ are displayed in figure 12.18, where
the time axis is logarithmic to visualize initial dispersion better.
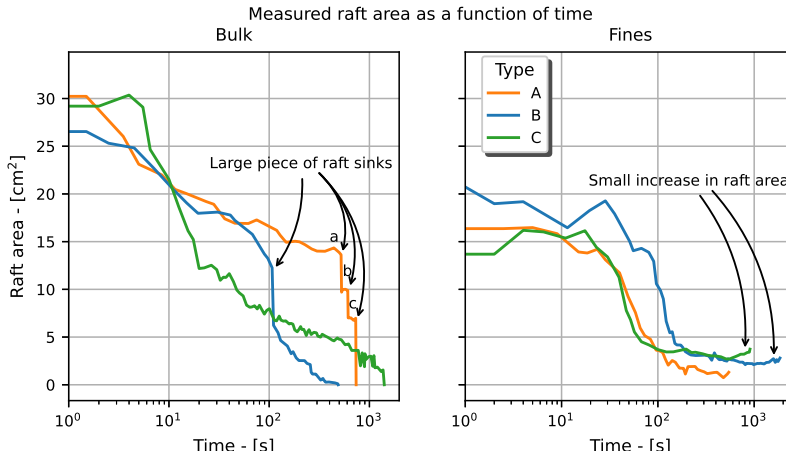
Figure 12.18: Measured raft area as a function of time, where a, b and c denotes sinking
of rafts pieces, which can be seen more detailed in figure 12.15.

Initial dissolution rate is given in table 12.4, calculated as the rate the surface is disin-
tegrated in $cm^2\ s^{-1}$ at steepest part of the curve in Figure 12.18, normalized with the
initial surface area.

Table 12.4: Initial rate of surface dissolving in $cm^2\ s^{-1}$ at steepest part, set relative to the
measured area of raft a t=0 s.

Type	Batch	Initial dissolution rate [%/s]
A	Bulk	-0.38
	Fines	-0.08
B	Bulk	-0.54
	Fines	-0.13
C	Bulk	-0.57
	Fines	-0.09

The video recordings give detailed observations of the alumina feeding and formation
of a raft. For feeding of bulk alumina, figure 12.15 and 12.16, it is seen that a structure
forms over most of the available surface, and the surface area decreases faster at the

beginning and pieces fall into the bottom of the bath. This behavior has been seen in see-through cells [82], [90] and is also quite similar to the behavior observed by Kaszás *et al.* [59].

During recordings, stable temperature is also a challenge. Measurement done after finishing the recording suggest that the melt is close to its liquidus. The low temperature will then increase the formation of frozen bath and delay the melting time. This is also a problem encountered by Kaszás [65], who has conducted similar type of experiments. Covering the top with a transparent quartz plate is possible, although fumes will reduce the view of the bath surface.

Alumina qualities and fines

Figure 12.19 states the correlation coefficients between the mass gain at 60 seconds holding time and selected parameters for the samples extracted in paper V, both for bulk and fines.

Mass gain [g]

-0.74	<45µm										
0.74	-1	D_{50}									
-0.68	0.97	-0.96	LOI(1000 °C)								
0.12	-0.04	0.09	0.13	MOI (300 °C)							
0.61	-0.9	0.89	-0.97	-0.34	BET						
-0.61	0.88	-0.87	0.96	0.23	-0.98	α-Al_2O_3					
0.6	-0.89	0.88	-0.97	-0.26	0.98	-0.99	γ-Al_2O_3				
-0.67	0.97	-0.96	0.99	0.16	-0.97	0.93	-0.94	F			
-0.31	0.14	-0.16	0.1	-0.38	-0.03	0.15	-0.05	0.01	S		
-0.71	0.96	-0.95	0.96	0.14	-0.92	0.87	-0.87	0.97	0.15	Na	
-0.66	0.9	-0.9	0.92	0.26	-0.91	0.84	-0.84	0.95	0.12	0.99	Ca
-0.73	0.98	-0.98	0.96	-0.05	-0.91	0.92	-0.93	0.95	0.2	0.92	0.85	C
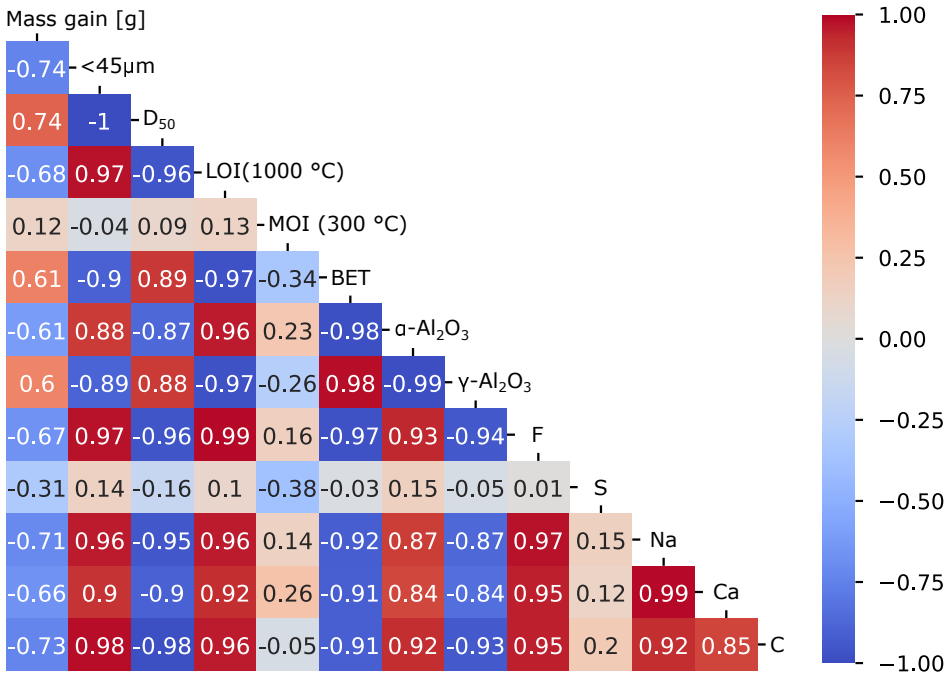
Figure 12.19: Correlation coefficients between selected parameters and the mass gains of samples after holding time 60 s in paper V. <45µm is fraction of grains below 45 µm, while D_{50} refers to the statistical values to define the width of the particle size of the distribution curve.

The rafts created from fines are smaller in mass and are shaped as pellets, shown in figure 12.8, and have lesser amount of frozen bath around them. The CT-image in figure 12.10, shows a grayer area in its interior, thus indicating that the powder spreads out poorer and in lesser degree gets in contact with the bath. The same is seen in the recordings, figure 12.17.

The mass loss rate for rafts created from fines are lower than for bulk, thus indicating a slower dissolution rate. From the correlation matrix presented in figure 12.19, it is clear that almost all other measured properties are correlated with the fines, and it is thus hard to conclude if any other parameters affected the mass of the raft.

A high amount of fines in alumina is associated with poor flow behavior and slower dissolution. However, Alumina C used in paper V had the highest fraction of fines, below the recommended values stated in table 2.1 and was also reported from the industry to have a high flow funnel time, which was an important reason for choosing this alumina batch in the campaign. This alumina dissolved well and did not show any unusual behavior in the recordings, and it was not seen to cause disturbances in the industry either [151]. This illustrates that observations in industry might not always be in accordance of what the literature suggests.

Alumina A showed a similar behavior when investigated in the see-through cell [82], where a bigger part of the powder dispersed quickly, whereas the remainder dissolved more slowly. Neither the thesis by Bracamonte [82] nor this one have been able to identify any specific parameters that explains this behavior.

Chapter 13: Modeling Results

13.1 Heat transfer cases

Stefan case

A plot of the phase front as a function of time is shown in figure 13.1, where both the analytical and simulated solution are shown. The current numerical solution was on average 0.014 m (2.1 % relative to the final position) below the analytical one, which were not found to increase nor decrease during time.
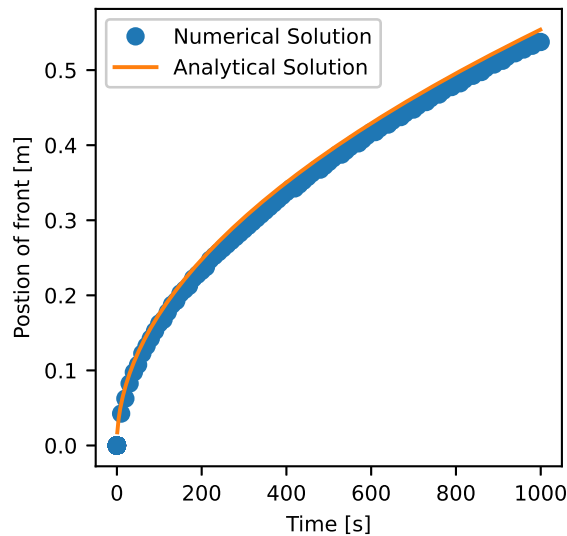
Figure 13.1: The analytical solution of the Stefan problem compared with the numerical one.

The results from this case demonstrate that the temperature equation and the source term for energy are implemented correctly.

Floating body

A selection of cases is presented in figure 13.2. A factorial regression analysis, where the response was set as the lowest value the center of mass had was conducted in Minitab where the individual parameters and their two-way interactions were considered. Each

of the individual parameters had a significant positive impact on the depth which the body penetrated, i.e a higher T_i increased the depth. U_0 and T_i had the highest relative impacts, with respectively 32 and 31 %.
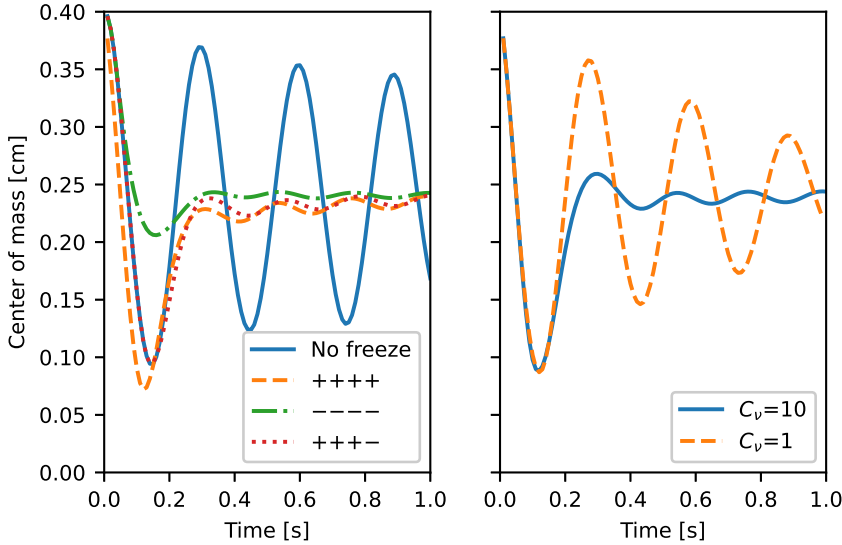
Figure 13.2: Left: The center of mass as a function of time for the floating object at four different configurations. Solid line: no freezing, dashed line: all factors had high values, dash-dot line: all factors had low values, dotted line: all factors except initial velocity had high values. Value of the factors are given in table 10.3. Right: comparison of having $C_v = 10$ (full) vs 1 (dashed) for the case where the initial velocity is at its high value, while the other factors are low.

This case shows that the initial velocity had the highest effect on the raft movement, followed by temperature and heat capacity. Decreasing the temperatures and the heat capacity will increase the layer of solidified bath and promote damping of the object. The initial velocity increases the penetration depth, although it does not have any effect on the thickness formed around the object. When reducing C_v for the rigid object (right plot in figure 13.2), a larger layer of freeze must form before the effect becomes visible.

Feeding of a dose

Figure 13.3 shows distribution of different phases, including frozen bath, and the temperature in parts of the domain, when $C_v = 0.01$. Images of the phases and freeze at t=0.1 for the different values of C_v are shown in 13.4. The center of mass in the four cases, calculated along the axis going vertically in the center of the system is plotted in figure 13.5, while figure 13.6 shows the fraction of bath solidified and the average

temperature of the alumina dose.
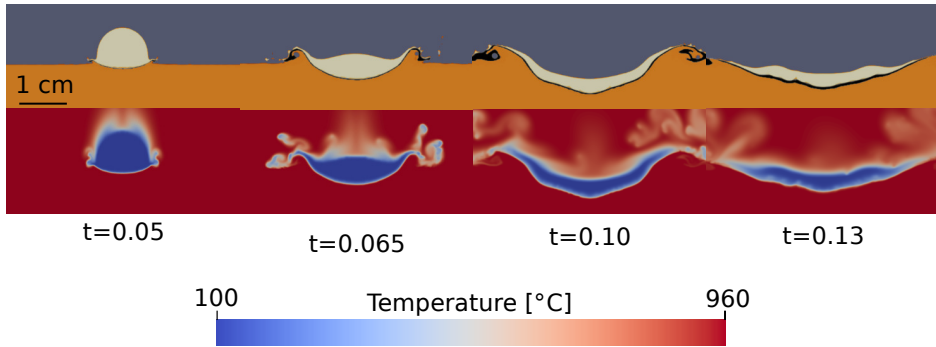
Figure 13.3: The phase compositions of molten bath (orange), alumina (beige), air (dark gray) and frozen bath (black), and the temperature distribution in the same area (from cold blue to hot red) for four selected times, when $C_v = 0.1$.
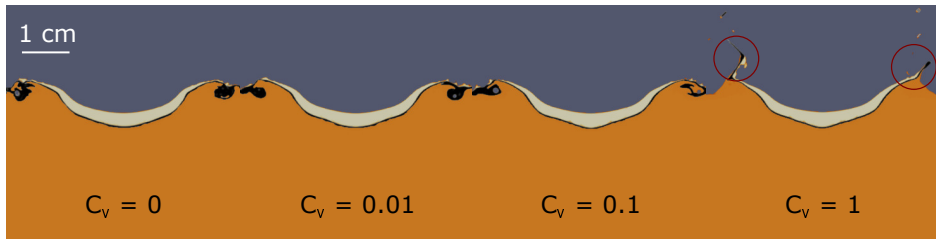
Figure 13.4: The phase composition of molten bath (orange), alumina (beige), air (dark gray) and frozen bath (black) for the cases with varying damping strength at t=0.1 s. The red circles show waves due to numeric effects.
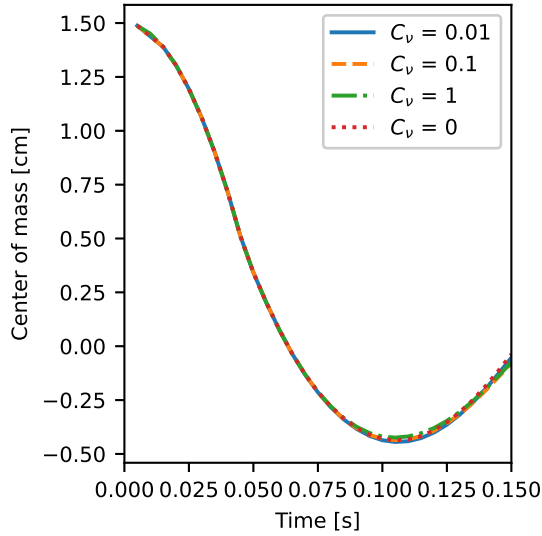
Figure 13.5: The center of mass as a function of time for alumina at x=0, i.e the center of the system for the different damping strengths.
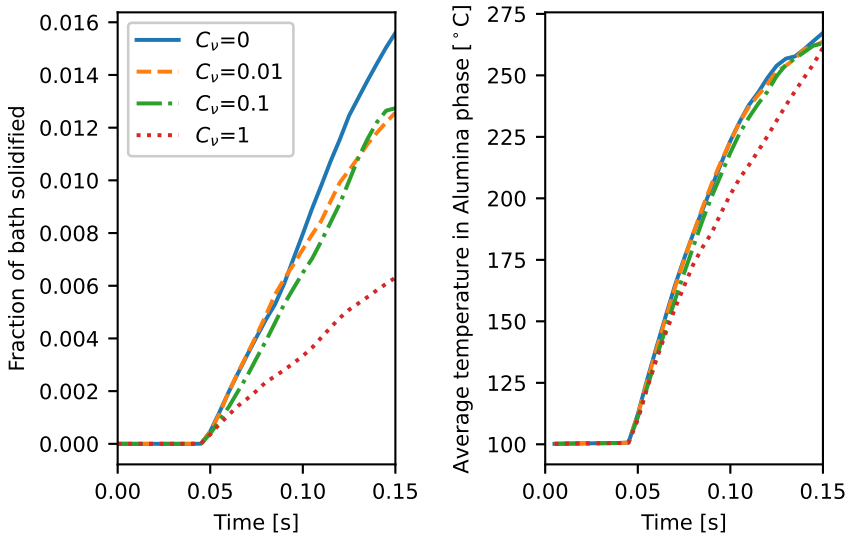
Figure 13.6: Left: fraction of bath frozen in the system for the four different damping strengths. Right: the average temperature in the alumina phase for the same cases.

When a cold dose hits the bath, a layer of freeze will form, as the bath becomes colder. By assuming the dose to be spherical, it corresponds to addition of about 0.5 grams into the melt. Based on earlier findings [63], it is therefore not expected that melting of the frozen layer has started within the investigated time interval, which is in accordance with the results in figure 13.6.

As seen in figure 13.4 and 13.5, the added momentum source term does not affect the formation of raft in any large degree. The layer of freeze will become thin, as the dose spread out, resulting in limiting damping effect. C_v cannot be higher than 1, as this results in numerical issues, for example the waves marked with the circles in figure 13.4. With $C_v = 1$, an even thicker layer of freeze is needed to observe any damping effect (see figure 13.2), and it also hinders heat from being transported and hence bath to freeze, as shown in figure 13.6. In addition, the dose's velocity while entering the bath were around 0.4 m s^{-1}, which is 10 times larger than for the rigid object, and the movement will in these cases therefore in a small degree be affected by heat transfer.

13.2 Granular cases

Verification cases

The results from case 4 are presented in figure 13.7, where y is normalized by the column height H, and U is normalized by U_{max}, which is the analytical solution at $y = H$, i.e the top of the columns. More detailed plots for the upper part of the column for the different angles are provided in figure 13.8. The average normalized deviation between the cases and the analytical solutions are presented in table 13.1.
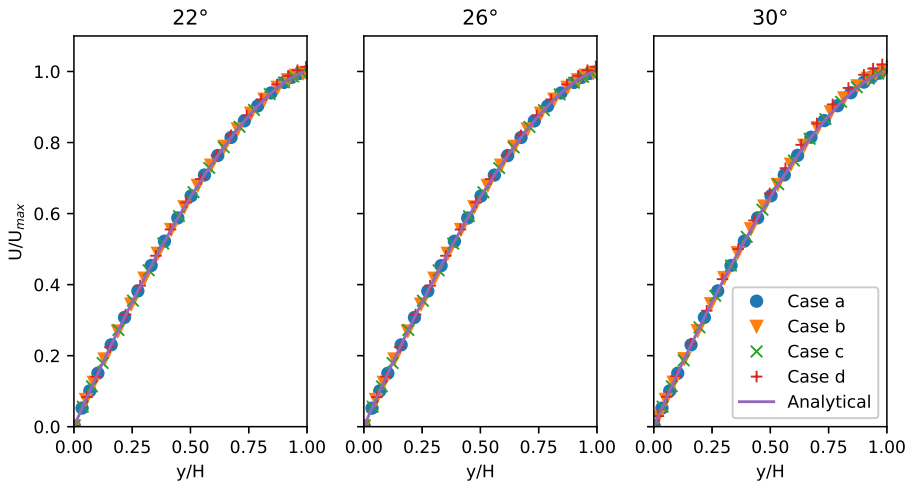
Figure 13.7: Velocity profiles of a granular column on an inclined plane for selected angles. Case a: single phase flow, Case b: multiphase flow with two identical granular phases. Case c: Granular phase with an overlapping fluid with $\rho_f = 1$, Case d: Granular phase with an overlapping fluid with $\rho_f = 150$. The analytical solution U_{max} is the velocity at the top of the column, and H is constant 5 cm for all cases.

Table 13.1: Overview of the different cases ran for verification of the $\mu(I)$-rheology on the inclined plane. Case 4a: single phase case, 4b: two identical phase, 4c: granular column with light fluid, 4d: granular flow with denser fluid.

Angle	Case 4a	Case 4b	Case 4c	Case 4d
22°	0.14 %	0.02 %	0.02 %	0.76 %
26°	0.04 %	0.01 %	0.04 %	0.75 %
30°	0.12 %	0.37 %	0.13 %	1.98 %
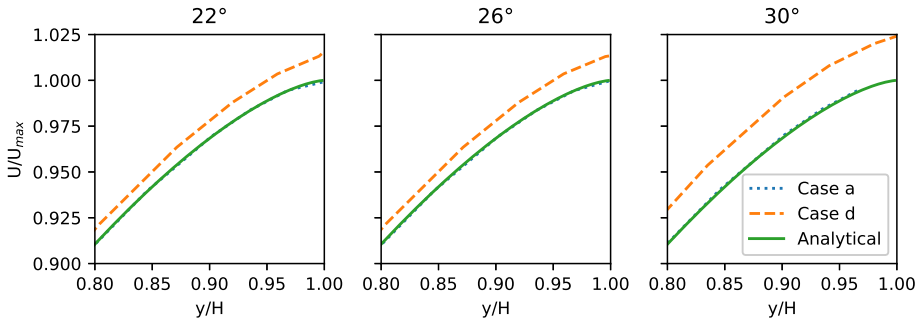
Figure 13.8: Detailed view of the velocity profiles showed in fig 13.7 at the highest area of the granular column, containing the analytical solution. Case a: single phase flow Case d: Granular phase with an overlapping fluid with $\rho_f = 150 \, \text{kg m}^{-3}$.

As expected, the velocity profiles for case 4a-c fit well with the analytical solution. Case 4d deviates, where the overlapping fluid increase the velocity above of the grains close to its interface, which is expected [144]. From figure 13.8 it seems that the deviation increased at a higher incline, confirmed by the results in table 13.1. These results verify the model and also illustrate that the velocity profile will be affected by fluids, also as expected.

For case 4, the interface between granular material and fluid for selected times are shown in figure 13.9.
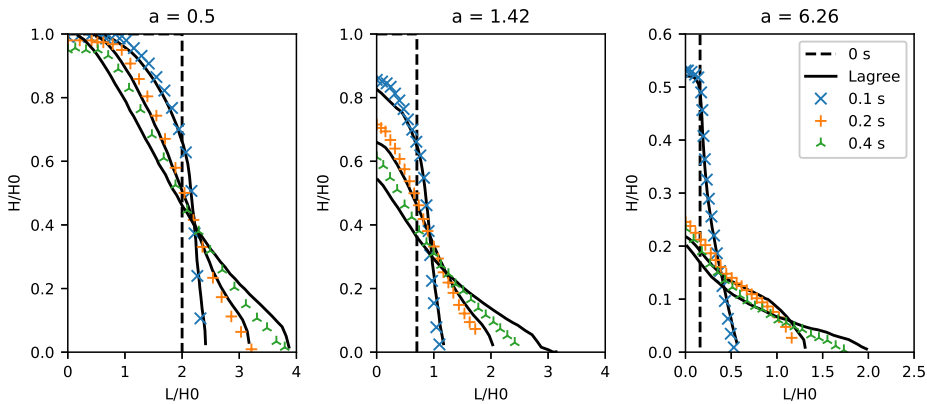
Figure 13.9: The grain-air interface during a granular column collapse for selected times, where the aspect ratio given as title.

An average normalized deviation between the results from Lagrée and the current work is calculated in x and y-direction, presented in table 13.2. The average value is calculated between $0.2x_L < x < 0.8x_L$, where x_L denotes the highest x-value the solution by Lagrée had at the selected time, thereby neglecting the relatively large uncertainty on the fringes of the column.

Table 13.2: The relative deviation between the numerical solution in this work and the solution by Lagrée et al. [144] for selected aspect ratios a. The average value is calculated between $0.2x_L < x < 0.8x_L$, where x_L denotes the highest x-value the solution by Lagrée had at the selected time.

	t=0.1		t=0.2		t=0.4	
a	$\Delta \bar{x}$	$\Delta \bar{y}$	$\Delta \bar{x}$	$\Delta \bar{y}$	$\Delta \bar{x}$	$\Delta \bar{y}$
0.50	16.6 %	1.8 %	5.2 %	3.3 %	7.1 %	7.1 %
1.42	6.6 %	2.8 %	4.1 %	6.1 %	7.7 %	19.2 %
6.26	3.2 %	4.6 %	9.6 %	8.5 %	7.7 %	12.8 %

The observed behavior shows similarities with the earlier published cases, although the deviation is smaller at 0.1 and 0.2 s (5.9 and 6.0 %) than after 0.4 s (10.3 %) in table 13.2. As the numerical frameworks are realized in two different software, with a difference in schemes and routines, some deviation is expected. The developed model is therefore found to be suitable for further investigations.

Parametric sensitivity

The cases never come to a complete stop, and in this work, a quasi-steady state is assumed to be encountered at t=2 s, where the shape seems to be stabilized. Changing μ_2 had the largest effect on the angle with a relative contribution of 42.2 %, followed by I_0 (30.8 %), d (13.1 %) as well as the interactions $\mu_2 \cdot I_0$ (8.4 %) and $\mu_2 \cdot d$ (4.5 %). Their contributions are visualized in figure 13.10, where a) displays the main effects, while b) and c) respectively shows the interactions $\mu_2 \cdot I_0$ and $\mu_2 \cdot d$
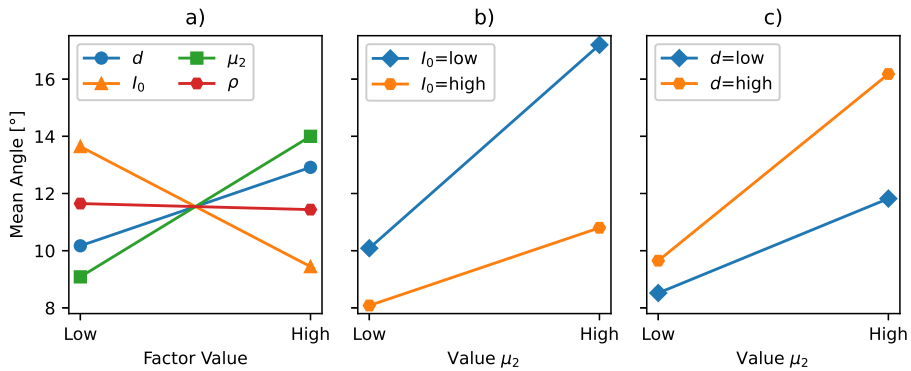
Figure 13.10: Plots illustrating how the different parameters affect the final angle of the heap in case 6, measured as illustrated in figure 10.6. a) the main effects. b) The interaction plot between μ_2 and I_0. c) The interaction plot between μ_2 and d. The values of "high" and "low" are stated in table 10.6.
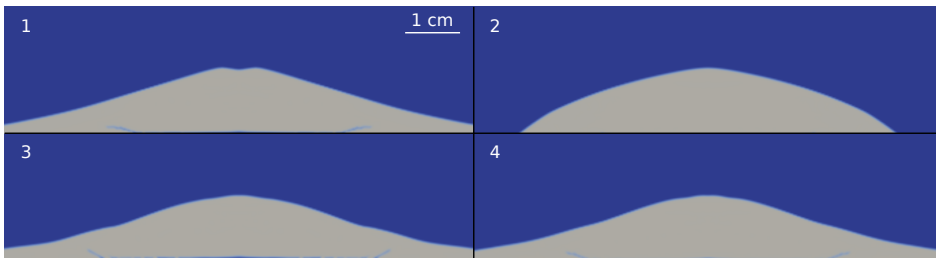
Figure 13.11: Heaps of powder for case 6 after 2 s an assumed steady state. 1: All factors are high. 2: μ_2 and d high, I_0 and ρ low. 3: μ_2 and d low, I_0 and ρ high. 4: All factors are low.

Figure 13.12 shows a factorial plot for the main effects with the same statistical analysis as the former case, and found that μ_2 had the highest relative contribution on the angle with 44.75 %, followed by I_0 (32.22 %) $\mu_2 \cdot I_0$ (11.57 %) and h (8.78 %). Table 13.3 shows the difference in angles between the original and the regularized case.
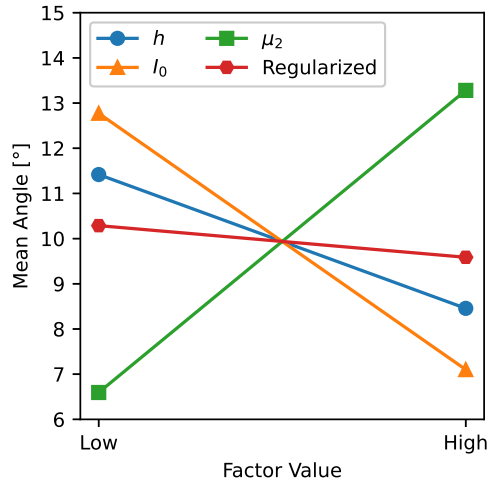
Figure 13.12: Plot illustrating how the different factors in case 7 affect the angle of the heap, measured as shown in figure 10.6. The values of "high" and "low" are stated in table 10.6.
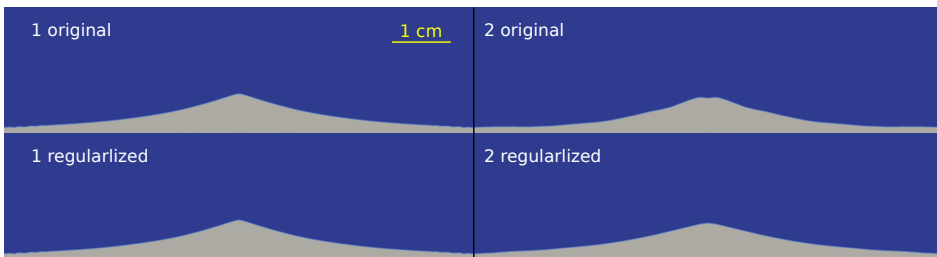
Figure 13.13: Heaps of powder for case 7 after 2 s, an assumed steady state for the original model (upper) and regularized model (below). 1 All other factors are set to their "high" value. 2: μ_2 is "low", h and I_0 are "high" cf. table 10.6 for numerical values corresponding to "high" and "low".

Table 13.3: The measured angles and their difference for the original and regularized $\mu(I)$-model in case 7. + represents that the factor is set to a high value, while - is for a low value.

h	I_0	μ_2	Original	Regularized	Difference
+	+	+	7.54	6.85	0.68
+	+	-	4.87	4.52	0.36
+	-	+	16.66	16.66	0
+	-	-	5.40	5.14	0.27
-	+	+	10.50	10.08	0.43
-	+	-	7.57	4.87	2.70
-	-	+	19.26	18.68	0.58
-	-	-	10.49	9.90	0.59

When μ_2 increases, a higher value of $\mu(I)$ (ref eq. (10.29)), and hence a larger value of ν can be obtained. The increased viscosity in the powder will decrease its ability to spread out. The same tendency can be seen from I_0 and d. Increasing I_0 will decrease the value of $\mu(I)$ and ν, while an increase of d will increase $\mu(I)$, which can be seen by inserting (10.30) into (10.29). μ_2 will increase the possible value of $\mu(I)$ while I_0 and d only affect the possible value created, which explain the two interaction effects. ρ was discarded from the model due to low effect. It will have the same effect as d, but since it is varied in lesser magnitude, its effect on $\mu(I)$ will be smaller. The same tendencies for μ_2, I_0 and its interactions are seen in case 4. The increase of spreading with increased drop height is also expected, as higher velocity for the powder when hitting the surface leads to larger spreading.

Applying the regularized model reduced the final angle of the heap (table 13.3), and the shape will for some cases also be slightly different, as seen in the right images in figure 13.13. However, the model did not have a significant impact relative to the variation of the other factors. Applying the regularized model in case 3 would probably not change the results significantly.

d and ρ have in these cases quite obvious interpretations for the case of alumina. d will not be uniform and must be interpreted as the average value of a selected dose. The parameters are however not completely independent of each other. For example, reducing the particle size, d, are found to decrease the flowability of alumina and hence increasing the angle of repose [19], here interpreted as μ_1. The chosen value in this work (30°) represents an alumina with a quite good flowability [19], and hence the particle diameter is expected to be high.

Three-phase cases

Snapshots of the μ(I)-rheology is shown in figure 13.14, compared with reference cases. The dose with low viscosity (left) spreads out fast, and parts of the dose flow out of the image. For a high viscous fluid (right), the dose is held together in one piece, which is spread out due to the back wave approaching at t=0.3. When the μ(I)-rheology is applied (center), small parts are dispersed into the melt, while two big parts are released from the main dose at t=0.4.
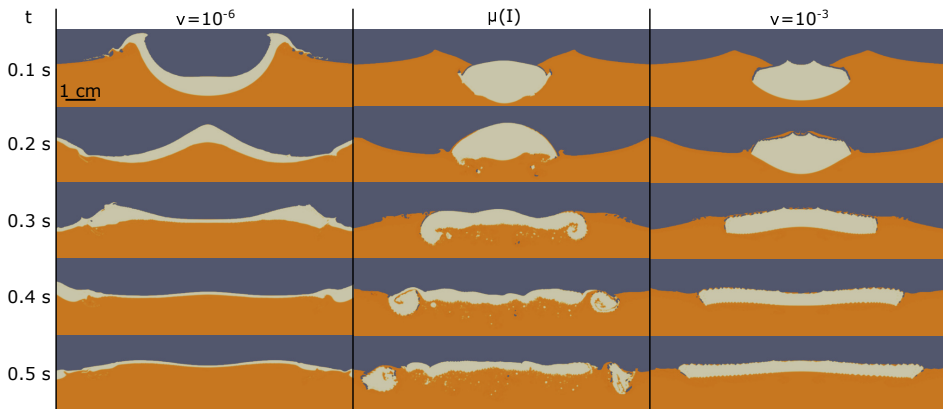
Figure 13.14: The phase compositions of bath (orange), alumina (beige), air (gray) for selected times, for the following cases: left: Newtonian fluid with $\rho = 1200$ and $v = 10^{-6}$. Center: Fluid with the μ(I)-properties. Right: Newtonian fluid with $\rho = 1200$ and $v = 10^{-3}$.

Theses cases show that the μ(I)-rheology has a different behavior than a Newtonian fluid. As seen at 0.3 s, the created wave will stretch the dose out and for the μ(I)-rheology, smaller parts are segregated from the created rafts and flakes seem to disperse into the bath. From previous studies of feeding in a water model [124], a similar tendency with bigger parts of the dose floating away was seen when little convection was applied. Further, dispersion of particle as so called snowing has been observed earlier in a see-through cell [82].

Simulating the dose as a high viscous fluid, showed at the rightmost column in figure 13.14 is also presented as a possible approach. It is easier to execute, but it did not allow for parts of the dose to detach, both as smaller flakes and bigger lumps. The resulting raft structure seen at t=0.5 s is uniform for the viscous fluid, while lab experiments [125] suggest that the structure is more irregular, and thus more similar to the structure achieved by the μ(I)-rheology.

Coupled case

Selected images for the coupled case are shown in figure 13.15. There is a slight difference in behavior for the case with freezing. Solidification of bath holds the two chunks which were detached together, and it spreads out 8.2 cm in this case, versus 9.1 cm in the previous, when freezing was not applied.
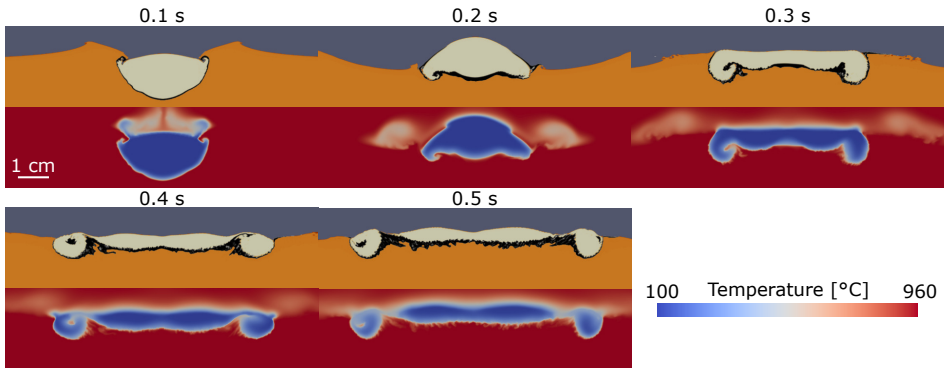
Figure 13.15: Phase composition of bath (orange), alumina (beige), air (gray) and bath (black), and temperature field for the coupled case for selected times.

The results from this case (figure 13.15) illustrate that the two developed models can be coupled together. The frozen bath will create a coherent raft and the measurements of raft width shows that the freezing model slightly dampens the movement. In this case, no smaller parts of powder have detached from the raft, which was the case when only the μ(I)-rheology was applied. In this setup, the initial contact between bath and alumina will cause freezing to occur immediately, hence limiting the contact between alumina and the liquid bath.

13.3 Benchmark cases

The benchmark cases were run in parallel on 20 cores, with a constant time step of 10^{-6} s to t=0.01 s. The running times are presented in table 13.4

Table 13.4: The running time for the benchmark cases, with the increase of running time set relative to the base case.

Case	Time [s]	Increase
Base	29 006	0 %
μ(I)	33 479	13.4 %
Temperature field	29 316	0.9 %
Solidification	29 801	2.4 %
All combined	34 281	15.8 %

The results demonstrate that the μ(I)-rheology is the most time-consuming model. As the current work aimed to implement and test different models, the code is not completely optimized. However, the computational time might also be improved even more by optimizing the cases, where the potential might be higher than by improving the model.

Part V

Conclusions and further work

Chapter 14: Main conclusions

The current thesis has investigated alumina feeding and seven goals were presented in the introduction.

The first goal was to investigate how alumina feeding influenced hydrogen fluoride emissions at industrial scale. This was achieved by measuring the HF-concentration over 43 consecutive days in the duct of a cell, with an average concentration of 400 ppm. A rapid rise is occurring after each feeding, followed by a slower decline. Analysis of data suggests that the feeding cycle play an important role, where a general higher concentration of HF was measured when the cell overfed, i.e more frequent feedings. Of regular operations, ambient humidity and anode change seems to have a significant role, although the latter one could be masked by changes in the feeding cycle.

The second goal aimed to develop a physical model for alumina feeding and the subsequent raft formation in a full-scale model at room temperature. This was achieved by replacing bath with water and alumina with an organic powder in a container simulating the center channel of an industrial cell. Rafts formed in this setup have floating times varying between 35 and 550 seconds and show similar behavior as those formed in an industrial cell. Particle size distribution, water temperature and bubble frequency were varied, where all of them had a significant effect on the dissolution rate. The particle size was found to be the most important one, where the dissolution time increased almost five-fold, when halving the mean particle diameter of the added batch.

In the third goal, a laboratory setup for generation and extraction of rafts was developed, and further extended to allow for recordings of alumina additions from above. Regular secondary alumina had mass loss rates varying between 0.42 and 1.57 $\mathrm{g\,min^{-1}}$, and consisted of a porous structure with a large bulge or a crater in the center, and thinner flakes spreading out. Recordings suggest that the addition method is the main reason for the structure, where freezing of bath will strengthen it, and feeding of alumina on a flat plate showed the same geometry.

The developed setup was further used to study the effect of different parameters, set as the fourth goal.

The mass of rafts was used to measure the effect of preheating alumina, where it was found that rafts do not form at temperatures above 500-600 °C. To obtain this in an industrial setting will be challenging, demanding sufficient change of the current feeder

setup with unknown costs.

CT was applied to quantify the porosity of the rafts. Rafts from secondary alumina had an average porosity of 8.3 %, while the value for rafts from primary alumina was 0.8 %. Adding alumina with higher content of adsorbed water did not increase the porosity, for neither primary nor secondary alumina. Hence, the reason for the porosity found in rafts is probably a result of the dry scrubbing process.

Rafts created from fines were found to have a different structure, being shaped as a pellet, with no flakes around it, and with mass loss rates spanning from 0.06 to 1.15 gmin^{-1}. CT revealed that the rafts from fines are more heterogeneous, with powder encapsulated within a layer of frozen bath. The reduced spreading of powder results in lesser freeze of bath, and thus a reduced mass gain. No alumina parameters other than fines were found to affect the mass or the mass loss rate in a significant manner.

The effect on adding LiF was also investigated by retrieving samples from an industrial bath with 0, 2.5 and 5 wt% at a constant superheat of 12 °C. Significant larger rafts were formed at 5 wt% after 3 minutes, compared with having no LiF, while no such effect was seen at 2.5 wt%.

Numerical modeling of alumina feeding within a continuous framework has been proposed in OpenFOAM, where sub-models considering solidification of bath (goal 5) and modeling the alumina powder as a continuous phase (goal 6) have been implemented, together with a multiphase solver accounting for transfer of mass, momentum, and energy (goal 7).

Assuming the raft to be a rigid object, it was found that increased freeze thickness increased the damping effect. If alumina is assumed to be a fluid, the effect of freezing was not visible, due to a too thin layer of freeze.

Alumina powder was simulated through the μ(I)-rheology, which also has been implemented as a generalized Newtonian Fluid. Parametric studies in an powder-air system reveal that the μ(I)-parameters of I_0 and μ_2 have a large impact on the final shape. In a three-phase air-alumina-bath system, alumina with the μ(I)-rheology could be segregated into smaller pieces, in contrast to letting the powder be a high viscous fluid.

Combining the two models was done successfully and shows that frozen bath will form in areas between the alumina pieces, hence creating a larger coherent raft compared with only applying the μ(I)-rheology. The freezing of bath did also in this case have a limiting effect on the raft shape.

The current work has increased our understanding of raft formation during alumina feeding. Several properties, both linked to alumina quality and operational conditions are found to affect the formation of rafts, and their structure at lab scale. A remaining challenge is to relate the current results to industry, where the interdependencies are more challenging to quantify.

Chapter 15: Suggestions for future work

Water model

If working further with the water model, a dimensional analysis should be carried out, similar as the one conducted by Chesonis and LaCamera [94], but also including grain-liquid relations. Further, PIV might be considered as an opportunity to quantify the created velocity field, and hence being able to create a flow similar to that found in a real cell. Finally, it might also be valuable as a validation tool for the numerical models developed, due to better parameter control.

Lab-induced rafts

Convection has not been applied in any of the furnace experiments in this thesis. Applying either bubbled induced convection or stirring would have led to a better dispersion and aid the breaking of the thin flakes formed around the raft. However, implementing convection during raft sampling would have been challenging as the designed sampler in these experiments covered most of the available bath area. An easier approach would be to apply it with video recordings.

The origin of the pore formed in rafts still remains unknown, although the current work suggest that the formation is due to products added to the alumina during dry scrubbing, for example adsorbed HF, sulfur and carbon dust. Preforming raft sampling experiments with primary alumina containing higher levels of the components individually can therefore aid in determining what causes the pores.

The study in paper V revealed that the alumina types act different, although no cause other than content of fines were identified. The current study was limited to only three types, and more types of alumina with altered properties might be needed to quantify effect of single parameters. Investigating the surface property of alumina with SEM might also be considered, as it was not done in this work.

Structural hydroxides might also contribute to the pore formation, and if the reaction for forming HF from the hydroxides is an electrochemical as some have suggested [52], it might be fruitful perform electrolysis during the raft sampling experiments. One should also consider to use themogravimetric analysis (TGA) instead of muffle furnace experiments to quantify the loss of ignition, as one can be able to quantify the amount of different transition phases of alumina (shown in figure 2.2) [19].

Reproducibility should also be improved. Several measures have already been made to stabilize the temperature, and improving the raft sampler should therefore be focused on further.

If requirement for temperature control are still not met, one might need to consider another furnace design with better insulation without the possibility to extract raft. This will though require a precise and reliable method for measuring the alumina concentration in the bath. A possible candidate might be the sensor developed by Bracamonte [82].

Modeling

The current cases including freezing (case 3 and 9) show that the damping strength is weak. This might be improved by allowing for bath to mix into the alumina, thus increasing the area where the damping effect can occur. Allowing for infiltration should anyway be implemented, since it is found to be an important mechanism in the disintegration of rafts [102], [103].

For the added source terms, solidification and melting of bath is not an isothermal process and a more advanced model, such as a linear dependence between solidus-liquidus or Scheil equation should be considered [135].

For improving the $\mu(I)$-rheology for alumina, parameter values must be identified by experiments, in particular the parameters μ_2 and I_0, which are currently unknown. Possible experimental setups to identify the parameters are flow down an inclined plane, collapse of a column or release of a dose on a flat plane. As mentioned earlier, parameter dependence will probably occur and thus, experiments should be carried out with varying particle sizes, in order to get an overview on the range the parameters might have.

Several phenomena are still missing in order to develop a complete raft model. Many of those are already discussed by other researchers [98], [103]. Firstly, alumina must be able to dissolve in the melt, since in most cases, a significant fraction of the added dose will dissolve immediately after addition. Also, the formation of pores due to evolution of gas is found in lab scale rafts, and should also be accounted for.

The literature review, chapter 7, shows that the most relevant studies are those conducted by Roger *et al.* [98], which modeled alumina feeding through a Lagrange-Lagrange framework. They were able to compute 10 seconds computational time per hour, which is superior performance to what has been realized in the current work. They are taking advantage of that the simulations can be executed on a massively parallel scale, utilizing Graphic Processor Unit technology. If the access to units is limited, the proposed

Eulerian framework will be more suitable.

Another benefit is that several of the larger scale models are developed in this framework [105], [108], [111], and it could hence be coupled together in later work. Finally, owing to the maturity of the Eulerian approach, multiple additional physical models are readily available, i.e MHD [108], turbulence [152] and mass transfer [111], facilitating further extensions of the proposed framework.

A developed model should with improvements be able to study the alumina feeding and dissolution in detail, and effects of different parameters. Although the current model is too computational time-demanding to run at real time, it can be used to identify key findings that must be considered for the larger scale and faster models. In particular the estimating dissolution rate of rafts and how it changes during its disintegration would be highly beneficial.

Industrial measurements

This work has been mostly limited to lab-scale work and modeling. In an industrial cell, the problem is even more complex, both due to the high number of parameters, but also the fact that good dissolution behavior is one of several requirements for the alumina, as discussed in section 2.3. Investigations of effects, both related to operations and alumina properties in industrial scale are necessary, although it requires good planning and execution over longer periods. This might involve measure alumina qualities after dry scrubbing, as the properties are changed during the transport through the plant and GTC. Cell parameters, such as current efficiency, sludge levels and eventually anode effect frequency can be used as response parameters.

Bibliography

[1] O.-A. Lorentsen, "125 years of the Hall-Héroult process, what made it a success?" In *Molten Salts Chemistry and Technology*, M. Gaune-Escard and G. M. Haarberg, Eds., Chichester, UK: John Wiley & Sons, Ltd, May 11, 2014, pp. 103–112. DOI: 10.1002/9781118448847.ch1k.

[2] G. P. Tarcy, H. Kvande, and A. Tabereaux, "Advancing the industrial aluminum process: 20th century breakthrough inventions and developments," *JOM*, vol. 63, no. 8, pp. 101–108, Aug. 1, 2011. DOI: 10.1007/s11837-011-0120-4.

[3] Norsk Hydro ASA. (2022). "Norge," [Online]. Available: https://www.hydro.com/no-NO/om-hydro/hydro-locations-worldwide/europe/norway/ (visited on 04/04/2022).

[4] Alcoa Corporation. (2022). "Alcoa – Norway," [Online]. Available: https://www.alcoa.com/norway/no (visited on 04/04/2022).

[5] The Norwegian Water Resources and Energy Directorate. (2022). "Kraftproduksjon - NVE," [Online]. Available: https://www.nve.no/energi/energisystem/kraftproduksjon/ (visited on 04/04/2022).

[6] A. Solheim and E. Skybakmoen, "Mass- and heat transfer during dissolution of alumina," in *Light Metals 2020*, A. Tomsett, Ed., ser. The Minerals, Metals & Materials Series, Springer, Cham, 2020, pp. 664–671. DOI: 10.1007/978-3-030-36408-3_90.

[7] J. Thonstad, P. Fellner, G. M. Haarberg, J. Híveš, H. Kvande, and Å. Sterten, *Aluminium Electrolysis: Fundamentals of the Hall-Héroult Process. 3rd*. Düsseldorf: Aluminium-Verlag, 2001.

[8] R. K. Jain, M. P. Taylor, S. B. Tricklebank, and B. J. Welch, "A study of the relationship between the properties of alumina and its interaction aluminium smelting electrolytes," in *1st Intl. Symp. Molten Salt Chem. and Tech., Kyoto, Japan*, Kyoto, Japan, 1983, pp. 59–64.

[9] P. Lavoie, M. P. Taylor, and J. B. Metson, "A review of alumina feeding and dissolution factors in aluminum reduction cells," *Metallurgical and Materials Transactions B*, vol. 47, no. 4, pp. 2690–2696, Aug. 1, 2016. DOI: 10.1007/s11663-016-0680-3.

[10] X. Wang, "Alumina dissolution in aluminum smelting electrolyte," in *Light Metals 2009*, G. Bearne, Ed., 2009, pp. 383–388.

[11]   S. Aase, S. Bekkevoll, and S. A. Forberg, "A model based parametric study of alu-
        mina feeding and dissolution," BSc, Norwegian University of Science and Tech-
        nology, Trondheim, 2020.

[12]   S. Bekkevoll, "Alumina Dissolution in Cryolite Melts - Effect of Secondary Alu-
        mina Properties on Dissolution and Raft Behavior," M.S. thesis, Norwegian Uni-
        versity of Science and Technology, Trondheim, 2022.

[13]   L. Hudson, "Alumina production," in *Production of Aluminium and Alumina*,
        ser. Critical Reports on Applied Chemistry, A. Burkin, Ed., vol. 20, Chichester:
        John Wiley & Sons, 1987, pp. 11–46.

[14]   K. Grjotheim and H. Kvande, Eds., *Introduction to Aluminium Electrolysis- Un-
        derstanding the Hall-Heroult Process*, Düsseldorf: Aluminium-Verlag, 1993.

[15]   K. Grjotheim and B. Welch, *Aluminium smelter technology : a pure and applied
        approach*, 2nd ed. Düsseldorf: Aluminium-Verlag, 1988.

[16]   B. Whittington and D. Ilievski, "Determination of the gibbsite dehydration reac-
        tion pathway at conditions relevant to bayer refineries," *Chemical Engineering
        Journal*, vol. 98, no. 1, pp. 89–97, Mar. 15, 2004. DOI: 10.1016/S1385-8947(03)
        00207-9.

[17]   S. Ose, A. Sørhuus, A. Dyrøy, and M. Karlsen, "Alumina handling in the smelter
        — from port to pot," in *Light Metals 2016*, E. Williams, Ed., Springer, Cham, 2016,
        pp. 487–492. DOI: 10.1007/978-3-319-48251-4_80.

[18]   C. Duwe, "Alumina storage and handling," in *Smelter Grade Alumina from Baux-
        ite: History, Best Practices, and Future Challenges*, ser. Springer Series in Ma-
        terials Science, B. E. Raahauge and F. S. Williams, Eds., Springer, Cham, 2022,
        pp. 649–678. DOI: 10.1007/978-3-030-88586-1_12.

[19]   S. J. Lindsay and P. Lavoie, "Alumina quality, HF removal, dissolution and alu-
        minum purity," in *Smelter Grade Alumina from Bauxite: History, Best Practices,
        and Future Challenges*, ser. Springer Series in Materials Science, B. E. Raahauge
        and F. S. Williams, Eds., Springer, Cham, 2022, pp. 577–648. DOI: 10.1007/978-
        3-030-88586-1_11.

[20]   "Aluminium oxide primarily used for the production of aluminium — parti-
        cle size analysis for the range of 45 um to 150 um — method using electro-
        formed sieves," ISO 2926, 2013. [Online]. Available: https://www.iso.org/
        standard/52316.html.

[21]   L. M. Perander, Z. D. Zujovic, T. F. Kemp, M. E. Smith, and J. B. Metson, "The na-
        ture and impacts of fines in smelter-grade alumina," *JOM*, vol. 61, no. 11, pp. 33–
        39, Nov. 1, 2009. DOI: 10.1007/s11837-009-0164-x.

[22] "Aluminium oxide primarily used for the production of aluminium — measurement of the angle of repose," ISO 902, 1976. [Online]. Available: `https://www.iso.org/standard/5306.html`.

[23] "Aluminium oxide primarily used for the production of aluminium — determination of specific surface area by nitrogen adsorption," ISO 8008, 2005. [Online]. Available: `https://www.iso.org/standard/39383.html`.

[24] "Aluminium oxide primarily used for the production of aluminium — method for the determination of tapped and untapped density," ISO 18842, 2015. [Online]. Available: `https://www.iso.org/standard/63550.html`.

[25] "Aluminium oxide primarily used for the production of aluminium — determination of loss of mass at 300 degrees c and 1 000 degrees c," ISO 806, 2004. [Online]. Available: `https://www.iso.org/standard/36360.html`.

[26] M. M. Hyland, A. R. Gillespie, J. B. Metson, and R. Huglen, "Predicting moisture content on smelter grade alumina from measurement of the water isotherm," in *Light Metals 1997*, Warrendale, Pa: Minerals, Metals & Materials Society, 1997.

[27] L. M. Perander, M. A. Stam, M. M. Hyland, and J. B. Metson, "Towards redefining the alumina specifications sheet — the case of HF emissions," in *Light Metals 2011*, S. J. Lindsay, Ed., Springer, Cham, 2011, pp. 285–290. DOI: `10.1007/978-3-319-48160-9_51`.

[28] Granutools. (). "Granutools | GranuFlow," Granutools, [Online]. Available: `https://www.granutools.com/en/granuflow` (visited on 12/21/2022).

[29] HMKTest. (). "Hall flow meter," [Online]. Available: `http://www.hallflowmeter.com/` (visited on 12/21/2022).

[30] H. K. Versteeg and W. Malalasekera, *An introduction to computational fluid dynamics: the finite volume method*, 2nd ed. Harlow: Pearson/Prentice Hall, 2007, xii+503.

[31] CPPMechEngTutorials, *Fluid mechanics: Topic 10.1 - lagrangian vs eulerian descriptions of flow*, Feb. 25, 2017. [Online]. Available: `https://www.youtube.com/watch?v=iItS2O8Fcf8` (visited on 05/18/2022).

[32] C. E. Brennen, *Fundamentals of Multiphase Flow*. Cambridge [England] ; New York: Cambridge University Press, 2005, 345 pp.

[33] C. Greenshields and H. Weller, *Notes on Computational Fluid Dynamics: General Principles*. Reading, UK: CFD Direct Ltd, 2022, 291 pp., ISBN: 1-399-92078-2. [Online]. Available: `https://doc.cfd.direct/notes/cfd-general-principles/`.

[34] E. Skybakmoen, A. Solheim, and Å. Sterten, "Alumina solubility in molten salt systems of interest for aluminum electrolysis and related phase diagram data,"

Metall Mater Trans B, vol. 28, no. 1, pp. 81–86, Feb. 1, 1997. DOI: 10.1007/s11663-997-0129-9.

[35] J. Thonstad, A. Solheim, S. Rolseth, and O. Skar, "The dissolution of alumina in cryolite melts," in *Essential Readings in Light Metals: Volume 2 Aluminum Reduction Technology*, G. Bearne, M. Dupuis, and G. Tarcy, Eds., Springer, Cham, 2016, pp. 105–111. DOI: 10.1007/978-3-319-48156-2_14.

[36] N. P. Østbø, "Evolution of alpha phase alumina in agglomerates upon addition to cryolitic melts," Ph.D. dissertation, Norwegian University of Science an Technology - NTNU, Trondheim, 2002. [Online]. Available: https://ntnuopen.ntnu.no/ntnu-xmlui/handle/11250/244446.

[37] J. Thonstad, F. Nordmo, and J. B. Paulsen, "Dissolution of alumina in molten cryolite," *METALLURGICAL TRANSACTIONS*, vol. 3, no. 2, pp. 407–412, Feb. 1, 1972. DOI: 10.1007/BF02642044.

[38] R. G. Haverkamp and B. J. Welch, "Modelling the dissolution of alumina powder in cryolite," *Chemical Engineering and Processing: Process Intensification*, vol. 37, no. 2, pp. 177–187, 1998. DOI: 10.1016/S0255-2701(97)00048-2.

[39] G. I. Kuschel and B. J. Welch, "Further studies of alumina dissolution under conditions similar to cell operation," in *Essential Readings in Light Metals: Volume 2 Aluminum Reduction Technology*, G. Bearne, M. Dupuis, and G. Tarcy, Eds., Springer, Cham, 2016, pp. 112–118. DOI: 10.1007/978-3-319-48156-2_15.

[40] S. J. Lindsay, "Key physical properties of smelter grade alumina," in *Light Metals 2014*, J. Grandfield, Ed., Hoboken, Wiley, 2014, pp. 597–601. DOI: 10.1007/978-3-319-48144-9_101.

[41] J. Tessier, G. P. Tarcy, E. Batista, X. Wang, and C. E. Suarez, "Towards on-line monitoring of alumina properties at a pot level," in *Light Metals 2012*, Springer, Cham, 2012, pp. 633–638. DOI: 10.1007/978-3-319-48179-1_108.

[42] G. J. McIntosh, J. B. Metson, P. Lavoie, T. Niesenhaus, T. Reek, and L. Perander, "The impact of alumina quality on current efficiency and energy efficiency in aluminum reduction," in *Light Metals 2016*, E. Williams, Ed., Springer, 2016, pp. 417–422. DOI: 10.1007/978-3-319-48251-4_68.

[43] S. Rolseth and J. Thonstad, "Agglomeration and dissolution of alumina in cryolite baths," in *Extraction, Refining, and Fabrication of Light Metals*, M. Sahoo and P. Pinfold, Eds., ser. Proceedings of Metallurgical Society of Canadian Institute of Mining and Metallurgy, Amsterdam: Pergamon, 1991, pp. 177–190. DOI: 10.1016/B978-0-08-041444-7.50021-4.

[44] D. I. Walker, T. Utigard, and M. P. Taylor, "Alumina agglomerates in aluminum smelters," in *Light Metals 1995*, J. W. Evans, Ed., TMS, 1995, pp. 425–434.

[45]   O. Kobbeltvedt, S. Rolseth, and J. Thonstad, "The dissolution behaviour of alumina in cryolite bath on a laboratory scale and in point fed industrial cells," in *VIII Al sympózium*, Ziar nad Hronom: ZSNP, Sep. 1995, pp. 127–135.

[46]   O. Kobbeltvedt, J. Thonstad, and S. Rolseth, "On the mechanisms of alumina dissolution with relevance to point feeding aluminium cells," in *Light Metals 1996*, W. Hale, Ed., Warrendale, Pa: TMS, 1996.

[47]   N. Dando, X. Wang, J. Sorensen, and W. Xu, "Impact of thermal pretreatment on alumina dissolution rate and HF evolution," in *Light Metals 2010*, J. A. Johnson, Ed., Warrendale, Pa: TMS, 2010, pp. 541–546.

[48]   S. E. Gylver, N. H. Omdahl, A. K. Prytz, A. J. Meyer, L. P. Lossius, and K. E. Einarsrud, "Alumina feeding and raft formation: Raft collection and process parameters," in *Light Metals 2019*, C. Chesonis, Ed., ser. The Minerals, Metals & Materials Series, Springer, 2019, pp. 659–666. DOI: 10.1007/978-3-030-05864-7_81.

[49]   S. E. Gylver, N. H. Omdahl, S. Rørvik, I. Hansen, A. Nautnes, S. N. Neverdal, and K. E. Einarsrud, "The micro- and macrostructure of alumina rafts," in *Light Metals 2019*, C. Chesonis, Ed., ser. The Minerals, Metals & Materials Series, Springer, 2019, pp. 689–696. DOI: 10.1007/978-3-030-05864-7_85.

[50]   D. Picard, J. Tessier, G. Gauvin, D. Ziegler, H. Alamdari, and M. Fafard, "Investigation of the frozen bath layer under cold anodes," *Metals*, vol. 7, no. 9, p. 374, Sep. 15, 2017. DOI: 10.3390/met7090374.

[51]   W. Haupin and H. Kvande, "Mathematical model of fluoride evolution from hall-héroult cells," in *Essential Readings in Light Metals: Volume 2 Aluminum Reduction Technology*, G. Bearne, M. Dupuis, and G. Tarcy, Eds., Springer, Cham, 2016, pp. 903–909. DOI: 10.1007/978-3-319-48156-2_133.

[52]   M. Hyland, E. Patterson, and B. Welch, "Alumina structural hydroxyl as a continuous source of HF," in *Essential Readings in Light Metals: Volume 2 Aluminum Reduction Technology*, G. Bearne, M. Dupuis, and G. Tarcy, Eds., Springer, Cham, 2016, pp. 936–941. DOI: 10.1007/978-3-319-48156-2_138.

[53]   M. L. Slaugenhaupt, J. N. Bruggeman, G. P. Tarcy, and N. R. Dando, "Effect of open holes in the crust on gaseous fluoride evolution from pots," in *Essential Readings in Light Metals: Volume 2 Aluminum Reduction Technology*, G. Bearne, M. Dupuis, and G. Tarcy, Eds., Springer, Cham, 2016, pp. 930–935. DOI: 10.1007/978-3-319-48156-2_137.

[54]   C. Sommerseth, K. S. Osen, T. A. Aarhaug, E. Skybakmoen, A. Solheim, C. Rosenkilde, and A. P. Ratvik, "Correlation between moisture and HF formation in the aluminium process," in *Light Metals 2011*, John Wiley & Sons, Ltd, 2011, pp. 339–344. DOI: 10.1002/9781118061992.ch61.

[55] E. C. Patterson, "Fluoride emissions from aluminium electrolysis cells," Ph.D. dissertation, The University of Auckland, Auckland, 2002.

[56] K. S. Osen, T. A. Aarhaug, A. Solheim, E. Skybakmoen, and C. Sommerseth, "HF measurements inside an aluminium electrolysis cell," in *Light Metals 2011*, S. J. Lindsay, Ed., Springer, Cham, 2011, pp. 263–268. DOI: 10.1007/978-3-319-48160-9_47.

[57] N. E. Richards, S. Rolseth, J. Thonstad, and R. G. Haverkamp, "Electrochemical analysis of alumina dissolved in cryolite melts," in *Light Metals 1995*, J. W. Evans, Ed., Warrendale, Pa.: Minerals, Metals & Materials Society, 1995, pp. 391–404.

[58] D. W. Townsend and L. G. Boxall, "Crusting behavior of smelter aluminas," in *Essential Readings in Light Metals: Volume 2 Aluminum Reduction Technology*, G. Bearne, M. Dupuis, and G. Tarcy, Eds., Springer, 2016, pp. 613–621. DOI: 10.1007/978-3-319-48156-2_91.

[59] C. Kaszás, L. Kiss, S. Poncsák, S. Guérard, and J.-F. Bilodeau, "Spreading of alumina and raft formation on the surface of cryolitic bath," in *Light Metals 2017*, A. P. Ratvik, Ed., ser. The Minerals, Metals & Materials Series, Springer, Cham, 2017, pp. 473–478. DOI: 10.1007/978-3-319-51541-0_59.

[60] R. G. Haverkamp, "Surface studies and dissolution studies of fluorinated alumina," Ph.D. dissertation, The University of Auckland, Auckland, 1992. (visited on 07/08/2019).

[61] W. E. Haupin and W. C. McGrew, "See-through hall-heroult cell," in *Essential Readings in Light Metals*, G. Bearne, M. Dupuis, and G. Tarcy, Eds., Hoboken, NJ, USA: John Wiley & Sons, Inc., Apr. 8, 2013, pp. 234–239. DOI: 10.1002/9781118647851.ch34.

[62] Y. Yang, B. Gao, Z. Wang, Z. Shi, and X. Hu, "The formation and dissolution of crust upon alumina addition into cryolite electrolyte," *JOM*, vol. 67, no. 9, pp. 2170–2180, Sep. 2015. DOI: 10.1007/s11837-015-1525-2.

[63] D. Walker, T. Utigard, J. Toguri, and M. Taylor, "Behaviour of alumina powder agglomerates upon addition to cryolite-based electrolytes," in *Advances in Production and Fabrication of Light Metals and Metal Matrix Composites;*, Edmonton, Alberta, Canada, Aug. 1992, pp. 23–37.

[64] C. Kaszás, L. I. Kiss, S. Poncsák, J.-F. Bilodeau, and S. Guérard, "Flotation and infiltration of artificial rafts on the surface of molten cryolite," in *Proceedings of 34th International ICSOBA Conference*, Quebec, Canada, 2017.

[65] C. Kaszás, L. I. Kiss, S. Poncsak, S. Guerard, J. Alarie, and T. Roger, "Flotation of alumina on the surface of the electrolyte in an aluminum electrolysis cell," *Metall and Materi Trans B*, May 4, 2020. DOI: 10.1007/s11663-020-01836-6.

[66] S. Poncsák, L. Rakotondramanana, L. I. Kiss, T. Roger, S. Guérard, and J.-F. Bilodeau, "Evolution of mechanical resistance of alumina raft exposed to the bath in hall-héroult cells," in *Light Metals 2019*, C. Chesonis, Ed., ser. The Minerals, Metals & Materials Series, Springer, Cham, 2019, pp. 667–673. DOI: 10.1007/978-3-030-05864-7_82.

[67] J. Alarie, T. Roger, L. I. Kiss, S. Poncsák, S. Guérard, and J.-F. Bilodeau, "Validation of the gravimetric method to properly follow alumina dissolution in cryolitic bath," in *Light Metals 2020*, A. Tomsett, Ed., ser. The Minerals, Metals & Materials Series, Springer, Cham, 2020, pp. 680–687. DOI: 10.1007/978-3-030-36408-3_92.

[68] J. Alarie, L. I. Kiss, S. Poncsák, R. Santerre, S. Guérard, and J.-F. Bilodeau, "Influence of additives on alumina dissolution in superheated cryolite melts," in *Light Metals 2021*, L. Perander, Ed., ser. The Minerals, Metals & Materials Series, Springer, Cham, 2021, pp. 533–540. DOI: 10.1007/978-3-030-65396-5_75.

[69] L. Bracamonte, K. E. Einarsrud, C. Rosenkilde, and E. Sandnes, "Oxide sensor measurements and simultaneous optical observations during dissolution of alumina in cryolite melt," in *Light Metals 2022*, D. Eskin, Ed., ser. The Minerals, Metals & Materials Series, Springer, Cham, 2022, pp. 381–391. DOI: 10.1007/978-3-030-92529-1_52.

[70] A. Bagshaw, G. I. Kuschel, M. P. Taylor, S. Tricklebank, and B. J. Welch, "Effect of operating conditions on the dissolution of primary and secondary (reacted) alumina powders in electrolytes," in *Light Metals 1985*, H. Bohner, Ed., The Metallurgical Society of AIME, 1985, pp. 649–659.

[71] J. Gerlach, U. Hennig, and K. Kern, "The dissolution of aluminum oxide in cryolite melts," *Metall Mater Trans B*, vol. 6, no. 1, pp. 83–86, Mar. 1, 1975. DOI: 10.1007/BF02825681.

[72] R. Hovland, S. Rolseth, and A. Solheim, "On the alumina dissolution in cryolitic melts," presented at the Proc. of the Intl. Symp. on Light Metals Processing and Applications, Quebec, Aug. 29, 1993, pp. 3–16.

[73] R. K. Jain, S. Tricklebank, B. J. Welch, and D. J. Williams, "Interaction of aluminas with aluminum smelting electrolytes," in *Light Metals 1983*, E. M. Adkins, Ed., The Metallurgical Society of AIME, 1983, pp. 609–622.

[74] G. I. Kuschel and B. J. Welch, "Effect of alumina properties and operation of smeltin cells on the dissolution behavior of alumina," in *Porceedings of the Second International Alumina Quality Workshop*, Perth, 1990, pp. 58–70.

[75] O. Kobbeltvedt, "Dissolution kinetics for alumina in cryolite melts : Distribution of alumina in the electrolyte of industrial aluminium cells," Ph.D. dissertation,

Norwegian University of Science and Technology, Department of Electrochemistry, Trondheim, 1997.

[76] S. Rolseth, R. Hovland, and O. Kobbeltvedt, "Alumina agglomeration and dissolution in cryolitic melts," in *Light Metals 1994*, U. Mannweiler, Ed., 1994, pp. 351–357.

[77] K. Rye, S. Rolseth, J. Thonstad, and K. Zhanling, "Behavior of alumina on addition to cryolitic baths," in *Porceedings of the Second International Alumina Quality Workshop*, Perth, 1990, pp. 24–38.

[78] N. V. Vasyunina, I. P. Vasyunina, Y. G. Mikhalev, and A. M. Vinogradov, "The solubility and dissolution rate of alumina in acidic cryolite aluminous melts," *Russ. J. Non-ferrous Metals*, vol. 50, no. 4, pp. 338–342, Aug. 1, 2009. DOI: 10.3103/S1067821209040051.

[79] Y. Yang, B. Gao, Z. Wang, Z. Shi, and X. Hu, "Effect of physiochemical properties and bath chemistry on alumina dissolution rate in cryolite electrolyte," *JOM*, vol. 67, no. 5, pp. 973–983, May 1, 2015. DOI: 10.1007/s11837-015-1379-7.

[80] A. N. Bagshaw and B. J. Welch, "The influence of alumina properties on its dissolution in smelting electrolyte," in *Essential Readings in Light Metals: Volume 1 Alumina and Bauxite*, D. Donaldson and B. E. Raahauge, Eds., Cham: Springer, Cham, 2016, pp. 783–787. DOI: 10.1007/978-3-319-48176-0_107.

[81] L. Bracamonte, V. Aulie, C. Rosenkilde, K. E. Einarsrud, and E. Sandnes, "Dissolution characteristics and concentration measurements of alumina in cryolite melts," in *Light Metals 2021*, L. Perander, Ed., ser. The Minerals, Metals & Materials Series, Springer, Cham, 2021, pp. 495–503. DOI: 10.1007/978-3-030-65396-5_70.

[82] L. Bracamonte, "Development of an electrochemical sensor for alumina concentration measurements and dissolution characteristics of alumina in cryolite melt.," Ph.D. dissertation, Nowegian University of Science and Technology, Trondheim, 2022.

[83] R. G. Haverkamp, B. J. Welch, and J. B. Metson, "The influence of fluorination on the dissolution rate of alumina in smelter electrolyte," in *Light Metals*, Warrendale, Pa: TMS, 1994, pp. 365–370.

[84] L. A. Isaeva, A. B. Braslavskii, and P. V. Polyakov, "Effect of the content of the alpha-phase and granulometric composition on the dissolution rate of alumina in cryolite-alumina melts," *Russian Journal of Non-Ferrous Metals*, vol. 50, no. 6, pp. 600–605, Dec. 1, 2009. DOI: 10.3103/S1067821209060078.

[85] C. Kaszás, "Behaviour of alumina powder fed into molten electrolytic bath," Ph.D. dissertation, Université du Québec à Chicoutimi, Chicoutimi, 2020, 162 pp.

[Online]. Available: `https://constellation.uqac.ca/6373/` (visited on 02/22/2022).

[86]   M. Kheiri, U. Hennig, and R. Kammel, "Krustenbildung und krustenigenschaften beim einsatz sekundärer aluminiumoxide für die aluminium-reduktionselektrolyse," *Metall*, vol. 43, no. 9, pp. 858–862, 1989.

[87]   M. Kheiri, J. Gerlach, U. Hennig, and R. Kammel, "Bildung und verhalten von krusten sowie bodenschlamm bei der aluminium-reduktionselektrolyse," *Erzmetall*, vol. 40, no. 3, pp. 127–131, 1987.

[88]   X. Liu, S. F. George, and V. A. Wills, "Visualisation of alumina dissolution in cryolitic melts," in *Light Metals 1994*, U. Mannweiler, Ed., 1994, pp. 359–359.

[89]   C. Sommerseth, K. S. Osen, C. Rosenkilde, A. J. Meyer, L. T. Kristiansen, and T. A. Aarhaug, "A method for comparing the HF formation potential of aluminas with different water contents," in *Light Metals 2012*, C. E. Suarez, Ed., Springer, Cham, 2012, pp. 827–832. DOI: `10.1007/978-3-319-48179-1_143`.

[90]   Y. Yang, B. Gao, Z. Wang, Z. Shi, and X. Hu, "Mechanism of dissolution behavior of the secondary alumina," *Metallurgical and Materials Transactions B: Process Metallurgy and Materials Processing Science*, vol. 44, no. 5, pp. 1296–1303, 2013. DOI: `10.1007/s11663-013-9901-1`.

[91]   Y. Yang, B. Gao, Z. Wang, Z. Shi, X. Hu, and J. Yu, "Dispersion caused by carbon dioxide during secondary alumina dissolution: A lab-scale research," *Metall Mater Trans B*, vol. 45, no. 3, pp. 1150–1156, Jun. 1, 2014. DOI: `10.1007/s11663-014-0065-4`.

[92]   Y. Yang, B. Gao, X. Hu, Z. Wang, and Z. Shi, "Influence of LOI on alumina dissolution in molten aluminum electrolyte," in *Molten Salts Chemistry and Technology*, John Wiley & Sons, Ltd, 2014, pp. 77–83. DOI: `10.1002/9781118448847.ch1h`.

[93]   J. Alarie, L. I. Kiss, L. Dion, M. Truchon, R. Santerre, S. Guérard, and J.-F. Bilodeau, "Empirical prediction of alumina dissolution rate in a cryolitic melt: Comparison with the existing literature," in *Light Metals 2022*, D. Eskin, Ed., ser. The Minerals, Metals & Materials Series, Springer, Cham, 2022, pp. 349–356. DOI: `10.1007/978-3-030-92529-1_48`.

[94]   D. C. Chesonis and A. F. LaCamera, "The influence of gas-driven circulation on alumina distribution and interface motion in a hall-heroult cell," in *Light metals 1990*, C. Bickert, Ed., vol. 1990, TMS, 1990, pp. 211–220.

[95]   M. A. Cooksey and W. W. Yang, "PIV measurement on physical models of aluminium reduction cells," in *Light Metals 2006*, T. J. Galloway, Ed., TMS, 2006, pp. 359–365.

[96] Y. Feng, W. Yang, M. Cooksey, and M. Schwarz, "Development of bubble driven flow CFD model applied for aluminium smelting cells," *The Journal of Computational Multiphase Flows*, vol. 2, no. 3, pp. 179–188, Sep. 1, 2010. DOI: 10.1260/1757-482X.2.3.179.

[97] L. Rakotondramanana, L. I. Kiss, S. Poncsák, R. Santerre, S. Guerard, J.-F. Bilodeau, and S. Richer, "Mass transport by waves: Bath-metal interface deformation, rafts collision and physical model," in *Light Metals 2021*, L. Perander, Ed., ser. The Minerals, Metals & Materials Series, Springer, Cham, 2021, pp. 344–350. DOI: 10.1007/978-3-030-65396-5_50.

[98] T. Roger, L. Kiss, L. Dion, S. Guérard, J. F. Bilodeau, G. Bonneau, R. Santerre, and K. Fraser, "Modeling of the heat exchange, the phase change, and dissolution of alumina injected in electrolysis cells," in *Light Metals 2022*, D. Eskin, Ed., ser. The Minerals, Metals & Materials Series, Springer, Cham, 2022, pp. 363–370. DOI: 10.1007/978-3-030-92529-1_50.

[99] T. Roger, K. Fraser, L. Kiss, S. Poncsák, S. Guérard, J. F. Bilodeau, and G. Bonneau, "Development of a mathematical model to simulate raft formation," in *Light Metals 2020*, A. Tomsett, Ed., ser. The Minerals, Metals & Materials Series, Springer, Cham, 2020, pp. 688–695. DOI: 10.1007/978-3-030-36408-3_93.

[100] A. Bouvais, L. Dion, T. Roger, L. Kiss, G. Bonneau, F. Bilodeau, and S. Guerard, "Experimental study and visualization of the thermal and dissolution flux using schlieren methods to improve the understanding of the kinetics of alumina dissolution in cryolitic melts," in *Proceedings of 39th International ICSOBA Conference*, Virtual: The International Committee for Study of Bauxite, Alumina & Aluminium, 2021, p. 14.

[101] A. Kovács, C. Breward, K. Einarsrud, S. Halvorsen, E. Nordgård-Hansen, E. Manger, A. Münch, and J. Oliver, "A heat and mass transfer problem for the dissolution of an alumina particle in a cryolite bath," *International Journal of Heat and Mass Transfer*, vol. 162, p. 120 232, Dec. 2020. DOI: 10.1016/j.ijheatmasstransfer.2020.120232.

[102] A. Kovács, "Modelling the feeding process for aluminium production," Ph.D. dissertation, University of Oxford, Oxford, 2021. [Online]. Available: https://ora.ox.ac.uk/objects/uuid:a90128d2-6841-4347-9c78-d3f9ba770177 (visited on 08/03/2022).

[103] V. Dassylva-Raymond, L. I. Kiss, S. Poncsak, P. Chartrand, J.-F. Bilodeau, and S. Guérard, "Modeling the behavior of alumina agglomerate in the hall-héroult process," in *Light Metals 2014*, J. Grandfield, Ed., Hoboken, Wiley, 2014, pp. 603–608. DOI: 10.1007/978-3-319-48144-9_102.

[104] C. Kaszás, L. Kiss, S. Guérard, and J.-F. Bilodeau, "Behavior of powders on the surface of a liquid," in *Light Metals 2015*, M. Hyland, Ed., Springer, Cham, 2015, pp. 639–642. DOI: 10.1007/978-3-319-48248-4_107.

[105] B. Bardet, T. Foetisch, S. Renaudier, J. Rappaz, M. Flueck, and M. Picasso, "Alumina dissolution modeling in aluminium electrolysis cell considering MHD driven convection and thermal impact," in *Light Metals 2016*, E. Williams, Ed., 2016, pp. 315–319. DOI: 10.1007/978-3-319-48251-4_52.

[106] V. Bojarevics, "Dynamic modelling of alumina feeding in an aluminium electrolysis cell," in *Light Metals 2019*, C. Chesonis, Ed., ser. The Minerals, Metals & Materials Series, Springer, Cham, 2019, pp. 675–682. DOI: 10.1007/978-3-030-05864-7_83.

[107] V. Bojarevics, "In-line cell position and anode change effects on the alumina dissolution," in *Light Metals 2021*, L. Perander, Ed., Springer, Cham, 2021, pp. 584–590. DOI: 10.1007/978-3-030-65396-5_80.

[108] V. Bojarevics and M. Dupuis, "Advanced alumina dissolution modelling," in *Light Metals 2022*, D. Eskin, Ed., ser. The Minerals, Metals & Materials Series, Springer, Cham, 2022, pp. 339–348. DOI: 10.1007/978-3-030-92529-1_47.

[109] L. Dion, L. I. Kiss, S. Poncsák, and C.-L. Lagacé, "Simulator of non-homogenous alumina and current distribution in an aluminum electrolysis cell to predict low-voltage anode effects," *Metall and Materi Trans B*, vol. 49, no. 2, pp. 737–755, Apr. 1, 2018. DOI: 10.1007/s11663-018-1174-2.

[110] K. E. Einarsrud, S. E. Gylver, and E. Manger, "CFD modelling of alumina feeding," in *Light Metals 2018*, O. Martin, Ed., ser. The Minerals, Metals & Materials Series, Springer, Cham, 2018, pp. 557–564. DOI: 10.1007/978-3-319-72284-9_73.

[111] S. T. Johansen, K. E. Einarsrud, A. Solheim, and K. J. Vachaparambil, "A pragmatic model for alumina feeding," in *Light Metals 2022*, D. Eskin, Ed., ser. The Minerals, Metals & Materials Series, Springer, Cham, 2022, pp. 503–511. DOI: 10.1007/978-3-030-92529-1_67.

[112] X. Liu, Y. Yang, Z. Wang, W. Tao, T. Li, and Z. Zhao, "CFD modeling of alumina diffusion and distribution in aluminum smelting cells," *JOM*, vol. 71, no. 2, pp. 764–771, Feb. 1, 2019. DOI: 10.1007/s11837-018-3260-y.

[113] L. Rakotondramanana, L. I. Kiss, S. Poncsák, S. Guérard, and J.-F. Bilodeau, "Mass transport by waves on the bath metal interface in electrolysis cell," in *Light Metals 2020*, A. Tomsett, Ed., ser. The Minerals, Metals & Materials Series, Springer, Cham, 2020, pp. 510–516. DOI: 10.1007/978-3-030-36408-3_71.

[114] T. Richer, L. Dion, L. I. Kiss, S. Guérard, J.-F. Bilodeau, and L. Rakotondramanana, "Mass transport by waves: Physical model with coalescence, fragmentation, and

displacement on a bath-metal interface," in *Light Metals 2022*, D. Eskin, Ed., ser. The Minerals, Metals & Materials Series, Cham: Springer, Cham, 2022, pp. 371–380. DOI: 10.1007/978-3-030-92529-1_51.

[115]   T. Roger, L. Kiss, K. Fraser, S. Poncsák, S. Guérard, and J.-F. Bilodeau, "Development of a mathematical model to follow alumina injection," in *Light Metals 2019*, C. Chesonis, Ed., ser. The Minerals, Metals & Materials Series, Springer, Cham, 2019, pp. 683–688. DOI: 10.1007/978-3-030-05864-7_84.

[116]   T. Roger, K. Fraser, L. Kiss, S. Poncsák, S. Guérard, J. F. Bilodeau, G. Bonneau, and R. Santerre, "Coupled SPH-DEM to simulate the injection of a powder into a liquid with heat transfer and phase change," in *Light Metals 2021*, L. Perander, Ed., ser. The Minerals, Metals & Materials Series, Springer, Cham, 2021, pp. 368–376. DOI: 10.1007/978-3-030-65396-5_53.

[117]   S. Zhan, M. Li, J. Zhou, J. Yang, and Y. Zhou, "CFD simulation of dissolution process of alumina in an aluminum reduction cell with two-particle phase population balance model," *Applied Thermal Engineering*, vol. 73, no. 1, pp. 805–818, Dec. 2014. DOI: 10.1016/j.applthermaleng.2014.08.040.

[118]   S.-q. Zhan, M.-m. Jiang, J.-f. Wang, and J.-h. Yang, "Improved CFD modeling of full dissolution of alumina particles in aluminum electrolysis cells considering agglomerate formation," *Transactions of Nonferrous Metals Society of China*, vol. 31, no. 11, pp. 3579–3590, Nov. 1, 2021. DOI: 10.1016/S1003-6326(21)65749-7.

[119]   H. Zhang, S. Yang, H. Zhang, J. Li, and Y. Xu, "Numerical simulation of alumina-mixing process with a multicomponent flow model coupled with electromagnetic forces in aluminum reduction cells," *JOM*, vol. 66, no. 7, pp. 1210–1217, Jul. 1, 2014. DOI: 10.1007/s11837-014-1020-1.

[120]   V. Bojarevics and K. Pericleous, "Shallow water model for aluminium electrolysis cells with variable top and bottom," in *Light Metals 2008*, vol. 2, Warrendale, Pa: TMS, 2008, p. 403.

[121]   Neo Monitors. (). "LaserGas II SP – neo monitors," [Online]. Available: https://neomonitors.com/lasergas-ii-sp/ (visited on 05/03/2022).

[122]   X. Wang, B. Hosler, and G. Tarcy, "Alcoa STARprobe™," in *Light Metals 2011*, S. J. Lindsay, Ed., Springer, Cham, 2016, pp. 483–489. DOI: 10.1007/978-3-319-48160-9_86.

[123]   (). "Norsk klimaservicesenter," [Online]. Available: https://seklima.met.no/observations/ (visited on 08/09/2020).

[124]   S. E. Gylver, S. Aase, S. Bekkevoll, S. A. K. Forberg, and K. E. Einarsrud, "A water model study of alumina feeding and dispersion," in *Light Metals 2022*, D. Eskin,

Ed., ser. The Minerals, Metals & Materials Series, Springer,Cham, 2022, pp. 357–362. DOI: 10.1007/978-3-030-92529-1_49.

[125] S. E. Gylver, A. Solheim, H. Gudbrandsen, Å. H. Follo, and K. E. Einarsrud, "Lab scale experiments on alumina raft formation," in *Light Metals 2020*, A. Tomsett, Ed., ser. The Minerals, Metals & Materials Series, Springer, Cham, 2020. DOI: 10.1007/978-3-030-36408-3_89.

[126] A. Solheim, S. Rolseth, E. Skybakmoen, L. Støen, Å. Sterten, and T. Støre, "Liquidus temperatures for primary crystallization of cryolite in molten salt systems of interest for aluminum electrolysis," *Metall and Materi Trans B*, vol. 27, no. 5, p. 739, Oct. 1, 1996. DOI: 10.1007/BF02915602.

[127] T. Holzmann, *Mathematics, Numerics, Derivations and OpenFOAM®*. Holzmann CFD, 2016.

[128] R. B. Bird, *Transport phenomena*, 2nd ed., in collab. with W. E. Stewart and E. N. Lightfoot. New York: Wiley, 2002, XII, 895.

[129] D. A. Drew and S. L. Passman, *Theory of Multicomponent Fluids*, red. by J. E. Marsden and L. Sirovich, ser. Applied Mathematical Sciences. New York, NY: Springer, 1999, vol. 135. DOI: 10.1007/b97678.

[130] C. W. Hirt and B. D. Nichols, "Volume of fluid (VOF) method for the dynamics of free boundaries," *Journal of Computational Physics*, vol. 39, no. 1, pp. 201–225, Jan. 1, 1981. DOI: 10.1016/0021-9991(81)90145-5.

[131] S. S. Deshpande, L. Anumolu, and M. F. Trujillo, "Evaluating the performance of the two-phase flow solver interFoam," *Comput. Sci. Disc.*, vol. 5, no. 1, p. 014 016, Nov. 2012. DOI: 10.1088/1749-4699/5/1/014016.

[132] J. U. Brackbill, D. B. Kothe, and C. Zemach, "A continuum method for modeling surface tension," *Journal of Computational Physics*, vol. 100, no. 2, pp. 335–354, Jun. 1, 1992. DOI: 10.1016/0021-9991(92)90240-Y.

[133] V. R. Voller, M. Cross, and N. C. Markatos, "An enthalpy method for convection/diffusion phase change," *International Journal for Numerical Methods in Engineering*, vol. 24, no. 1, pp. 271–284, 1987. DOI: 10.1002/nme.1620240119.

[134] V. R. Voller and C. Prakash, "A fixed grid numerical modelling methodology for convection-diffusion mushy region phase-change problems," *International Journal of Heat and Mass Transfer*, vol. 30, no. 8, pp. 1709–1719, Aug. 1, 1987. DOI: 10.1016/0017-9310(87)90317-6.

[135] C. R. Swaminathan and V. R. Voller, "A general enthalpy method for modeling solidification processes," *MTB*, vol. 23, no. 5, pp. 651–664, Oct. 1, 1992. DOI: 10.1007/BF02649725.

[136] M. Torabi Rad, "solidificationMeltingSource: A built-in fvOption in OpenFOAM® for simulating isothermal solidification," in *OpenFOAM® : Selected Papers of the*

11th Workshop, J. M. Nóbrega and H. Jasak, Eds., Springer, Cham, 2019, pp. 455–464. DOI: 10.1007/978-3-319-60846-4_32.

[137]   P. Jop, Y. Forterre, and O. Pouliquen, "A constitutive law for dense granular flows," *Nature*, vol. 441, no. 7094, pp. 727–730, Jun. 2006. DOI: 10.1038/nature04801.

[138]   D. Gidaspow, *Multiphase flow and fluidization: continuum and kinetic theory descriptions*. San Diego: Academic press, 1994.

[139]   GDR MiDi, "On dense granular flows," *Eur. Phys. J. E*, vol. 14, no. 4, pp. 341–365, Aug. 1, 2004. DOI: 10.1140/epje/i2003-10153-0.

[140]   T. Barker and J. M. N. T. Gray, "Partial regularisation of the incompressible mu(i)-rheology for granular flow," *Journal of Fluid Mechanics*, vol. 828, pp. 5–32, Oct. 2017, Publisher: Cambridge University Press. DOI: 10.1017/jfm.2017.428.

[141]   U. Ayachit, *The ParaView Guide: A Parallel Visualization Application*. Clifton Park, NY, USA: Kitware, Inc., 2015, 276 pp., ISBN: 978-1-930934-30-6.

[142]   The OpenFOAM Foundation. (). "OpenFOAM," [Online]. Available: https://openfoam.org/ (visited on 03/17/2022).

[143]   A. Jarosch, *Incompressible mu(i) rheology for OpenFOAM*, original-date: 2021-03-18T12:13:26Z, Jun. 16, 2022. DOI: 10.5281/zenodo.4964189. [Online]. Available: https://github.com/alexjarosch/OpenFOAM-muI (visited on 06/21/2022).

[144]   P.-Y. Lagrée, L. Staron, and S. Popinet, "The granular column collapse as a continuum: Validity of a two-dimensional navier–stokes model with a mu(i)-rheology," *Journal of Fluid Mechanics*, vol. 686, pp. 378–408, Nov. 2011, Publisher: Cambridge University Press. DOI: 10.1017/jfm.2011.335.

[145]   V. Alexiades and A. D. Solomon, *Mathematical Modeling of Melting and Freezing Processes*, 1st ed. Washington, DC: CRC Press, 1993. DOI: 10.1201/9780203749449.

[146]   P. Jop, Y. Forterre, and O. Pouliquen, "Crucial role of sidewalls in granular surface flows: Consequences for the rheology," *J. Fluid Mech.*, vol. 541, no. -1, p. 167, Oct. 11, 2005. DOI: 10.1017/S0022112005005987.

[147]   S. E. Gylver, Å. H. Follo, V. Aulie, H. M. Granlund, A. Sørhuus, E. Sandnes, and K. E. Einarsrud, "On gaseous emissions during alumina feeding," in *Light Metals 2021*, L. Perander, Ed., ser. The Minerals, Metals & Materials Series, Springer, Cham, 2021, pp. 504–510. DOI: 10.1007/978-3-030-65396-5_71.

[148]   S. E. Gylver, S. Bekkevoll, S. Rørvik, and K. E. Einarsrud, "The formation and disintegration of rafts from different aluminas and fines," *Metals*, vol. 12, no. 11, p. 1876, Nov. 2022. DOI: 10.3390/met12111876. [Online]. Available: https://www.mdpi.com/2075-4701/12/11/1876 (visited on 11/05/2022).

[149]   B. J. Welch and G. I. Kuschel, "Crust and alumina powder dissolution in aluminum smelting electrolytes," *Journal of Metals*, vol. 59, no. 5, pp. 50–54, 2007. DOI: 10.1007/s11837-007-0065-9.

[150] C. A. Schneider, W. S. Rasband, and K. W. Eliceiri, "NIH image to ImageJ: 25 years of image analysis," *Nature Methods*, vol. 9, no. 7, pp. 671–675, Jul. 1, 2012, ISSN: 1548-7105. DOI: 10.1038/nmeth.2089.

[151] Alcoa Mosjøen, *Personal communication*, Email, Sep. 20, 2022.

[152] C. Greenshields, *OpenFOAM v8 User Guide*. London, UK: The OpenFOAM Foundation, 2020. [Online]. Available: https://doc.cfd.direct/openfoam/user-guide-v8.

Appendix A: Source code

This appendix displays parts of the code that is added to the mixture equation in order to create the temperature equation. Further, the complete source code for the solidification model and the μ(I)-rheology are displayed.

A.1 Implementation of the temperature equation

This part is limited to show only how the mixture model in multiphaseInterFOAM is edited, where phase averaged values of κ and c_p are declared defined. How it is implemented in the energy equation is already demonstrated in listing 10.1. The rest of the source code is available at OpenFOAM.org[12]

Listing A.1: Part of the code displaying how the thermal properties are declared. It is added from line 251 in the orginal source code[1].

```
1    //- Return the heat conductivity
2   tmp<volScalarField> kappa() const;
3
4   //- Return the conductivity for patch
5   tmp<scalarField> kappa(const label patchi) const;
6
7   //- Return the face-interpolated dynamic thermal conductivity
8   tmp<surfaceScalarField> kappaf() const;
9
10   //- Return the heat capacity
11   tmp<volScalarField> cp() const;
12
13   //- Return the capacity for patch
14   tmp<scalarField> cp(const label patchi) const;
15
16   //- Return the face-interpolated dynamic thermal conductivity
17   tmp<surfaceScalarField> cpf() const;
```

Listing A.2: Part of the code displaying how the thermal properties are defined. It is added from line 246 in the orginal source code[2].

```
1    Foam::tmp<Foam::volScalarField>
2   Foam::multiphaseTempMixture::kappa() const
3   {
4     PtrDictionary<phase>::const_iterator iter = phases_.begin();
5
6     tmp<volScalarField> tkappa = iter()*iter().kappa();
7     volScalarField& kappa = tkappa.ref();
8
9     for (++iter; iter != phases_.end(); ++iter)
10     {
11       kappa +=iter()*iter().kappa();
12     }
13
14     return tkappa;
15   }
16
```

---

[1]https://cpp.openfoam.org/v8/multiphaseMixture_8H_source.html
[2]https://cpp.openfoam.org/v8/multiphaseMixture_8C_source.html

```
17
18   Foam::tmp<Foam::scalarField>
19   Foam::multiphaseTempMixture::kappa(const label patchi) const
20   {
21     PtrDictionary<phase>::const_iterator iter = phases_.begin();
22
23     tmp<scalarField> tkappa = iter().boundaryField()[patchi]*iter().kappa().value();
24
25     scalarField& kappa = tkappa.ref();
26
27     for (++iter; iter != phases_.end(); ++iter)
28     {
29       kappa += iter().boundaryField()[patchi]*iter().kappa().value();
30     }
31
32     return tkappa;
33   }
34
35
36   Foam::tmp<Foam::surfaceScalarField>
37   Foam::multiphaseTempMixture::kappaf() const
38   {
39     PtrDictionary<phase>::const_iterator iter = phases_.begin();
40
41     tmp<surfaceScalarField> tkappaf =
42     fvc::interpolate(iter())*iter().kappa();
43     surfaceScalarField& kappaf = tkappaf.ref();
44
45     for (++iter; iter != phases_.end(); ++iter)
46     {
47       kappaf +=
48       fvc::interpolate(iter())*iter().kappa();
49     }
50
51     return tkappaf;
52   }
53
54   Foam::tmp<Foam::volScalarField>
55   Foam::multiphaseTempMixture::cp() const
56   {
57     PtrDictionary<phase>::const_iterator iter = phases_.begin();
58
59     tmp<volScalarField> tcp = iter()*iter().cp();
60     volScalarField& cp = tcp.ref();
61
62     for (++iter; iter != phases_.end(); ++iter)
63     {
64       cp += iter()*iter().cp();
65     }
66
67     return tcp;
68   }
69
70
71   Foam::tmp<Foam::scalarField>
72   Foam::multiphaseTempMixture::cp(const label patchi) const
73   {
74     PtrDictionary<phase>::const_iterator iter = phases_.begin();
75
76     tmp<scalarField> tcp = iter().boundaryField()[patchi]*iter().cp().value();
77     scalarField& cp = tcp.ref();
78
79     for (++iter; iter != phases_.end(); ++iter)
80     {
81       cp += iter().boundaryField()[patchi]*iter().cp().value();
82     }
83
84     return tcp;
85   }
86
87   Foam::tmp<Foam::surfaceScalarField>
88   Foam::multiphaseTempMixture::cpf() const
89   {
90     PtrDictionary<phase>::const_iterator iter = phases_.begin();
91
```

```
92      tmp<surfaceScalarField> tcpf =
93      fvc::interpolate(iter())*iter().cp();
94      surfaceScalarField& cpf = tcpf.ref();
95
96      for (++iter; iter != phases_.end(); ++iter)
97      {
98        cpf +=
99        fvc::interpolate(iter())*iter().cp();
100     }
101
102     return tcpf;
103   }
```

A.2 Solidification-melting model

The model consists of four files: The first one declares the model and all the parameters used. Listing A.4 display most of the definitions, except from reading of coefficient and addition to the energy source term, displayed in listings A.5 and A.6, respectively.

Listing A.3: Declaration of the solidification class

```
1   /*---------------------------------------------------------------------------*\
2     =========                 |
3     \\      /  F ield          | OpenFOAM: The Open Source CFD Toolbox
4      \\    /   O peration      | Website:  https://openfoam.org
5       \\  /    A nd            | Copyright (C) 2017-2018 OpenFOAM Foundation
6        \\/     M anipulation   |
7   -----------------------------------------------------------------------------
8   License
9     This file is part of OpenFOAM.
10
11    OpenFOAM is free software: you can redistribute it and/or modify it
12    under the terms of the GNU General Public License as published by
13    the Free Software Foundation, either version 3 of the License, or
14    (at your option) any later version.
15
16    OpenFOAM is distributed in the hope that it will be useful, but WITHOUT
17    ANY WARRANTY; without even the implied warranty of MERCHANTABILITY or
18    FITNESS FOR A PARTICULAR PURPOSE.  See the GNU General Public License
19    for more details.
20
21    You should have received a copy of the GNU General Public License
22    along with OpenFOAM.  If not, see <http://www.gnu.org/licenses/>.
23
24  Class
25    Foam::fv::multiVOFSolidificationMelting
26
27  Description
28    Solidification and melting model for VoF simulations.
29
30  See also
31    Foam::fv::solidificationMeltingSource
32
33  SourceFiles
34    multiVOFSolidificationMelting.C
35    multiVOFSolidificationMeltingIO.C
36
37  \*---------------------------------------------------------------------------*/
38
39  #ifndef multiVOFSolidificationMelting_H
40  #define multiVOFSolidificationMelting_H
41
42  #include "fvMesh.H"
43  #include "volFields.H"
44  #include "cellSetOption.H"
45  #include "Function1.H"
46
47  // * * * * * * * * * * * * * * * * * * * * * * * * * * * * * * * * * * * * * * //
48
49  namespace Foam
50  {
51    namespace fv
52    {
53
54      /*---------------------------------------------------------------------------*\
55      Class multiVOFSolidificationMelting Declaration
56      \*---------------------------------------------------------------------------*/
57
58      class multiVOFSolidificationMelting
59      :
60      public cellSetOption
61      {
62          // Private data
63
64          //- Latent heat of fusion [J/kg]
```

```
65          scalar L_;
66
67          //- Phase fraction under-relaxation coefficient
68          scalar relax_;
69
70          //- Mushy region momentum sink coefficient [1/s]; default = 10^5
71          scalar Cu_;
72
73          //- Coefficient used in porosity calc - default = 0.001
74          scalar q_;
75
76          //- Solidification temperature of the Melt [K]
77          scalar Tsol_; //ADDED
78
79          //- Liquidus temperature of the Melt [K]
80          scalar Tliq_; //ADDED
81
82          //- Heat capacity [J/K mol]
83          scalar CpL_; //ADDED
84
85          // Name of the phase
86          word phaseName_;
87
88          //- Constant for viscosity term
89          scalar Cnu_; //ADDED
90
91          //- Exponential cosntant for the viscosity soruce term
92          scalar A_;
93
94          //- Solid phase fraction
95          volScalarField alphaSolid_;
96
97          //- Viscosity source added to the bath
98          volScalarField nuSource_;
99
100         //- Current time index (used for updating)
101         label curTimeIndex_;
102
103
104         // Private Member Functions
105
106         //- Return the name of the solid phase fraction
107         word alphaSolidName() const;
108
109         //- Update the model
110         void update();
111
112         //- Helper function to apply to the energy equation
113         template<class RhoFieldType>
114         void apply(const RhoFieldType& rho, fvMatrix<scalar>& eqn);
115
116         //- Disallow default bitwise copy construct
117         multiVOFSolidificationMelting(const multiVOFSolidificationMelting&);
118
119         //- Disallow default bitwise assignment
120         void operator=(const multiVOFSolidificationMelting&);
121
122
123         public:
124
125         //- Runtime type information
126         TypeName("multiVOFSolidificationMelting");
127
128
129         // Constructors
130
131         //- Construct from explicit source name and mesh
132         multiVOFSolidificationMelting
133         (
134         const word& sourceName,
135         const word& modelType,
136         const dictionary& dict,
137         const fvMesh& mesh
138         );
139
```

```
140          /*
141          // Member Functions
142          // Add explicit and implicit contributions
143          //- Add explicit contribution to enthalpy equation
144          */  virtual void addSup(fvMatrix<scalar>& eqn, const label fieldi);

146          //- Add implicit contribution to momentum equation
147          virtual void addSup(fvMatrix<vector>& eqn, const label fieldi);


150          // Add explicit and implicit contributions to compressible equation

152          //- Add explicit contribution to compressible enthalpy equation
153          virtual void addSup
154          (
155          const volScalarField& rho,
156          fvMatrix<scalar>& eqn,
157          const label fieldi
158          );

160          //- Add implicit contribution to compressible momentum equation
161          virtual void addSup
162          (
163          const volScalarField& rho,
164          fvMatrix<vector>& eqn,
165          const label fieldi
166          );


169          // IO

171          //- Read source dictionary
172          virtual bool read(const dictionary& dict);
173      };


176      // * * * * * * * * * * * * * * * * * * * * * * * * * * * * * * * * * //

178    } // End namespace fv
179 } // End namespace Foam

181 // * * * * * * * * * * * * * * * * * * * * * * * * * * * * * * * * * * * //

183 #ifdef NoRepository
184 #include "multiVOFSolidificationMeltingTemplates.C"
185 #endif

187 // * * * * * * * * * * * * * * * * * * * * * * * * * * * * * * * * * * * //

189 #endif

191 // ************************************************************************* //
```

Listing A.4: Definition of the solidification class, exlcuding reading of coeficient and addition of the energy source term

```
1    /*---------------------------------------------------------------------------*\
2    =========                 |
3    \\      /  F ield         | OpenFOAM: The Open Source CFD Toolbox
4     \\    /   O peration     | Website:  https://openfoam.org
5      \\  /    A nd           | Copyright (C) 2017-2018 OpenFOAM Foundation
6       \\/     M anipulation  |
7    -----------------------------------------------------------------------------
8    License
9    This file is part of OpenFOAM.
10
11   OpenFOAM is free software: you can redistribute it and/or modify it
12   under the terms of the GNU General Public License as published by
13   the Free Software Foundation, either version 3 of the License, or
14   (at your option) any later version.
15
16   OpenFOAM is distributed in the hope that it will be useful, but WITHOUT
17   ANY WARRANTY; without even the implied warranty of MERCHANTABILITY or
18   FITNESS FOR A PARTICULAR PURPOSE.  See the GNU General Public License
19   for more details.
20
21   You should have received a copy of the GNU General Public License
22   along with OpenFOAM.  If not, see <http://www.gnu.org/licenses/>.
23
24   \*---------------------------------------------------------------------------*/
25
26   #include "multiVOFSolidificationMelting.H"
27   #include "zeroGradientFvPatchFields.H"
28   #include "addToRunTimeSelectionTable.H"
29   #include "fvmLaplacian.H"
30
31
32   // * * * * * * * * * * * * * Static Member Functions * * * * * * * * * * * * //
33
34   namespace Foam
35   {
36     namespace fv
37     {
38       defineTypeNameAndDebug(multiVOFSolidificationMelting, 0);
39
40       addToRunTimeSelectionTable
41       (
42       option,
43       multiVOFSolidificationMelting,
44       dictionary
45       );
46     }
47   }
48
49
50   // * * * * * * * * * * * * * Private Member Functions  * * * * * * * * * * * * //
51
52   void Foam::fv::multiVOFSolidificationMelting::update()
53   {
54     if (curTimeIndex_ == mesh_.time().timeIndex())
55     {
56       return;
57     }
58
59     if (debug)
60     {
61       Info<< type() << ": " << name_
62       << " - updating solid phase fraction" << endl;
63     }
64
65     alphaSolid_.oldTime();
66     nuSource_.oldTime();
67
68     const volScalarField& TVoF = mesh_.lookupObject<volScalarField>("T");
69     const volScalarField& alphaVoF = mesh_.lookupObject<volScalarField>(phaseName_);
70
71     forAll(cells_, i)
72     {
```

```
73        const label celli = cells_[i];
74
75        const scalar alphaSolidNew =
76        alphaSolid_[celli] -relax_*(TVoF[celli]-Tsol_)*CpL_/L_;
77        alphaSolid_[celli] = min (alphaVoF[celli],max(0,alphaSolidNew));
78        nuSource_[celli] = alphaVoF[celli]*pos(Tliq_ - TVoF[celli])*Cnu_*exp((Tsol_-TVoF[celli])*pos(TVoF[celli]-
          Tsol_)*A_);//(Tsol_-TVoF[celli])*), Cnu_)*pos(Tliq_-TVoF[celli]);
79      }
80
81      alphaSolid_.correctBoundaryConditions();
82
83      curTimeIndex_ = mesh_.time().timeIndex();
84    }
85
86
87    Foam::word Foam::fv::multiVOFSolidificationMelting::alphaSolidName() const
88    {
89      const volScalarField& alphaVoF = mesh_.lookupObject<volScalarField>(phaseName_);
90
91      return IOobject::groupName(alphaVoF.name(), "solid");
92    }
93
94
95    // * * * * * * * * * * * * * * * * Constructors  * * * * * * * * * * * * * * * //
96
97    Foam::fv::multiVOFSolidificationMelting::multiVOFSolidificationMelting
98    (
99    const word& sourceName,
100   const word& modelType,
101   const dictionary& dict,
102   const fvMesh& mesh
103   )
104   :
105   cellSetOption(sourceName, modelType, dict, mesh),
106   L_(readScalar(coeffs_.lookup("L"))), //Edited
107   relax_(coeffs_.lookupOrDefault("relax", 0.9)),
108   Cu_(coeffs_.lookupOrDefault<scalar>("Cu", 100000)),
109   q_(coeffs_.lookupOrDefault("q", 0.001)),
110   Tsol_(readScalar(coeffs_.lookup("Tsol"))), //Added
111   Tliq_(readScalar(coeffs_.lookup("Tliq"))), //Added
112   CpL_(readScalar(coeffs_.lookup("CpL"))),
113   phaseName_(coeffs_.lookup<word>("phase")),
114   Cnu_(readScalar(coeffs_.lookup("Cnu"))),
115   A_(readScalar(coeffs_.lookup("A"))),
116   alphaSolid_
117     (
118     IOobject
119     (
120       alphaSolidName(),
121       mesh.time().timeName(),
122       mesh,
123       IOobject::READ_IF_PRESENT,
124       IOobject::AUTO_WRITE
125     ),
126     mesh,
127     dimensionedScalar("alpha1", dimless, 0),
128     zeroGradientFvPatchScalarField::typeName
129   ),
130   nuSource_
131   (
132     IOobject
133     (
134       "nuSource",
135       mesh.time().timeName(),
136       mesh,
137       IOobject::READ_IF_PRESENT,
138       IOobject::AUTO_WRITE
139     ),
140     mesh,
141     dimensionedScalar("nuSource", dimViscosity*dimDensity, 0),
142     zeroGradientFvPatchScalarField::typeName
143   ),
144   curTimeIndex_(-1)
145   {
146     fieldNames_.setSize(2);
```

```
147      fieldNames_[0] = "U";
148      fieldNames_[1] = "T";
149      applied_.setSize(fieldNames_.size(), false);
150    }
151
152
153    // * * * * * * * * * * * * * * * Member Functions  * * * * * * * * * * * * * * //
154
155    void Foam::fv::multiVOFSolidificationMelting::addSup
156    (
157    fvMatrix<scalar>& eqn,
158    const label fieldi
159    )
160    {
161      apply(geometricOneField(), eqn);
162    }
163
164
165    void Foam::fv::multiVOFSolidificationMelting::addSup
166    (
167    const volScalarField& rho,
168    fvMatrix<scalar>& eqn,
169    const label fieldi
170    )
171    {
172      apply(rho, eqn);
173    }
174
175
176    void Foam::fv::multiVOFSolidificationMelting::addSup
177    (
178    fvMatrix<vector>& eqn,
179    const label fieldi
180    )
181    {
182      if (debug)
183      {
184        Info<< type() << ": applying source to " << eqn.psi().name() << endl;
185      }
186
187      update();
188
189      const volVectorField& UField = mesh_.lookupObject<volVectorField>("U");
190
191      eqn += nuSource_*fvm::laplacian(UField);
192    }
193
194
195    void Foam::fv::multiVOFSolidificationMelting::addSup
196    (
197    const volScalarField& rho,
198    fvMatrix<vector>& eqn,
199    const label fieldi
200    )
201    {
202      // Momentum source uses a Boussinesq approximation - redirect
203      addSup(eqn, fieldi);
204    }
205
206
207    // ************************************************************************* //
```

Listing A.5: Lookup of the coefficient used in solidfication melting model

```
1   /*--------------------------------------------------------------------------*\
2   =========                 |
3   \\      /  F ield          | OpenFOAM: The Open Source CFD Toolbox
4    \\    /   O peration       | Website:  https://openfoam.org
5     \\  /    A nd             | Copyright (C) 2017-2018 OpenFOAM Foundation
6      \\/     M anipulation    |
7   --------------------------------------------------------------------------
8   License
9   This file is part of OpenFOAM.
10
11  OpenFOAM is free software: you can redistribute it and/or modify it
12  under the terms of the GNU General Public License as published by
13  the Free Software Foundation, either version 3 of the License, or
14  (at your option) any later version.
15
16  OpenFOAM is distributed in the hope that it will be useful, but WITHOUT
17  ANY WARRANTY; without even the implied warranty of MERCHANTABILITY or
18  FITNESS FOR A PARTICULAR PURPOSE.  See the GNU General Public License
19  for more details.
20
21  You should have received a copy of the GNU General Public License
22  along with OpenFOAM.  If not, see <http://www.gnu.org/licenses/>.
23
24  \*--------------------------------------------------------------------------*/
25
26  #include "multiVOFSolidificationMelting.H"
27
28  // * * * * * * * * * * * * Private Member Functions  * * * * * * * * * * * //
29
30  bool Foam::fv::multiVOFSolidificationMelting::read(const dictionary& dict)
31  {
32    if (cellSetOption::read(dict))
33    {
34      coeffs_.lookup("L") >> L_;
35      coeffs_.lookup("Tsol") >>Tsol_; //ADDED
36      coeffs_.lookup("Tliq") >>Tliq_; //ADDED
37      coeffs_.lookup("CpL") >> CpL_;
38      coeffs_.lookup("phase") >> phaseName_;
39      coeffs_.readIfPresent("relax", relax_);
40      coeffs_.readIfPresent("Cu", Cu_);
41      coeffs_.readIfPresent("q", q_);
42      coeffs_.lookup("Cnu") >> Cnu_;
43      coeffs_.lookup("A") >> A_;
44
45      return true;
46    }
47    else
48    {
49      return false;
50    }
51
52    return false;
53  }
54
55
56  // ************************************************************************* //
```

Listing A.6: Addition of the energy source term

```
1   /*---------------------------------------------------------------------------*\
2     =========                 |
3     \\      /  F ield         | OpenFOAM: The Open Source CFD Toolbox
4      \\    /   O peration     | Website:  https://openfoam.org
5       \\  /    A nd           | Copyright (C) 2017-2018 OpenFOAM Foundation
6        \\/     M anipulation  |
7   -----------------------------------------------------------------------------
8   License
9   This file is part of OpenFOAM.
10
11  OpenFOAM is free software: you can redistribute it and/or modify it
12  under the terms of the GNU General Public License as published by
13  the Free Software Foundation, either version 3 of the License, or
14  (at your option) any later version.
15
16  OpenFOAM is distributed in the hope that it will be useful, but WITHOUT
17  ANY WARRANTY; without even the implied warranty of MERCHANTABILITY or
18  FITNESS FOR A PARTICULAR PURPOSE.  See the GNU General Public License
19  for more details.
20
21  You should have received a copy of the GNU General Public License
22  along with OpenFOAM.  If not, see <http://www.gnu.org/licenses/>.
23
24  \*---------------------------------------------------------------------------*/
25
26  #include "fvcDdt.H"
27  // * * * * * * * * * * * * * Private Member Functions  * * * * * * * * * * * //
28
29  template<class RhoFieldType>
30  void Foam::fv::multiVOFSolidificationMelting::apply
31  (
32  const RhoFieldType& rho,
33  fvMatrix<scalar>& eqn
34  )
35  {
36    if (debug)
37    {
38      Info<< type() << ": applying source to " << eqn.psi().name() << endl;
39    }
40
41    update();
42
43    dimensionedScalar L("L", dimEnergy/dimMass, L_); //Added in order to give L dimensions
44    dimensionedScalar CpVoF("CpVOF", dimEnergy/dimMass/dimTemperature ,CpL_);
45
46    eqn += L/CpVoF*(fvc::ddt(rho, alphaSolid_));
47  }
48  // ************************************************************************* //
```

A.3 μ(I)-rheology

The current section shows the declaration and definition of the μ(I)-rheology as a viscosity model are implemented.

Listing A.7: Declaration of the viscosity model.

```
1   /*---------------------------------------------------------------------------*\
2   =========                 |
3   \\      /  F ield         | OpenFOAM: The Open Source CFD Toolbox
4    \\    /   O peration     | Website:  https://openfoam.org
5     \\  /    A nd           | Copyright (C) 2011-2018 OpenFOAM Foundation
6      \\/     M anipulation  |
7   -----------------------------------------------------------------------------
8   License
9   This file is part of OpenFOAM.
10
11  OpenFOAM is free software: you can redistribute it and/or modify it
12  under the terms of the GNU General Public License as published by
13  the Free Software Foundation, either version 3 of the License, or
14  (at your option) any later version.
15
16  OpenFOAM is distributed in the hope that it will be useful, but WITHOUT
17  ANY WARRANTY; without even the implied warranty of MERCHANTABILITY or
18  FITNESS FOR A PARTICULAR PURPOSE.  See the GNU General Public License
19  for more details.
20
21  You should have received a copy of the GNU General Public License
22  along with OpenFOAM.  If not, see <http://www.gnu.org/licenses/>.
23
24  Class
25  Foam::viscosityModels::muIMultiPhase
26
27  Description
28  Calculating viscosity based on muI approach.
29
30  SourceFiles
31  muIMultiPhase.C
32
33  \*---------------------------------------------------------------------------*/
34
35  #ifndef muIMultiPhase_H
36  #define muIMultiPhase_H
37
38  #include "viscosityModel.H"
39  #include "dimensionedScalar.H"
40  #include "volFields.H"
41  #include "fvcGrad.H"
42
43  // * * * * * * * * * * * * * * * * * * * * * * * * * * * * * * * * * * * * //
44
45  namespace Foam
46  {
47    namespace viscosityModels
48    {
49
50      /*-------------------------------------------------------------------------*\
51      Class muIMultiPhase Declaration
52      \*-------------------------------------------------------------------------*/
53
54      class muIMultiPhase
55      :
56      public viscosityModel
57      {
58        // Private data
59
60        dictionary muIMultiPhaseCoeffs_;
61
62        dimensionedScalar mu2_;
63        dimensionedScalar mu1_;
64        dimensionedScalar muinf_;
65        dimensionedScalar I0_;
66        dimensionedScalar rhos_;
```

```
67          dimensionedScalar d_;
68          dimensionedScalar Dsmall_;
69          dimensionedScalar nuMin_;
70          dimensionedScalar nuMax_;
71          dimensionedScalar rho_;
72          dimensionedScalar pMin_;
73          dimensionedScalar alphaReg_;
74          dimensionedScalar IN1_;
75          dimensionedScalar A_m_;
76
77          volScalarField nu_;
78          mutable volScalarField muI_;
79          mutable volScalarField I_;
80          mutable volScalarField SR_;
81          mutable volScalarField PmuI_;
82
83
84          // Private Member Functions
85
86          //- Calculate and return the laminar viscosity
87          tmp<volScalarField> calcNu() const;
88
89          //ADDED Calculate muI
90          tmp<volScalarField> calcmuI() const;
91
92          //ADDED Calculate I
93          tmp<volScalarField> calcI() const;
94
95          //ADDED Calculate strain
96          tmp<volScalarField> calcStrain() const;
97
98          //ADDED Calculate Pcalc
99          tmp<volScalarField> Pcalc() const;
100
101         public:
102
103         //- Runtime type information
104         TypeName("muIMultiPhase");
105
106
107         // Constructors
108
109         //- Construct from components
110         muIMultiPhase
111         (
112         const word& name,
113         const dictionary& viscosityProperties,
114         const volVectorField& U,
115         const surfaceScalarField& phi
116         );
117
118
119         //- Destructor
120         virtual ~muIMultiPhase()
121         {}
122
123
124         // Member Functions
125
126         //- Return the laminar viscosity
127         virtual tmp<volScalarField> nu() const
128         {
129           return nu_;
130         }
131
132         //- Return the laminar viscosity for patch
133         virtual tmp<scalarField> nu(const label patchi) const
134         {
135           return nu_.boundaryField()[patchi];
136         }
137
138         //- Return the friction coefficient muI
139         virtual tmp<volScalarField> muI() const
140         {
141           return muI_;
```

```
142          }
143
144          //- Return the inertial number I
145          virtual tmp<volScalarField> I() const
146          {
147            return I_;
148          }
149
150          //- Return strain
151          virtual tmp<volScalarField> SR() const
152          {
153            return SR_;
154          }
155
156          //- Return the effective pressure
157          virtual tmp<volScalarField> PmuI() const
158          {
159            return PmuI_;
160          }
161
162          //- Correct the values
163          virtual void correct()
164          {
165            initRegParameter();
166            PmuI_ = Pcalc();
167            SR_ = calcStrain();
168            I_=calcI();
169            muI_ = calcmuI();
170            nu_ = calcNu();
171          }
172
173
174
175          //- Read transportProperties dictionary
176          virtual bool read(const dictionary& viscosityProperties);
177
178          //- Calculate the initial regularization parameters
179          virtual void initRegParameter();
180        };
181
182
183      // * * * * * * * * * * * * * * * * * * * * * * * * * * * * * * * //
184
185    } // End namespace viscosityModels
186  } // End namespace Foam
187
188  // * * * * * * * * * * * * * * * * * * * * * * * * * * * * * * * * * //
189
190  #endif
191
192  // ************************************************************************* //
193
```

Listing A.8: Definiton of the viscosity model.

```
1    /*---------------------------------------------------------------------------*\
2      =========                 |
3      \\      / F ield          | OpenFOAM: The Open Source CFD Toolbox
4       \\    /   O peration      | Website:  https://openfoam.org
5        \\  /    A nd            | Copyright (C) 2011-2018 OpenFOAM Foundation
6         \\/     M anipulation  |
7    -------------------------------------------------------------------------------
8    License
9        This file is part of OpenFOAM.
10
11       OpenFOAM is free software: you can redistribute it and/or modify it
12       under the terms of the GNU General Public License as published by
13       the Free Software Foundation, either version 3 of the License, or
14       (at your option) any later version.
15
16       OpenFOAM is distributed in the hope that it will be useful, but WITHOUT
17       ANY WARRANTY; without even the implied warranty of MERCHANTABILITY or
18       FITNESS FOR A PARTICULAR PURPOSE.  See the GNU General Public License
19       for more details.
20
21       You should have received a copy of the GNU General Public License
22       along with OpenFOAM.  If not, see <http://www.gnu.org/licenses/>.
23
24    \*---------------------------------------------------------------------------*/
25
26    #include "muIMultiPhase.H"
27    #include "addToRunTimeSelectionTable.H"
28    #include "surfaceFields.H"
29
30    // * * * * * * * * * * * * * * Static Data Members * * * * * * * * * * * * * * //
31
32    namespace Foam
33    {
34      namespace viscosityModels
35      {
36        defineTypeNameAndDebug(muIMultiPhase, 0);
37
38        addToRunTimeSelectionTable
39        (
40        viscosityModel,
41        muIMultiPhase,
42        dictionary
43        );
44      }
45    }
46
47
48    // * * * * * * * * * * * * Private Member Functions  * * * * * * * * * * * * * //
49
50    Foam::tmp<Foam::volScalarField>
51    Foam::viscosityModels::muIMultiPhase::calcNu() const
52    {
53      Info<< "Calculating viscosity\n" << endl;
54      return max
55      (
56      nuMin_,
57      min
58      (
59      nuMax_,
60      (calcmuI())/(calcStrain()+dimensionedScalar("Vsmall", dimless/dimTime, 1e-09))*Pcalc()/rho_
61
62      )
63      );
64
65    }
66
67    Foam::tmp<Foam::volScalarField>
68    Foam::viscosityModels::muIMultiPhase::calcmuI() const
69    {
70      dimensionedScalar IVsmall("IVsmall", dimless, VSMALL);
71      return (
72      pos(IN1_ - calcI())*sqrt(alphaReg_/max((log(A_m_) - log(calcI() + IVsmall)), IVsmall))
73      +
74      pos(calcI() - IN1_)*(mu1_*I0_ + mu2_*calcI() + muinf_*pow(calcI(), 2))/(I0_ + calcI())
```

```
75      );
76    }
77
78    Foam::tmp<Foam::volScalarField>
79    Foam::viscosityModels::muIMultiPhase::calcI() const
80    {
81      return d_*calcStrain()/(sqrt(Pcalc()/rho_));
82    }
83
84    Foam::tmp<Foam::volScalarField>
85    Foam::viscosityModels::muIMultiPhase::calcStrain() const
86    {
87      return sqrt(2.0)*mag(symm(fvc::grad(U_)));
88    }
89
90    Foam::tmp<Foam::volScalarField>
91    Foam::viscosityModels::muIMultiPhase::Pcalc() const
92    {
93      const objectRegistry& db = U_.db();
94      if (db.foundObject<volScalarField>("p")) {
95        Info<< "Calculate I based on pressure" << endl;
96        const volScalarField& ptot = U_.mesh().lookupObject<volScalarField>("p");
97        return max(ptot, pMin_);
98      } else {
99        Info<< "Effective pressure given as uniform field" << endl;
100       return   tmp<volScalarField>
101       (
102       new volScalarField
103         (
104           IOobject
105           (
106             "peff0",
107             U_.time().timeName(),
108             U_.db(),
109             IOobject::NO_READ,
110             IOobject::NO_WRITE,
111             false
112           ),
113           U_.mesh(),
114           pMin_
115         )
116       );
117     }
118
119   }
120
121   void Foam::viscosityModels::muIMultiPhase::initRegParameter()
122   {
123     // The first part is estumates values for canculating the I limit where the
124     // problem are ill-posed.
125     //Set tan(theta) as an average
126     scalar tanTheta = tan((atan(mu1_) + atan(mu2_))/2.).value();
127     //Set lowest value og I close to zero
128     scalar Ilow = 1e-9;
129     // Higher I value
130     scalar Ihigh = (I0_*(tanTheta-mu1_)/(mu2_ - tanTheta)).value();
131     // Temporary I value
132     scalar IReg = (Ilow +Ihigh)/2.;
133
134     // Calculate the low value
135     while(Ihigh - Ilow > 1e-9)
136     {
137       IReg = (Ilow +Ihigh)/2.;
138
139       scalar muIReg = (mu1_ + IReg*(mu2_ - mu1_)/(IReg + I0_)).value();
140       //muPrime as dmuI/dI
141       scalar muPrime = ((I0_*(mu2_ - mu1_))/(IReg + I0_)/(IReg + I0_)).value();
142       // Inupnu is the fraction used in the C eq 3.9 in Barker & Gray
143       scalar Inupnu = muPrime*IReg/muIReg;
144       // C equation 3.9 in Barker & Gray 2017
145       scalar C = 4*Inupnu*Inupnu - 4*Inupnu + muIReg*muIReg*(1 - Inupnu/2.)*(1 - Inupnu/2.);
146       if (C < 0.)
147       Ihigh = IReg;
148       else
149       Ilow = IReg;
```

```
150        }
151        // IN1_ is the final value
152        IN1_.value() = IReg;
153        // A minus according to eq 6.4
154        A_m_ = IN1_*exp(alphaReg_*pow(IO_ + IN1_, 2)/pow(mu1_*IO_ + mu2_*IN1_ + muinf_*IN1_*IN1_, 2));
155
156   }
157   // * * * * * * * * * * * * * * * * Constructors  * * * * * * * * * * * * * * //
158
159   Foam::viscosityModels::muIMultiPhase::muIMultiPhase
160   (
161   const word& name,
162   const dictionary& viscosityProperties,
163   const volVectorField& U,
164   const surfaceScalarField& phi
165   )
166   :
167   viscosityModel(name, viscosityProperties, U, phi),
168   muIMultiPhaseCoeffs_(viscosityProperties.optionalSubDict(typeName + "Coeffs")),
169   mu2_("mu2", dimless ,muIMultiPhaseCoeffs_),
170   mu1_("mu1", dimless, muIMultiPhaseCoeffs_),
171   muinf_("muinf", dimless, muIMultiPhaseCoeffs_),
172   IO_("IO", dimless, muIMultiPhaseCoeffs_),
173   rhos_("rhos", dimDensity, muIMultiPhaseCoeffs_),
174   d_("d", dimLength, muIMultiPhaseCoeffs_),
175   Dsmall_("Dsmall", dimless/dimTime, muIMultiPhaseCoeffs_),
176   nuMin_("nuMin", dimViscosity, muIMultiPhaseCoeffs_),
177   nuMax_("nuMax", dimViscosity, muIMultiPhaseCoeffs_),
178   rho_("rho", dimDensity, muIMultiPhaseCoeffs_),
179   pMin_("pMin", dimPressure, muIMultiPhaseCoeffs_),
180   alphaReg_("alphaReg", dimless, muIMultiPhaseCoeffs_),
181   IN1_("IN1", dimless, 0.),
182   A_m_("A_m", dimless, 0.1), //NOTE: with these calculations, A_m > 0 in order for equation in calcmuI() to work
183   nu_
184   (
185        IOobject
186        (
187          name,
188          U_.time().timeName(),
189          U_.db(),
190          IOobject::NO_READ,
191          IOobject::AUTO_WRITE
192        ),
193        calcNu()
194   ),
195   muI_
196   (
197   IOobject
198        (
199          "MuI",
200          U_.time().timeName(),
201          U_.db(),
202          IOobject::NO_READ,
203          IOobject::AUTO_WRITE
204        ),
205        calcmuI()
206   ),
207   I_
208   (
209        IOobject
210        (
211          "I",
212          U_.time().timeName(),
213          U_.db(),
214          IOobject::NO_READ,
215          IOobject::AUTO_WRITE
216        ),
217        calcI()
218   ),
219   SR_
220   (
221        IOobject
222        (
223          "SR",
224          U_.time().timeName(),
```

```
225      U_.db(),
226      IOobject::NO_READ,
227      IOobject::AUTO_WRITE
228    ),
229    calcStrain()
230  ),
231  PmuI_
232  (
233    IOobject
234    (
235      "PmuI",
236      U_.time().timeName(),
237      U_.db(),
238      IOobject::NO_READ,
239      IOobject::AUTO_WRITE
240    ),
241    Pcalc()
242  )
243  {}
244
245
246  // * * * * * * * * * * * * * Member Functions  * * * * * * * * * * * * * * //
247
248  bool Foam::viscosityModels::muIMultiPhase::read
249  (
250  const dictionary& viscosityProperties
251  )
252  {
253    viscosityModel::read(viscosityProperties);
254
255    muIMultiPhaseCoeffs_ = viscosityProperties.optionalSubDict(typeName + "Coeffs");
256
257    muIMultiPhaseCoeffs_.lookup("mu2") >> mu2_;
258    muIMultiPhaseCoeffs_.lookup("mu1") >> mu1_;
259    muIMultiPhaseCoeffs_.lookup("muinf") >> muinf_;
260    muIMultiPhaseCoeffs_.lookup("I0") >> I0_;
261    muIMultiPhaseCoeffs_.lookup("rhos") >> rhos_;
262    muIMultiPhaseCoeffs_.lookup("d") >> d_;
263    muIMultiPhaseCoeffs_.lookup("Dsmall") >> Dsmall_;
264    muIMultiPhaseCoeffs_.lookup("nuMin") >> nuMin_;
265    muIMultiPhaseCoeffs_.lookup("nuMax") >> nuMax_;
266    muIMultiPhaseCoeffs_.lookup("rho") >> rho_;
267    muIMultiPhaseCoeffs_.lookup("pMin") >> pMin_;
268    muIMultiPhaseCoeffs_.lookup("alphaReg") >> alphaReg_;
269
270    initRegParameter();
271
272    return true;
273  }
274
275
276  // ************************************************************************* //
277
```

Paper I

Lab Scale Experiments on Alumina Raft Formation

Sindre Engzelius Gylver, Asbjørn Solheim, Henrik Gudbrandsen,
Åste Hegglid Follo, and Kristian Etienne Einarsrud

Abstract

During feeding of alumina into a Hall-Héroult cell, rafts floating on the bath surface may be formed. In this study, rafts were created in a laboratory furnace by adding 4 g secondary alumina in industrial bath. Samples were withdrawn from the bath in a time interval between 30 and 300 s. The experiments show that at 970 °C, rafts will be formed within 30 s, and then slowly dissolve again with a constant rate of 0.8 g/min. Pores were found in the samples, giving extra buoyancy to the raft, thus increasing the floating time. Same experimental setup was used to investigate the effect of preheating of alumina, where it was found that coherent rafts will form up to at least 500 °C.

Keywords

Alumina feeding • Rafts • Aluminum

Introduction

Alumina is the principal raw material used in the Hall-Héroult process in order to produce aluminum. As smelters reduce their bath volume and anode-cathode distance, efficient feeding and dissolution of alumina becomes more important.

S. E. Gylver (✉) · Å. H. Follo · K. E. Einarsrud
Department of Material Science and Engineering, NTNU, Trondheim, Norway
e-mail: sindre.e.gylver@ntnu.no

Å. H. Follo
e-mail: aste.hegglid.follo@elkem.no

K. E. Einarsrud
e-mail: kristian.e.einarsrud@ntnu.no

A. Solheim · H. Gudbrandsen
SINTEF Industry, Trondheim, Norway
e-mail: Asbjorn.Solheim@sintef.no

H. Gudbrandsen
e-mail: Henrik.Gudbrandsen@sintef.no

When alumina is added into the molten bath, it will have temperature below the liquidus of the bath. Temperature differences will lead to freezing of bath around the alumina particles, which will create floating agglomerates known as rafts. Formation of rafts is unfortunate, as it hinders dissolution of alumina, which might lead to anode effects. In addition, rafts may sink to the metal pad, or even further below, creating sludge. A better understanding of the mechanisms behind formation and dissolution of rafts is therefore crucial in order to obtain a more efficient feeding.

Formation of rafts in industrial cells has been observed in earlier work [1], where rafts were formed with floating times varying from 5 to 140 s. Anode age and thus available bath surface and circulation, as well as the acidity of the bath were suggested to have a significant effect on the floating time of the rafts. However, achieving detailed observations and recordings on industrial scale are difficult to accomplish due to the high temperature and hazardous gases.

Laboratory experiments give more controllable and reproducible conditions for raft formation. For instance, as demonstrated by Kaszás et al. [2], image analysis can be used to estimate thickness and surface area of rafts following alumina addition. See-through cells, where one can observe addition of alumina from the side is also a promising approach, and has been used to observe the behavior of alumina upon addition and the dissolution [3,4]. X-ray furnaces have also been used for observations [5], demonstrating together with the other examples above that formations of rafts and agglomerates can be studied in detail.

Artificially produced agglomerates have been used as an alternative to alumina powder by several authors in order to achieve constant geometry and reproducible results. Walker et al. [5] packed alumina in a thin layer of aluminum foil, creating cylindrical shaped agglomerates. The agglomerates were immersed in bath and the mass gain as well as the thickness of the frozen layer as a function of time, temperature and AlF_3 concentration were measured. Increasing temperature and AlF_3 concentration yielded a smaller layer of frozen

bath, which was explained with the increase of superheat, i.e the difference between the liquidus of the bath and temperature. The same setup has been adapted by several researches [6,7], and also tested in industrial cells [8].

Use of cylindrical discs of compressed alumina is also a way of achieving a constant geometry, as demonstrated by Kaszás et al. [9]. Discs were removed after a certain floating time, and found that the density of the raft exceeded the bath's density, illustrating the effect surface tension will have on the floatability of rafts.

A comparison of agglomerates generated from both secondary and primary alumina shows that there will be more pores when secondary alumina is used [10]. The porosity was studied in the work by Yang et al. [4], whose samples contained porosities in 6–8 explained by rapid release of hydroxyl and moisture upon additions into the bath. Computed Tomography (CT) on industrial samples revealed that the distribution and size of pores will vary within a raft [11]. Pores will reduce the apparent density of rafts, thus contributing to buoyancy.

Pre-heating of alumina is a possibility to avoid raft formation. By adding hotter alumina, less bath will freeze around the particles, which may reduce raft formation. Hot exhaust gas has been investigated as a possible source of heat [12]. Experiments by Kobbeltvedt [6] suggest that preheating will result in more dispersed alumina, which will dissolve rapidly. For the alumina that will agglomerate, preheating had no positive effect, which was explained by decreased moisture content. Preheating will not assist the dissolution itself, which is suggested to be limited by mass transfer [13].

The current work investigates the behavior of alumina rafts, by adding alumina into an industrial bath, and removing agglomerates after a certain time. The goal is to create a setup that is closer to actually feeding in industrial cells, while still giving reproducible results. In such a setup, individual factors affecting dissolution can be studied in detail. In the present study, the effects of holding time as well as alumina temperatures on raft mass are investigated. Samples obtained from this setup were characterized with CT, which can be compared with samples of rafts from industrial cells [11].

Experimental Details

Setup

The experiments were conducted in a custom-made open top furnace, consisting of a steel pipe with an inner diameter of 15 cm and a height of 41 cm. The furnace can be used for temperatures up to 1200 °C, and it is heated by a heating element that winds around the pipe. During experiments, the top of the pipe was thermally insulated in order to preserve heat.
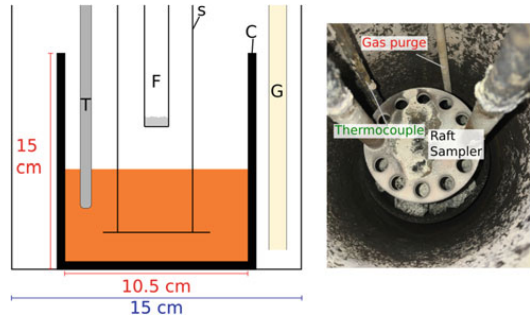

Fig. 1 Left: Vertical cross section of the furnace, equipped with thermocouple (T), feeding pipe (F), raft sampler (S), carbon crucible (C) and gas purge (G). Right: Image of the furnace seen from above

Table 1 Physical data for the materials in the first set of experiments

Bath properties	Value
Bath acidity	10.8 wt%
Alumina content at start	2.3 wt%
Alumina properties	Value
>152.5 μm	9.7%
44–152.5 μm	81.8%
<45 μm	8.5%

A carbon crucible, with dimensions shown in Fig. 1, was filled with bath while nitrogen was purged into the furnace in order to avoid oxidation. Temperature was monitored with a S-type thermocouple placed inside a steel tube at the periphery of the crucible, immersed about 4 cm into the bath. A raft sampler was made in stainless steel, shaped as an 8 cm diameter plate with holes around its periphery. Feeding was done through a 50 cm long pipe with an inner diameter of 1 cm, equipped with a lid mounted on its bottom. The lid was actuated by a spring button on the top of the pipe. Alumina was released from about 5 cm above the bath surface. Alumina from two different suppliers were used in each of the two experiments described in sections "Formation and Dissolution of Rafts" and "Preheating". Although this in principle would introduce an additional uncertainty, the PSD and composition (determined by XRD, cf. Tables 1 and 2) were so similar that the effect is believed to be negligible or at least comparable to other uncertainties in the setup.

Formation and Dissolution of Rafts

Bath and alumina have properties described by Table 1, where rafts were sampled at a bath temperature about 970 °C. The sampler with the created raft was withdrawn between 30 and 300 s after addition of alumina. After extraction of the ladle

Table 2 Physical data for the chemicals in the second set of experiments

Bath properties	Value
Bath acidity	10.9 wt%
Alumina content at start	2.1 wt%
Alumina properties	*Value*
>152.5 μm	8.7%
44–152.5 μm	75.6%
<45 μm	15.7%

from the furnace, it was cooled in ambient conditions, before raft samples were removed and stored for further processing.

All samples were weighed and photographed after cooling and extraction from the ladle, and further post-processed in ImageJ [14] in order to calculate surface area.

Preheating

Properties of the bath and alumina are given in Table 2, while the bath temperature was between 955 and 960 °C. 4 g alumina was added into the bath with a holding time of 30 or 60 s, where a thermocouple was placed inside the feeding tube in order to monitor the temperature of the alumina. Removal and further image processing of rafts were performed as described in previous section "Formation and Dissolution of Rafts".

Characterization

Selected rafts were cut and the cross sections were studied in a Nikon SMZ 800 N optical Microscope. Micro computed X-ray tomography (μCT) was used to analyze the macroscopic structure. The data was acquired by a Nikon XT H225 ST instrument (cone beam volume CT), using a tungsten reflection target and an aluminum filter of 1 mm, with an acceleration voltage of 140 kV and a current of 220 μA. The imaging was done with an integration time of 1 s, amplification of 18 dB, with 3142 projections per 360°.

Results

The mass gain, i.e. the difference between the masses of formed raft and added alumina, as a function of holding time is shown in Fig. 2a, estimated to decrease with a rate of 0.8 g/min. A similar plot of surface area is given in Fig. 2b.

Surface area and variation of mass gain for different alumina temperatures are plotted in Fig. 3, where the holding time is 30 and 60 s for (a) and (b), respectively.

Images of selected non-preheated samples from optical microscopy and CT is shown in Fig. 4, while Fig. 5 shows calculated porosity and density of a raft. The porosity is reported as a percentage of pores relative to the entire horizontal cross-sectional area of the sample (including the pores), with an average porosity of 7.1% for the samples analyzed.

Discussion and Conclusions

Alumina rafts have been created in a laboratory cell, where holding time and preheating of alumina were investigated.

As expected, bath freezes around cold alumina as it is added to the bath. Even at 970 °C, the mass gain is above the mass of alumina added to the bath. Melting of bath will then further reduce the mass of the rafts, as seen in Fig. 2a. At this temperature, the created rafts dissolve at 0.8 g/min, which is in the same order as found by Yang et al. [4].

The spread in data observed in 2 is believed to originate from two sources. Firstly, parts of the raft may have been lost during removal of the raft sampler from the furnace, thereby reducing the measured mass. Secondly, parts of the raft could remain on the sampler following extraction, again reducing the overall measured mass of the raft. As bath could freeze to the sampler independently of raft formation, it was not possible to quantify the mass loss of the raft by measuring the sampler weight before and after experiments.

Figure 6 present calculated theoretical masses of rafts from the following reaction

$$\gamma - Al_2O_3(T_{add}) + x \cdot Na_3AlF_6(l, 960°C) = $$
$$\alpha - Al_2O_3(950°C) + x \cdot Na_3AlF_6(s, 950°C) \qquad (1)$$
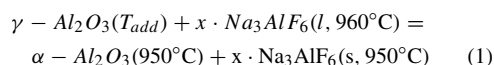
where T_{add} is the temperature of added alumina, and x is the amount of cryolite required to freeze, represented by solid bath in the figure.

At low alumina temperatures, the calculated raft weight is lower than the theoretical one, which is probably because a fraction of the alumina batch will dissolve immediately [16]. At higher preheating temperatures, in particular for longer holding times, the weight is higher than the calculated effect. This could be due to infiltration of liquid bath inside of the raft, which will freeze upon sampling.

The effect of preheating (Fig. 3) shows that coherent rafts will form until alumina is heated to 500–600 °C. Above this temperature, most of the alumina will dissolve as dispersed particles. Since the dissolution of agglomerates is found to be controlled by mass transfer [13], preheating below 500 °C will have no effect on its dissolution time. The experiments by Kobbeltvedt [6] showed that more alumina will disperse at even lower temperatures. However, stirring was applied in his experiments, which will be beneficial for dispersion. In

Fig. 2 **a** Mean mass gain of rafts, given as the difference between raft weight and mass alumina added, and surface area (**b**) for holding times between 30 and 300 s and bath temperature of 970 °C. The error bars indicate a 95% confidence interval. There are at least 3 measurements at each time
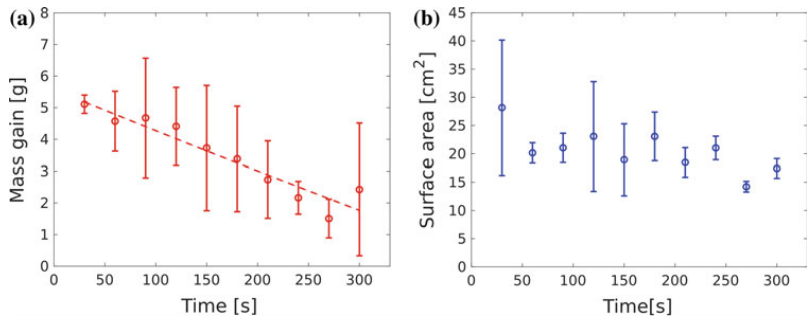

Fig. 3 Mass gain and surface area for different preheating temperatures. **a** Holding time 30 s. **b** Holding time 60 s. The bath temperature was between 955 and 960 °C
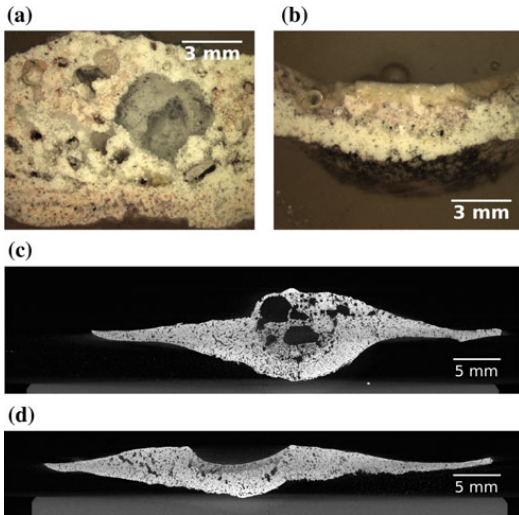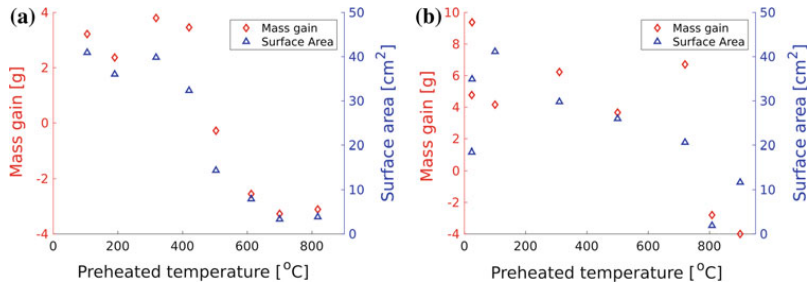

Fig. 4 Images of the cross section of four different samples. **a** Floating time time 300 s, **b** Floating time 90 s, **c** floating time 60 s, **d** floating time 210 s

Fig. 5 Calculated density and porosity of sample with holding time 60 s and bath temperature 970 °C

his experiments, the dissolution of agglomerates was rather unchanged with increased preheating temperature. Volatiles, in particular moisture, are found to have a positive effect on dissolution by breaking rafts apart [17]. Removal of these upon preheating will also create rafts that are harder to dissolve.

Preheating alumina up to 500–600 °C in an industrial cell might be challenging. Simulations indicate that this is possible by heat exchange of the exhaust gas [12], but measures must probably be taken to avoid that water vapor driven off in the hot zone condenses at the colder zones causing clogging. Preheating will require changes to traditional cell design and the effect on operational costs is uncertain.

Figure 4 illustrates the variation of the appearance of the rafts collected. While some will have large cavities covered around frozen bath (a and c), others contains a crater (b and d).
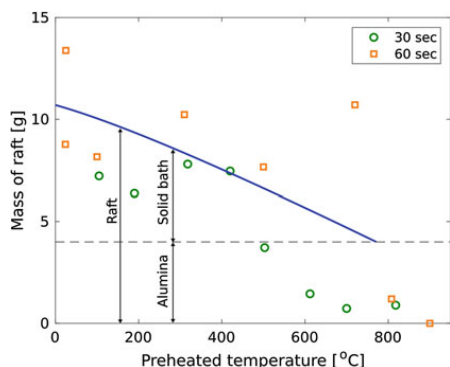
Fig. 6 Theoretical mass of raft consisting of solid bath and alumina, assuming no initial dispersion and that all added alumina is converted from α to γ. Thermodynamic data from JANAF [15]

Cavities are presented in earlier work [11] and believed to be formed due to moisture in alumina, which again lead to formation of water vapor and HF-gas. By assuming that alumina contains about 0.5 mass% moisture, 34 mL of water vapor will be released at 100 °C and normal pressure [18]. This will be more than enough to create the pores and cavities observed. The craters could be formed in similar way, where the top of the layer has melted before collection. Pores and cavities will reduce the apparent density of the raft, hence increase its ability to float.

The trends found in apparent density and porosity (Fig. 5) are in the same range as those found in industrial rafts [11]. Laboratory rafts are much smaller, and some of them contain unproportionly large cavities. These cavities will contribute to very high calculated porosity. The real porosity of rafts should therefore be smaller in some areas.

The experimental setup gives possibilities to create alumina rafts under controlled conditions. In order to increase the relevance to industrial rafts, stirring should be considered. In addition, the mass of alumina added to available bath surface area is smaller in this setup than for an industrial cell, pointing out that dose size should be increased. Collection and further characterization of lab-induced rafts created under different conditions should increase the understanding of formation and dissolution rafts, thus pointing out ways for further technology development.

References

1. S.E. Gylver, N.H. Omdahl, A.K. Prytz, A.J. Meyer, L.P. Lossius, K.E. Einarsrud, in *Light Metals 2019*, ed. by C. Chesonis (Springer International Publishing, 2019), pp. 659–666
2. C. Kaszás, L. Kiss, S. Poncsák, S. Guérard, J.F. Bilodeau, in *Light Metals 2017*, ed. by A.P. Ratvik (Springer, Cham, 2017), pp. 473–478
3. X. Liu, S.F. George, V.A. Wills, in *Light Metals 1994*, ed. by U. Mannweiler (1994), pp. 359–359
4. Y. Yang, B. Gao, Z. Wang, Z. Shi, X. Hu, Journal of Metals **67**(9), 2170 (2015)
5. D. Walker, T. Utigard, J. Toguri, M. Taylor, in *Advances in Production and Fabrication of Light Metals and Metal Matrix Composites;* (Edmonton, Alberta, Canada, 1992), pp. 23–37
6. O. Kobbeltvedt, Dissolution kinetics for alumina in cryolite melts : distribution of alumina in the electrolyte of industrial aluminium cells. Phd thesis, Norwegian University of Science and Technology, Department of Electrochemistry, Trondheim (1997)
7. N.P. Østbø, Evolution of alpha phase alumina in agglomerates upon addition to cryolitic melts. PhD Thesis, Norwegian University of Science an Technology - NTNU, Trondheim (2002)
8. D.I. Walker, T. Utigard, M.P. Taylor, in *Light Metals 1995*, ed. by J.W. Evans (TMS, 1995), pp. 425–434
9. C. Kaszás, L.I. Kiss, S. Poncsák, J.F. Bilodeau, S. Guérard, in *Proceedings of 34th International ICSOBA Conference* (Quebec, Canada, 2017)
10. S. Rolseth, J. Thonstad, in *Extraction, Refining, and Fabrication of Light Metals*, ed. by M. Sahoo, P. Pinfold (Pergamon, Amsterdam, 1991), Proceedings of Metallurgical Society of Canadian Institute of Mining and Metallurgy, pp. 177–190
11. S.E. Gylver, N.H. Omdahl, S. Rørvik, I. Hansen, A. Nautnes, S.N. Neverdal, K.E. Einarsrud, in *Light Metals 2019*, ed. by C. Chesonis (Springer International Publishing, 2019), pp. 689–696
12. D.S. Severo, V. Gusberti, in *Proceedings of 35th International ICSOBA Conference*, vol. 46 (Hamburg, Germany, 2017), vol. 46, pp. 1059–1071
13. J. Thonstad, A. Solheim, S. Rolseth, O. Skar, in *Essential Readings in Light Metals: Volume 2 Aluminum Reduction Technology*, ed. by G. Bearne, M. Dupuis, G. Tarcy (Springer International Publishing, Cham, 2016), pp. 105–111
14. W. Rasband. ImageJ (1997). https://imagej.nih.gov/ij/
15. T. Allison. JANAF Thermochemical Tables, NIST Standard Reference Database 13 (1996). http://kinetics.nist.gov/janaf/
16. R.K. Jain, S. Tricklebank, B.J. Welch, D.J. Williams, in *Light Metals 1983*, ed. by E.M. Adkins (The Metallurgical Society of AIME, 1983), pp. 609–622
17. R.G. Haverkamp, Surface studies and dissolution studies of fluorinated alumina. PhD Thesis, The University of Auckland, Auckland (1992)
18. W. Wagner, *International Steam Tables : Properties of Water and Steam Based on the Industrial Formulation IAPWS-IF97*, 2nd edn. (Springer Berlin Heidelberg, 2008)

Paper II

On Gaseous Emissions During Alumina Feeding

Sindre Engzelius Gylver, Åste Hegglid Follo, Vegard Aulie,
Helene Marie Granlund, Anders Sørhuus, Espen Sandnes,
and Kristian Etienne Einarsrud

Abstract

Aluminium electrolysis involves feeding of alumina into a cryolite-based bath. Water originating from alumina as well as from air reacts with fluorides and results in HF evolution. Untreated HF gas is a significant environmental and economical issue. HF is, however, effectively adsorbed in (primary) alumina before being fed back to the cell as secondary alumina, thereby recycling the fluoride. As alumina is fed to the cell, it forms a raft, delaying the dissolution process and linked to several operational challenges. The goal of the current work is twofold; first, water content is investigated in a lab-scale setting, aiming to explain raft porosity, ultimately causing it to float rather than disperse in the bath. Secondly, the evolution of HF is investigated for different alumina in industrial measurements performed at Alcoa Mosjøen, aiming to identify correlations between gas evolution and alumina properties.

S. E. Gylver · Å.H. Follo · V. Aulie · E. Sandnes ·
K. E. Einarsrud (✉)
Department of Material Science and Engineering, NTNU,
Trondheim, Norway
e-mail: kristian.e.einarsrud@ntnu.no

S. E. Gylver
e-mail: sindre.e.gylver@ntnu.no

Å.H. Follo
e-mail: aste.hegglid.follo@elkem.no

V. Aulie
e-mail: vegaraul@stud.ntnu.no

E. Sandnes
e-mail: espen.sandnes@ntnu.no

H. M. Granlund
Alcoa Norway Ans, Mosjøen, Norway
e-mail: Helene.Marie.Eng.Granlund@alcoa.com

A. Sørhuus
GE Power Norway AS, Oslo, Norway
e-mail: anders.sorhuus@ge.com

Keywords

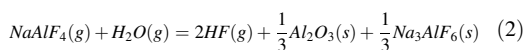Alumina feeding • Rafts • HF emissions

Introduction

Besides being the principal raw material, alumina plays an important role as a cleansing agent in modern smelters. By the dry scrubbing process, toxic hydrogen fluoride gas is adsorbed onto fresh alumina, creating what is known as secondary alumina. Other benefits include the recycling of fluorides back to the cell and better dissolution of alumina [1].

HF is generated when water reacts with fluorides present in the bath, either to entrained bath:

$$\frac{2}{3}AlF_3(diss) + H_2O(g) = 2HF(g) + \frac{1}{3}Al_2O_3(diss) \quad (1)$$

or by hydrolysis of pot fume [2]
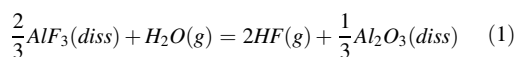
$$NaAlF_4(g) + H_2O(g) = 2HF(g) + \frac{1}{3}Al_2O_3(s) + \frac{1}{3}Na_3AlF_6(s) \quad (2)$$

The source of water is mainly from moisture present in the alumina, although hydrogen in the anodes as well as ambient moisture is also of importance. Hyland et al. [3] point out that hydrogen incorporated into the crystal lattice, also known as structural hydroxides, contributes significantly to the formation of HF. These groups are often measured as LOI 350–1000, and will be released slowly as alumina is dissolved and results in a slower and more continuous release of HF gas, compared to more loosely bound water.

Alumina is added in batches through point feeders, where about 1 kg of powder is added at each feeding. Upon an addition, a rigid structure known as a raft, floating on the bath surface, might be formed. Rafts from industrial cells have been collected and characterized in earlier work, revealing a porous structure as well as large cavities [4]. Rolseth and Thonstad [5] created crusts by adding alumina to bath in a

lab-scale furnace, revealing that the crusts created from secondary alumina have a more porous structure than from primary. The source of the pores is, however, not thoroughly investigated yet, but it is believed to be related to the release of moisture and hydroxyl groups [6] or impurities such as sulfur [7] or fluorides [8] forming gaseous species such as SO_2 and HF, which gets trapped as the bath solidifies.

Measurements of HF has been done in several smelters. Previous measurements suggest that the HF content is about 200–400 ppm in the duct, and is dependent on cell technology [9–11]. The evolution of HF has been found to be closely related with the feeding cycle, where a peak in HF content is registered short time after alumina is added, explained by the moisture contribution from alumina. A rise in the HF concentration is also observed when the cell is overfeeding.

Previous industrial data suggest that the condition of feeding hole and crust has a major effect on the measured HF content. By creating a portable probe connected to a Tuneable Diode Laser (TDL), Osen et al. [12] were able to measure the HF content at several positions in an industrial cell. They measured HF content up to 9000 ppm in the feeding hole, while the content above the crust far away from the feeding hole was 5–10 ppm. Slaugnehapt et al. [9] covered the feeding holes while monitoring the HF evolution from the off gas. They observed that the effect of a closed feeding hole was much larger than low bath ratio and high temperature, which will increase the vapor pressure of the bath.

The effect on routine operations is also observed, in particular, by Patterson [11]. During anode change, high values of HF were measured, which was explained by a large surface of bath available as the anode is removed. Metal tapping was also observed to increase HF evolution, and is explained by change in crust integrity due to anode movement after tapping. Increased humidity has also been observed to affect the measured content, due to more available water in the atmosphere.

The current work aims to extend the existing body of knowledge related to HF evolution during alumina feeding. Dedicated lab-scale experiments are performed in order to study the link between moisture, HF evolution, and raft porosity, while industrial measurements have been carried out over 43 consecutive days in order to investigate the influence of cell operations and conditions of HF evolution.

Experimental Details

Formation of Rafts

The lab-scale experiments were performed with industrial bath with properties as given in Table 1. Primary and secondary alumina from the industry was used for the experiments, with particle size distribution given in Table 1. Since the main goal of the current work is to study the effect of water content, other parameters, such as fluoride and α-content, are not quantified in this study. Different water content was achieved by either drying or hydrating the powder, summarized as LOI Room Temperature (RT)-1000 in Table 1 for primary and secondary alumina. The LOI values used in the current work are considerably higher than that expected in an industrial setting, but were used in order to more easily observe any trends.

The setup and method for generating and extracting rafts were based on the work of Gylver et al. [13], as sketched in Fig. 1. A carbon crucible was filled with 1300 g of industrial bath, corresponding to a molten bath height of 6.5 cm, and placed in a furnace with inner diameter of 15 and 41 cm height. The furnace was purged with 99.999 % pure nitrogen gas in order to decrease air burn on the carbon crucible. Temperature was monitored throughout the experiments using an S-type thermocouple placed inside a steel tube at the periphery of the crucible, immersed about 4 cm into the bath. In order to prevent heat loss during the experiment, the furnace was covered during addition and formation of rafts, thus preventing visual observations.

Alumina feeding was done through a 50-cm-long pipe with an inner diameter of 1 cm, equipped with a bottom-mounted lid, which was actuated by a spring button on the top of the pipe, placed such that alumina was released 2 cm above the bath surface. 4 grams of alumina was added to the bath, and the created raft was removed from the bath after 60 s and cooled under ambient conditions. A total of 18 rafts were created.

After extraction, the rafts were weighed and photographed and their structure was analyzed using micro-computed X-ray tomography (μCT). The data was acquired using a Nikon XT H225 ST instrument (cone beam volume CT), using a tungsten reflection target and an aluminum filter of 1 mm, with an acceleration voltage of 140 kV and a current of 150 μA. The imaging was done with an integration time of 1 s, amplification of 18 dB, with 3142 projections per 360°. Images obtained by μCT were further processed in ImageJ [14] in order to determine raft porosity.

Industrial HF Measurements

A Neo Monitors Lasergas™ II SP was installed in the off-gas channel, 15 m away from the cell at the Alcoa Mosjøen plant. The TDL monitored the HF content all day long, in the period of July 4–August 15, 2019, with measurement intervals varying between 1 and 10 s, which was adjusted manually.

Table 1 Physical data of the bath and particle distribution for the alumina types

Bath properties	Value
Bath acidity	10.8 wt%
Alumina content at start	2.3 wt %
Primary alumina properties	*Value*
+ 149 µm	1.1 %
−44 µm	9.8 %
−20 µm	1.2 %
LOI RT-1000 Dry	2.81 %
LOI RT-1000 Medium	4.29 %
LOI RT-1000 Hydrated	5.67 %
Secondary alumina properties	*Value*
+ 149 µm	3.2 %
−44 µm	7.7 %
−20 µm	0.5 %
LOI RT-1000 Dry	3.57 %
LOI RT-1000 Medium	5.02 %
LOI RT-1000 Hydrated	6.37 %
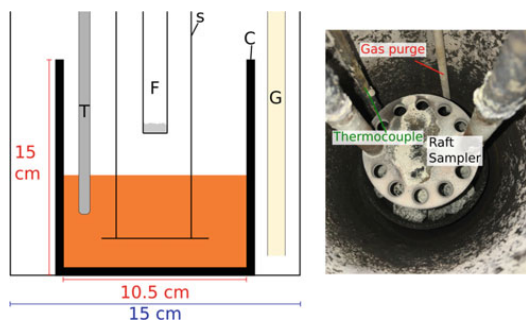
Fig. 1 Left: Vertical cross section of the furnace, equipped with thermocouple (T), feeding pipe (F), raft sampler (S), carbon crucible (C), and gas purge (G). Right: Image of the furnace seen from above

The temperature was measured with STARprobe™ [15] every second day as a part of routine operations. As a part of the campaign, a higher voltage was applied to the cell for one day, in order to obtain a higher bath temperature. Measurements with STARprobe™ were conducted six times on this day with approximately 2 h between each measurement.

Results and Discussion

Lab Scale Rafts

Sample CT images of rafts created from primary and secondary alumina are shown in Fig. 2, while Fig. 3 shows the calculated porosity for all collected samples. The porosity is reported as the amount of (closed) pores relative to the entire horizontal cross-sectional area of the sample. The (closed) pores are actual voids in the raft, which otherwise consists of alumina particles in a bath matrix [4].

The porosity is due to both small pores and larger cavities, also observed in earlier work, and is found to be more important for the rafts created from secondary alumina. Rafts generated from secondary alumina typically had a large cavity in the central regions (see lower image in Fig. 2), while those generated from primary were typically thin and disk-like. Considering Fig. 3a, there is no apparent link between the porosity and LOI RT-1000. This is believed to be due to excess water on the surface flashing off immediately after addition. Results for LOI 350–1000, Fig. 3b, however, indicate that higher values of this parameter are linked to greater porosities. The LOI 350–1000 interval will account for release of both structural water and fluoride impurities [8] present in the (secondary) alumina, thus indicating that the pores at least in part can be explained by HF gas which becomes trapped in the raft as it is formed.

Industrial Measurements

Figure 4 demonstrates the measured HF content under normal operations. Each feeding event (red dots in sub-figures b,c,d) is typically followed by a peak in HF, which then drops off more slowly. The peaks are typically registered about 30 s after feeding. An examination of data during high measurement frequency was calculated to be 31.73 ± 0.24 s. Corresponding delays between feeding events and peak values have been observed in earlier measurements within the same cell technology [10]. Several factors are believed to contribute to this delay, relating to HF gas formation and subsequent transport from the bath and into the duct where concentrations are measured. Under normal conditions, this transport will take place through the feeding hole. If the feeding hole is closed, the time for the
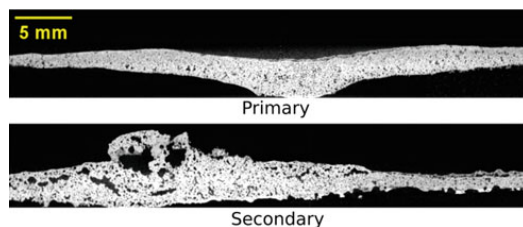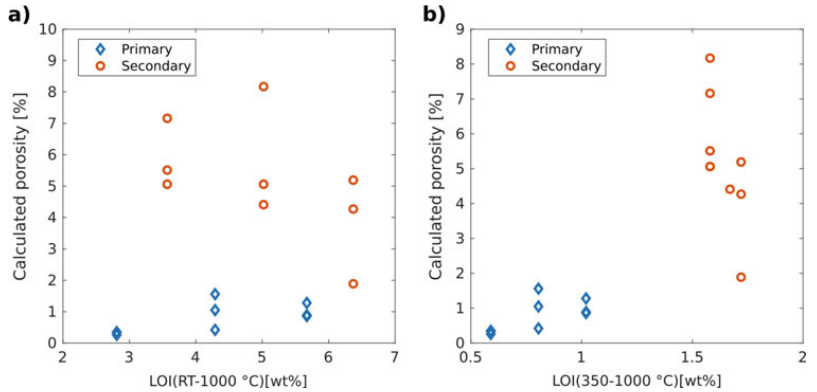

Fig. 2 CT images of rafts created from primary (top) and secondary (bottom) alumina

Fig. 3 The calculated porosity for rafts created from primary (diamonds) and secondary (circles) alumina, with different water contents—represented as LOI RT-1000 (**a**) and LOI 350–1000 (**b**). (Color figure online)

HF to arrive in the duct will increase, which can explain some of the variations seen in our measurements.

As seen in Fig. 4, the increase in HF content is rapid, while it declines more slowly. While this behavior is the expected response from a ideal reactor experiencing a pulse —e.g. feeding—the decline may also be related to delayed gas release arising due to bath freezing around the added alumina, forming a raft, as readily observed in the same cell design [16] previously. Gas may also be trapped within the porous structure of the raft, as observed both under lab-scale conditions, as in the current work, and in industry [4].

The data presented in Fig. 4 indicates the presence of two timescales, one being the time between each subsequent feeding event, denoted as t_f, and one related to the (typical) length of the feeding cycle, t_c. In order to quantify the impact of the various cell operations and conditions, mean and extremal quantities are calculated for each of the time-scales considered. Denoting the measured HF concentration by $C(t)$, the time-averaged concentration between two feeding events, $\bar{C}_{fa}$ and over a given feeding cycle, $\bar{C}_{ca}$ is given as

$$\bar{C}_{fa} = \frac{1}{t_f} \int_{t_f} C(t)dt \tag{3}$$

$$\bar{C}_{ca} = \frac{1}{t_c} \int_{t_c} C(t)dt. \tag{4}$$

The base values for a single feeding event C_{fb} and the full cycle, C_{cb}, are defined as

$$C_{fb} = min|C(t)|_{t_f} \tag{5}$$

$$C_{cb} = mean(C_{fb})|_{t_c}, \tag{6}$$

where $min|C(t)|_{t_f}$ and $mean(C)|_{t_c}$ signify the minimum and arithmetic values over the time interval in question. Correspondingly, the peak values C_{fp} and C_{cp} are calculated as

$$C_{fp} = max|C(t)|_{t_f} \tag{7}$$

$$C_{cp} = mean(C_{fp})|_{t_c}. \tag{8}$$

Finally, the peak-to-peak values are defined as

$$C_{f,P2P} = C_{fp} - C_{fb} \tag{9}$$

and

$$C_{c,P2P} = C_{cp} - C_{cb}. \tag{10}$$

Statistics for all calculated parameters are presented in Table 2. Evidently, there is considerable deviation in the dataset, in particular, for the quantities defined for the feedings.

From the raw data presented in Fig. 4, there appears to be some trends with respect to feed values C_{fi} (i.e. Eqs. 3, 5, 7 and 9), following changes in the feeding cycle, tapping, and anode change, which can explain some of the variation observed in Table 2. These possible trends are investigated further and quantified in the following paragraphs.

Considering changes in the feeding cycle, a total of 711 cycles were investigated. Within each cycle j, a linear regression model was made for each of the variables C_{fi}:

$$C(t)_{fi} = b_i - a_i t, \quad t \in t_c^j, \tag{11}$$

as illustrated in Fig. 5.

The slopes a_i were assumed to be normal distributed and a t-test with the null hypothesis $a = 0$ vs $a > 0$ was

Fig. 4 Measurements of HF during normal operations. **a** Typical measurement of HF content during 3 hours. **b** A section of the measurement from (**a**), where fast feeding occurs. Feedings are indicated with red dots. **c** Measurement during anode change. **d** Measurement during tapping. (Color figure online)
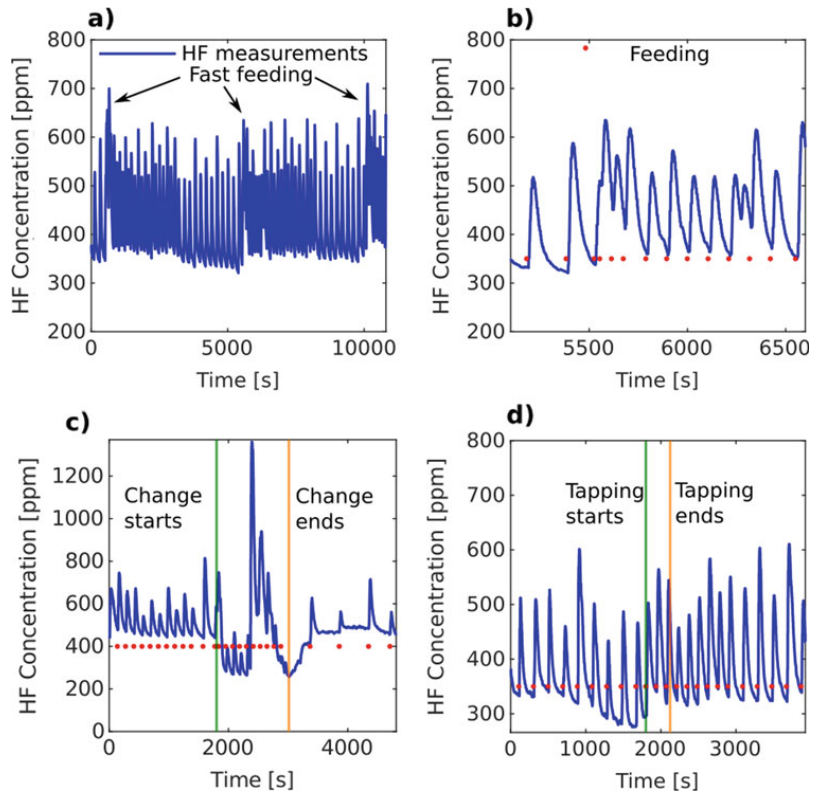
performed in order to determine any significant trends, with main results presented in Table 3. As shown in the table, both $\bar{C}_{fa}$ and C_{fb} meet the hypothesis, while C_{fp} and $C_{f,P2P}$ do not. These results indicate that the HF emissions are lower as the cell is underfed, since less alumina and hence surplus fluoride is entering the cell.

Table 2 Mean and standard deviation for the concentration values described by Eqs. (3)–(10) for the entire campaign

Quantity	Mean [ppm]	Standard deviation
$\bar{C}_{fa}$	424.14	80.70
$\bar{C}_{ca}$	413.82	54.14
C_{fb}	332.33	63.44
C_{cb}	334.16	47.40
C_{fp}	581.31	97.89
C_{cp}	583.69	66.68
$C_{f,P2P}$	248.98	76.78
$C_{c,P2P}$	249.53	43.70

For tapping and anode change, average C_{fi} values were calculated for the ten feedings before and the ten first feedings after the operation. For the anode change operation, these averages $\tilde{C}_{fa}$ are shown in Fig. 6. A hypothesis test shows that the HF concentration after anode change is significantly lower after anode change than before. It should, however, be noted that alumina is fed at a lower frequency following anode change (cf. Fig. 4) and it is therefore challenging to distinguish if the anode change itself affects the emissions or if the observation is due to the altered feeding conditions.

The same procedure was used to investigate the tapping process, but no significant difference was found for this operation.

For temperature, average properties were calculated based on five feeding events before and after the temperature was measured, as shown in Fig. 7. The current data indicates a significant positive correlation between temperature and HF emissions, which is in accordance with earlier research [2].

Finally, HF measurements were compared to the absolute humidity in proximity of the smelter [17]. A representative example showing humidity and measured HF concentration
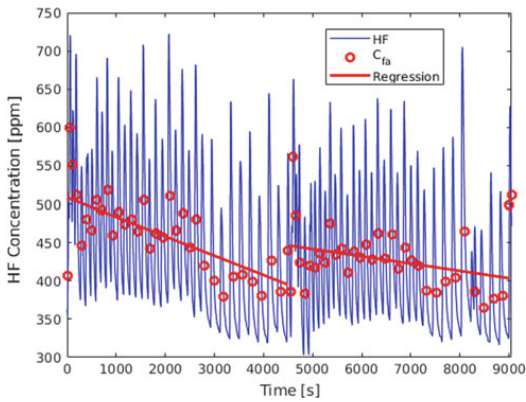
Fig. 5 Two feeding cycles where $\bar{C}_{fa}$ and its estimated regression lines are shown. (Color figure online)
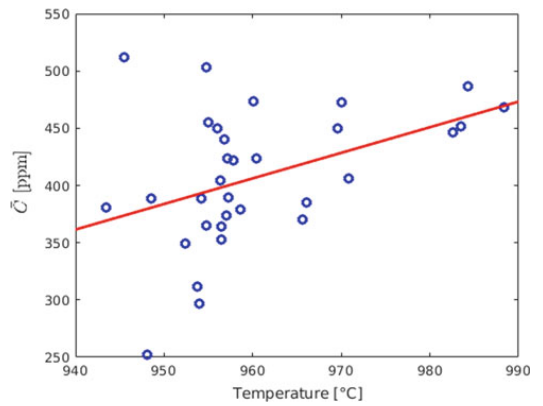
Table 3 Results from one-sided hypothesis test

Quantity	$\bar{a}_i$	Lower limit
$\bar{C}_{fa}$	0.027	0.022
C_{fb}	0.021	0.017
C_{fp}	0.0037	−0.0078
$C_{f,P2P}$	−0.0175	−0.028
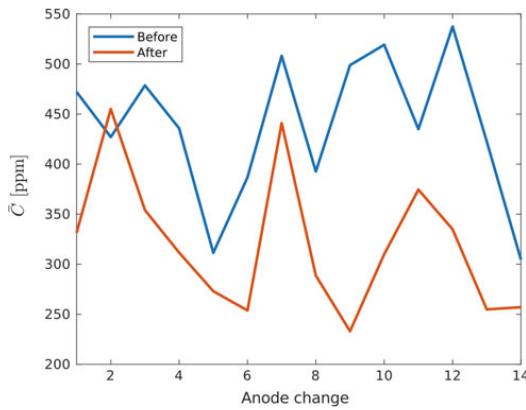
Fig. 6 $\bar{C}_1$ calculated for 10 feedings right before/after anode change, where 14 different anode changes are considered. (Color figure online)

over 3 days is shown in Fig. 8. There is considerable variation in both humidity and HF emissions. However, the Pearson correlation coefficient between these two parameters was calculated to be 0.30, indicating no significant correlation in the current campaign.

Fig. 7 Temperatures and $\bar{C}$, where $\bar{C}$ is calculated as a mean from five feedings before and five feedings after the temperature were measured

Fig. 8 The calculated values of $\bar{C}_{ca}$ and C_{cb} together with relative humidity plotted over 3 consecutive days

Conclusions

Alumina feeding and HF evolution are investigated on both lab and industrial scales.

Lab-scale measurements show that there is a significant difference in porosity between rafts generated from primary and secondary alumina. The difference appears to be related to LOI 350–1000, i.e. structural hydroxides and fluoride impurities, indicating that the porous structures observed are due to HF evolution. While the porous structures are believed to contribute significantly to the buoyancy of the rafts and thereby delay dissolution, several other alumina properties will affect the dissolution as well. These factors will be investigated in future work.

Industrial-scale measurements have been performed over 43 consecutive days, aiming to investigate possible correlations between HF emissions and cell operations and conditions. On average, the HF concentration was measured to be around 400 ppm in the duct during the campaign.

A rapid rise in measured HF is observed after each feeding, followed by a slower decline. Whether the rate of decline is dependent on the raft floating time was beyond the scope of this work, but will be looked into in the future.

The feeding cycle appears to play a significant role on the measured HF content. As the the cell is underfeeding, the measured HF concentration is also being reduced. Of regular operations, anode change seems to have a significant role, although this could be masked by changes in the feeding cycle. Tapping does not appear to play a significant role. A correlation between bath temperature and HF content was found, while no correlation between HF content and humidity was identified.

References

1. K. Grjotheim and H. Kvande, Eds., *Introduction to Aluminium Electrolysis-Understanding the Hall-Heroult Process*. Düsseldorf: Aluminium-Verlag, 1993.
2. W. Haupin and H. Kvande, "Mathematical Model of Fluoride Evolution from Hall-Héroult Cells," in *Essential Readings in Light Metals: Volume 2 Aluminum Reduction Technology*, G. Bearne, M. Dupuis, and G. Tarcy, Eds. Cham: Springer International Publishing, 2016, pp. 903–909.
3. M. Hyland, E. Patterson, and B. Welch, "Alumina Structural Hydroxyl as a Continous Source of HF," in *Essential Readings in Light Metals: Volume 2 Aluminum Reduction Technology*, G. Bearne, M. Dupuis, and G. Tarcy, Eds. Cham: Springer International Publishing, 2016, pp. 936–941.
4. S. E. Gylver et al., "The Micro- and Macrostructure of Alumina Rafts," in Light Metals 2019, 2019, pp. 689–696.
5. S. Rolseth and J. Thonstad, "Agglomeration and dissolution of alumina in cryolite baths," in *Extraction, Refining, and Fabrication of Light Metals*, Amsterdam, 1991, pp. 177–190.
6. Y. Yang, B. Gao, Z. Wang, Z. Shi, and X. Hu, "The Formation and Dissolution of Crust Upon Alumina Addition into Cryolite Electrolyte," *Journal of Metals*, vol. 67, no. 9, pp. 2170–2180, Sep. 2015.
7. R. Meirbekova, G. M. Haarberg, J. Thonstad, and G. Saevarsdottir, "Influence of Sulfur Species on Current Efficiency in the Aluminum Smelting Process," *Metall and Materi Trans B*, vol. 47, no. 2, pp. 1309–1314, Apr. 2016.
8. A. R. Gillespie, M. M. Hyland, and J. B. Metson, "The Surface Chemistry of Secondary Alumina from the Dry Scrubbing Process," in *Essential Readings in Light Metals: Volume 2 Aluminum Reduction Technology*, G. Bearne, M. Dupuis, and G. Tarcy, Eds. Cham: Springer International Publishing, 2016, pp. 956–961.
9. M. L. Slaugenhaupt, J. N. Bruggeman, G. P. Tarcy, and N. R. Dando, "Effect of Open Holes in the Crust on Gaseous Fluoride Evolution from Pots," in *Essential Readings in Light Metals: Volume 2 Aluminum Reduction Technology*, G. Bearne, M. Dupuis, and G. Tarcy, Eds. Cham: Springer International Publishing, 2016, pp. 930–935.
10. C. Sommerseth et al., "Correlation between Moisture and HF Formation in the Aluminium Process," in *Light Metals 2011*, S. J. Lindsay, Ed. Cham: Springer International Publishing, 2011, pp. 339–344.
11. E. C. Patterson, "Fluoride emissions from aluminium electrolysis cells," PhD Thesis, The University of Auckland, Auckland, 2002.
12. K. S. Osen, T. A. Aarhaug, A. Solheim, E. Skybakmoen, and C. Sommerseth, "HF Measurements Inside an Aluminium Electrolysis Cell," in *Light Metals 2011*, S. J. Lindsay, Ed. Cham: Springer International Publishing, 2011, pp. 263–268.
13. S. E. Gylver, A. Solheim, H. Gudbrandsen, Å. H. Follo, and K. E. Einarsrud, "Lab Scale Experiments on Alumina Raft Formation," in *Light Metals 2020*, Cham, 2020, pp. 659–663.
14. W. S. Rasband, *ImageJ*. Bethesda, Maryland, USA: U. S. National Institutes of Health, 1997, https://imagej.nih.gov/ij/.
15. X. Wang, B. Hosler, and G. Tarcy, "Alcoa STARprobe™," in Light Metals 2011, S. J. Lindsay, Ed. Cham: Springer International Publishing, 2016, pp. 483–489.
16. S. E. Gylver, N. H. Omdahl, A. K. Prytz, A. J. Meyer, L. P. Lossius, and K. E. Einarsrud, "Alumina Feeding and Raft Formation: Raft Collection and Process Parameters," in Light Metals 2019, 2019, pp. 659–666.
17. "Norsk Klimaservicesenter." https://seklima.met.no/observations/ (accessed Aug. 09, 2020).

Paper III

A Water Model Study of Alumina Feeding and Dispersion

Sindre Engzelius Gylver, Simen Aase, Simen Bekkevoll,
Sigmund Andres Kvammen Forberg
and Kristian Etienne Einarsrud

Abstract

In the Hall-Héroult process, alumina is fed periodically into a cryolite bath, typically forming so-called rafts. While rafts have been observed and sampled in industry, the governing mechanisms for raft formation are not easily assessed in this setting. In this paper, we present a parametric study of alumina feeding and dispersion, where the liquid is kept close to its freezing point, to which cooled (soluble) particles are added. The effect of the temperature difference between particles and liquid, particle size distribution (PSD), and gas induced convection is considered and assessed. Results from the water model experiments show a strong impact of PSD on the raft floating time. High amounts of fines increased resulting in floating times between 240 and 550 s, compared to 35–135 seconds in the case of coarser particles. Increased temperature and convection contributed positively to dispersion, although less significantly than the PSD.

Introduction

Alumina is the principal raw material used in the Hall-Heroult process. It is fed through batches in point feeders at a few locations in the cell, making dissolution and distribution of the alumina a critical factor for achieving an efficient process. When alumina is added, it can agglomerate and form a floating porous structure consisting of alumina powder and frozen bath [1]. These so-called rafts will delay alumina from dissolving, as heat is required to melt the frozen layer formed.

Earlier investigations have found that the floating time of rafts in industrial cells is influenced by bath convection, represented by the age of the anodes around the observed zone, bath composition, and the moisture- and fluoride content in the alumina [2]. The amount of fines has also been identified as having a negative impact on cell performance [3], and finer particles are found to dissolve more slowly [4]. Kuschel and Welch [4] also noted that fines are problematic from a feeding perspective, as they can blow back as dust, never reaching the bath. While industrial, in-situ observations of alumina feeding give the complete picture, detailed and quantitative observations are challenging due to the presence of high temperatures, fumes, and process-related disturbances (i.e. feeding cycles, anodic gas bubbles, and cell operations), which disturb recordings and thereby limit the post-processing of the dissolution process.

The use of see-through cells can provide valuable insights into the interactions between alumina and bath [5] and provide a way to study effects of both bath- and alumina properties [6]. A drawback with many of these cells is the small sizes of the crucibles, limiting proper resolution of large-scale effects, such as convection patterns due to anodic bubbles. That convection enhance dissolution is also confirmed in lab studies,

S. E. Gylver ( ) · S. Aase · S. Bekkevoll · S. A. K. Forberg ·
K. E. Einarsrud
Department of Material Science and Engineering, NTNU, Trondheim,
Norway
e-mail: sindre.e.gylver@ntnu.no

S. Aase
e-mail: simeaa@stud.ntnu.no

S. Bekkevoll
e-mail: simenbek@stud.ntnu.no

S. A. K. Forberg
e-mail: saforber@stud.ntnu.no

K. E. Einarsrud
e-mail: kristian.e.einarsrud@ntnu.no

both by studying the addition of powder [4] and a sintered alumina disc immersed into the bath [7], albeit without visual observation of the dissolution process.

Water modeling is an alternative approach to study effects and interactions occurring in an electrolysis cell, as such models can be created on a real scale. Chesonis and LaCamera [8] used a full scale model to study the interface motion and how gas-driven flow affected the alumina distribution. In the case of a three-phase model (air, bath, and metal), a light mineral oil is used for the bath while the water represents the metal pad. When considering only the bath-metal interface, water and air were used. In a water-air system, where sodium chloride acted as a tracer, they could observe that gas-driven flow is more important for an efficient distribution and dissolution of powder than electromagnetic flow. The effect of current density was simulated with the release of bubbles from the anodes and was found to decrease the distribution time of alumina.

Cooksey and Yang [9] demonstrated how Particle Image Velocimetry (PIV) can be used to quantify liquid velocities and the turbulence of their physical model, which in this particular case was used to study the effects of slotted anodes. Their studies also demonstrate how PIV measurements can be used to validate models from Computational Fluid Dynamic (CFD) [10]. Rakotondramanana et al. [11] simulated and tracked the motion of a raft floating on the bath-metal interface using mineral oil and water and used PIV for verifying the movement of fluid particles. Finally, Roger et al. [12] illustrate how the Schlieren imaging can be used to observe thermal effects, in this case the freezing of liquid around cold particles. The above referenced literature illustrates that water modeling is a valuable tool for both achieving real cell size as well as for validation of theoretically derived models.

In the current work, a new water model has been developed in which alumina feeding, dispersion, and dissolution can be studied in detail. Previous models have mostly been focusing on the overall distribution and convection pattern in the cell, while this model aims to understand the interactions that occur when a dose of alumina hits the bath. Several experiments are performed with the objective of simulating the formation of rafts, using a suitable replacement for alumina, and studying how different parameters affect the formation and dispersion of the rafts. Recordings from an industrial cell at Alcoa Mosjøen are used for comparing the model to reality.

Experimental Details

Water Model

The water model represents a cross section of the center channel in an industrial cell, shown in Fig. 1. Perforated tubes, through which compressed air can be passed, are placed on both the long and short sides of the model to simulate anodic bubbles and convection along the center channel, respectively. The inner tube diameter was 2 cm with 1 mm holes placed every 2 cm, resulting in a steady bubble curtain and convection pattern. In order to represent the quasi-periodic bubbling observed industrially, cf. Einarsrud and Sandnes [13], the perforated tubes along the long side were centered in a half-pipe of sheet metal, with an inner diameter 4 cm.

The short sides of the model have separate compartments which can be filled with ice in order to maintain the temperature of the water close to its freezing point. The feeder resembles an independent (Pechiney) feeder [14] and holds up to 1 liter of powder material, which can be released by opening a lid that is controlled by pressurized air. After release, the dose proceeds to a ceramic ring representing a crater with outer diameter 28.5 cm and inner diameter 9 cm with an incline of 30°, before falling freely approximately 15 cm into the water.

A Sony Cybershot DSC-RX10 IV camera is mounted on the top of the model as shown in Fig. 1, to record the formation and disintegration of the raft.

Various organic powders were considered for representing alumina and assessed based on safety, flowability through the feeder, ability to dissolve in water without discoloring or foaming, and ability to float on water. Following the initial trials, a commercial artificial sweetener consisting mainly of maltodextrin and aspartame was selected. The sweetener has a bulk density of approximately 280 kg/m3, which gives a density ratio to water that is comparable to alumina and cryolite. It was crushed into different size fractions and stored in a freezer holding –80 °C for at least 48 h prior to addition. The temperature of the powder after being poured to the feeder was typically measured to be –50 °C. The low temperature of powder and water allowed for water to freeze around the powder upon feeding, resembling observations in industry.

In the current study, the effects of particle size, bubble frequency, and bath temperature were considered by factorial design, assigning each of the parameters low and high values, resulting in an experimental matrix shown in Table 1. High and low values of particle size (coarse and fine) are represented by the particle distributions shown in Fig. 2, water temperature was 7 and 1 °C, and the bubble frequency by air flow through the perforated tubes of 200 and 75 L/min, respectively. Three parallels were performed for each condition.

Industrial Measurements

For comparison, recordings of alumina feeding and raft formation in an industrial setting were performed at Alcoa Mosjøen. The procedure was similar as in earlier work [2], where the crust was broken to obtain a free surface for observations. Feeding was recorded with Sony Cybershot DSC-RX10 IV camera. In contrast to earlier experiments [2],

Fig. 1 **a** Image of the water model with 1: camera, 2: feeder, 3: pipes for simulating anodic bubbles, and 4: chamber for storing ice. **b** Sketch of the water model seen from above
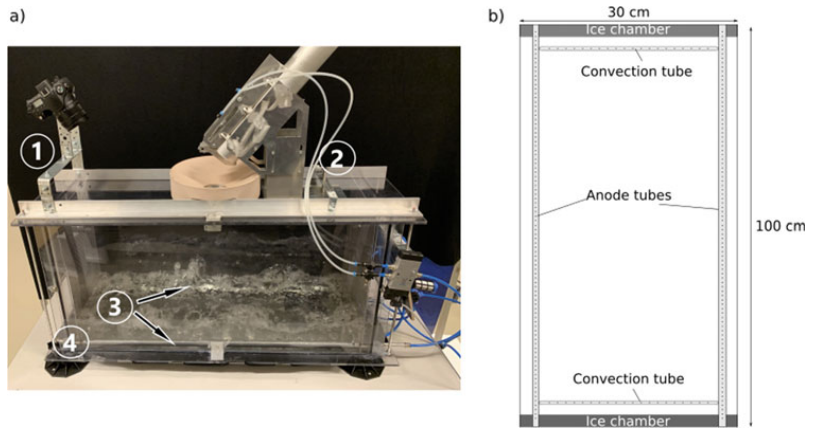
Table 1 Experimental matrix with description of the different configurations considered

Experiment	Particle size	Bubble frequency	Water temperature
1–3	Fine	Low	Low
4–6	Fine	Low	High
7–9	Fine	High	High
10–12	Fine	High	Low
13–15	Coarse	Low	High
16–18	Coarse	Low	Low
19–21	Coarse	High	Low
22–24	Coarse	High	High

Fig. 2 Size distribution (histogram) and cummulative size distribution (graphs) for the material used, measured by microscopy and post-processed with imageJ [15]
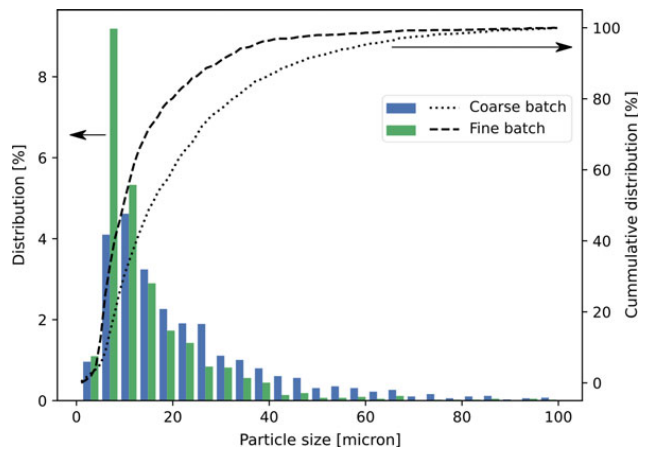
feeding was not studied close to the tapping hole, but at the transverse side of the cell. It was done in order to avoid unfavorable magnetic conditions influencing the camera, and the feeder is equally positioned relative to the anodes on this location.

Results and Discussion

Images from two selected experiments are shown in Fig. 3. By processing the images in ImageJ [15], the surface area is calculated as a function of time, shown for four of the
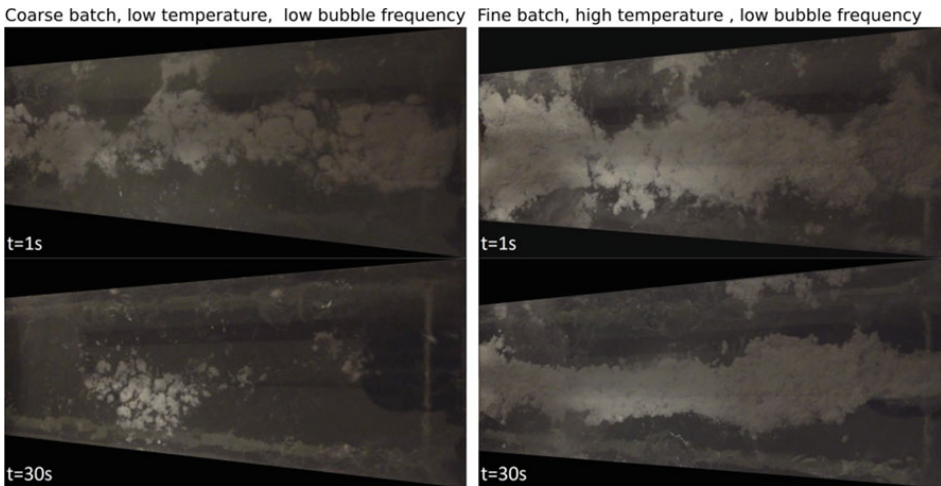
Fig. 3 Images from two of the experiments

Fig. 4 Surface area as a function
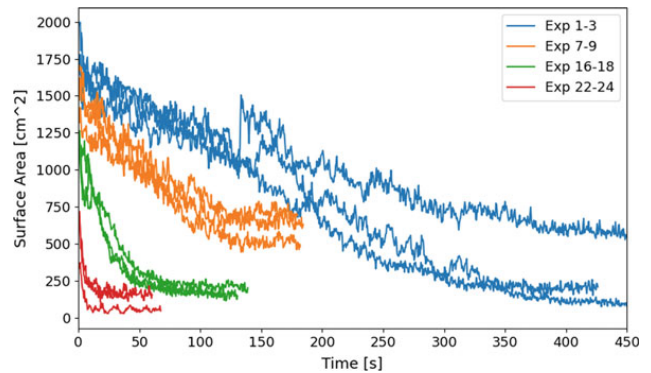of time for selected experiments

Table 2 Results from the water model experiments. The rates are calculated as cm^2/s and divided with the initial surface area

Experiment	Floating time [s]	Initial area [cm^2]	Total rate [%/s]	Initial rate [%/s]	Final rate [%/s]
1–3	530	1846	–0.13	–0.16	–0.11
4–6	303	1963	–0.24	–0.25	–0.23
7–9	192	1482	–0.27	–0.29	–0.24
10–12	258	1346	–0.18	–0.20	–0.15
13–15	65	1251	–1.21	–1.65	–0.81
16–18	123	1051	–0.62	–0.94	–0.31
19–21	50	657	–1.70	–3.27	–0.20
22–24	37	594	–1.91	–3.79	–0.12

configurations (FLL, FHH, CLL, and CHH) in Fig. 4. Some disturbances, such as sunken powder and light reflections from bubbles will be processed as raft imageJ, explaining why the graphs never reach zero in Fig. 4. As seen in the figures, the floating times, initial surface area, and dissolution rates vary in the different configurations. Average results for each configuration are summed up in Table 2. The total dissolution rate is calculated as a linear regression between the initial and end times of the dissolution curves, while the initial and final rates are calculated from the first and second half of
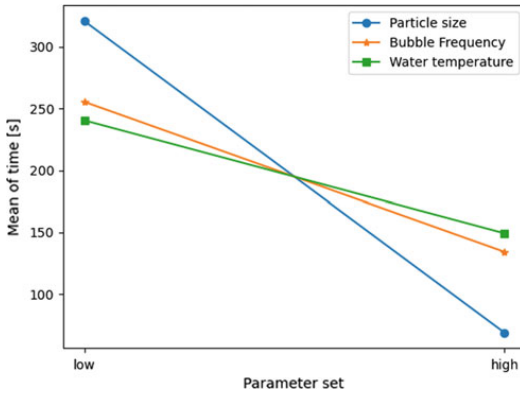
Fig. 5 Calculated main effects of the three different parameters

the floating time, respectively. All of the rates in the table are relative to the initial surface area.

By using floating time as a response, the main effects of different parameters can be calculated, shown in Fig. 5. Particle size has the highest effect on the floating time, followed by bubble frequency and at last bath temperature. Also, in the cases of the fine batch, the effect of convection and temperature is larger than that for coarse particles, which can be seen by comparing the difference of experiment 1–3 and 7–9 with 16–18 and 22–24 in Fig. 4, indicating that there are interactions between the parameters.

The different particle sizes represent the amount of fines present in a batch of alumina. It is expected that a higher amount of fines results in slower dissolution. By the rates calculated in Table 2, the dissolution for the cases of more fines (Experiment 1–12 in Table 2) has a gradual decrease over the whole floating time, while the coarse batch experiences a larger initial slope. The initial surface area from fines is also larger than coarse batch, indicating poorer dispersion and wetting for fines. The chosen powder has some differences in both particles sizes and microstructure, but the behavior still resembles what has been observed in industrial cells. Fines have been found to have a negative impact on operations [3] and dissolve more poorly in lab experiments [4].

Higher bubble frequency reduced floating time and initial surface area, due to more convection enhancing dispersion and aiding in breaking the rafts. This is in accordance with what has been observed in lab experiments [4, 7] and industrial cells [2], where a correlation between anode age and bubble frequency was adopted. It should be noted that the aim of the current work was to investigate the (relative) effect of bubble induced convection rather than a quantitative assessment of specific velocities. As such, similarities between bubble behavior and size in the water model and industrial cell were not assessed further.

Increased bath temperature also led to an decrease of the raft floating time, although less than the particle size and bubbles. If assuming equal Stefan numbers for the water and cryolite, defined as

$$Ste = \frac{C_p}{L} \cdot (T - T_M) \quad (1)$$

where C_p and L are the specific heat capacity and the latent heat of fusion, respectively, and the term $T - T_M$ becomes the superheat of the system. The superheats for the water model at 1 and 7°C will then be calculated to be 3.5 and 24.6 for molten cryolite. The latter one is far higher than what is normal in industrial operations, meaning that the effect might be even smaller when considering a real interval. Superheat was not found to influence raft floating time in an industrial cell [2], and recent experiments found its effect on the dissolution flux to be smaller relative to convection and additives [7].

Figure 6a shows images from feeding in an industrial cell, while Fig. 6b shows the surface area as a function of time, processed the same way as the recording from the water model experiments. Recordings of several feeding events were performed, but disturbances in the images, in particular from fumes, resulted in that only a single recording had sufficient quality for post-processing.

Although observed from a different location, the floating time of the formed raft corresponds to what has been observed in the same type of cells [2] previously, and the curve shown in Fig. 6 is assessed as being representative. The behavior observed in industry resembles observations in the water model. In both cases, a raft is spreading out on the available surface, followed by a decrease in the surface area from the sides. In some cases, in particular for the fine batches, parts of the raft sink down to the bottom of the cell, which is similar with the formation of sludge.

The initial rate relative to the surface area was calculated to be –2.34 % per s in the industrial measurement, which by comparing with Table 2 is closest to experiments 19–24. Earlier observations have observed floating time varying between 5 and 140 s, corresponding to the experiments with coarse particles.

Conclusions

The current work simulated alumina raft formation using a water model, using an organic powder as a substitute for alumina. Rafts formed in this setup have floating times varying between 35 and 550 s and show similar behavior as those formed in an industrial cell. PSD, bubble frequency, and water temperature were varied and every parameter was found to have a significant effect on the floating time of the raft, with
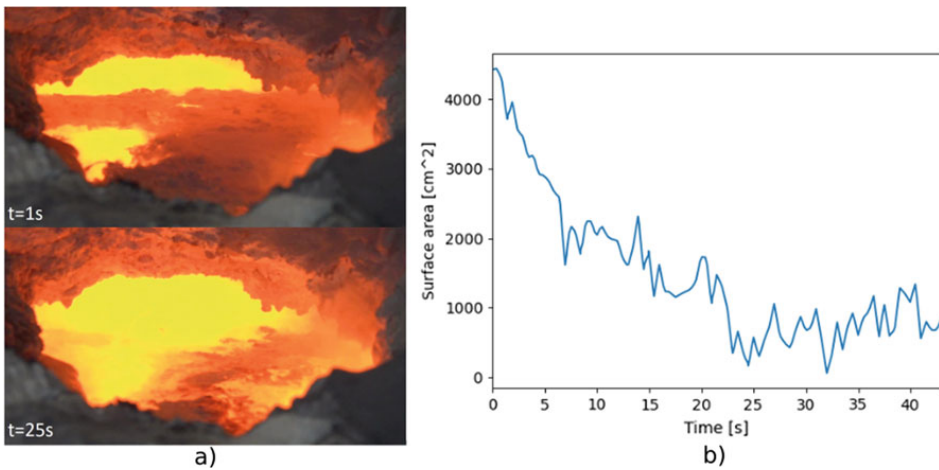
Fig. 6 **a** Images from recording of feeding in an industrial cell and **b** the observed surface area as a function of time

particle size being the most important one; reducing the D_{50} by 50% leads to an almost five-fold increase in dissolution time.

The behavior, dissolution rates of the visible surface area as well as the floating times are found to be in the same order for the coarse grained batch and rafts formed in an industrial cell. The first half of the dissolution rate is found to be higher than the second one. Fines are found to cover a larger amount of available surface area and dissolve more slowly and at a more constant rate than the coarse batch. Future work will aim to investigate whether similar tendencies can be found also in experiments based on see-through cells.

References

1. S. E. Gylver et al., "The Micro- and Macrostructure of Alumina Rafts," in *Light Metals 2019*, 2019, pp. 689–696.
2. S. E. Gylver, N. H. Omdahl, A. K. Prytz, A. J. Meyer, L. P. Lossius, and K. E. Einarsrud, "Alumina Feeding and Raft Formation: Raft Collection and Process Parameters," in *Light Metals 2019*, 2019, pp. 659–666.
3. S. J. Lindsay, "Key Physical Properties of Smelter Grade Alumina," in *Light Metals 2014*, J. Grandfield, Ed. Hoboken, Wiley, 2014, pp. 597–601.
4. G. I. Kuschel and B. J. Welch, "Further Studies of Alumina Dissolution under Conditions Similar to Cell Operation," in *Essential Readings in Light Metals: Volume 2 Aluminum Reduction Technology*, G. Bearne, M. Dupuis, and G. Tarcy, Eds. Cham: Springer International Publishing, 2016, pp. 112–118.
5. L. Bracamonte, V. Aulie, C. Rosenkilde, K. E. Einarsrud, and E. Sandnes, "Dissolution Characteristics and Concentration Measurements of Alumina in Cryolite Melts," in *Light Metals 2021*, Cham, 2021, pp. 495–503.
6. Y. Yang, B. Gao, Z. Wang, Z. Shi, and X. Hu, "Effect of Physiochemical Properties and Bath Chemistry on Alumina Dissolution Rate in Cryolite Electrolyte," *Journal of Metals*, vol. 67, no. 5, pp. 973–983, May 2015.
7. J. Alarie, L. I. Kiss, S. Poncsák, R. Santerre, S. Guérard, and J.-F. Bilodeau, "Influence of Additives on Alumina Dissolution in Superheated Cryolite Melts," in *Light Metals 2021*, 2021, pp. 533–540.
8. D. C. Chesonis and A. F. LaCamera, "The influence of gas-driven circulation on alumina distribution and interface motion in a Hall-Heroult cell," in *Light metals 1990*, 1990, pp. 211–220.
9. M. A. Cooksey and W. W. Yang, "PIV measurement on physical models of aluminium reduction cells," in *Light Metals 2006*, 2006, pp. 359–365.
10. Y. Q. Feng, W. Yang, M. Cooksey, and M. P. Schwarz, "Development of Bubble Driven Flow CFD Model Applied for Aluminium Smelting Cells," *The Journal of Computational Multiphase Flows*, vol. 2, no. 3, pp. 179–188, Sep. 2010
11. L. Rakotondramanana et al., "Mass Transport by Waves: Bath-Metal Interface Deformation, Rafts Collision and Physical Model," in *Light Metals 2021*, 2021, pp. 344–350.
12. T. Roger et al., "Development of a Mathematical Model to Simulate Raft Formation," in *Light Metals 2020*, 2020, pp. 688–695.
13. K.E. Einarsrud and E. Sandnes, "Anodic Voltage Oscillations in Hall-Heroult Cells," in *Light Metals 2011*, 2011, pp. 555–560.
14. J.L Gerphagnon and C. Wolter, Aluminium Pechiney, "Assembly for Spot Feeding Alumina to an Elctrolytic Tank for the Production of Aluminium", Patent US 4,437,964, AU B-14958/83, FR 8209700, 1984
15. W. S. Rasband, ImageJ. Bethesda, Maryland, USA: U. S. National Institutes of Health, 1997. Accessed: Jun. 17, 2021. [Online]. Available: https://imagej.nih.gov/ij/

Paper IV

This paper is awaiting publication and is not included in NTNU Open

Paper V

Article

The Formation and Disintegration of Rafts from Different Aluminas and Fines

Sindre Engzelius Gylver [1,*], Simen Bekkevoll [1], Stein Rørvik [2] and Kristian Etienne Einarsrud [1]

[1] Department of Materials Science and Engineering, Norwegian University of Science and Technology NTNU, NO-7491 Trondheim, Norway
[2] SINTEF Industry, Metal Production and Processing, NO-7465 Trondheim, Norway
*   Correspondence: sindre.e.gylver@ntnu.no; Tel.: +47-48252061

Abstract: Raft formation is a frequently encountered problem during alumina feeding in the Hall-Héroult-process and will delay alumina from being dissolved into the melt. The mechanisms for the formation and disintegration of rafts are however not thoroughly understood yet. The current study investigates the dissolution behavior and raft structure from three different types of secondary alumina in a lab cell, with a particular attention to effect of fines, and involves both sampling of rafts and video recordings of the feeding. The mass loss rate was calculated to vary between -1.57 and -0.42 g min^{-1} for regular bulk alumina, and -1.15 and -0.06 g min^{-1} for fines. Rafts created from bulk alumina were flat with a distinct bulge or crater placed in the center of it, while rafts created from fines had a pellet-shaped structure and traces of undissolved alumina in the middle. The observed structure is due to the initial spreading of powder, confirmed by video recordings.

Keywords: aluminum production; alumina feeding; raft; fines

1. Introduction

Aluminum is today produced by the Hall-Héroult-Process, where alumina is dissolved into a cryolitic melt and aluminum is formed by an electrochemical reaction together with carbon:

$$2Al_2O_3(diss) + 3C(s) \rightarrow 4Al(l) + 3CO_2(g). \tag{1}$$
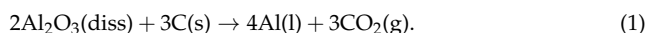
The process is carried out at approximately 960 °C, and alumina is added regularly from point feeders, placed at one or several position in the cell. Ensuring an efficient dissolution and distribution of alumina is important in order to maintain stable operations. When added to the melt, some particles might agglomerate together and create rafts, consisting of alumina and frozen bath. These rafts hinders contact between powder and liquid, and must hence disintegrate and the frozen bath must melt in order for alumina to be further dissolved [1].

Studies of rafts have been intensified over the last years, and formation of rafts has been recorded in industrial cells [2], where bath circulations and temperature were found to affect the raft floating time, together with the moisture and fluoride content of the alumina. By extracting samples from the cell and further processing them by micro X-ray computed tomography (μCT) , it is revealed that the rafts are porous structures with an average density of 1.76 g/cm^3 and a porosity of 12.72% [3]. Earlier results by Walker et al. [4] found the apparent density of collected agglomerates to be between 2.2 and 2.4 g/cm^3 and porosities between 24.7 and 22.8% in the time span of 15–60 s. However, both the sampling technique and characterization method is different, which might be the cause of the varying results.

The effect of different parameters has mainly been studied at lab scale, where one of the largest studies has been conducted by Kuschel and Welch [5,6]. They observe that the cell conditions, in particular electrolyte velocity and superheat, can affect the

dissolution time with 300–500%. The alumina properties can affect the dissolution time by approximately 50%, and properties summarized to promote fast dissolution were a high volatile content, i.e., high loss on ignition (LOI), and low flow funnel time, where the latter one is closely related to particle size distribution (PSD). It is in accordance with findings by other researches [7,8]. Fines have been reported to be problematic in operations [9], as they are harder to transport and feed to the cells, and poorer wetting will inhibit dissolution.

Bath properties will also affect the dissolution rate, and recently, Alarie et al. [10] developed an empirical equation based on results from their own [11] and several other research groups [7,12–14], where only the bath temperature, AlF_3- and Al_2O_3-content were found to be significant, and is used as input parameters.

Retrieving samples from a lab-cell has been conducted in earlier work, where rafts with a similar structure as industrial one were collected, and the effects of alumina temperature [15], adsorbed water content and dry-scrubbing have been studied [16]. From the latter one it was observed that rafts created from secondary alumina had a higher porosity than those formed from primary. This is in accordance with studies on alumina crusts [17], where a lower density and hence higher porosity were found, and it was concluded that carbon content in the powder was the origin of the pores. Kaszás [18] did however find that rafts from alumina with a higher content of moisture were more porous.

Equipment suitable for observing the alumina addition has also become more common in recent years. The development of see-through cells, containing a quartz crucible which becomes transparent when heated up, and enables the opportunity for observing dissolution from the side. When secondary alumina is added, the powder stays on the interface before particles and fragments sink into the bath and are gradually dissolved [19,20]. It is believed that the effect of volatiles, in particular carbon dust, is emphasized as an important parameter for faster dissolution in these setup [21].

Kaszás et al. [22] recorded the spreading and disintegration from above in a 7.6 cm × 7.6 cm squared crucible, and provided image analysis to measure the visible surface area, which was found to be between 25 and 20 cm^2 5 s after addition. A rapid decrease in surface area was observed for the first 25 s after feeding, before stabilizing with a more or less constant surface area. For the addition of 1 g alumina, the powder gets fully wetted within the first 10 s after addition, and rafts stay afloat on the surface for a long period, up to 5 min for 1 g additions and 10 min for addition of 2 g. Later, the effect of adding carbon to alumina was studied [18]. A challenge for this setup is to preserve heat, and the top was therefore covered with a plate of quartz during parts of the experiments.

The current work studies the dissolution and the structure of rafts formed from different types of secondary alumina and their corresponding fraction of fines. Experiments with these types have already been carried out in a see through-cell [20,23], hence gaining a foundation for comparison of different setups.

2. Methods and Materials

2.1. Materials

For each alumina used in the current work, two batches denoted as bulk and fines will be considered. The bulk alumina represents the alumina used in the industry, with a typical PSD between 0 and 250 μm. Alumina fines consist of sieved out alumina grains with a particle size ≤ 45 μm. The PSD is obtained by laser diffraction with the results displayed in Figure 1, analyzed by Hydro Aluminium.

Physicochemical properties are given in Table 1, while the content of impurity elements are shown in Table 2. Moisture on ignition (MOI) and LOI were measured using the ISO-standard, while the other properties were determined by Hydro Aluminium, using industry standard measurements.

The industrial bath was also analyzed by Hydro Aluminium, where the most essential features of the bath are listed in Table 3 with liquidus and solubility limit estimated from empirical Equations [24,25].
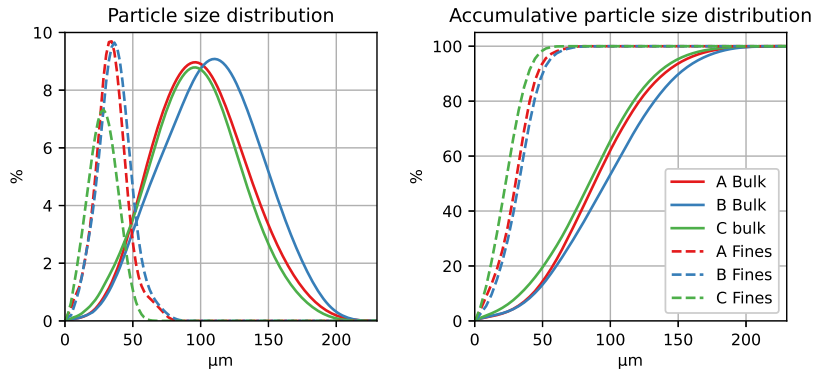
Figure 1. PSD of the different aluminas displayed to the left, and accumulative PSD to the right.

Table 1. Selected alumina properties.

Alumina Type	LOI (1000 °C) [%]	MOI (300 °C) [%]	BET Surface [m²/g]	α Alumina [%]	γ Alumina [%]
A bulk	1.86	1.5	73.9	1.2	39.7
B bulk	2.11	2.65	65	2.5	37.2
C bulk	2.33	1.7	69.8	1.8	38.1
A fines	4.54	1.84	55.2	4.5	35
B fines	5.59	2.33	43.8	9.3	30.4
C fines	5.03	1.36	52.4	7.4	32

Table 2. The content in wt% of the different elements found in alumina samples.

Alumina	F	C	S	Na	P	Ca	Fe
A bulk	1.2	0.22	0.32	0.5634	0.0017	0.0129	0.0127
B bulk	1.75	0.24	0.24	0.5389	0.0021	0.018	0.0194
C bulk	1.96	0.26	0.21	0.5089	0.0023	0.0086	0.0123
A fines	4.69	1.74	0.23	1.6868	0.0174	0.1105	0.1065
B fines	5.21	2.52	0.23	1.6568	0.0125	0.0883	0.0845
C fines	4.55	2.04	0.26	1.367	0.0107	0.0548	0.0661

Table 3. Chemistry and calculated properties of the industrial bath at initial concentrations.

Bath Chemistry	
Bath acidity [wt%]	10.6
CaF$_2$ [wt%]	5.34
Al$_2$O$_3$ [wt%]	3.82
Bath Properties	
Superheat	13.5
Liquidus temperature [°C] [24]	956.5
Bath temperature [°C]	970
Al$_2$O$_3$ solubility limit [wt%] [25]	8.62

2.2. Setup

Both raft sampling experiments and video recordings were conducted in the same customized tube furnace with an open top, sketched in Figure 2a). The furnace body consists of a steel pipe with an inner diameter of 15 cm and is heated with an element winded around its body. The outer shell of the furnace is coupled to a water-cooled system and thermal insulation is put on the top to preserve heat as long as practical possible. A carbon crucible with an inner diameter of 10.5 cm is placed inside the furnace body, filled with 1500 g of industrial bath. Nitrogen gas is purged into the furnace environment to avoid oxidation and air burn of the carbon crucible. A thermocouple (S-type) is placed inside a steel tube to monitor the bath temperature regularly, approximately 4 cm below the bath surface. Alumina is fed through a 50 cm long steel pipe with an inner diameter of 1 cm with a spring-driven lid at the end, operated by a knob at the top. The dose is released 5 cm above the bath surface, and one dose of 4 g alumina is fed each time, both for raft sampling experiments and video recordings. Following the extraction of a raft, the bath surface was cleared mechanically and the system was allowed to reach the sought operating temperature before a new batch was fed. Typically, the time interval between the feedings was 30–45 min.
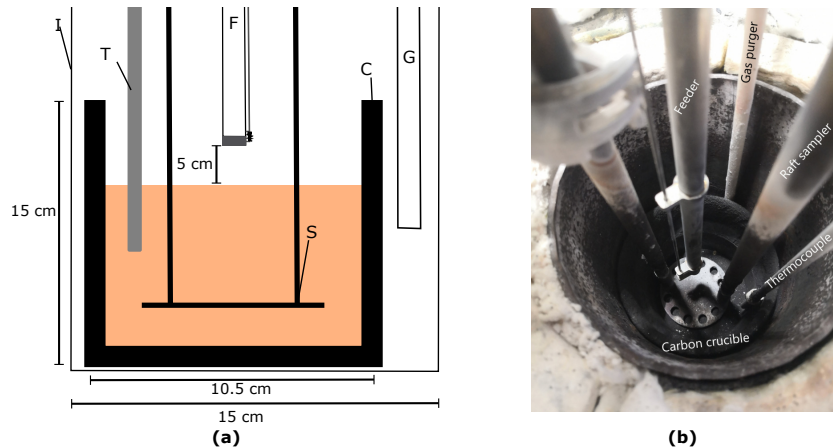

Figure 2. (**a**) Cross sectional illustration of the furnace. **I** represents the furnace body with its inner diameter, **C** is the carbon crucible with dimensions, **G** is the pipe used for gas purging, and **S** is the sampler used for raft sampling. **T** is the tube holding the thermocouple, and **F** is the feeder. (**b**) The experimental setup in cold conditions with all the equipment used.

A custom designed raft sampler is used to collect the rafts formed on the bath surface and is immersed into the melt prior to alumina feeding. It is made of stainless steel and consists of an 8 cm diameter plate, with ten holes of 1 cm diameter drilled around its periphery. Two solid steel rods are welded onto the steel plate to work as handlebars when the sampler is lowered and raised in the melt. An image of the experimental setup for raft sampling is shown in Figure 2b). Rafts are retrieved from the melt after 60 and 180 s, and a minimum of 5 rafts from each time interval were sampled.

Selected raft samples were analyzed using micro-computed X-ray tomography (μCT). The μCT data was acquired by a Nikon C1 compact large-envelope 5-axis X-ray μCT instrument (cone beam volume CT). A tungsten 225 kV UltraFocus reflection target was used, with an acceleration voltage of 125 kV and a current of 175 μA. The X-rays were not filtered. The imaging was done with an integration time of 250 ms, amplification of 18 dB, with 6283 projections per 360°. The detector panel in the instrument is a Varex 1621 EHS with 2000 × 2000 pixels of size 200 × 200 μm, total panel size 40 × 40 cm^2. The distance from source to sample was 174.06 mm, distance from source to detector was 772.78 mm,

resulting in a voxel size of 90.1 μm. The images were exported as 16-bit TIFF and processed in the public domain software ImageJ [26] using scripts developed at SINTEF.

Minor changes in the experimental setup are done to facilitate video recording of the dissolution process. A GoPro Hero8 Black camera is used to record the surface, and is placed inside a transparent camera house mounted to a flexible arm attached to the frame holding the furnace set-up. To limit the disturbance of fume during recording and ensure some cooling of the camera house, a fan was placed under the flexible arm holding the camera, as seen in Figure 3. The recording and the sampling experiments were conducted separately from each other, as the sampler would hinder the view for the camera.

Lastly, experiments at room temperature were conducted, where alumina was released from 5 cm onto a flat surface with the same feeding pipe as described earlier.

Figure 3. Image of the experimental setup with the camera placed above the surface opening.

3. Results

The mass gain, interpreted as the mass of the raft subtracted from the total dose added, is plotted in Figure 4, including a 95% confidence interval. The mass loss rate for the types with its 95% confidence interval is given in Table 4.
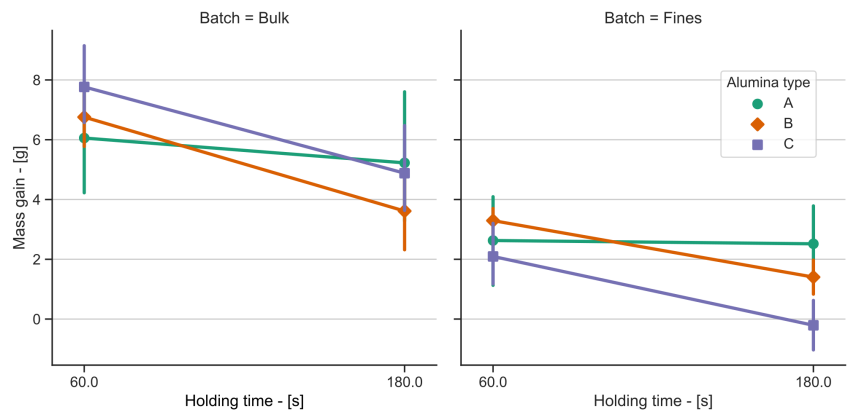

Figure 4. Mean mass gain of rafts, given as the difference between raft weight and mass alumina added, for bulk (**left**) and fines (**right**) of the three alumina types A, B and C. The error bars indicate the 95% confidence interval.

Table 4. Mass loss rates and 95% Confidence interval for the different alumina types.

Batch	Type	Mass Loss Rate [g/min]	95% Confidence Interval
Bulk	A	−0.42	[−2.04, 1.21]
	B	−1.57	[−2.64, −0.50]
	C	−1.44	[−2.61, −0.28]
Fines	A	−0.06	[−1.32, 1.21]
	B	−0.94	[−1.41, −0.48]
	C	−1.15	[−2.04, −0.27]

Figure 5 states the correlation coefficients between the mass gain at 60 s holding time and selected parameters. Correlation between other parameters are also shown in the same figures.
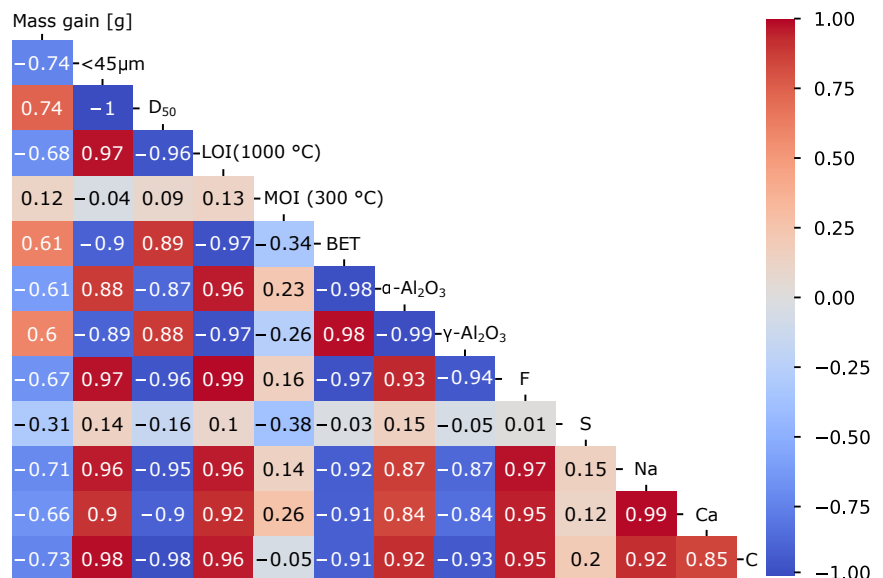

Figure 5. Correlation coefficients between selected parameters and the mass gains of samples after holding time 60 s. <45 μm is fraction of grains below 45 μm, while D_{50} corresponds to the width of the particle size distribution curve shown in Figure 1.

Three cross-sectional CT-images are shown in Figure 6 for two rafts from bulk alumina after 60 and 180 s and one raft created from fines. The grey values are proportional to the X-ray linear attenuation at the given volume point. The linear attenuation coefficient depends on both the density and the atomic weight of the material; where the atomic weight has a higher influence than the density. Average apparent porosity measurements between bulk, fines and holding time are displayed in Figure 7, reported as a percentage of pores relative to the entire volume of the sample (including the pores). Density is calculated as the measured mass of raft divided by the volume obtained from CT-analysis, and was on average 2.25 g cm^{-3} for bulk and 2.18 g cm^{-3} for fines. No significant difference between the different types was seen, and it was therefore chosen to only compare bulk and fines in general.
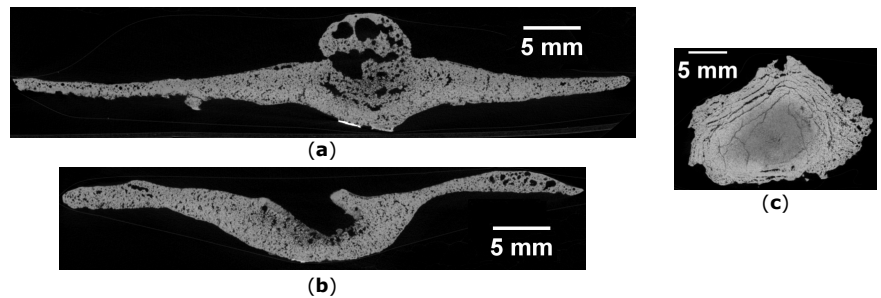
Figure 6. Cross-sectional CT images of selected rafts, where the raft's top is facing upwards. (**a**) Raft from bulk alumina with holding time 60 s. (**b**) Raft from bulk alumina with holding time 180 s. (**c**) Raft from fine alumina with holding time 60 s.
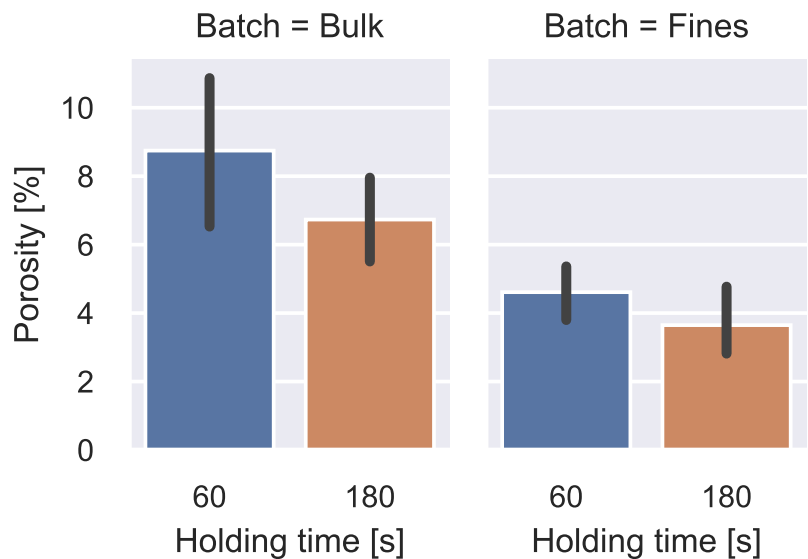

Figure 7. Mean porosity for the bulk and fine samples for the different holding times, reported as a percentage of pores relative to the entire horizontal cross-sectional area of the sample (including the pores).

CT images provided the opportunity to generate 3D plots of the rafts, using the "Interactive 3D Surface Plot" plugin in ImageJ. The 3D plots are generated from projection images, representing the average attenuation values in the Z-direction, shown in Figure 8d). By processing the images further, values corresponding to density and thickness of the rafts can be obtained, showed, respectively, for (b) and (c) in Figures 8 and 9.
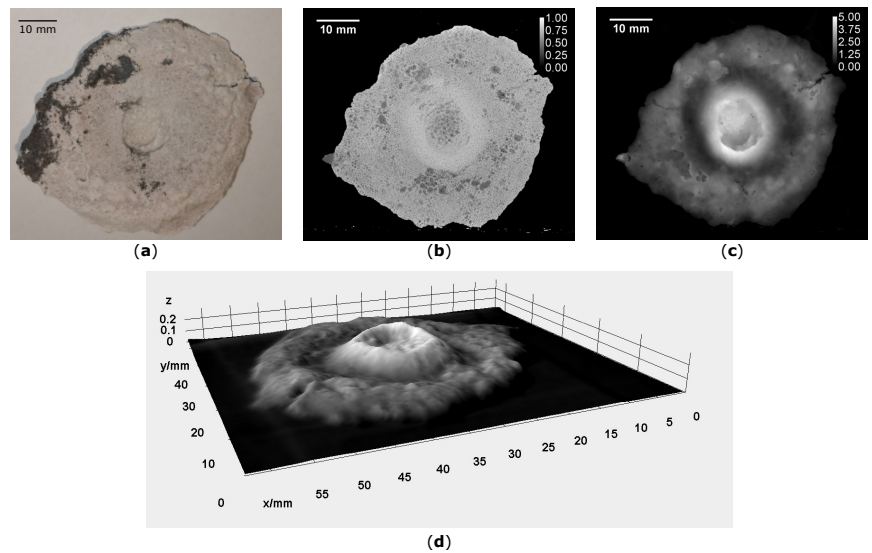
Figure 8. Images of a raft from alumina bulk type B. (**a**) Image of raft from above. (**b**) Projected CT image of the raft seen from above, displaying the average density. (**c**) Projected CT image of the raft seen from above, displaying the thickness of the raft.The scale is given in mm. (**d**) 3D-image plot seen from the side.
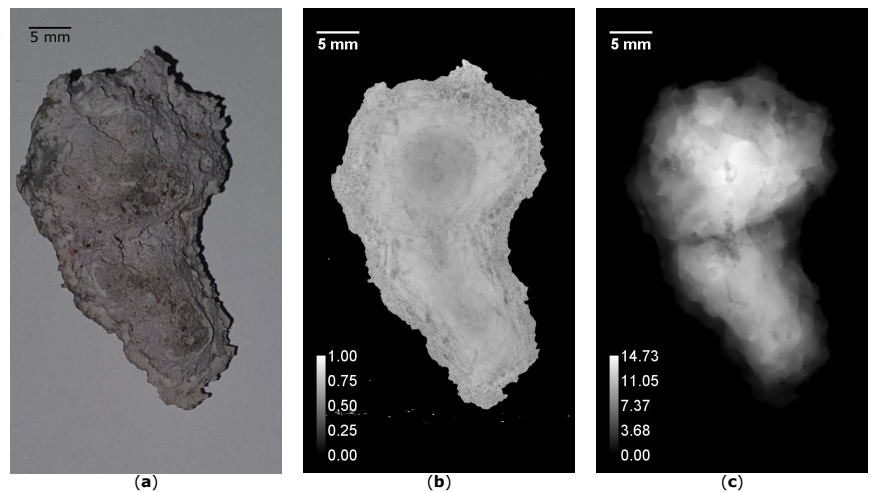

Figure 9. Images of a raft from alumina fines type A. (**a**) Image of raft from above. (**b**) Projected CT image of the raft seen from above, displaying the average density. (**c**) Projected CT image of the raft seen from above, displaying the thickness of the raft. The scale is given in mm.

One video recording of each of the alumina types from the bulk and fines batch was performed during the experimental session. The videos were later treated in ImageJ [26] to measure raft area as a function of time. As the quality of the recordings was not adequate for a fully automated image analysis, raft area was measured by using a brushing tool in ImageJ on the slides with sufficient quality. The measurements performed in ImageJ are displayed in Figure 10, where the time axis is logarithmic to visualize initial dispersion better. The sinking of small subrafts denoted as a, b and c, are shown in detail in Figure 11. Selected images of the initial raft formation from fines are shown in Figure 12.
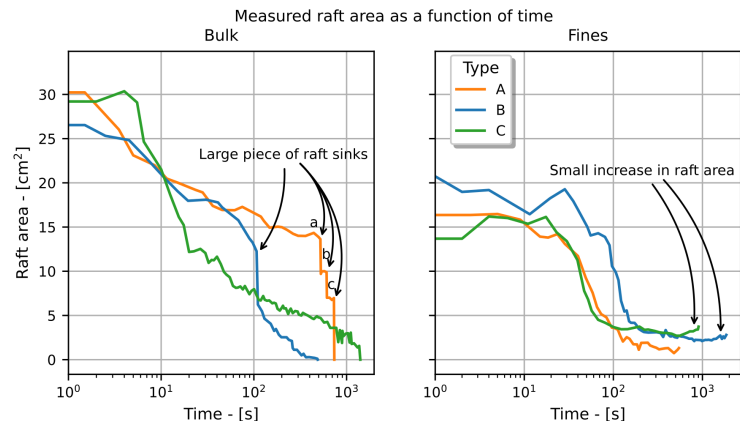
Figure 10. Measured raft area as a function of time, where a, b and c denotes sinking of rafts pieces, which can be seen more detailed in Figure 11.
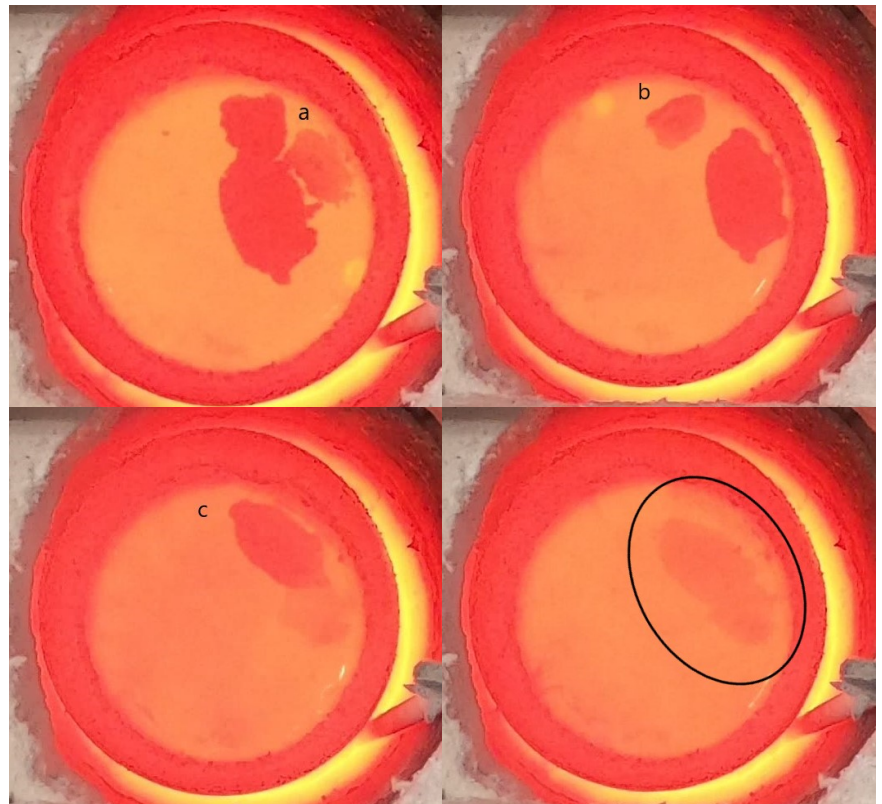

Figure 11. Images of descending subrafts (**a**–**c**) of bulk alumina type A, denoted in Figure 10. In the last frame, it is possible to see the descended rafts on the bottom of the crucible.

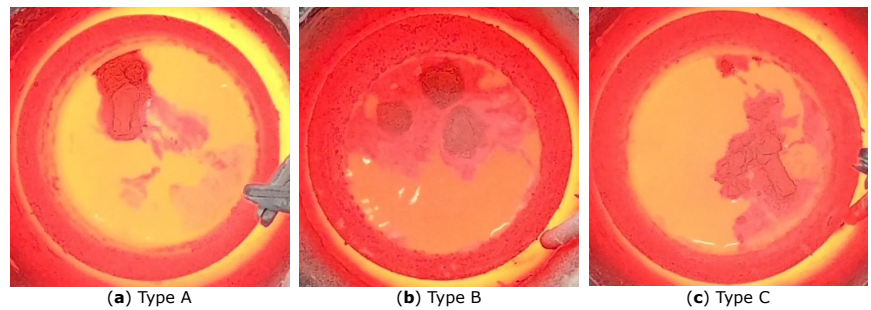(**a**) Type A   (**b**) Type B   (**c**) Type C

Figure 12. Selected images from the video recording of fines, selected from right after feeding to display the dispersion.

Initial dissolution rate in Table 5 is calculated as the rate the surface is disintegrated in $cm^2\ s^{-1}$ at steepest part of the curve in Figure 10, normalized with the initial surface area.

Table 5. Initial rate of surface dissolving in $cm^2\ s^{-1}$ at steepest part, set relative to the measured area of raft a t = 0 s.

Type	Batch	Initial Dissolution Rate [%/s]
A	Bulk	−0.38
	Fines	−0.08
B	Bulk	−0.54
	Fines	−0.13
C	Bulk	−0.57
	Fines	−0.09

When a dose was fed on a flat plate, it spreads out as a circular structure, shown in Figure 13. A similar structure was seen for fines, although it spread out more poorly and created a higher heap.

Above   Side
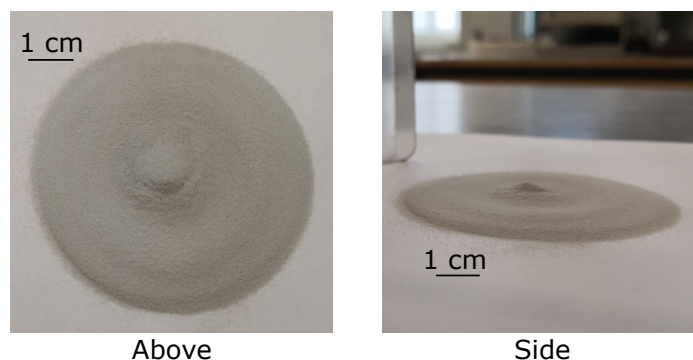
Figure 13. Results of cold experiments for bulk alumina, type A.

4. Discussion

There are characteristic differences between the rafts collected from bulk and fines. Rafts created from the bulk have more than doubled in size relative to the amount added (4 g), where the increased mass must be due to bath freezing around the cold particles, while the mass gain for fines are significantly lower, in particular after 60 s. Rafts created from fines are shaped as compact pellets, being smaller in size and mass, seen in Figure 9a).

Bulk alumina disperse well on the bath surface to form larger disc-shaped rafts of frozen bath and alumina, floating on the bath surface with a distinctive bulge or crater at the center, as seen in on the CT-images of bulk alumina in Figure 6. The darker gray scale at the center of the raft from fines shown in the same figure indicates unsaturated alumina at the core encapsulated with frozen bath around it. The video recordings support this where the powder stays together in one or a few lumps.

The dissolution behavior of different types investigated seems to vary. As seen in Table 4, alumina type B and C have calculated mass rates which are significant below zero, while this is not the case for type A. A similar tendency is seen for the corresponding fines for the different types as well, and the initial dissolution rate from the video recordings (Table 5) also indicates that A disintegrate slower at the beginning.

The correlation matrix in Figure 5 shows that the increased fraction of fines decreases the mass of formed rafts at a holding time of 60 s, with a similar trend seen at 180 s. In this setup, fines generate smaller rafts, but in general, fines have a negative impact on the dissolution, also seen by the lower rates in Table 4. Figure 5 also reveal that fines are closely related with several of the other parameters and it is therefore not possible to conclude if any other of the parameters affect the mass of the formed raft.

The errorbars in Figure 4 and confidence intervals in Table 4 reveal that there still is variation present in the dataset. As commented by Kuschel and Welch [5] operating conditions, in particular superheat and convection will affect the dissolution rate in a larger degree than alumina properties. In the current setup, it was not possible to monitor the temperature or observe the bath surface during the sampling experiments. As such, the observed variation may be due to these factors.

Earlier work in same setup [15] calculated a dissolution rate of 0.8 g/min, which is in the same order as the current experiments. Since the lab conditions are within the validity range of the model by Alarie et al. [10], predicted dissolution rate can be calculated and compared with the observed one. Assuming the $\dot{m}_{ref} = 2.4689$, the predicted dissolution rate will be 0.63 g min^{-1} for all the types, as the empirical equation only uses bath properties as variables. Four out of six of the rates are found to be above predicted one, which should be expected, as the rate calculated in these set of experiments are not the actual dissolution rate of alumina, but rather the mass loss rate of rafts, which will include melting of bath. Therefore, the current dissolution measurements, at least for type B and C are within an expected range.

Common for all rafts from the bulk is the porous structure with irregularities in pore size and shape as seen in Figure 6. Larger cavities are mostly observed at the centre bulge, with some randomly scattered pores varying in size in the periphery. Additionally, all rafts from the bulk have a similar grayscale throughout the sample, indicating that the sample has a relatively homogeneous composition of bath and alumina. The calculated porosity shown in Figure 7 is higher for rafts from bulk aluminas after 60 s. A probable cause for the behavior can be seen in Figure 6, where a large pore is located inside spherical lump, which is melted away after 180 s for most samples. Earlier results in the same setup [15,16] have found porosity values around 8%, which is similar with the findings in this work.

The 3D-images give valuable information of the raft structure. For the bulk alumina, the darker areas in (Figure 8b) shows pores, which is scattered around the rafts. In addition (Figure 8c) shows that the rafts is at its thickest at in the middle. Disintegration will therefore begin from the sides, since it is the most porous and thinnest areas. Rafts from fines (Figure 9) are thicker and fewer pores, and will hence disintegrate more slowly. Another interesting finding is the similarities between the rafts (Figure 9) and the cold experiments shown in Figure 13. This indicates that the addition method is the dominating factor for the raft shape, not solidification of bath.

Video recordings provide valuable observations of the raft formation and alumina dissolution. As seen from the recordings and the images, well-dispersed alumina dissolves immediately or relatively fast within the first 30–60 s, while agglomerate forms to stay afloat on the bath surface. Raft A (Figure 11) is disintegrated into smaller parts that sink to

the bottom of the crucible, while a large piece sinks for type B, seen in Figure 10. This in accordance with observations from the see through cell [19,20]. Similar tendencies are also seen when recording from above [22] with a faster dissolution the first 25 s after addition, and sinking of rafts at the end.

The small pellets from the fines managed to stay afloat until the camera shut down due to overheating. No distinct difference in dissolution rate and behavior could be seen from the curves in the graph from Figure 10. The end of the curves shows a small increase in surface area for types B and C, due to a lack of heat at the bath surface. Insufficient heat causes more bath to freeze onto the floating raft, preventing it from sinking into the melt as it becomes more hydrostatically stable, an issue also faced by Kaszás et al. [22]. The dissolution might also be delayed as the bath close to the raft gets saturated with alumina and will not be transported away from the raft, due to small degree of convection present.

Considering the findings of Bracamonte [23], who studied the same alumina types in their dissertation, observations of the dissolution process are very similar to the ones obtained in this work. For the bulk alumina, type A had the best dispersion on the bath surface as it tended to form rafts with a large surface area, but dissolved slower. Alumina B and C dissolved faster, and no significant difference is found between them. The fine alumina showed less dispersion after feeding and was found to have a more compact crust characterized by a finer porosity, i.e., smaller pores, which is also observed in the CT images. The main deviation are trends in dissolution behavior across batches for alumina type A, where Bracamonte did not notice any significant difference between the bulk and fines for alumina type A during their experiments, contrary to the result in the current experiments. In this setup, the added amount of alumina relative to the bath volume is much lower creating one or several floating rafts, while in the see-through cell a crust like structure was created on the top.

5. Conclusions and Further Work

The current work has investigated the raft formation of different alumina types, with a special attention of rafts formed from the fine particles in a batch. In this setup, the types exhibited different behavior for raft formation. Type A had the best initial dispersion, but its mass loss rate was slower. It is however not possible to conclude why type A is behaving different. The surface properties of the particles is not investigated in this work, and will be considered in further work.

Rafts formed from fines were initially smaller than those formed from bulk, with an average mass loss rate of -0.71 vs. -1.15 g min^{-1}. CT revealed that the rafts from fines are more inhomogeneous, with powder encapsulated within a layer of frozen bath. The reduced spreading of powder results in lesser freeze of bath, and thus a reduced mass gain. The fraction of fines were in this work found to be correlated with multiple of the other properties investigated, and it is thus not possible to identify if there are any other parameters that affect the mass gain of rafts.

Recordings from above reveal that the shape of the raft is mainly dependent on how the powder spread out when added, and comparison with cold experiments supported it. Solidification of bath and agglomeration then strengthen the structure and disintegration will further occur from the sides.

In a real cell, convection is created by gas bubbles generated under the anodes and movement in the metal pad caused by magnetic fields, and is found to affect the dissolution in a larger degree [5] than alumina properties. This might be the case for the disintegration and dissolution for rafts as well. Performing further experiments with stirring should therefore be considered, although it might requires a change in sampling technique.

Data Availability Statement: The data presented in this study are available on request from the corresponding author.

Conflicts of Interest: The authors declare that they have no conflict of interest.

References

1. Lavoie, P.; Taylor, M.P.; Metson, J.B. A Review of Alumina Feeding and Dissolution Factors in Aluminum Reduction Cells. *Metall. Mater. Trans.* **2016**, *47*, 2690–2696. [CrossRef]
2. Gylver, S.E.; Omdahl, N.H.; Prytz, A.K.; Meyer, A.J.; Lossius, L.P.; Einarsrud, K.E. Alumina Feeding and Raft Formation: Raft Collection and Process Parameters. In *Light Metals 2019*; The Minerals, Metals & Materials Series; Chesonis, C., Ed.; Springer: Cham, Switzerland, 2019; pp. 659–666. [CrossRef]
3. Gylver, S.E.; Omdahl, N.H.; Rørvik, S.; Hansen, I.; Nautnes, A.; Neverdal, S.N.; Einarsrud, K.E. The Micro- and Macrostructure of Alumina Rafts. In *Light Metals 2019*; The Minerals, Metals & Materials Series; Chesonis, C., Ed.; Springer: Cham, Switzerland, 2019; pp. 689–696. [CrossRef]
4. Walker, D.I.; Utigard, T.; Taylor, M.P. Alumina agglomerates in aluminum smelters. In *Light Metals 1995*; Evans, J.W., Ed.; TMS: Warrendale, PA, USA, 1995; pp. 425–434.
5. Kuschel, G.I.; Welch, B.J. Further Studies of Alumina Dissolution under Conditions Similar to Cell Operation. In *Essential Readings in Light Metals: Volume 2 Aluminum Reduction Technology*; Bearne, G., Dupuis, M., Tarcy, G., Eds.; Springer: Cham, Switzerland, 2016; pp. 112–118. [CrossRef]
6. Kuschel, G.I.; Welch, B.J. Effect of Alumina Properties and Operation of Smelting Cells on the Dissolution Behavior of Alumina. In Proceedings of the Second International Alumina Quality Workshop, Perth, Australia, 14–19 October 1990; pp. 58–70.
7. Bagshaw, A.N.; Welch, B.J. The Influence of Alumina Properties on its Dissolution in Smelting Electrolyte. In *Essential Readings in Light Metals: Volume 1 Alumina and Bauxite*; Donaldson, D., Raahauge, B.E., Eds.; Springer: Cham, Switzerland, 2016; pp. 783–787. [CrossRef]
8. Yang, Y.; Gao, B.; Hu, X.; Wang, Z.; Shi, Z. Influence of LOI on Alumina Dissolution in Molten Aluminum Electrolyte. In *Molten Salts Chemistry and Technology*; John Wiley & Sons, Ltd.: Hoboken, NJ, USA, 2014; pp. 77–83. [CrossRef]
9. Lindsay, S.J. Key Physical Properties of Smelter Grade Alumina. In *Light Metals 2014*; Grandfield, J., Ed.; Wiley: Hoboken, NJ, USA, 2014; pp. 597–601. [CrossRef]
10. Alarie, J.; Kiss, L.I.; Dion, L.; Truchon, M.; Santerre, R.; Guérard, S.; Bilodeau, J.F. Empirical Prediction of Alumina Dissolution Rate in a Cryolitic Melt: Comparison with the Existing Literature. In *Light Metals 2022*; The Minerals, Metals & Materials Series; Eskin, D., Ed.; Springer: Cham, Switzerland, 2022; pp. 349–356. [CrossRef]
11. Alarie, J.; Kiss, L.I.; Poncsák S.; Santerre, R.; Guérard, S.; Bilodeau, J.F. Influence of Additives on Alumina Dissolution in Superheated Cryolite Melts. In *Light Metals 2021*; The Minerals, Metals & Materials Series; Perander, L., Ed.; Springer: Cham, Switzerland, 2021; pp. 533–540. [CrossRef]
12. Isaeva, L.A.; Braslavskii, A.B.; Polyakov, P.V. Effect of the content of the α-phase and granulometric composition on the dissolution rate of alumina in cryolite-alumina melts. *Russ. J. -Non-Ferr. Met.* **2009**, *50*, 600–605. [CrossRef]
13. Jain, R.K.; Tricklebank, S.; Welch, B.J.; Williams, D.J. Interaction of Aluminas with Aluminum Smelting Electrolytes. In *Light Metals 1983*; Adkins, E.M., Ed.; The Metallurgical Society of AIME: Wilkes-Barre, PA, USA, 1983; pp. 609–622.
14. Gerlach, J.; Hennig, U.; Kern, K. The dissolution of aluminum oxide in cryolite melts. *Metall. Mater. Trans.* **1975**, *6*, 83–86. [CrossRef]
15. Gylver, S.E.; Solheim, A.; Gudbrandsen, H.; Follo, Å.H.; Einarsrud, K.E. Lab Scale Experiments on Alumina Raft Formation. In *Light Metals 2020*; The Minerals, Metals & Materials Series; Tomsett, A., Ed.; Springer: Cham, Switzerland, 2020; pp. 659–663. [CrossRef]
16. Gylver, S.E.; Follo, Å.H.; Aulie, V.; Granlund, H.M.; Sørhuus, A.; Sandnes, E.; Einarsrud, K.E. On Gaseous Emissions During Alumina Feeding. In *Light Metals 2021*; The Minerals, Metals & Materials Series; Perander, L., Ed.; Springer: Cham, Switzerland, 2021; pp. 504–510. [CrossRef]
17. Kheiri, M.; Hennig, U.; Kammel, R. Krustenbildung und Krusteneigenschaften beim Einsatz sekundärer Aluminiumoxide für die Aluminium-Reduktionselektrolyse. *Metall* **1989**, *43*, 858–862.
18. Kaszás, C. Behaviour of Alumina Powder Fed into Molten Electrolytic Bath. Ph.D. Thesis, Université du Québec à Chicoutimi, Chicoutimi, QC, Canada, 2020.
19. Yang, Y.; Gao, B.; Wang, Z.; Shi, Z.; Hu, X. Mechanism of Dissolution Behavior of the Secondary Alumina. *Metall. Mater. Trans. B Process. Metall. Mater. Process. Sci.* **2013**, *44*, 1296–1303. [CrossRef]

20. Bracamonte, L.; Einarsrud, K.E.; Rosenkilde, C.; Sandnes, E. Oxide Sensor Measurements and Simultaneous Optical Observations During Dissolution of Alumina in Cryolite Melt. In *Light Metals 2022*; The Minerals, Metals & Materials Series; Eskin, D., Ed.; Springer: Cham, Switzerland, 2022; pp. 381–391. [CrossRef]
21. Yang, Y.; Gao, B.; Wang, Z.; Shi, Z.; Hu, X.; Yu, J. Dispersion Caused by Carbon Dioxide During Secondary Alumina Dissolution: A Lab-Scale Research. *Metall. Mater. Trans. B* **2014**, *45*, 1150–1156. [CrossRef]
22. Kaszás, C.; Kiss, L.; Poncsák S.; Guérard, S.; Bilodeau, J.F. Spreading of Alumina and Raft Formation on the Surface of Cryolitic Bath. In *Light Metals 2017*; The Minerals, Metals & Materials Series; Ratvik, A.P., Ed.; Springer: Cham, Switzerland, 2017; pp. 473–478. [CrossRef]
23. Bracamonte, L. Development of an Electrochemical Sensor for Alumina Concentration Measurements and Dissolution Characteristics of Alumina in Cryolite Melt. Ph.D. Thesis, Norwegian University of Science and Technology, Trondheim, Norway, 2022.
24. Solheim, A.; Rolseth, S.; Skybakmoen, E.; Støen, L.; Sterten, Å.; Støre, T. Liquidus temperatures for primary crystallization of cryolite in molten salt systems of interest for aluminum electrolysis. *Metall. Mater. Trans. B* **1996**, *27*, 739–744. [CrossRef]
25. Skybakmoen, E.; Solheim, A.; Sterten, Å Alumina solubility in molten salt systems of interest for aluminum electrolysis and related phase diagram data. *Metall. Mater. Trans. B* **1997**, *28*, 81–86. [CrossRef]
26. Schneider, C.A.; Rasband, W.S.; Eliceiri, K.W. NIH Image to ImageJ: 25 years of image analysis. *Nat. Methods* **2012**, *9*, 671–675. [CrossRef] [PubMed]

Paper VI

CFD Modelling of Solidification and Melting of Bath during Raft Formation

Sindre Engzelius Gylver[1*] and Kristian Etienne Einarsrud[1]

[1]Department of Material Science and Engineering, NTNU, Alfred Getz' veg 2, Trondheim, NO-7034, Norway.

*Corresponding author(s). E-mail(s): sindre.e.gylver@ntnu.no;
Contributing authors: kristian.e.einarsrud@ntnu.no;

Abstract

The dissolution of alumina in cryolite is a complex process, and better understanding is needed to ensure stable cell conditions and high energy efficiency. Additions of cold powder result in freezing of bath that hinders dissolution, and creation of rafts. The current work aims to develop and demonstrate a CFD framework in OpenFOAM for freezing of bath on a fed dose of alumina, based on the volume of fluid (VOF) method, where appropriate source- and sink terms are applied. Essential features have been verified by comparison with a Stefan problem, while simulating the dose as a floating rigid object demonstrate that a larger layer of freeze increase the damping of its movement. When simulating the dose as an immiscible fluid, spreading will hinder enough freeze to be formed around the dose. Hence, the added source terms behave as intended, but improvements on the alumina-bath interactions are needed.

Keywords: CFD Modelling, Alumina Feeding, Rafts

1 Introduction

Alumina is, together with carbon, the raw materials used for producing aluminum in the Hall-Héroult process and is added regularly to the electrolyte through point feeders, located at one or several positions in the cell. Modern cells tend to increase in size without a proportional increase of feeder locations,

and one feeder must therefore distribute alumina over a higher surface area than earlier. In addition, the anodic-cathodic-distance is decreasing, resulting in lesser available volume for alumina to dissolve in [1], which means that efficient dissolution becomes even more critical.

When a batch of alumina is added, some of the grains might not be dissolved immediately, but form so-called rafts, being a rigid porous body consisting of frozen bath and alumina [2]. Dissolution of single grains in stagnant fluids are however found to be mainly diffusion controlled [3]. However, agglomerates might consist of several thousand grains and this assumption will not hold. Solheim and Skybakmoen [4] propose that heat transfer will restrict the dissolution when a coat of frozen layer is present around the raft, and their calculation showed that the freezing and melting only accounts for about 10 % of the total dissolution time. Even though the solidification and melting itself account for only a small fraction of the dissolution process, it cannot be neglected, as demonstrated in the work by Bardet et al. [5], who simulated the alumina concentration in an industrial cell and concluded that the temperature equation must be considered as high superheat is an important driving force for the alumina dissolution. In addition, the freezing of bath can affect the initial geometry of the formed agglomerates, hence determine the available contact area between surface and bath. A model that can predict the formed raft is therefore needed in order to understand the complete picture of dissolution.

The time for bath to melt and freeze around alumina will vary depending on size and geometry. For a single grain with d=50 μm in a stagnant liquid, bath will have frozen and melted within 0.1 s [3], while larger studies by immersing premade agglomerates into the melt showed a total freezing-melting time of approximately 50 s for 5 g [6] and 150 s for 280 g [6].

Dassylva-Raymond et al. [7] base their work on experimental results [6] when developing a model that describes the whole agglomeration process, which also include infiltration of bath into the raft, sintering and dissolution, but do not consider the effect of convection in the bath. Kovács [3] also investigates the freezing, melting infiltration and dissolution, assuming the alumina dose to be a porous lump.

Roger et al. [8] developed a coupled model in a Lagrangian framework, by using discrete element method (DEM) to determine the movement of the alumina particles, while smoothed particle hydrodynamics (SPH) was used to compute the flow of bath. A heat transfer model based on the heat conduction equation was also included, where phase change of the bath was modeled using an enthalpy method. Raft formation was modeled by a cohesion force between alumina particles where bath solidification could occur. They have also implemented the effect of natural convection due to temperature dependent density changes successfully.

In Computational Fluid Dynamics (CFD), a regular approach is to use an enthalpy-porosity technique [9–11], achieved by applying additional source

terms to the different balance equations and is implemented in several CFD-software [12, 13].

The current work investigates how solidification can be modeled for a multiphase system, where one of the fluids can solidify and melt. This is followed by a demonstration of the models for a system where a raft is subjected to freezing. The said models have been realized in OpenFOAM [14], an open-source framework for numerical simulations.

2 Governing equations

Solidification by the enthalpy-porosity method is modeled by adding appropriate source terms to the momentum and energy equation. Assuming that density differences only affect the buoyancy by Boussinesq approximation [15], balances of mass, momentum and energy are written as

$$\nabla \cdot \boldsymbol{u} = 0, \tag{1}$$

$$\frac{\partial}{\partial t}(\rho \boldsymbol{u}) + \nabla \cdot (\rho \boldsymbol{u} \boldsymbol{u}) = -\nabla p + \nabla \cdot \boldsymbol{\tau} + \rho \boldsymbol{g} \beta (T - T_{ref}) + \boldsymbol{S_d}, \tag{2}$$

$$\frac{\partial}{\partial t}(\rho c_p T) + \nabla \cdot (\rho c_p \boldsymbol{u} T) = \nabla \cdot (\kappa \nabla T) + S_h. \tag{3}$$

$\boldsymbol{u}$ and p are respectively the velocity and pressure, ρ is the density, $\nabla \cdot \boldsymbol{\tau}$ is the viscous stress tensor and $\boldsymbol{g}$ is the gravity. β, T, T_{ref} c_p, and κ are respectively the coefficient of thermal expansion, temperature, a reference temperature, specific heat capacity and thermal conductivity.

$\boldsymbol{S_d}$ dampens the velocity towards zero when the fluid solidifies and can be modeled based on Darcy's law [9]:

$$\boldsymbol{S_d} = -C \frac{(g_s)^2}{(1 - g_s)^3 + q} \boldsymbol{u}, \tag{4}$$

where C is a constant that express the "strength" of the source term, normally in the order of 10^5. q is a small constant needed to avoid singularity and g_s expresses the fraction of solidified liquid in a cell volume, and will have a material dependent relationship with temperature [10]. Assuming an isothermal process, mostly applied for pure metals, g_s can be expressed as

$$g_s = \begin{cases} 1 & \text{for } T < T_M, \\ 0 & \text{for } T > T_M, \end{cases} \tag{5}$$

where a discontinuity in g_s occurs at the melting point, T_M. $\boldsymbol{S_d}$ will then become the dominating term in equation (2) as g_s approaches one.

For the energy equation, the term S_h accounts for the enthalpy change due to change of state: [11]:

$$S_h = -\rho L \left[\frac{\partial g_s}{\partial t} + \nabla \cdot (\boldsymbol{u} g_s) \right] \tag{6}$$

where L is the heat of fusion. The convective term can in case of isothermal process be neglected [11].

3 Establishment of a multiphase model

The system investigated will contain multiple phases: bath, air, and alumina. The Volume of Fluid (VOF) method [16] is used to distinguish the different phases from each other. Considering a system with N fluids, the amount of a fluid k is expressed by volumetric fraction, α_k, in each computational cell and will have the following balance:

$$\frac{\partial \alpha_k}{\partial t} + \boldsymbol{u} \cdot \nabla \alpha_k = 0. \tag{7}$$

This equation will be solved for $N-1$ of the fluids, while the last one is solved by the constraint

$$\sum_{i}^{N} \alpha_i = 1. \tag{8}$$

In areas where only one component is present, the single phase (equations (1)-(3)) will in principle be solved. When multiple phases are present in the same area, the equations must be solved using volume-averaged values, which in the case for density will be:

$$\rho_m = \sum_{k}^{N} \alpha_k \rho_k, \tag{9}$$

where the subscript m denotes that it is a mixture. For a system without reactions where the bath phase α_b will solidify and melt, the balance equations can be written as

$$\nabla \cdot \boldsymbol{u} = 0, \tag{10}$$

$$\frac{\partial}{\partial t} (\rho_m \boldsymbol{u}) + \nabla \cdot (\rho_m \boldsymbol{u}\boldsymbol{u}) = \nabla \cdot \boldsymbol{\tau} - \nabla p + \rho_m \boldsymbol{g} + \boldsymbol{F}_{ST} + \boldsymbol{S}_d. \tag{11}$$

$$\frac{\partial}{\partial t} (\rho c_{p,m} T) + \nabla \cdot (\rho_m c_{p,m} \boldsymbol{u} T) = \nabla \cdot (k_m \nabla T) + S_h, \tag{12}$$

$\boldsymbol{F}_{ST}$ expresses the interactions between phases as surface tension. S_h will still have the same form as earlier, while the definition of g_s is slightly changed:

$$g_s = \begin{cases} \alpha_b & \text{for } T < T_M, \\ 0 & \text{for } T > T_M, \end{cases} \tag{13}$$

which ensures that solidification only will occur in the bath phase. The compressible buoyancy effects are also neglected, since density changes in liquid cryolite is small as a function of temperature [17].

The source term presented in equation (4) will in principle reduce the velocity to zero. However, in a multiphase system, solidified bath should be affected by movement of the surrounding phases, having a non-zero relative velocity. A possible approach is to apply a temperature dependent viscosity that gain a relatively large value when the fluid becomes solidified [11]. In the current work, the "solid viscosity" is not implemented by varying the actual viscosity of the fluid, but rather by modifying the source term from (4):

$$\boldsymbol{S}_d = \nu_{sol} \cdot \nabla^2 \boldsymbol{u}, \tag{14}$$

where ν_{sol} is dependent on temperature,

$$\nu_{sol} = \begin{cases} \alpha_b C_\nu & \text{for } T \le T_M, \\ \alpha_b C_\nu \exp\left[A \cdot (T_M - T)\right)\right] & \text{for } T_M \le T \le T_L, \\ 0 & \text{for } T > T_L. \end{cases} \tag{15}$$

C_ν is and A are user defined constants. In practice, the source term will add an imposed viscosity to the bath phase that increase exponentially from T_L and down to T_M, from zero to C_ν, where the exponential formulation is used in order to avoid numerical issues that can arise when a viscosity is rapidly increased.

4 Implementation

The fvOptions utility in OpenFOAM provides an opportunity to include source terms to equations, and apply them on multiple solvers without needing to modify the code. The model described is already implemented for single phase solvers, and a detailed description is already published [12].

For a time step $n + 1$, the values of g_s is calculated by the algorithm

$$g_s^* = g_s^n - \frac{\gamma c_p}{L} (T - T_M)$$
$$g_s^{n+1} = \max\left[0, \min\left(\alpha_b, g_s^*\right)\right], \tag{16}$$

where γ is an under-relaxation factor. The initial value of g_s is by default zero.

The solvers applied in the current cases are either interFoam or multiphaseInterFoam, depending of the number of phases. It should be noted that these solvers by default are isothermal, and that the energy equation - written for temperature - as such has been implemented in order to simulate sought effects. The solver is based on the PIMPLE algorithm [18] for pressure-velocity coupling to solve the momentum- and mass equation, followed by the energy equation. Source terms are calculated prior to solving the momentum equation.

5 Cases

Three cases were investigated with the following purposes:

1. A Stefan case, to verify that the temperature equation and fraction of solidified bath were implemented correctly.
2. A case with a rigid body floating on the surface, to investigate the effect on the developed momentum source term.
3. A three-phase case with cold alumina dose entering a bath on cryolite, to investigate the consequences of alumina being a phase.

   The setups are shown in figure 1.
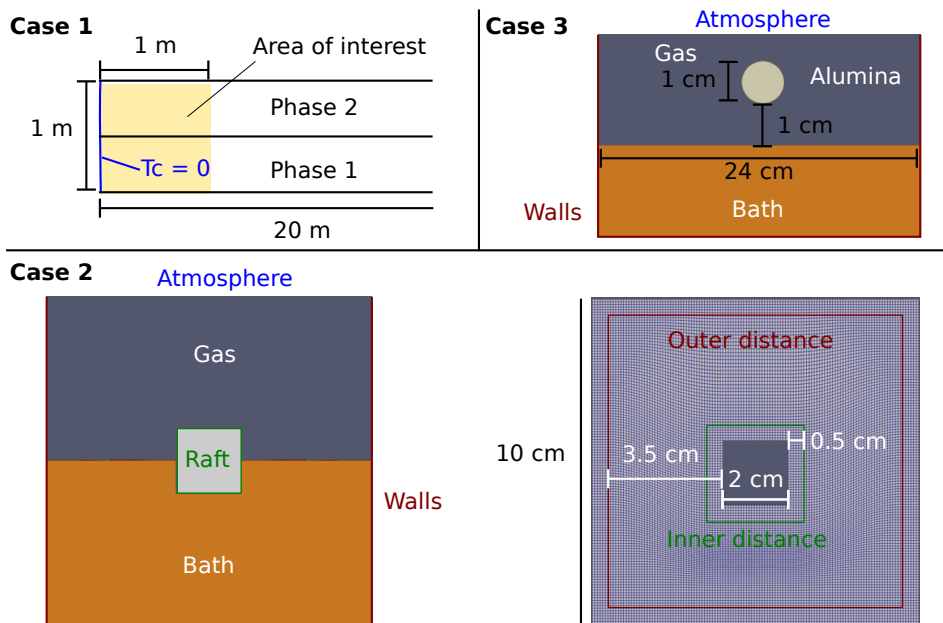
Fig. 1 Overview of the cases investigated: **Case 1** Stefan case. **Case 2** Rigid body case, with boundaries and phases present (left) and Deformation of mesh with inner and outer distance (right). **Case 3** Cold alumina dose falling into cryolitic bath.

5.1 Stefan case

A slab of liquid with infinite length, temperature T_L , and freezing point at $T_m < T_L$ is considered. The left wall of the domain will have a temperature $T_s < T_m$ at $t = 0$, thus creating moving phase front driven by diffusion, where the position of the solidifying front, $X(t)$, can be expressed as [19]

$$X(t) = 2\lambda\sqrt{g_s t}. \tag{17}$$

λ is found solving the Stefan equation:

$$\lambda\sqrt{\pi} = \frac{St_s}{\exp(\lambda^2)\mathrm{erf}(\lambda)} - \frac{St_l}{\vartheta\exp(\vartheta^2\lambda^2)\mathrm{erfc}(\vartheta\lambda)}, \tag{18}$$

where ϑ expresses the ratio of thermal diffusivity between the liquid and solid part, while Stefan number expresses the ratio of sensible heat to latent heat for respectively the solid and the liquid part, written as:

$$St_s = \frac{c_p(T_M - T_s)}{L}, \tag{19}$$

$$St_l = \frac{c_p(T_L - T_M)}{L}, \tag{20}$$

where it is assumed that the solid and the liquid part have the same heat capacity.

The case was set up as a 2D case consisting of four walls, where freezing occurs within a distance of 1 m from the left wall in the investigated time interval, marked as the area of interest. The right wall is 20 meters away and while the distance between upper and lower wall is 1 meter. The long geometry was used in order to obtain conditions similar to that of the analytical solution, i.e. an infinite domain. The mesh in the area of interest is uniform with rectangular cells that is 5 mm wide and 33.33 mm high, and the width increase to the right after 1 meter. Properties of the phases are shown in table 1, and is set such as the Stefan number and thermal diffusivity of the phases are equal, thus resulting in an equal movement of freezing front. The system has an initial temperature of 100 ˚C, while left wall has a temperature of 0 ˚C. Since the case is without any convection and isothermal, only the first term in equation (6) was considered.

Time was discretized with a Crank Nicolson scheme, while gradients and Laplacian terms were discretized with a linear scheme and an upwind scheme was used for divergence.

Table 1 Physical properties for case 1.

Property	Symbol	Phase 1	Phase 2	Unit
Density	ρ	1000	1	kg m^{-3}
Heat Capacity	c_p	1	1	J kg^{-1} ˚C^{-1}
Viscosity	ν	0.01	0.01	m^{2}s^{-1}
Thermal conductivity	κ	10	0.01	Wm^{-1}˚C^{-1}
Latent heat of fusions	L	10	10	J kg^{-1}
Melting point	T_M	10	10	˚C

5.2 Floating body

To investigate the pure effect of the damping source term, a raft is considered to be a cubic rigid object floating on a bath of cryolite with air above, as seen in figure 1**a)**. The cases are limited to 2D and the body is only allowed to move up and down. When movement of the rigid object occurs, the mesh is being deformed in the area that is set by an inner and outer distance away from the object, illustrated in figure 1**b)** with dimensions.

The raft is partly immersed in the melt, with center of mass located 0.4 cm above the surface and has a constant temperature below the melting point of the bath, denoted as T_{raft}. Boundary conditions are given in table 2, while table 3 states the properties for the system, where an asterisk marks that the value set is not based on literature value. It is mainly due to that the values cannot be found, except from heat capacity of air, which was set to a high value to avoid that bath freezes due to faster cooling of air. A factorial design was performed, where the effects of bath- and raft- temperature, bath heat capacity and the raft's initial velocity, to illustrate the effect of different drop height, were varied, with values given in table 4. An additional case with reduced damping strength was also run where all factors besides the velocity were low.

Table 2 Boundary conditions for case 2 and 3

Field	Atmosphere	Walls	Raft (Case 2 only)
Velocity	inlet-outlet	No slip	Moving wall velocity
Pressure	Fixed 0	Zero gradient	Zero gradient
Phase fraction	Fixed air	Zero gradient	Zero gradient
Temperature	Zero gradient	Zero Gradient	Fixed, case dependent

The initial mesh consisted of 153 600 quadratic cells with 0.25 mm length. Time was discretized by a Crank Nicolson scheme, while a linear scheme was applied on the convection and Laplacian terms. For divergence, Van Leer was used for velocity and the phase fraction, while the rest was solved with a upwind scheme. The movement of the rigid object was solved by the Newmark-beta method.

5.3 Feeding of a dose

The third case simulates a dose of alumina falling into a liquid bath, where the effect of solidification and its interactions with several phases are investigated. For simplicity, alumina is assumed to be a Newtonian fluid. The Boundary conditions and properties are given in table 2 and 3, respectively. The time was in this case discretized with a forward Euler scheme, while gradients and divergence were respectively discretized by a cubic Scheme and Fromm's scheme. The walls at the sides are placed a long distance away to avoid any unwanted

Table 3 Properties of system for case 2 and 3. An asterisk denotes that the value is set, and not a literature value.

Property	Symbol	Value case 2	Value case 3	Unit
Alumina density	ρ_a	-	1200	kg m^{-3}
Bath density	ρ_b	2000	2000	kg m^{-3}
Gas density	ρ_g	1	1	kg m^{-3}
Raft density	ρ_r	1200	-	kg m^{-3}
Alumina viscosity	ν_a	-	10^{-6}*	m^{2}s^{-1}
Bath viscosity	ν_b	10^{-6}	10^{-6}	m^{2}s^{-1}
Gas viscosity	ν_g	$1.48 \cdot 10^{-5}$	$1.48 \cdot 10^{-5}$	m^{2}s^{-1}
Alumina heat capacity	$c_{p,a}$	-	1200*	J kg^{-1} °C^{-1}
Bath heat capacity	$c_{p,b}$	Varies	2200	J kg^{-1} °C^{-1}
Gas heat capacity	$c_{p,g}$	10000*	700	J kg^{-1} °C^{-1}
Alumina Thermal Conductivity	κ_a	-	8	W °C^{-1}m^{-1}
Bath Thermal Conductivity	κ_b	0.8	0.8	W °C^{-1}m^{-1}
Gas Thermal Conductivity	κ_g	$2 \cdot 10^{-2}$	$2 \cdot 10^{-2}$	W °C^{-1}m^{-1}
Latent Heat of Fusion	L	530 000	530 000	J kg^{-1}
Temperature constant	T_L	959*	959*	°C
Melting point	T_M	950*	950*	°C
Damping strength	C_ν	10*	Varies	m^{2}s^{-1}
Constant	A	1*	1*	-
Gravity	g	9.81	9.81	m s^{-2}
Initial temperature	T_i	Varies	960	°C
Initial temperature alumina	T_a	-	100	°C
Initial velocity of raft	U_0	Varies	-	m s^{-1}

Table 4 The low and high value of the parameters investigated for case 2.

Property	Low	High	Unit
T_i	965	980	°C
T_{raft}	100	500	°C
$c_{p,b}$	1600	2200	J kg^{-1} °C
U_0	0	0.03	m s^{-1}

boundary effects. The mesh is uniform with a cell size of 0.125 mm in 4 cm to the left and right, while being graded to become more coarser out. A total of five cases were run, four where C_ν was set to be respectively 0. 0.01, 0.1 and 1, while one case was run without the applying the extra source terms.

6 Results

6.1 Stefan case

A plot of the phase front as a function of time is shown in figure 2, where both the analytical and simulated solution are shown. The current numerical solution was on average 0.014 m below the analytical one, which were not found to increase nor decrease throughout during time.
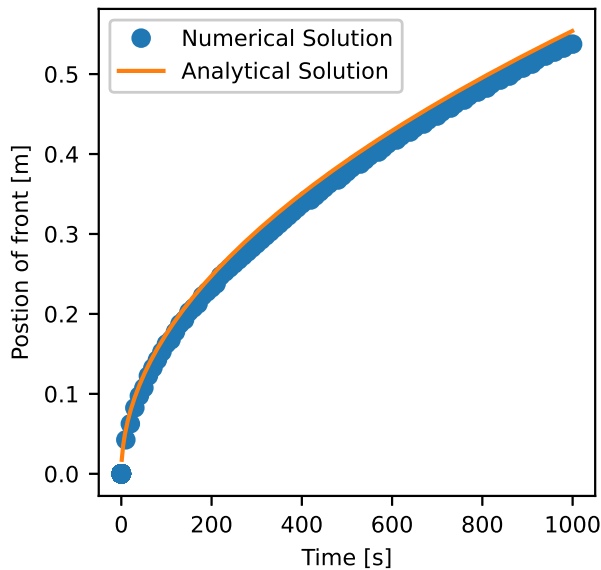
Fig. 2 The analytical solution of the Stefan problem compared with the numerical one.

6.2 Floating body

A selection of cases is presented in figure 3. A factorial regression analysis, where the response was set as the lowest value the center of mass had was conducted in Minitab. In that case, individual parameters and their two-way interactions were considered. Each of the individual parameters had a significant positive impact on the depth which the body penetrated, i.e a higher T_i increased the depth. U_0 and T_i had the highest relative impacts, with respectively 32 and 31 %.

6.3 Feeding of a dose

Figure 4 shows the distribution of different phases, including frozen bath, and the temperature in parts of the domain, when $C_\nu = 0.01$. Images of the phases and freeze at t=0.1 for the different values of C_ν are shown in 5.

7 Discussion

The results from the Stefan case, fig. 2, demonstrate that temperature equation in interfoam (eq. (12)) and the source term for energy are implemented correctly.

The rigid object study showed that the initial velocity had the highest effect, followed by temperature and heat capacity. Decreasing the temperatures and the heat capacity will increase the layer of solidified bath and promote damping of the object. The initial velocity increases the penetration depth, although it does not have any effect on the layer formed around the object.
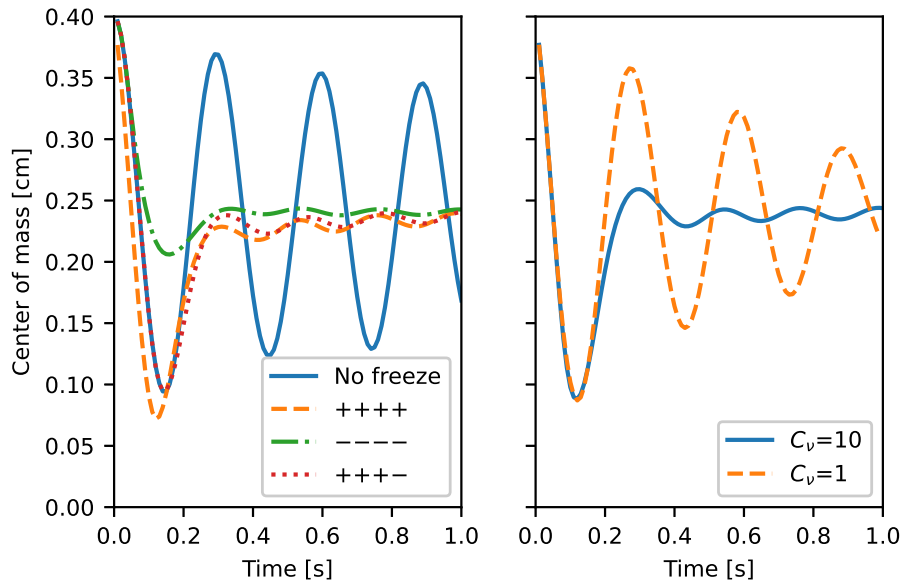
Fig. 3 Left: The center of mass as a function of time for the floating object at four different configurations. Solid line: no freezing, dashed line: all factors had high values, dash-dot line: all factors had low values, dotted line: all factors except initial velocity had high values. Value of the factors are given in table 4. Right: comparison of having $C_\nu = 10$ (full) vs 1 (dashed) for the case where the initial velocity is at its high value, while the other factors are low.

When reducing C_ν for the rigid object (right plot in figure 3), a larger layer of freeze must form before the effect becomes visible.

When a cold dose hits the bath, a layer of freeze will form, as the bath becomes colder. By assuming the dose to be spherical, it corresponds to add about 0.5 gram into the melt. Based on earlier findings [6], it is therefore not expected that melting of the frozen layer has started within the investigated time interval.

As seen in figure 5, the added momentum source term does not affect the formation of raft in any large degree. The layer of freeze will become thin as the dose spreads out, resulting in limiting damping effect. C_ν cannot be higher than 1, as this results in numerical issues, for example the strange waves seen in fig 5. With $C_\nu = 1$, an even thicker layer of freeze is needed to observe any damping effect (see fig 3). In addition, the dose's velocity while entering the bath were around 0.4 m s^{-1}, which is 10 times larger than for the rigid object, and the movement will in these cases therefore in a small degree be affected by heat transfer.

The current cases demonstrate that modelling solidification of bath in the context of the volume of fluid is a possible approach. The issues with the current cases might be improved by allowing for bath mix into the alumina, thus increasing the area where the damping effect can occur. Allowing for
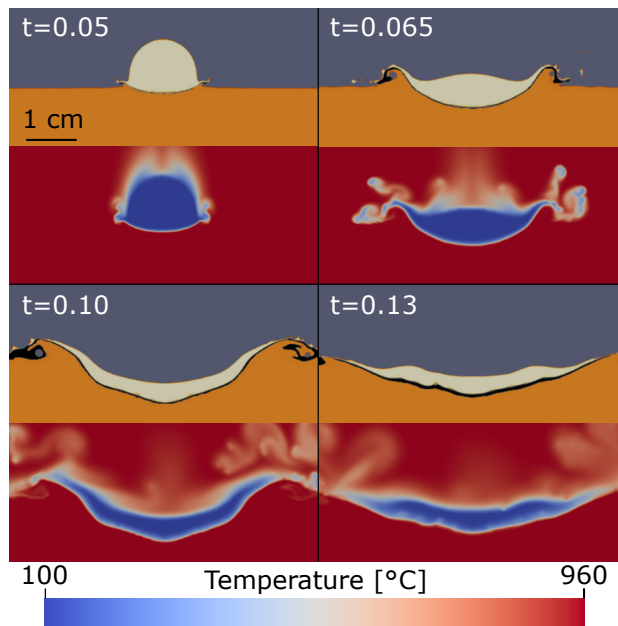
Fig. 4 The phase compositions of molten bath (orange), alumina (beige), air (dark gray) and frozen bath (black), and the temperature distribution in the same area (from cold blue to hot red) for four selected times, when $C_\nu = 0.1$.
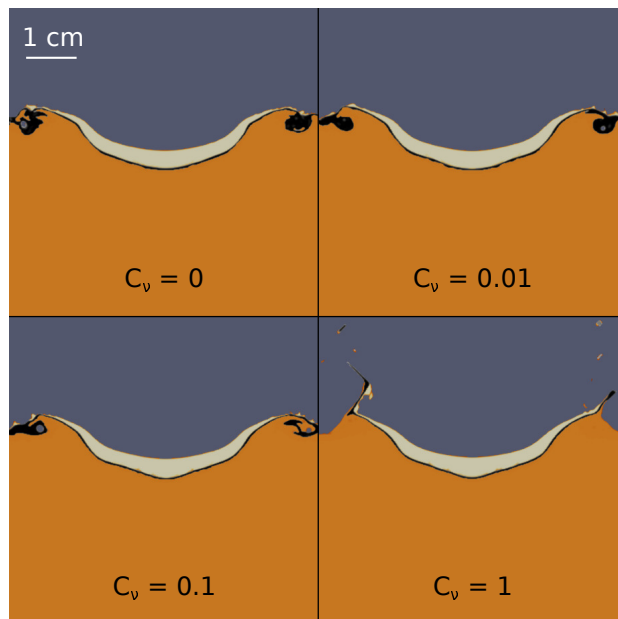

Fig. 5 The phase composition of molten bath (orange), alumina (beige), air (dark gray) and frozen bath (black) amount for the cases with varying damping strength at t=0.1 s.

infiltration should anyway be implemented, since it is found to be an important mechanism in the disintegration of rafts [3, 7].

When considering the added source terms, solidification and melting of bath is not an isothermal process and a more advanced model, such as a linear dependence between solidus-liquidus or Scheil equation should be considered [10]. The variation of density of liquid is relatively small [17] and will be important for convection in a stagnant bath [8], which is not the case for a real cell. Frozen bath samples are found to have densities about 500 kg m^{-3} above liquid bath [20], which might affect the momentum balance, and should be considered when developing the model.

8 Conclusion and further work

A framework for solidification and melting has been implemented in Open-FOAM in the context of the Volume of Fluid method. A parametric study on a rigid object highlights the importance of thermal masses in raft formation and saw an increase in damping as the freeze layer thickness increased. If alumina is assumed to be a fluid, the effect of freezing was not visible, due to a too thin layer of freeze.

The current model provides a foundation for further work. An improved model should therefore allow bath to infiltrate into the powder, which eventually will allow more bath to freeze. In addition, a more suitable rheology for alumina should be found. The model should also consider a more complex temperature dependency and density changes due to solidfying, and validation by studying a freezing object in water should also be considered.

References

[1] Lavoie, P., Taylor, M.P., Metson, J.B.: A Review of Alumina Feeding and Dissolution Factors in Aluminum Reduction Cells. Metall Mater Trans B **47**(4), 2690–2696 (2016). https://doi.org/10.1007/s11663-016-0680-3.

[2] Gylver, S.E., Omdahl, N.H., Rørvik, S., Hansen, I., Nautnes, A., Neverdal, S.N., Einarsrud, K.E.: The Micro- and Macrostructure of Alumina Rafts. In: Chesonis, C. (ed.) Light Metals 2019. The Minerals, Metals & Materials Series, pp. 689–696. Springer, Cham (2019)

[3] Kovacs, A.: "Modelling the feeding process for aluminium production". PhD Thesis, University of Oxford, Oxford (2021).

[4] Solheim, A., Skybakmoen, E.: Mass- and Heat Transfer During Dissolution of Alumina. In: Tomsett, A. (ed.) Light Metals 2020. The Minerals, Metals & Materials Series, pp. 664–671. Springer, Cham (2020).

[5] Bardet, B., Foetisch, T., Renaudier, S., Rappaz, J., Flueck, M., Picasso, M.: Alumina Dissolution Modeling in Aluminium Electrolysis Cell Considering MHD Driven Convection and Thermal Impact. In: Williams, E. (ed.) Light Metals 2016, pp. 315–319 (2016).

[6] Walker, D.: Alumina in aluminum smelting and its behaviour after addition to cryolite-based electrolytes, Phd thesis, University of Toronto, Toronto, 1993.

[7] Dassylva-Raymond, V., Kiss, L.I., Poncsak, S., Chartrand, P., Bilodeau, J.-F., Guérard, S.: Modeling the behavior of alumina agglomerate in the Hall-Héroult process. In: Grandfield, J. (ed.) Light Metals 2014, pp. 603–608. Wiley, Hoboken, (2014).

[8] Roger, T., Kiss, L., Dion, L., Guérard, S., Bilodeau, J.F., Bonneau, G., Santerre, R., Fraser, K.: Modeling of the Heat Exchange, the Phase Change, and Dissolution of Alumina Injected in Electrolysis Cells. In: Eskin, D. (ed.) Light Metals 2022. The Minerals, Metals & Materials Series, pp. 363–370. Springer, Cham (2022).

[9] Voller, V.R., Prakash, C.: A fixed grid numerical modelling methodology for convection-diffusion mushy region phase-change problems. International Journal of Heat and Mass Transfer **30**(8), 1709–1719 (1987). https://doi.org/10.1016/0017-9310(87)90317-6.

[10] Swaminathan, C.R., Voller, V.R.: A general enthalpy method for modeling solidification processes. MTB **23**(5), 651–664 (1992). https://doi.org/10.1007/BF02649725.

[11] Voller, V.R., Cross, M., Markatos, N.C.: An enthalpy method for convection/diffusion phase change. International Journal for Numerical Methods in Engineering **24**(1), 271–284 (1987). https://doi.org/10.1002/nme.1620240119

[12] Torabi Rad, M.: solidificationMeltingSource: A Built-in fvOption in OpenFOAM®︎ for Simulating Isothermal Solidification. In: Nóbrega, J.M., Jasak, H. (eds.) OpenFOAM®︎ : Selected Papers of the 11th Workshop, pp. 455–464. Springer, Cham (2019). https://doi.org/10.1007/978-3-319-60846-4_32.

[13] Muhammad, M.D., Badr, O., Yeung, H.: Validation of a CFD Melting and Solidification Model for Phase Change in Vertical Cylinders. Numerical Heat Transfer, Part A: Applications **68**(5), 501–511. Taylor & Francis, (2015). https://doi.org/10.1080/10407782.2014.994432.

[14] OpenCFD: OpenFOAM®︎ - Official home of The Open Source Computational Fluid Dynamics (CFD) Toolbox. http://www.openfoam.com

Accessed 2019-05-06

[15] Bird, R.B.: Transport Phenomena, 2nd ed. edn. Wiley, New York (2002)

[16] Hirt, C.W., Nichols, B.D.: Volume of fluid (VOF) method for the dynamics of free boundaries. Journal of Computational Physics **39**(1), 201–225 (1981).

[17] Grjotheim, K., Kvande, H. (eds.): Introduction to Aluminium Electrolysis-Understanding the Hall-Heroult Process. Aluminium-Verlag, Düsseldorf (1993)

[18] Greenshields, C., Weller, H.: Notes on Computational Fluid Dynamics: General Principles. CFD Direct Ltd, Reading, UK (2022). https://doc.cfd.direct/notes/cfd-general-principles/

[19] Alexiades, V., Solomon, A.D.: Mathematical Modeling of Melting and Freezing Processes, 1st edn. CRC Press, Washington, DC (1993).

[20] Poncsák, S., Rakotondramanana, L., Kiss, L.I., Roger, T., Guérard, S., Bilodeau, J.-F.: Evolution of Mechanical Resistance of Alumina Raft Exposed to the Bath in Hall-Héroult Cells. In: Chesonis, C. (ed.) Light Metals 2019. The Minerals, Metals & Materials Series, pp. 667–673. Springer, Cham (2019).

Paper VII

Modeling alumina feeding with the μ(I)-rheology

Sindre Engzelius Gylver[1*] and Kristian Etienne Einarsrud[1]

[1*]Department of Material Science and Engineering, NTNU, Alfred Getz' veg 2, Trondheim, NO-7034, Norway.

*Corresponding author(s). E-mail(s): sindre.e.gylver@ntnu.no;
Contributing authors: kristian.e.einarsrud@ntnu.no;

Abstract

Efficient feeding and dissolution of alumina is necessary in order to maintain a stable Hall-Héroult-process. One dose of alumina contains several thousand grains and simulating the motion of individual particles is in practice impossible. The current work proposes to model the alumina dose through a continuous formulation, using the μ(I)-rheology. The rheology is implemented as a viscosity model in OpenFOAM and initial verification cases showed an average deviation below 0.1% and a benchmark case had an average deviation of 7.4 %. A parametric study, where grains were simulated to collapse on a flat surface identified the two rheology parameters μ_2 and I_0 to be of particular importance, accounting for more than 70% of the variation seen. Finally, three-phase cases simulating the feeding of a dose in cryolite was conducted, and the μ(I)-rheology was able to let the parts of the dose disperse into the melt and detach, which is in accordance with what has been seen in experiments. The current work was also able to couple the model with an earlier developed solidification model, hence creating a framework for developing a full model for alumina feeding.
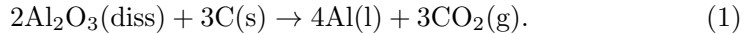
Keywords: Aluminum Production, Alumina Feeding, μ(I)-rheology, CFD

1 Introduction

Aluminum is produced by the Hall-Héroult process, which is an electrochemical process, conducted in large cells at approximately 960 °C. Alumina powder is

dissolved in a bath of molten cryolite and reacts with carbon anodes to produce the metal:

$$2\text{Al}_2\text{O}_3(\text{diss}) + 3\text{C}(\text{s}) \rightarrow 4\text{Al}(\text{l}) + 3\text{CO}_2(\text{g}). \tag{1}$$

In most cells, alumina is added in batches through point feeders, which are located at several positions. Modern cells tend to increase in amperage and hence size, resulting in that one feeder needs to distribute alumina over a higher surface area than earlier. In addition, the anodic-cathodic-distance (ACD) is decreasing, resulting in lesser available volume for alumina to dissolve in [1]. A batch of alumina might not be dissolved immediately after addition, and so-called rafts might be formed, being a rigid porous body consisting of frozen bath and alumina [2]. A better understanding in how rafts are formed and behave will aid the development of technology for better alumina dissolution and distribution, ultimately resulting in a more efficient process.

Modeling is a valuable tool in aiding our understanding of the alumina addition and several models aim to estimate the alumina distribution in cells [3, 4, 5, 6, 7], which can be applied in order to optimize feeder position and addition frequency. Zhan et al. [7] consider formation and dissolution of rafts in their model based in Computational Fluid Dynamics (CFD), where an empirical formulation based on experiments is proposed. The model by Boreajevics and Dupuis [4] also account for raft formation, but both dimensions and dissolution rates of rafts must be given as input parameters, and are thus not known.

Models for understanding and predicting how alumina is dissolved are needed in order for the larger model to predict the distribution properly. Studies when assuming alumina to be dispersed spheres indicate that the process can be explained by a shrinking sphere model [8]. Modeling dissolution of a single raft have been done by several authors, by assuming spherical or flat geometries [9, 10, 11, 12].

In practice, however, rafts have been observed to have a more complex geometry, in industrial cells [13], where alumina spreads over the free surface with varying thickness. A similar structure is seen in an analogous model at room temperature [14], and smaller rafts created in a lab cell [15] was found to have a non-uniform thickness. In addition, the mentioned models are not able to account for how addition method affect the formation, which is also found to be of importance [16]. In see-through cells [17] it is observed that rafts form on the top of the surface and smaller parts loosen and snow into the melt.

Recently, Roger et al. [18] developed a coupled model in a Lagrangian framework, by using discrete element method (DEM) to determine the movement of the alumina particles, while smoothed particle hydrodynamics (SPH) was used to compute the bath flow. In addition, a heat transfer model based on the heat conduction equation was introduced, and phase change of the bath was modeled using an entalphy method. A drawback with this model is the cost of computational time when the number of particles increase, although it can be improved by parallel computing. A continuous formulation, however, does not suffer from the same limitations relating to scale-up. Furthermore, due to

the maturity of the continuous formulations, a large amount of models and sub-models for various physics, for example turbulence [19], solidification [20], mass transfer and Magneto Hydrodynamics [4], are described in the literature, potentially facilitating further extensions for alumina feeding and dissolution.

The current work aims to study whether the alumina can be expressed with a continuous formulation, where the granular behavior of alumina is expressed by the developed µ(I)-rheology [21]. The model is implemented in the CFD-software OpenFOAM [22], where it is verified for both single- and multiphase solvers. Further, a parametric study aims to identify the relative importance of the model parameters. Finally, the framework is demonstrated in three-phase alumina-air-bath system, where it also is coupled with a framework allowing for the bath to freeze.

2 The µ(I)-rheology

Being able to describe granular flow as a continuum is of high benefit for several applications, for example in predicting avalanches [23] or to model sedimentation [24] and segregation [25]. A problem with these kind of flows are the high variation in flow behavior, ranging from solid-like (i.e. not deforming to shear forces) when put at rest, to liquid-like when poured or flowing through a pipe [21]. Roughly speaking, granular flows can be separated into dense- and dilute (or fluidized) regimes, depending upon the relative distance between particles and the strength of their interactions. The fluidized regime has successfully been described by the kinetic theory for granular flow (KTGF) [26]. It is in particular when in the dense regime, with a liquid-like behavior of particles, where there is a lack of good descriptions.

The $\mu(I)$-rheology is a possible approach to explain dense granular flows, which can be derived from relatively simple experiments [27], and further generalized to a three dimensional space [21]. With this approach, the granular media can be described as an incompressible fluid, which will then have the following mass- and momentum-balance

$$\nabla \cdot \boldsymbol{u} = 0, \tag{2}$$

$$\frac{\partial}{\partial t}\boldsymbol{u} + \nabla \cdot \boldsymbol{u}\boldsymbol{u} = -\frac{1}{\rho}\nabla p + \nabla \cdot \boldsymbol{\tau} + \boldsymbol{g}, \tag{3}$$

$\boldsymbol{u}$ and p are respectively the velocity and pressure, ρ is the density and $\boldsymbol{g}$ accounts for body forces working on the fluid. The rheology is implemented through the internal stress tensor, $\boldsymbol{\tau}$:

$$\boldsymbol{\tau} = \left(\frac{\mu(I)}{D_2}p\right)\boldsymbol{D}. \tag{4}$$

$\boldsymbol{D}$ is the strain rate tensor

$$\boldsymbol{D} = \left(\nabla \cdot \boldsymbol{u} + \nabla \cdot \boldsymbol{u}^T\right), \tag{5}$$

D_2 is the second invariant of $\boldsymbol{D}$ and $\mu(I)$ is a coefficient of friction, expressed as:

$$\mu(I) = \mu_1 + \frac{\mu_2 - \mu_1}{I_0/I + 1}, \tag{6}$$

where μ_1 is a threshold value for when a granular media is approaching a quasi-static state, and can be interpreted as angle of repose [28]. μ_2 and I_0 are two other material-dependent properties, cf Jop et al. [29] for further discussions on these parameters. I is the inertial number, defined as:

$$I = \frac{d\sqrt{2D_2}}{\sqrt{p/\rho}}. \tag{7}$$

Earlier work with this rheology has shown good agreement in cases of collapsing granular columns [30] and avalanches [23].

The presented model might for some cases be ill-posed for large and small I, and Barker et al. [31] have developed a regularized model, which will be applied in this work. Some additional parameters need to be added, and a new expression is defined for a low inertial number

$$\mu(I) = \begin{cases} \sqrt{\dfrac{a}{\log\left(\dfrac{A}{I}\right)}}, & \text{for } I \leq I_1 \\ \dfrac{\mu_1 I_0 + \mu_2 I + \mu_\infty I^2}{I_0 + I} & \text{for } I > I_1. \end{cases} \tag{8}$$

a is and μ_∞ are new material dependent constants. I_1 is the lowest number possible where the equations are well posed, and is find by solving the equation

$$4\left(\frac{I\mu'}{\mu}\right)^2 - 4\left(\frac{I\mu'}{\mu}\right) + \mu^2\left(1 - \frac{I\mu'}{2\mu}\right) = 0, \tag{9}$$

where

$$\mu' = \frac{d\mu}{dI}, \tag{10}$$

which can be determined by differentiating equation (6). A is a constant expressed as:

$$A = I_1\left(\frac{a\left(I_0 + I_1\right)^2}{\left(\mu_1 I_0 + \mu_2 I_1 + \mu_\infty I_1^2\right)}\right). \tag{11}$$

The viscous stress tensor can for an incompressible fluid be expressed as

$$\nabla \cdot \boldsymbol{\tau} = \nabla \cdot \left[2\rho\nu_{eff}\boldsymbol{D}\right], \tag{12}$$

where ν_{eff} is the sum of kinematic and turbulent viscosity. The kinematic viscosity of the fluid is expressed as a generalized Newtonian fluid [32], and can

hence be implemented to be dependent on other variables, which is beneficial when implementing the µ(I)-rheology.

$$\nu = \left(\frac{\mu(I)}{D_2} \frac{p}{\rho} \right).$$ (13)

3 Multiphase flow

In this work, the system investigated will consist of several, phases, and the Volume of Fluid (VOF) method [33] is applied in order to distinguish them from each other. In this method, a single set of momentum and continuity equations are solved in order to calculate the volume fraction of each phase in each computational cell of the system. For a system with N fluids, the amount of a fluid k is expressed by volumetric fraction, α_k, in each computational cell, which will have the following mass balance:

$$\frac{\partial \alpha_k}{\partial t} + \boldsymbol{u} \cdot \nabla \alpha_k = 0.$$ (14)

This equation will be solved for $N-1$ of the fluids, while the last one is solved by the constraint

$$\sum_i^N \alpha_i = 1.$$ (15)

The mass- and momentum balance can be written as

$$\nabla \cdot \boldsymbol{u} = 0,$$ (16)

$$\frac{\partial}{\partial t} (\rho_m \boldsymbol{u}) + \nabla \cdot (\rho_m \boldsymbol{u}\boldsymbol{u}) = -\nabla p + \nabla \cdot \boldsymbol{\tau} + \rho_m \boldsymbol{g}.$$ (17)

ρ_m is a phase averaged value, defined as:

$$\rho_m = \sum_k^N \alpha_k \rho_k.$$ (18)

In this framework, each phase can have its own viscosity model, and thus being calculated independent of each other before being phase-averaged

$$\nu_m = \sum_k^N \alpha_k \nu_k,$$ (19)

and further applied when calculating the shear rate tensor (eq. (12)).

4 Numerical realization

The current framework is implemented in OpenFOAM [22], where both the single-phase solver pimpleFOAM and the multiphase-solvers interFOAM and multiphaseInterFOAM are applied. For all solvers the pressure-velocity coupling is solved by the PIMPLE algorithm, described in detail by Greenshields and Weller [34], chapter 5.

The μ(I)-rheology is implemented as an incompressible viscosity model. It is based on source code already available [35], where the different equations presented in section 2 is solved as their own functions, with the following algorithm:

- D_2 and p_{eff} is calculated, where the latter ensures that the pressure is above zero.
- I is calculated as given in equation (7).
- If the regularized model is applied, I_1 is solved iterative by equations (9) and (10), followed by solving A, equation (11).
- Then, $\mu(I)$ is solved either by equation (6) or (8).
- Finally, the kinematic viscosity is calculated by equation (13).

5 Verification of solvers

5.1 Case 1: Inclined plane

When considering a single layer case along an inclined plane with an angle θ and boundary conditions as shown in figure 1, an analytical solution for the velocity profile exists, as derived by Lagrée et al. [30]

$$u = \frac{2}{3}I_\theta\sqrt{gd\cos\theta\frac{H^3}{d^3}}\left[1-\left(1-\frac{y}{H}\right)^{3/2}\right].\tag{20}$$

g is the magnitude of $\boldsymbol{g}$, d is the particle diameter and H is the height of the column. The inertial number in this case will then be constant:

$$I_\theta = I_0\left[\frac{\tan(\theta)-\mu_1}{\mu_2-\tan(\theta)}\right]\tag{21}$$
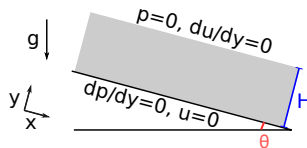

Fig. 1 Sketch of a flow down an inclined plane, where H is the height of the of the column and θ is the incline. Boundary conditions for pressure and velocity are also described in the figure.

The granular media is glass beads, with properties stated in table 1. For these cases, θ is chosen such that I is well posed, and the viscosity model applied in this case therefore calculate $\mu(I)$ by equation (6). The cases are set up as 1D-cases with cyclic boundary conditions on the in- and outflow and the rest of the boundary condition on the top and bottom is as described in figure 1. Four different cases for three different angles θ were ran, described in table 2. In case 1a, the viscosity model is applied with pimpleFoam to verify the model itself. Case 1b is a reproduction of case 1a in interFOAM, where both phases have identical properties, and should in principle yield the single-phase solution, eq. (20).

Case 1c and 1d are also two-phase problems, where the effect of overlaying fluids is investigated. In case 1c, the velocity of the granular material should match the analytical solution since the fluid is light, while the denser one in 1d, is expected to affect the velocity profile for the grains close to the interface [30].

The mesh had a uniform density of 35 cells/cm in the heights between 0.5 and 4.5 cm, while the density was 60 cells/cm above and below. Numerical schemes are shown in table 3, where cases 1b-d all used the same schemes. In order to reduce the computational time, a velocity field close to the analytical solution (eq. (20)) was imposed as an initial condition.

Table 1 Data used for case 1 and 2 based on experiments by Jop et al. [29].

Property	Symbol	Value
Particle diameter	d	0.5 mm
Bulk density	ρ_s	1500 kg m^{-3}
Rheology properties	μ_1	0.381
	μ_2	0.643
	I_0	0.279
	μ_∞	0.05
	a	2.1

Table 2 Overview of the different cases ran for verification of the $\mu(I)$-rheology on the inclined plane.

Property	Case 1a	Case 1b	Case 1c	Case 1d
Type	Single-phase	Multiphase	Multiphase	Multiphase
ρ_f	-	1500 kg m^{-3}	1 kg m^{-3}	150 kg m^{-3}
ν_f	-	$\mu(I)$	10^{-4}m^2 s^{-1}	10^{-3} m^2 s^{-1}
Granular column height	5 cm	2.5 cm	5 cm	5 cm
Fluid column height	-	2.5 cm	0.5 cm	0.5 cm

Table 3 Overview of the numerical schemes used in the single-phase.

Property	Scheme Single-phase	Scheme multiphase
$\frac{\partial}{\partial t}$	Backward	Forward
$\nabla \boldsymbol{u}$	Least squares	Least squares
default gradient	Gauss linear	Gauss linear
$\nabla \cdot (\boldsymbol{uu})$	Linear upwind	Linear upwind
$\nabla \cdot (\alpha \boldsymbol{u})$	-	van Leer
default divergence	Linear	Linear
default laplacian	Gauss linear	Gauss linear

5.2 Case 2: Granular column collapse

A collapse of a granular column into a heap was reproduced from the work of
Lagrée [30]. The system was set up as shown in figure 2. A quadratic mesh
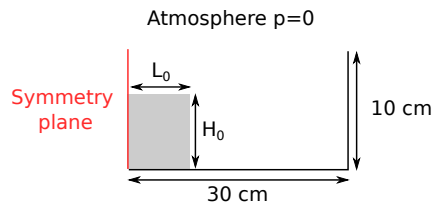with a uniform size of 0.25 mm was used. Three cases were run as described

Fig. 2 Setup for the granular column collapse, where the left side is a symmetry plane.
Right and lower boundary are described as a wall, and the top is an atmosphere.

in table 4, where the aspect ratio between height and length, a_0, is defined as

$$a_0 = \frac{L_0}{H_0}, \tag{22}$$

where H_0 and L_0 are the height and half of the length of the column. The
two-phase solver interFoam was used, and the viscosity of the mixture was in
this case calculated as a harmonic average:

$$\nu = \frac{1}{\alpha_1/\nu_1 + (1 - \alpha_1)/\nu_2}. \tag{23}$$

The density of the surrounding fluid was 1.5 kg m^{-3} and viscosity was assumed
to be constant for each case, stated in table 4. The same numerical schemes
as for the multiphase described in table 3 were used.

5.3 Results and discussion

The results from case 1 are presented in figure 3, where y is normalized by
the column height H, and U is normalized by U$_{max}$, which is the velocity at

Table 4 Overview of the three cases ran for the column collapse

Property	Case 2a	Case 2b	Case 2c
a [-]	0.5	1.42	6.26
L_0 [m]	0.0412	0.03261	0.0155
H_0 [m]	0.0206	0.0463	0.0972
ν_f [m^2 s^{-1}]	0.00120	0.00126	0.00060
g m s^{-2}	2.06	4.63	9.72

$y = H$ in equation (20), i.e the top of the columns. More detailed plots for the upper part of the column for the different angles are provided in figure 4. The average normalized deviation between the cases and the analytical solutions is presented in table 5.   As expected, the velocity profiles for case a-c with
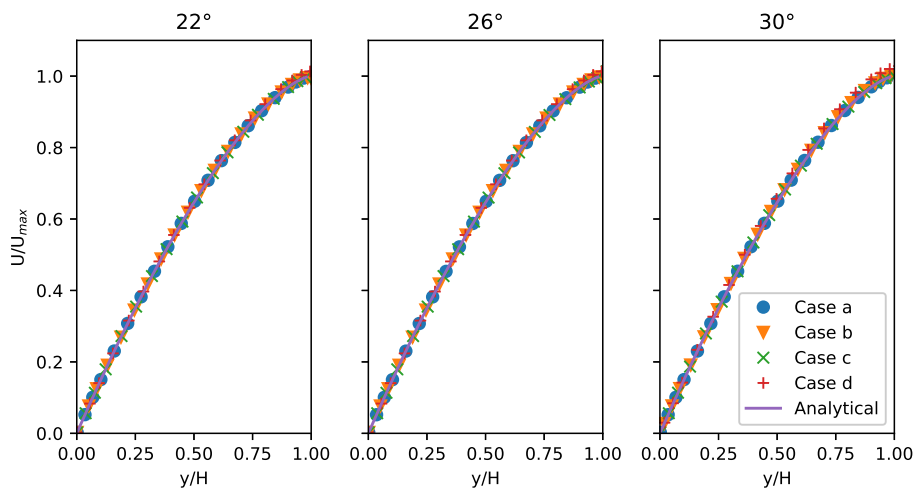

Fig. 3 Velocity profiles of a granular column on an inclined plane for selected angles. Case a: single-phase flow, Case b: multiphase flow with two identical granular phases. Case c: Granular phase with an overlapping fluid with $\rho_f = 1singlep$, Case d: Granular phase with an overlapping fluid with $\rho_f = 150$. The analytical solution U_{max} is calculated by eq (20) and H is constant 5 cm for all cases.

Table 5 Overview of the different cases ran for verification of the $\mu(I)$-rheology on the inclined plane.

Angle	Case 1a	Case 1b	Case 1c	Case 1d
22°	0.14 %	0.02 %	0.02 %	0.76 %
26°	0.04 %	0.01 %	0.04 %	0.75 %
30°	0.12 %	0.37 %	0.13 %	1.98 %

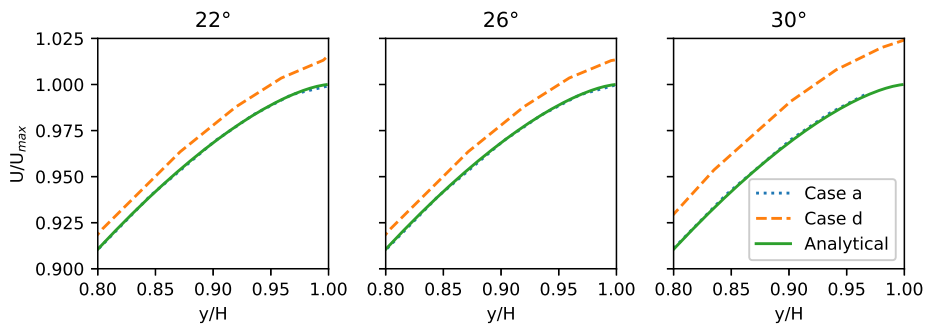the analytical solution stated in equation (20). Case 1d deviates from the

Fig. 4 Detailed view of the velocity profiles showed in fig. 3 at the highest area of the granular column, containing the analytical solution calculated from eq (20). Case a: single-phase flow Case d: Granular phase with an overlapping fluid with $\rho_f = 150$.

analytical solution, where the overlapping fluid increase the velocity above the grains close to its interface, which is expected [30]. From figure 4 it seems that the deviation increased at a higher incline, confirmed by the results in table 5. These results verify the model and illustrate that the velocity profile will be affected by fluids, as expected.

The interface between granular material and fluid for selected times are shown in figure 5. An average normalized deviation between the solution from
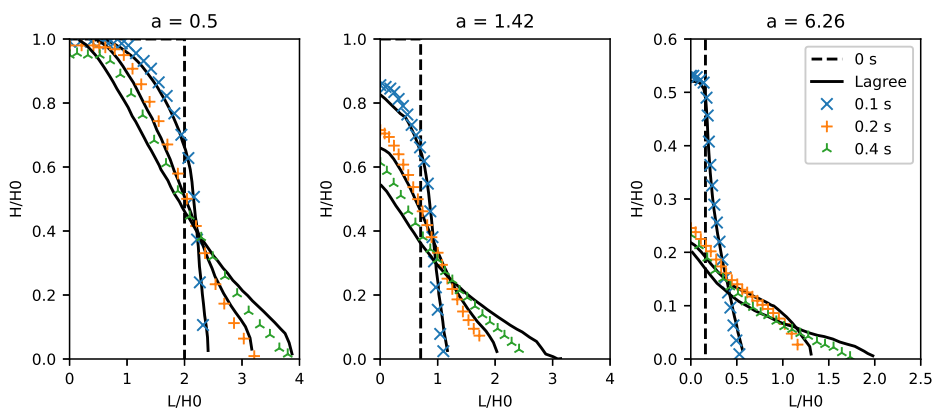

Fig. 5 The grain-air interface during a granular column collapse for selected times, where the aspect ratio given as title.

Lagrée and the current work is calculated in x and y-direction, presented in table 6. The average value is calculated between $0.2x_L < x < 0.8x_L$, where x_L denotes the highest x-value the solution by Lagrée had at the selected time, thereby neglecting the relatively large uncertainty on the fringes of the column.

Table 6 The relative deviation between the numerical solution in this work and the solution by Lagrée et al. [30] for selected aspect ratios a. The average value is calculated between $0.2x_L < x < 0.8x_L$, where x_L denotes the highest x-value the solution by Lagrée had at the selected time.

a	t=0.1		t=0.2		t=0.4	
	$\Delta\bar{x}$	$\Delta\bar{y}$	$\Delta\bar{x}$	$\Delta\bar{y}$	$\Delta\bar{x}$	$\Delta\bar{y}$
0.50	16.6 %	1.8 %	5.2 %	3.3 %	7.1 %	7.1 %
1.42	6.6 %	2.8 %	4.1 %	6.1 %	7.7 %	19.2 %
6.26	3.2 %	4.6 %	9.6 %	8.5 %	7.7 %	12.8 %

The observed behavior shows similarities, although the deviation is smaller at 0.1 and 0.2 s (5.9 and 6.0 %) than after 0.4 s (10.3 %). As the numerical frameworks are conducted in two different software, with a difference in schemes and routines, some deviation is expected. The developed model is therefore found to be suitable for further investigations.

6 Case studies

6.1 Case 3 and 4: Parameter sensitivity

A parametric study was conducted in order to quantify its sensitivity and get an overview on what values that might be suitable for alumina. To the authors' knowledge, no experiments for measuring μ(I)-parameters for alumina have been conducted. However, approximately values for bulk density ρ_a [36], particle diameter d, and angle of repose $\tan^{-1}\mu_1$ [37] are known.

The setup is an alumina-air system, shown in figure 6. All the cases are 2D with evenly-spaced quadratic mesh with a length of 0.125 mm. In case 4, the geometry is different as the dose is dropped from a higher distance. However, the mesh has the same resolution as case 3. Boundary conditions are given in table 7 and properties in 8.
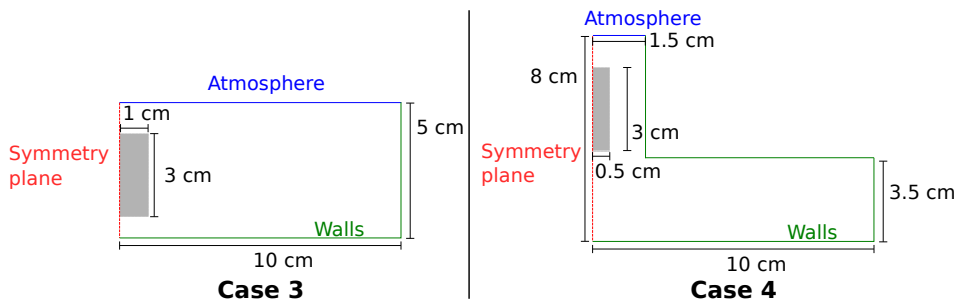

Fig. 6 Setup case 3 and 4, with dimensions and boundary conditions.

The studies were set as a 2^k study, where the cases had four factors each. The high and low values are given in table 9. The results from case 3 provided

Table 7 Boundary conditions for case 3, 4 and 5

Field	Atmosphere	Walls
Velocity	zero Gradient	No slip
Pressure	Fixed 0	Zero gradient
Phase fraction	Zero Gradient	Zero gradient

Table 8 Properties of system for case 3, 4 and 5.

Property	Symbol	Value case 3	Value case 4	Value case 5	Unit
Alumina density	ρ_a	Varies	1200	1200	kg m^{-3}
Bath density	ρ_b	-	-	2000	kg m^{-3}
Gas density	ρ_g	1	1	1	kg m^{-3}
Bath viscosity	ν_b	-	-	10^{-6}	m^2 s^{-1}
Gas viscosity	ν_g	$1.48 \cdot 10^{-5}$	$1.48 \cdot 10^{-5}$	$1.48 \cdot 10^{-5}$	m^2 s^{-1}
Gravity	g	9.81	9.81	9.81	m s^{-2}
Particle diameter	d	Varies	100	100	µm
Angle of repose	$\tan^{-1}\mu_1$	30	30	30	°
	$\tan^{-1}\mu_2$	Varies	Varies	60	°
	I_0	Varies	Varies	1	[-]
	μ_∞	-	0.05	0.05	[-]
	a	-	2.1	2.1	[-]
Drop height	h	0.5	Varies	0	cm

the basis for which parameters that will be pursued in case 4, where the fall height and the regularized model is introduced.

Table 9 Overview of the three cases ran for the column collapse

Property	Low	High	Used in case
$\tan^{-1}\mu_2$	40°	60°	3 and 4
I_0	0.1	1	3 and 4
d	20 µm	100 µm	3
ρ	800 kg m^3	1 200 kg m^3	3
h	2 cm	5 cm	4
Model	Original	Regularized	Case 4

Statistical analyses were conducted in Minitab, where the responses was set to be the final height of the column and an angle defined by the ratio height and length at y = 0.375 mm, sketched in figure 7.

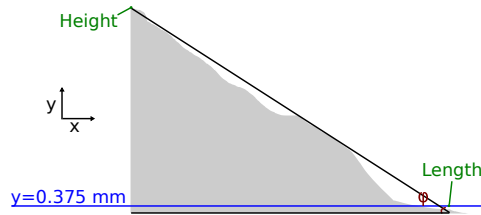The goal is to decide which factors, including interactions between them, that affect the shape significantly.

Fig. 7 Sketch illustrating how the length, height and angle ϕ are defined in case 3 and 4.

6.2 Case 5: Three-phase case

The case was simulating parts of the initial stage of alumina feeding, when the dose enters the molten bath, sketched in figure 8. The mesh is uniform with a cell size of 0.125 mm 4 cm to the left and right, while being graded to become more coarser further out. Time was in this case discretized with a forward Euler scheme, a cubic scheme for the gradients and Fromm's scheme for divergence. The walls at the sides are placed a long distance away to avoid unwanted reflections. One case was run with the μ(I)-rheology, with parameters stated in table 2, chosen based on experience from earlier results.

Two reference cases were ran, where the granular media was assumed to be a Newtonian fluid with kinematic viscosity respectively 10^{-6} m² s⁻¹ and 10^{-3} m² s⁻¹. The first case is to establish the differences between the developed model and liquid, while the other case with high viscosity is another possible approach to model the solid-state behavior occurring.
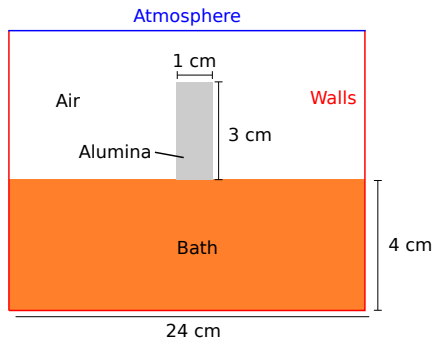

Fig. 8 Setup of case 5, including the initial and boundary conditions.

6.3 Case 6: Coupled case

Case 5 was further extended to account for the possibility for bath to solidify as it gets in contact with the cold dose. This has been investigated in earlier work [20] and only a brief introduction is therefore given.

The energy equation is introduced, written as

$$\frac{\partial}{\partial t}\left(\rho c_{p,m} T\right) + \nabla \cdot \left(\rho_m c_{p,m} \boldsymbol{u} T\right) = \nabla \cdot \left(k_m \nabla T\right) + S_h, \qquad (24)$$

where T is the temperature, while $c_{p,m}$ and k_m is respectively the phase average values of heat capacity and thermal conductivity. S_h is a source term that accounts for the change in entalphy due to the phase transition, written as

$$S_h = -\rho L \left[\frac{\partial g_s}{\partial t} + \nabla \cdot (\boldsymbol{u} g_s) \right]. \tag{25}$$

L is the latent heat of fusion, and g_s is the fraction of solidified bath, which is assumed to be isothermal and expressed as

$$g_s = \begin{cases} \alpha_b & \text{for } T < T_M, \\ 0 & \text{for } T > T_M, \end{cases} \tag{26}$$

where T_M is the melting point and α_b denotes the phase fraction of bath. A modified version of the momentum equation is written as

$$\frac{\partial}{\partial t} (\rho_m \boldsymbol{u}) + \nabla \cdot (\rho_m \boldsymbol{uu}) = \nabla \cdot \boldsymbol{\tau} - \nabla p + \rho_m \boldsymbol{g} + \boldsymbol{S}_d. \tag{27}$$

$\boldsymbol{S}_d$ dampens the relative velocity of the solidifying fluid towards zero, and is here implemented as a temperature dependent viscosity that gain a relatively large value when the fluid becomes solidified:

$$\boldsymbol{S}_d = \nu_{sol} \cdot \nabla^2 \boldsymbol{u}, \tag{28}$$

where ν_{sol} is dependent on temperature,

$$\nu_{sol} = \begin{cases} \alpha_b C_\nu & \text{for } T \leq T_M, \\ \alpha_b C_\nu \exp\left[\mathcal{A} \cdot (T_M - T)\right] & \text{for } T_M \leq T \leq T_L, \\ 0 & \text{for } T > T_L. \end{cases} \tag{29}$$

C_ν and $\mathcal{A}$ are user defined constants. In practice, the source term will add an imposed viscosity to the bath phase that increase exponentially from T_L and down to T_M, from zero to C_ν, where the exponential formulation is used in order to avoid numerical issues that can arise when the viscosity is rapidly increased.

The same initial conditions (figure 8) and properties (table 2) as for case 5 are used. The additional thermal properties are presented in table 10.

7 Results

7.1 Case 3: Initial parametric study

Owing to the dynamic nature of the formulation, the simulated fluids do not reach a complete halt within reasonable simulation times. A quasi-steady state is however reached at approximately 2 s, where the shape seems to be

Table 10 The additional thermal properties used for case 6.

Property	Symbol	Value	Unit
Alumina heat capacity	$c_{p,a}$	1200	J kg^{-1} °C^{-1}
Bath heat capacity	$c_{p,b}$	2200	J kg^{-1} °C^{-1}
Gas heat capacity	$c_{p,g}$	700	J kg^{-1} °C^{-1}
Alumina Thermal Conductivity	κ_a	8	W °C^{-1}m^{-1}
Bath Thermal Conductivity	κ_b	0.8	W °C^{-1}m^{-1}
Gas Thermal Conductivity	κ_g	0.02	W °C^{-1}m^{-1}
Latent Heat of Fusion	L	530 000	J kg^{-1}
Temperature constant	T_L	959	°C
Melting point	T_M	950	°C
Damping strength	C_ν	0.1	m^{2}s^{-1}
Constant	$\mathcal{A}$	1	-
Initial temperature	T_i	960	°C
Initial temperature alumina	T_a	100	°C

stabilized. Changing μ_2 had the largest effect on the angle with a relative contribution of 42.2 %, followed by I_0 (30.8 %), d (13.1 %) as well as the interactions $\mu_2 \cdot I_0$ (8.4 %) and $\mu_2 \cdot d$ (4.5 %). Their contributions are visualized in figure 9, where a) displays the main effects, while b) and c) respectively shows the interactions $\mu_2 \cdot I_0$ and $\mu_2 \cdot d$
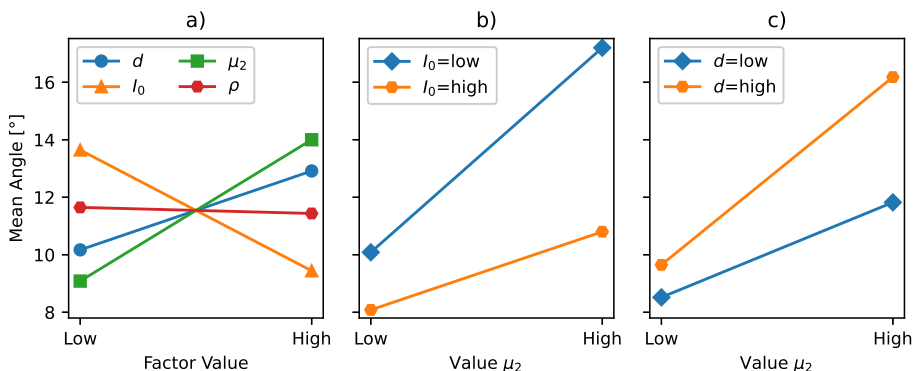

Fig. 9 Plots illustrating how the different parameters affect the final angle of the heap in case 3, measured as illustrated in figure 7. a) the main effects. b) The interaction plot between μ_2 and I_0. c) The interaction plot between μ_2 and d. The values of "high" and "low" are stated in table 9.

7.2 Case 4: Extended parametric study

Figure 11 shows a factorial plot for the main effects. The statistical analysis found that μ_2 had the highest relative contribution on the angle with 44.75 %, followed by I_0 (32.22 %) $\mu_2 \cdot I_0$ (11.57 %) and h (8.78 %). Figure 12 shows a comparison between the original an regularized model, while table 11 shows the difference in angles between them for all cases.
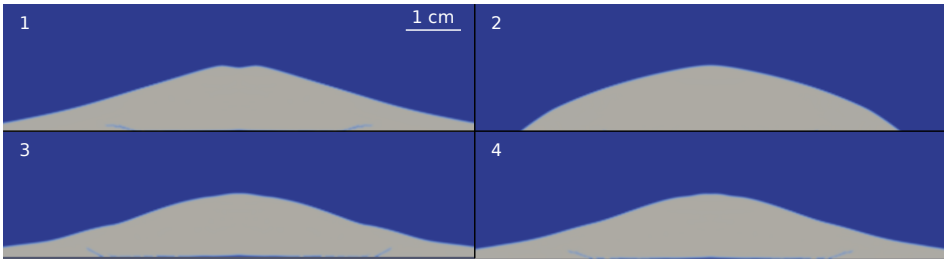
Fig. 10 Heaps of powder after 2 s, an assumed steady state. 1: All factors are high. 2: μ_2 and d high, I_0 and ρ low. 3: μ_2 and d low, I_0 and ρ high. 4: All factors are low.
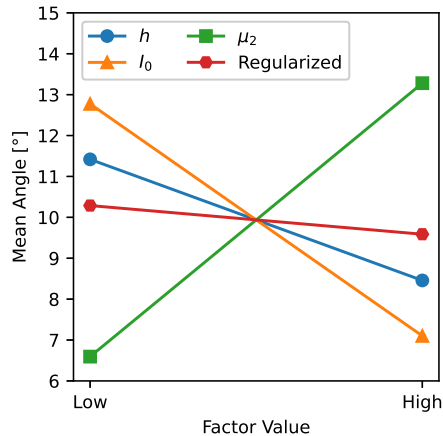

Fig. 11 Plot illustrating how the different factors in case 4 affect the angle of the heap, measured as showed in figure 7. The values of "high" and "low" are stated in table 9.
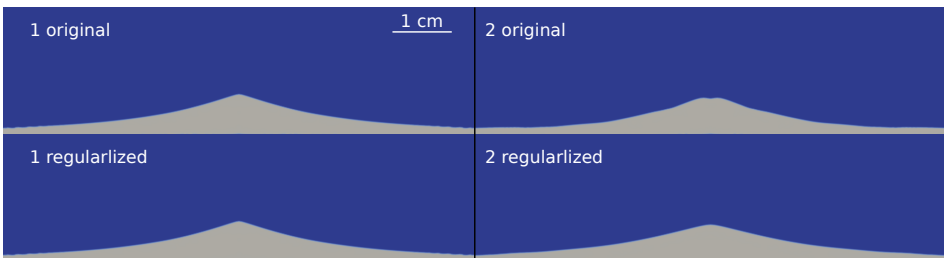

Fig. 12 Heaps of powder after 2 s, an assumed steady state for the original model (upper) and regularized model (below). 1 All other factors are set to their "high" value. 2: μ_2 is "low", h and I_0 are "high" cf. table 9 for numerical values corresponding to "high" and "low".

7.3 Three-phase cases

Snapshots of the μ(I)-rheology is shown in figure 13, compared with the reference cases. The dose with low viscosity (left) spreads out fast, and parts of the dose flow out of the image. For a high viscous fluid (right), the dose is held together in one piece, which is spread out due to the back wave approaching

Table 11 The measured angles and their difference for the original and regularized μ(I)-model. + represents that th factor is set to a high value, while - is for a low value.

h	I_0	μ_2	Original	Regularized	Difference
+	+	+	7.54	6.85	0.68
+	+	-	4.87	4.52	0.36
+	-	+	16.66	16.66	0
+	-	-	5.40	5.14	0.27
-	+	+	10.50	10.08	0.43
-	+	-	7.57	4.87	2.70
-	-	+	19.26	18.68	0.58
-	-	-	10.49	9.90	0.59

at t=0.3. When the μ(I)-rheology is applied (center), small parts are dispersed into the melt, while two big pieces detach from the main dose at t=0.4.
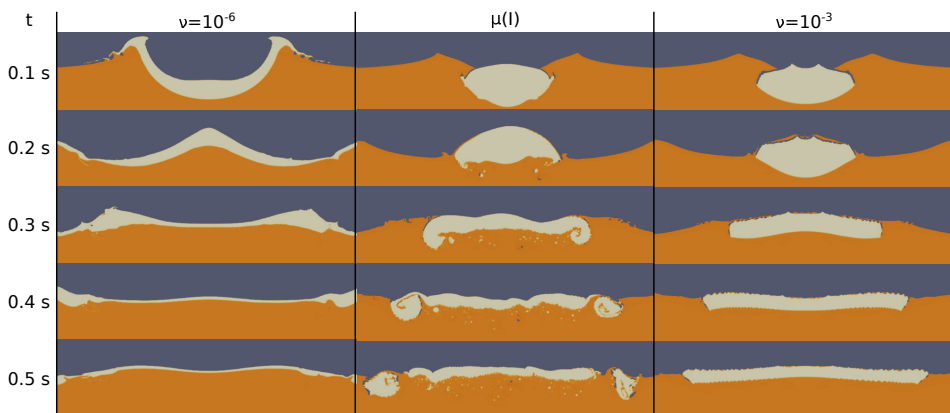
Fig. 13 The phase compositions of blue bath (orange), alumina (beige), air (gray) for selected times, for the following cases: left: Newtonian fluid with $\rho = 1200$ and $\nu = 10^{-6}$. Center: Fluid with the μ(I)-properties given in table 8. Right: Newtonian fluid with $\rho = 1200$ and $\nu = 10^{-3}$.

7.4 Coupled case

Selected images for the coupled case are shown in figure 14. There is a slight difference in behavior for the case with freezing. Solidification of bath holds the two chunks which were detached together, and it spreads out 8.2 cm in this case, versus 9.1 cm, hence exhibiting the desired damping effect.

8 Discussion

When μ_2 increases, a higher value of $\mu(I)$ (ref eq (6)), and hence a larger value of ν can be obtained. The increased viscosity in the powder will decrease its ability to spread out. The same tendency can be seen from I_0 and d. Increasing I_0 will decrease the value of $\mu(I)$ and ν, while an increase of d will increase $\mu(I)$,
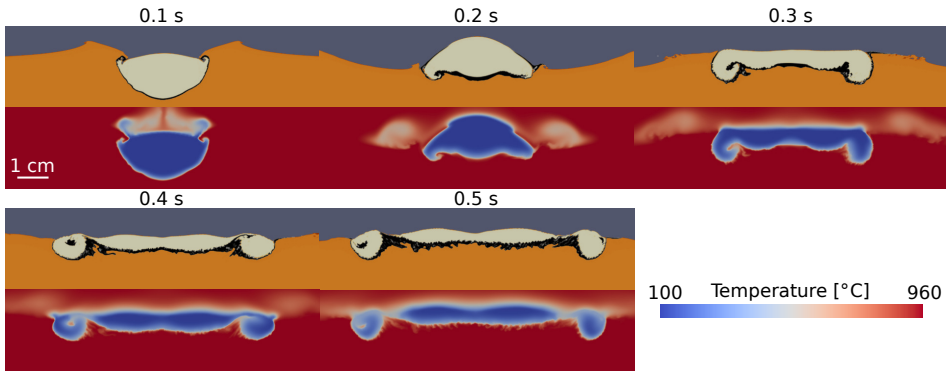
Fig. 14 Phase composition of bath (orange), alumina (beige), air (gray) and bath (black), and temperature field for the coupled case for selected times.

which can be seen by inserting (7) into (6). μ_2 will increase the possible value $\mu(I)$ while I_0 and d only affect the possible value created, which explain the two interaction effects. ρ was discarded from the model due to low effect. It will have the same effect as d, but since it is affected in lesser magnitude, its effect on $\mu(I)$ will be smaller. The same tendencies for μ_2, I_0 and its interactions are seen in case 4. The increase of spreading with increased drop height is also expected, as higher velocity for the powder when hitting the surface leads to larger spreading of powder.

Applying the regularized model reduced the final angle of the heap, table 11, and the shape will for some cases also be slightly different, as seen on the right images in figure 12. However, the model did not have a significant impact relative to the other factors in this work. Using the regularized model on case 3 would probably not have changed the results significantly, but it will be applied for the further cases.

The particle size d and density ρ have in these cases quite obvious interpretations for the case of alumina. d will not be uniform and must be interpreted as the average value of a selected dose. The values are however not completely independent of each other. For example, reducing the particle size, d, is found to decrease the flowability of alumina and hence increasing the angle of repose [37], here interpreted as μ_1. The chosen value in this work (30°) represents an alumina with a quite good flowability [37], and hence the particle diameter is expected to be high. μ_2 and I_0 do not have such a straightforward interpretation, and estimates of their values for alumina do not exist. This was the reason for large range when setting their "high" and "low" values in case 3 and 4, ultimately also resulting in high relative effects.

There is limited available experimental data that can be used for comparison of the current cases. Recent images from a master thesis [38], where alumina was released from a pipe onto a flat plate gave angles at approximately 10°. However, the images are not completely suitable for measuring angles. More experiments should therefore be carried out in order to determine parameters. As mentioned above, parameter dependence will probably occur

and the particle size should therefore be varied in order to get an overview on the range the values might have.

The three-phase cases in figure 13 show that the µ(I)-rheology has a different behavior than a Newtonian fluid. The created wave will stretch the dose out and for the µ(I)-rheology, smaller parts segregate from the created rafts and flakes seem to disperse into the bath. From previous studies of feeding in a water model [14], a similar tendency with bigger parts of the dose floating away was seen when no convection was applied. Further, dispersion of particle as so called snowing has been observed earlier in a see-through cell [17].

Simulating the dose as a high viscous fluid, showed at the rightmost column in figure 13, is also presented as a possible approach. It is easier to execute, but it did not allow for parts of the dose to detach, both as smaller flakes and bigger lumps. The resulting raft structure seen at t=0.5 s is uniform for the viscous fluid, while lab experiments [15] suggest that the structure is more irregular,and thus more similar to the structure achieved by the µ(I)-rheology.

The results from the coupled case (figure 14) illustrate the two developed models can be coupled together. The frozen bath will create a coherent raft and measurements show that in the freezing model slightly dampens the movement. In this case, no smaller parts of powder have detached from the raft, which was the case when only the µ(I)-rheology was applied. In this setup, the initial contact between bath and alumina will cause freezing to occur immediately, hence limiting the contact between alumina and the liquid bath. That might not be the case if the dose had been released from larger height.

9 Conclusion and further work

A framework for simulating the alumina dose through the µ(I)-rheology has been implemented verified and demonstrated in OpenFOAM. The verification is in good agreement with analytical solutions (less than 0.1% error on average) and a benchmark case (less than 8 % error on average).

The parametric studies highlight that the model is quite sensitive with regards to the rheology parameters I_0 and μ_2, which have not been measured for alumina yet. Experiments are needed in order to quantify these parameters further, as well as their dependency on other material parameters.

The two and three-phase cases illustrate that the µ(I)-rheology exhibits some of the desired features which cannot be realized using a simpler high viscosity Newtonian fluid approach. In particular, the ability to produce a heap-like structure with an actual angle of repose, as well as the complex interaction with fluid surfaces, forming non-uniform rafts and detachment of smaller pieces are qualitatively in good agreement with what is expected from practice.

Coupling the rheology with a model allowing for bath to freeze was successful, and shows that frozen bath will form in areas between the alumina pieces, hence creating a larger coherent raft compared with only applying the µ(I)-rheology. The freezing of bath did also in this case have a limiting effect

on the raft shape. Several other sub models should be implemented in further work, such as infiltration of bath and allowing for the powder to dissolve.

While some characteristics relating to alumina feeding are still not implemented, our opinion is that continuum scale models with advanced rheologies could serve as basis for further investigations.

Declarations

The authors declare no conflict of interest.

References

[1] P. Lavoie, M.P. Taylor, and J.B. Metson: *Metall Mater Trans B*, 2016, vol. 47, pp. 2690–6.

[2] S.E. Gylver, N.H. Omdahl, S. Rørvik, I. Hansen, A. Nautnes, S.N. Neverdal, and K.E. Einarsrud: *Light Metals 2019*, 2019, pp. 689–96.

[3] Bardet, T. Foetisch, S. Renaudier, J. Rappaz, M. Flueck, and M. Picasso: *Light Metals 2016*, 2016, pp. 315–9.

[4] V. Bojarevics and M. Dupuis: *Light Metals 2022*, 2022, pp. 339–48.

[5] L. Dion, L.I. Kiss, S. Poncsák, and C.-L. Lagacé: *Metall Mater Trans B*, 2018, vol. 49, pp. 737–55.

[6] S.T. Johansen, K.E. Einarsrud, A. Solheim, and K.J. Vachaparambil: *Light Metals 2022*, 2022, pp. 503–11.

[7] S. Zhan, M. Jiang, J. Wang, and J. Yang: *Trans. Nonferrous Met. Soc. China*, 2021, vol. 31, pp. 3579–90.

[8] R.G. Haverkamp and B.J. Welch *Chem. Eng. Process.*, 1998, vol. 37, pp. 177–87.

[9] Kovács, C.J.W. Breward, K.E. Einarsrud, S.A. Halvorsen, E. Nordgård-Hansen, E. Manger, A. Münch, and J.M. Oliver: *Int. J. Heat Mass Transfer*, 2020, vol. 162, p. 120232.

[10] V. Dassylva-Raymond, L.I. Kiss, S. Poncsak, P. Chartrand, J.-F. Bilodeau, and S. Guérard: *Light Metals 2014*, 2014, pp. 603–8.

[11] R. Hovland, S. Rolseth, and A. Solheim: *Proc. of the Intl. Symp. on Light Metals Processing and Applications*, pp 3-16.

[12] C. Kaszás, L. Kiss, S. Guérard, and J.-F. Bilodeau: *Light Metals 2015*, 2015, pp. 639–42.

[13] S.E. Gylver, N.H. Omdahl, A.K. Prytz, A.J. Meyer, L.P. Lossius, and K.E. Einarsrud: *Light Metals 2019*, 2019, pp. 659-666.

[14] Gylver, S. Aase, S. Bekkevoll, S.A.K. Forberg, and K.E. Einarsrud: *Light Metals 2022*, 2022, pp. 357–62.

[15] S.E. Gylver, A. Solheim, H. Gudbrandsen, Å.H. Follo, and K.E. Einarsrud: *Light Metals 2020*, 2020, pp. 659–63.

[16] A.N. Bagshaw and B.J. Welch: *Essential Readings in Light Metals*, vol. 1, 2016, pp. 783–7.

[17] L. Bracamonte: PhD, Norwegian University of Science and Technology, 2022.

[18] T. Roger, L. Kiss, L. Dion, S. Guérard, J.F. Bilodeau, G. Bonneau, R. Santerre, and K. Fraser: *Light Metals 2022*, 2022, pp. 363–70.

[19] K.E. Einarsrud, I. Eick, W. Bai, Y. Feng, J. Hua, and P.J. Witt: *Applied Mathematical Modelling*, 2017, vol. 44, pp. 3–24.

[20] S.E. Gylver and K.E. Einarsrud: *Light Metals 2023*, in press.

[21] P. Jop, Y. Forterre, and O. Pouliquen: *Nature*, 2006, vol. 441, pp. 727–30.

[22] OpenCFD: OpenFOAM® - Official home of The Open Source Computational Fluid Dynamics (CFD) Toolbox, http://www.openfoam.com, Accessed May 6, 2019.

[23] E.P. Montellà, J. Chauchat, B. Chareyre, C. Bonamy, and T.J. Hsu: *J. Fluid Mech.*, 2021, vol. 925, p. A13.

[24] J. Chauchat, Z. Cheng, T. Nagel, C. Bonamy, and T.-J. Hsu: *Geosci. Model Dev.*, 2017, vol. 10, pp. 4367–92.

[25] T. Barker, M. Rauter, E.S.F. Maguire, C.G. Johnson, and J.M.N.T. Gray: *J. Fluid Mech.*, 2021, vol. 909, p. A22.

[26] D. Gidaspow: *Multiphase Flow and Fluidization: Continuum and Kinetic Theory Descriptions*, Academic press, San Diego, 1994.

[27] GDR MiDi: *Eur. Phys. J. E*, 2004, vol. 14, pp. 341–65.

[28] M. Tankeo, P. Richard, and É. Canot: *Granular Matter*, 2013, vol. 15, pp. 881–91.

[29] P. Jop, Y. Forterre, and O. Pouliquen: *J. Fluid Mech.*, 2005, vol. 541, p. 167.

[30] P.-Y. Lagrée, L. Staron, and S. Popinet: *J. Fluid Mech.*, 2011, vol. 686, pp. 378–408.

[31] T. Barker and J.M.N.T. Gray: *J. Fluid Mech.*, 2017, vol. 828, pp. 5–32.

[32] R.B. Bird: *Transport Phenomena*, 2nd ed., Wiley, New York, 2002.

[33] C.W. Hirt and B.D. Nichols: *J. Comput. Phys.*, 1981, vol. 39, pp. 201–25.

[34] C. Greenshields and H. Weller: Notes on Computational Fluid Dynamics: General Principles, https://doc.cfd.direct/notes/cfd-general-principles/, Accessed 19 Sept 2022.

[35] Jarosch A.: Incompressible μ(I) rheology for OpenFOAM, https://github.com/alexjarosch/OpenFOAM-muI, Accessed 19 Sept 2022.

[36] K. Grjotheim and H. Kvande, eds.: *Introduction to Aluminium Electrolysis*, Aluminium-Verlag, Düsseldorf, 1993, pp. 61-86.

[37] B.E. Raahauge and F.S. Williams, *Smelter Grade Alumina from Bauxite: History, Best Practices, and Future Challenges*, Springer, Cham, 2022, pp. 577–648.

[38] S. Bekkevoll: MSc, Norwegian University of Science and Technology, 2022.

NTNU
Norwegian University of
Science and Technology